Ultrafast Dynamics in Ferromagnetic and Synthetic Ferrimagnet Materials

A thesis submitted in fulfilment of the requirements for the degree of Doctor of Philosophy in Physics to the

University of Exeter

August 2023

Author:

Connor R. J. Sait

Supervisors:

Robert J. Hicken

Paul S. Keatley

Maciej Dąbrowski

Declaration of Authorship

- Submitted by Connor Sait to the University of Exeter as a thesis for the degree of Doctor of Philosophy in Physics, Friday 14th April, 2023.
- This thesis is available for Library use on the understanding that it is copyright material and that no quotation from the thesis may be published without proper acknowledgement.
- I certify that all material in this thesis which is not my own work has been identified and that any material that has previously been submitted and approved for the award of a degree by this or any other University has been acknowledged.

Signed:

Date:

Abstract

In this thesis, investigations into the ultrafast dynamics of magnetic materials are presented.

The first of these is a study of the magnetisation dynamics predicted by an extended form of the Heisenberg model of ferromagnetism. The extension to the model consists of a reservoir of harmonic oscillators coupled to each spin, following from techniques used within the study of open quantum systems. The equations of motion are derived and the fluctuation dissipation relation is shown to be satisfied regardless of the specific form of coupling between the spins and reservoir. For an 'Ohmic' coupling in the limit of high temperature, the Landau Lifshitz Gilbert equation of spin dynamics with white noise thermal fluctuations is recovered. A 'Lorentzian' coupling is introduced which also converges to the Landau Lifshitz Gilbert dynamics under specific conditions. More generally, this form of coupling leads to different behaviour including non-Markovian dynamics and coloured noise thermal fluctuations. The equations of motion are then made semi-classical and numerically integrated under different conditions for a single spin system, highlighting the changes to both the dynamics and equilibrium behaviour predicted by a more general and quantum mechanically motivated model of spin dynamics.

The second investigation looks at the properties of [Ni/Pt]/Ir/Co transition metal synthetic ferrimagnets, and their capacity for all optical switching. These materials and their constituent layers are characterised using wide field Kerr microscopy, bringing to light their complex and highly temperature sensitive properties. A laser is introduced to this setup and used to establish the conditions necessary for all optical switching of the magnetisation state of the synthetic ferrimagnets. In addition, time resolved Kerr microscopy measurements are presented, showing the magnetisation dynamics on both precessional and ultrafast timescales, and offering information on the mechanism behind all optical switching in these systems.

The third investigation is on the development of microcoil devices for use in ultrafast time resolved measurement setups of magnetic materials. The characterisation of these devices is presented, along with magneto-optical measurements which show their potential for the generation of magnetic field pulses of sufficient strength to reset (i.e. saturate) magnetic samples between pulse-probe measurements.

Acknowledgements

Firstly, I would like to thank the members of my wonderful research group who have given me so much. I would like to thank Rob Hicken for his incredible support, understanding, and guidance in all aspects of my development as a researcher. Maciej Dąbrowski for his great help in improving my capabilities as an experimentalist, reader and writer. Paul Keatley for his assistance in the lab and the time taken to broaden my understanding as an experimentalist. Tom Loughran for much of the same and for various enjoyable and interesting conversations on science and philosophy. Additional thanks to Simon Horsley for his support and guidance in mathematics and theoretical physics and for his infectious positivity and excitement in discussing those topics. Thank you to all those I have worked with who have driven my development through collaboration, discussion, training and the sharing of their time and skills, I appreciate it all!

I would like to thank everybody who has shown me friendship and encouragement over the years, both during my time in Exeter and on my journey here. I am especially grateful to Kavya Palakot who has been there for me throughout my time in Exeter and shown me huge love, encouragement and support which has helped drive my success as a person. Thank you to my family, who have supported me and believed in me from the very beginning.

Thank you to those who have made the XM^2 Centre for Doctoral Training what it is. I've thoroughly enjoyed my time as a member of this group of researchers and I recognise the hard work put in by the Ph.D. candidates, lecturers and admin team to foster such a strong environment for growth and development. I would like to acknowledge the funding provided via the EPSRC Centre for Doctoral Training in Metamaterials (Grant No. EP/L015331/1).

Contents

List of Figures

List of Tables

List of Acronyms

3TM	Three Temperature Model
AFM	Antiferromagnet/Antiferromagnetic
AOS	All Optical Switching
AP	Antiparallel
ASD	Atomistic Spin Dynamics
CAD	Computer Aided Design
CMOS	Complimentary Metal Oxide Semiconductor
CNC	Computer Numerical Control
FDR	Fluctation Dissipation Relation
FFT	Fast Fourier Transform
FM	Ferromagnet/Ferromagnetic
HAMR	Heat Assisted Magnetic Recording
HD-AOS	Helicity Dependent All Optical Switching
HDD	Hard Disk Drive
HI-AOS	Helicity Independent All Optical Switching
IEC	Interlayer Exchange Coupling
IFE	Inverse Faraday Effect
LCP	Left Circularly Polarised
LED	Light Emitting Diode
LIA	Lock In Amplifier
LL	Landau-Lifshitz
LLG	Landau-Lifshitz-Gilbert
LLGB	Landau-Lifshitz-Gilbert-Brown
M3TM	Microscopic Three Temperature Model
MCD	Magnetic Circular Dichroism
MOFE	Magneto Optical Faraday Effect
MOKE	Magneto Optical Kerr Effect
NR	Negative Remanence

OPA	Optical Parametric Amplifier
P	Parallel
PMA	Perpendicular Magnetic Anisotropy
PSD	Power Spectral Density
RCP	Right Circularly Polarised
RE	Rare Earth
RKKY	Ruderman-Kittel-Kasuya-Yosida
RT	Room Temperature
SFi	Synthetic Ferrimagnet
SQUID	Superconducting Quantum Interference Device
TM	Transition Metal
TR-MOKE	Time Resolved Magneto Optical Kerr Effect
VSM	Vibrating Sample Magnetometer
WFKM	Wide Field Kerr Microscope / Wide Field Kerr Microscopy
XMCD	X-ray Magnetic Circular Dichroism

Physical Constants

Label	*Symbol*	*SI Value*
Electron gyromagnetic ratio	$\lvert\gamma_e\rvert$	$1.761 \times 10^{11}\ \frac{\mathrm{rad}}{\mathrm{s \cdot T}}$
Electron mass	m_e	$9.109 \times 10^{-31}\ \mathrm{kg}$
Elementary charge	e	$1.602 \times 10^{-19}\ \mathrm{C}$
Reduced Planck constant	$\hbar$	$1.055 \times 10^{-34}\ \mathrm{J \cdot s}$
Boltzmann constant	k_B	$1.381 \times 10^{-23}\ \frac{\mathrm{J}}{\mathrm{K}}$
Bohr magneton	μ_B	$9.274 \times 10^{-24}\ \frac{\mathrm{J}}{\mathrm{T}}$
Vacuum permeability	μ_0	$1.256 \times 10^{-6}\ \frac{\mathrm{T \cdot m}}{\mathrm{A}}$

SI Units

Unit	*Symbol*	*Base Units*
Second	s	s
Tesla	T	$\frac{\mathrm{kg}}{\mathrm{s^2 \cdot A}}$
Joule	J	$\frac{\mathrm{kg \cdot m^2}}{\mathrm{s^2}}$
Kilogram	kg	kg
Ampere	A	A
Coulomb	C	$\mathrm{A \cdot s}$
Metre	m	m
Kelvin	K	K

Chapter 1

Introduction

With the advent of modern computing technology, magnetic materials were identified as ideal media for storage of machine instructions and other computational data. This step was a natural evolution of the previous usage of magnetic wire, ribbons and tape to record audio signals [1] for use in radio broadcasting and telecommunications and video footage for use in television broadcast and cinematography. The use of ferromagnetic materials (i.e. those in which magnetic moments align through the exchange interaction, see section 2.1) for computational data storage has ranged from magnetic drums, magnetic tape, magnetic core and magnetoresistive random access memory, and floppy disks drives, to the continually improving magnetic hard disk drives (HDD's) which remain in wide use as computer data storage in the modern era. Innovations in magnetic HDD's have led to an exponential rate of increase in areal density as shown in figure 1.1.

The problems associated with further increasing areal density of magnetic hard disks are encapsulated by a concept known as the magnetic recording trilemma, based on conflicting requirements between the signal to noise ratio, writeability and thermal stability of a medium [4]. The conflict can be explained as follows. The crystal structure of a magnetic material is split into small grains which act as single domain particles in the limit of maximum signal to noise ratio. Increased areal density therefore requires smaller magnetic grains, however a reduction in the size of grains reduces their thermal stability (i.e. the ability of the grain to retain its magnetisation over time). To improve the thermal stability, anisotropy of the grains must be increased. In doing so, the fields required to write data is raised. The fields and therefore areal density achieviable is limited by the magnitude of fields that a magnetic write head can produce, and is estimated to have an upper bound on the order of 2 Tesla.

One branch of proposed solutions to the trilemma is that of magneto optical recording methods. Heat assisted magnetic recording (HAMR) is one such solution which uses a laser to provide heat which reduces the magnetisation and allows easier reversal of the grains by the write field. A technique known as all optical switching

(a)

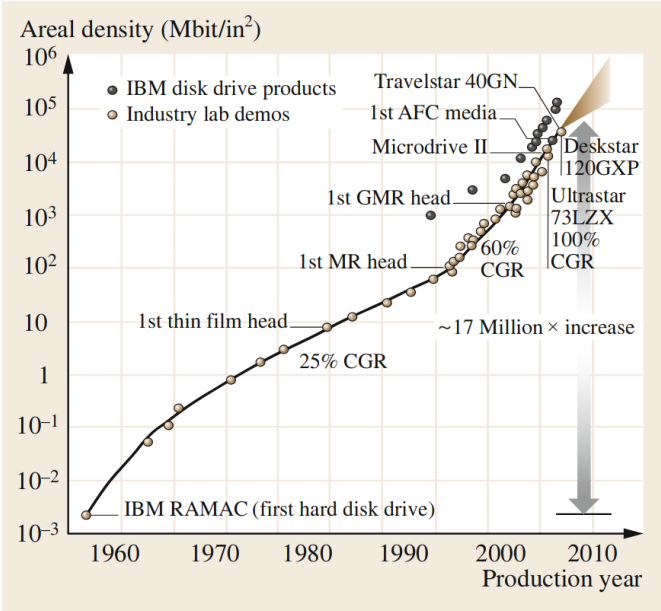

(b)

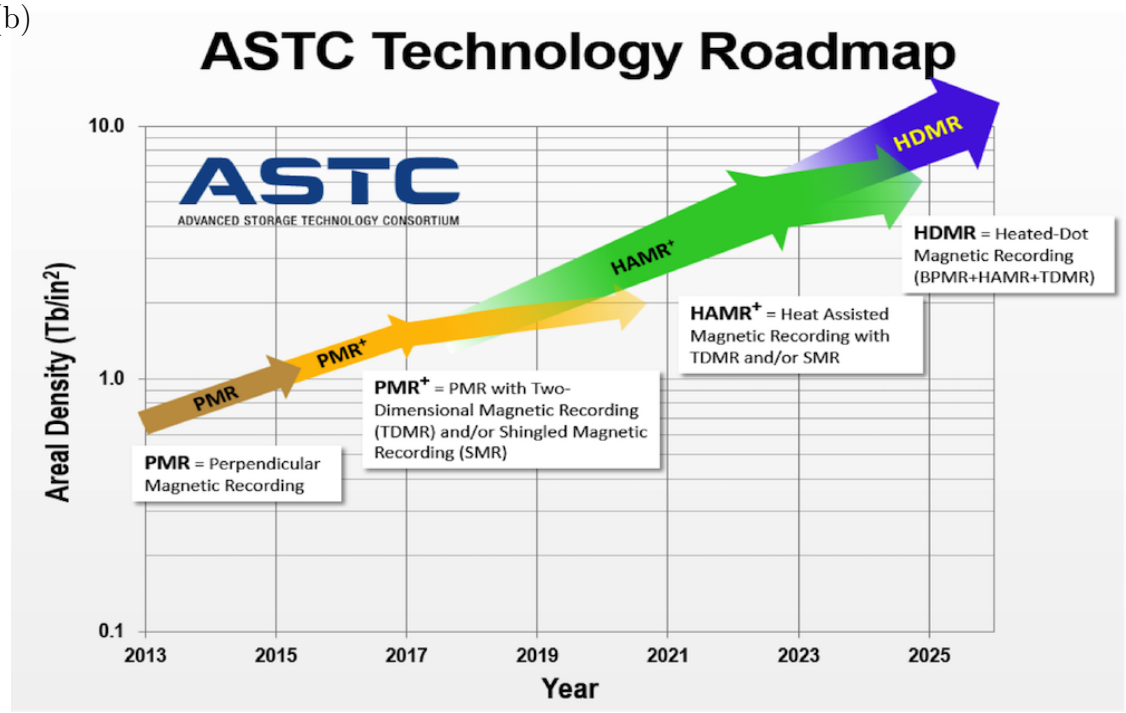

Figure 1.1: Improvements in HDD areal density over time. Panel (a) shows past improvements in areal density from the perspective of IBM, reproduced from [2]. Panel (b) shows the roadmap for improvements predicted by the 'Advanced Storage Technology Consortium' in 2017, reproduced from [3].

(AOS) in which electromagnetic radiation reverses the direction of magnetisation in the absense of an external magnetic field, is believe the provide a different solution to the recording trilemma through the generation of effective magnetic fields greater than those available from conventional write heads.

Only a limited number of samples have shown the AOS effect, and for those that do there are often additional constraints on their implementation in commercial technologies (such as high cost and rarity of materials, poor perpendicular magnetic anisotropy, low temperature requirements etc.). One category of materials which has shown promise is that of ferrimagnets, which are materials with a net total magnetisation in which the magnetic moments can be identified as belonging to one of two populations. Within each population the magnetic moments are aligned, but between them the moments are anti-aligned. The rare-earth based GdFeCo is an example of a ferrimagnet which has shown a strong switching response to all optical exposure [5]. In that alloy the two spin populations take the form of ferromagnetic Gd and FeCo sublattices, with AOS resulting as a thermal effect owing to the different demagnetisation rates of the sublattices [6, 7]. In that system, the FeCo sublattice demagnetises much faster than the Gd, following which a transient ferromagnetic state appears as a result of antiferromagnetic (AFM) type exchange interaction from Gd spins that continue to reverse. In the transient ferromagnetic state the Gd sublattice continues to demagnetise and eventually also switches as a reult of the continued AFM type exchange interaction. Multilayered structures also make good candidates for AOS materials due to their large perpendicular magnetic anisotropy which allows for improved areal density [2], and due to the tunability of their magnetic and magneto-optical properties through the choice of layer thickness. Synthetic ferrimagnets are ferrimagnets in which the two populations of moments make up seperate layers in a multilayer structure and therefore make another good candidate for similar reasons, along with the ability to tune the exchange coupling between layers. These systems have already been shown to be capable of AOS [8], but their full potential remains unexplored due to the overwhelming number of sample possibilities and relative recency of the field of study. Methods used to grow and characterise such samples continue to be refined, improving control over their properties.

In the search for all optical switching materials, wide field Kerr microscopy has become a popular tool. This technique can be used in combination with an ultrafast laser source to determine the properties of both sample and laser source required to observe the effect. The study of AOS was conceptualised after the observation of ultrafast demagnetisation [9] showed the capacity for magnetic manipulation on sub-picosecond timescales. Time resolved magneto optical Kerr microscopy using an ultrafast pump-probe measurement procedure has been a widely utilised method in the study of ultrafast spin dynamics since the earliest reported observations of this

effect [9]. The technique has been useful in making observations of many ultrafast magnetic phenomena, but requires a non standard method of magnetic state reset in order to make all optical switching measurements of a material at remanence.

One such method is to use a reset field from a pulsed microcoil system. A saturating (i.e. the magnetic moments in the material become fully aligned) pulsed field from a microcoil, where pulses occur between pump-probe measurements, is able to reset the sample to the same initial state for each measurement. The measurement of optical excitation can then occur at remanence without the additional effect of an external biasing field.

The processes discussed highlight how magnetisation dynamics occur on ultrafast, sub-picosecond time scales. Numerical simulations of magnetisation dynamics must therefore be integrated on the ultrafast timescale to capture a complete picture of the behaviour. Atomistic spin dynamics is a powerful numerical tool for the simulation of magnetisation dynamics. However, it was found that to match with experimentally observed ultrafast dynamics, a temperature rescaling procedure must be performed [10]. To improve our understanding of magnetic materials, it will be important to determine the reason why procedures like this are necessary to correctly predict their behaviour.

Within this thesis, the theories underpinning these numerical simulations of magnetic systems will be examined. In addition, the search for all optical switching behaviour within the transition metal synthetic ferrimagnet [Ni/Pt]/Ir/Co, and characterisation of its domains and other properties will be pursued through wide field Kerr microscopy measurements. Time resolved magneto optical Kerr effect measurements will also be presented as a tool to explore their ultrafast and precessional dynamics. Finally, a microcoil that is being developed for use in pump-probe setups will be introduced and characterised.

The contents of this thesis is arranged into seven chapters.

- In the second chapter an overview of concepts in the study of magnetism, magneto optics and open quantum systems is given. The quantum mechanical origins of ferromagnetism are discussed, along with the different contributions to the energy of ferromagnetic and synthetic ferrimagnet systems. The Heisenberg model of ferromagnetism is shown to predict precessional dynamics, and the Landau-Lifshitz-Gilbert equation is introduced as a more complete form of spin dynamics including a damping term. The Langevin equation is introduced as a simple model of dissipative dynamics, and the fluctuation dissipation theorem is introduced as a necessary condition in physical systems. Atomistic spin dynamics software is introduced as a predictive tool for magnetisation dynamics, and potential issues with the underlying model are discussed. Concepts relating to the polarisation of light are introduced and their relevance to the experimental magneto optical Faraday and Kerr effects are outlined. Fi-

nally, literature in the field of ultrafast magnetisation is discussed in sections on ultrafast demagnetisation and all optical switching of magnetic materials.

- In the third chapter, the setups used to perform experimental work are outlined and discussed. The techniques discussed are those of the vibrating sample magnetometer, wide field Kerr microscopy, time resolved magneto optical Kerr effect measurements, x-ray magnetic circular dichroism, and a magneto optical setup used to characterise microcoil devices. The calibration and usage of these systems are discussed, along with other details relevant to the interpretation of experimental data.

- The fourth chapter discusses the results of a theoretical investigation into magnetisation dynamics predicted by the Heisenberg model in combination with a model from the study of open quantum systems. This extended quantum Heisenberg model is used to derive the generalised equations of motion for a spin system, and the spin dynamics under specific conditions are shown and explained for a single spin in a semi-classical approach.

- The fifth chapter gives an account of experimental work performed on synthetic ferrimagnets in the search for materials suitable for all optical switching.

- The chapter focuses on the transition metal synthetic ferrimagnet [Ni/Pt]/Ir/Co and its constituent ferromagnetic layers. Samples are characterised using several techniques including wide field Kerr microscopy, which is used to determine their hysteresis and domains with respect to temperature. The effects of all optical exposure are then explored to determine the conditions required for all optical switching. Time resolved measurements of the magnetisation dynamics are also explored, building on the understanding of ultrafast optical manipulation for these systems.

- In the sixth chapter, an account of the development of a microcoil device is given. The devices are characterised by their voltage waveforms and different prototypes are compared and iterated upon to maximise their efficiency. The latest prototype is then explored within a magneto-optical setup, to explore the usefulness of these devices for the generation of short magnetic field pulses that could be implemented into time resolved pump-probe setups.

- The seventh chapter summarises the works shown within this thesis and makes suggestions for future works to be performed.

References

[1] James D. Livingston. 100 Years of Magnetic Memories. *Scientific American*, 279(5):106–111, 1998.

[2] Charbel Tannous and R. Lawrence Comstock. Magnetic Information-Storage Materials. In *Springer Handbook of Electronic and Photonic Materials*, Springer Handbooks. Springer International Publishing, Cham, 2017.

[3] John Paulsen. HAMR: The Next Leap Forward is Now. https://blog.seagate.com/craftsman-ship/hamr-next-leap-forward-now/, October 2017.

[4] R. F. L. Evans, R. W. Chantrell, U. Nowak, A. Lyberatos, and H.-J. Richter. Thermally induced error: Density limit for magnetic data storage. *Applied Physics Letters*, 100(10):102402, March 2012.

[5] C. D. Stanciu, F. Hansteen, A. V. Kimel, A. Kirilyuk, A. Tsukamoto, A. Itoh, and Th. Rasing. All-Optical Magnetic Recording with Circularly Polarized Light. *Physical Review Letters*, 99(4):047601, July 2007.

[6] I. Radu, K. Vahaplar, C. Stamm, T. Kachel, N. Pontius, H. A. Dürr, T. A. Ostler, J. Barker, R. F. L. Evans, R. W. Chantrell, A. Tsukamoto, A. Itoh, A. Kirilyuk, Th Rasing, and A. V. Kimel. Transient ferromagnetic-like state mediating ultrafast reversal of antiferromagnetically coupled spins. *Nature*, 472(7342):205–208, April 2011.

[7] T. A. Ostler, J. Barker, R. F.L. Evans, R. W. Chantrell, U. Atxitia, O. Chubykalo-Fesenko, S. El Moussaoui, L. Le Guyader, E. Mengotti, L. J. Heyderman, F. Nolting, A. Tsukamoto, A. Itoh, D. Afanasiev, B. A. Ivanov, A. M. Kalashnikova, K. Vahaplar, J. Mentink, A. Kirilyuk, Th Rasing, and A. V. Kimel. Ultrafast heating as a sufficient stimulus for magnetization reversal in a ferrimagnet. *Nature Communications*, 3, 2012.

[8] S. Mangin, M. Gottwald, C. H. Lambert, D. Steil, V. Uhlíř, L. Pang, M. Hehn, S. Alebrand, M. Cinchetti, G. Malinowski, Y. Fainman, M. Aeschlimann, and E. E. Fullerton. Engineered materials for all-optical helicity-dependent magnetic switching. *Nature Materials*, 13(3):286–292, February 2014.

[9] E. Beaurepaire, J. C. Merle, A. Daunois, and J. Y. Bigot. Ultrafast spin dynamics in ferromagnetic nickel. *Physical Review Letters*, 76(22):4250–4253, May 1996.

[10] R. F. L. Evans, U. Atxitia, and R. W. Chantrell. Quantitative simulation of temperature-dependent magnetization dynamics and equilibrium properties of elemental ferromagnets. *Physical Review B*, 91(14):144425, April 2015.

Chapter 2

Background

2.1 Ferromagnetism

In this section a brief introduction to ferromagnetic materials will be given, along with explanations for some of their most important properties. Ferromagnets are a class of materials which show a strong permeability to external magnetic fields, and can retain their magnetisation when the exeternal field is removed. They show hysteresis in that their magnetisation state depends on the history of the magnetic field applied.

The origins of ferromagnetic behaviour remained elusive until the 20th century. The macroscopic picture of ferromagnetism was established by the work of Pierre Weiss in 1907 [1], who developed the mean-field theory description of ferromagnets. The mean field theory postulates a field within a ferromagnetic material which originates from interactions between its constituent particles, and acts in addition to any externally applied field. The mean-field model was used to successfully describe the qualitative behaviour of ferromagnets both below and above the Curie point (i.e. the temperature above which a phase transistion to paramagnet-like behaviour occurs). In those works, Weiss also postulated the existance of magnetic domains to explain certain ferromagnetic phenomena (see section 2.1.4). Despite the useful phenomenological descriptions of Weiss, the microscopic origins of magnetic behaviour were not understood until the introduction of the exchange interaction by Heisenberg in 1928 [2]. Heisenberg's result is quantum mechanical in origin, and the description outlined in this section assumes a basic level of understanding of quantum mechanics on the part of the reader.

2.1.1 Magnetic Moments

The theory introduced by Heisenberg rests upon the idea of intrinsic angular momentum, proposed by Uhlenbeck and Goudsmit in 1925 [3]. Upon it's introduction this intrinsic angular momentum was interpreted as being due to electrons spinning

around an axis, and was therefore given the name 'spin'. Through this was realised to be an incorrect interpretation, the term spin remains in use to describe the intrinsic angular momentum of particles. In addition to spin, an electron can also have an orbital angular momentum (quantum number) l which is analogous to the classical picture of the angular momentum with the electron circulating a nucleus. The combined effect of spin and orbital angular momentum gives rise to a magnetic moment. For the orbital part, this is analogous to how a current loop gives rise to a magnetic field in the classical picture of electromagnetism through Ampère's circuital law. Taking the viewpoint of that model, the orbit of the electron around the nucleus gives rise to magnetic moment

$$\boldsymbol{\mu} = I\mathbf{A}, \tag{2.1.1}$$

where $I = -e\frac{\omega}{2\pi}$ is the current generated by an electron with charge $-e$ and angular velocity ω, and $\mathbf{A} = \frac{\pi r^2}{\omega}\boldsymbol{\omega}$ is the vector area of the circle with radius r that is swept out by the electron orbit. The angular momentum of a point mass m undergoing a circular motion with radius r is given by $\mathbf{L} = mr^2\boldsymbol{\omega}$, leading to the relationship between magnetic moment and orbital angular momentum

$$\boldsymbol{\mu} = -\frac{e}{2m}\mathbf{L}. \tag{2.1.2}$$

As was shown in 1922 through the Stern-Gerlach experiment [4], the spin angular momentum of a free electron is quantised. Similarly, the orbital angular momentum is also quantised. In a complete quantum mechanical description, it is not possible to measure (i.e. be certain of) more than one Cartesian component of the vector angular momentum simultaneously due to their non-commutativity [5]. As the foundational result of quantum mechanics, the Schrödinger equation [6] satisfies these requirements, and through consideration of the composition of its kinetic energy term ($\frac{\hat{p}^2}{2m}$) can be used to determine linear momentum $\hat{p}$, and thereby angular momentum $\hat{L}$ leading to the result that the quantum (orbital) angular momentum operators $\hat{L_z}$ when applied to a valid eigenstate, results in the eigenvalues [5]

$$\hat{L_z}\left|l_z\right\rangle = \hbar l_z \left|l_z\right\rangle, \tag{2.1.3}$$

where $l_z = 0, \pm 1, \pm 2, ...$ are the values of the orbital quantum number, $\hbar$ is the reduced Planck constant, and $|l_z\rangle$ is an eigenstate of the z-component of orbital angular momentum in Dirac notation. Therefore the z-component of magnetic moment due to orbital angular momentum is given by

$$\mu_{l,z} = -\mu_B l_z, \tag{2.1.4}$$

where m_e is the electron mass, and the quantity $\mu_B = -\frac{e\hbar}{2m_e}$ is known as the Bohr magneton. The spin angular momentum is also quantised, and only able to take one of two values

$$\hat{S}_z \left|s_z\right\rangle = \hbar s_z \left|s_z\right\rangle, \tag{2.1.5}$$

where $s_z = \pm\frac{1}{2}$ are the allowed values of the spin quantum number, and $|s_z\rangle$ is an eigenstate of the z-component of spin angular momentum. The total z-component of the magnetic moment is given by

$$\mu_z = -\mu_B(l_z + g_s s_z) = -g\mu_B s_z, \tag{2.1.6}$$

where $g = g_s + \frac{l_z}{s_z}$ is a quantity known as the spectroscopic splitting factor or the g-factor, and $g_s \approx 2$ is the electron spin g-factor. It is common for the orbital angular momentum contribution of atoms in a crystal to be quenched ($l_z = 0$) as a result of coupling with the crystal field, leading to $g \approx 2$ (see section 2.1.5). This allows the theory of ferromagnetism in many crystals (e.g. most metals) to be described in regards to only the spin component of angular momentum, while neglecting the effect of orbital angular momentum outside of minor contributions arising through the spin-orbit interaction. The magnetic moments $\mathbf{m}$ of electrons in a crystal are related to the magnetisation $\mathbf{M}$ in a classical description through

$$\mathbf{m} = \iiint_V \mathbf{M} dV. \tag{2.1.7}$$

The angular momentum contribution of nuclei that form the crystal structure is found to be neglible in comparison to that of the electrons, owing to the drastically larger mass of nuclei. The large mass results in a correspondingly drastic decrease in moment through equation 2.1.2.

2.1.2 Exchange Interaction

The exchange interaction was introduced in 1928 as an effect that gives rise to the Weiss mean-field, originating from the quantum mechanical behaviour of electrons in ferromagnetic systems [2]. In particular, the strong interaction inducing alignment between spins was shown to arise from the Pauli exclusion principle [7], which states that indistinguishable fermionic particles (i.e. those with half integer spins [8], such as electrons) cannot occupy the same state simultaneously. Here it will be shown how this condition gives rise to the exchange interaction.

The Pauli exclusion principle gives rise to the condition that wave functions that describe the state of multi-fermionic systems must be anti-symmetric with respect to the exchange of particle coordinates. This is because for antisymmetric wavefunctions, the probablilty that two particles will be found in the same state is

zero. The meaning of this condition for a candidate wavefunction is that on exchange of two electrons at positions $\mathbf{r}_1$ and $\mathbf{r}_2$, the sign of the wavefunction Ψ, the square of which gives the probability density of measured electron positions, is reversed. Considering the exchange of two electrons, this can be written as

$$\Psi(\mathbf{r}_1, \mathbf{r}_2) = -\Psi(\mathbf{r}_2, \mathbf{r}_1), \tag{2.1.8}$$

For N-electron systems in which the Hamiltonian can be written as the sum of single electron Hamiltonians $\hat{\mathcal{H}} = \sum_{i=1}^{N} \hat{\mathcal{H}}_\mathrm{i}$, both the Schröedinger equation $\hat{\mathcal{H}}\Psi = E\Psi$ through which the energy of a wavefunction is determined, and the fermionic exchange condition are only satisfied by the linear combination of wavefunction products given by the Slater determinent

$$\Psi(\mathbf{r}_1, \mathbf{r}_2, \ldots, \mathbf{r}_N) = \frac{1}{\sqrt{N!}} \begin{vmatrix} \psi_1(\mathbf{r}_1) & \psi_1(\mathbf{r}_2) & \ldots & \psi_1(\mathbf{r}_N) \\ \psi_2(\mathbf{r}_1) & \psi_2(\mathbf{r}_2) & \ldots & \psi_2(\mathbf{r}_N) \\ \vdots & \vdots & \ddots & \vdots \\ \psi_N(\mathbf{r}_1) & \psi_N(\mathbf{r}_2) & \ldots & \psi_N(\mathbf{r}_N) \end{vmatrix}, \tag{2.1.9}$$

where the component wave functions $\psi_i(\mathbf{r}_i)$ are the mutually orthogonal wave functions of electrons i. The constraint that two fermions cannot be found in the same state can be seen from the Slater determinent by considering the result of setting the wavefunction of any two particles as equivalent. For example if $\psi_1 = \psi_2$, by use of the knowledge that swapping two rows of a determinent flips its sign, by swapping the first two rows of the determinent it can be seen that $\Psi(\mathbf{r}_1, \mathbf{r}_2, \ldots, \mathbf{r}_N) = -\Psi(\mathbf{r}_1, \mathbf{r}_2, \ldots, \mathbf{r}_N)$, which can only be satisfied by $\Psi(\mathbf{r}_1, \mathbf{r}_2, \ldots, \mathbf{r}_N) = 0$ i.e. an unphysical solution.

The wavefunction ψ_i of an electron can be separated into its spatial and spin components as

$$\psi_i(\mathbf{r}_i) = \phi_i(\mathbf{r}_i)\chi, \tag{2.1.10}$$

where $\phi_i(\mathbf{r}_i)$ is the spatial part, and χ describes the spin orientation, which can take only one of the two values $\pm\hbar/2$ along the axis of quantisation. Because of this additional element of distinguishability, in a two electron system the antisymmetric wavefunction can take the explicit forms [9]

$$\Psi_S = \frac{1}{\sqrt{2}}[\phi(\mathbf{r}_1)\phi(\mathbf{r}_2) + \phi(\mathbf{r}_2)\phi(\mathbf{r}_1)]\chi_S, \tag{2.1.11}$$

where χ_S is an antisymettric singlet spin state (S=0, antiparallel spins), or

$$\Psi_T = \frac{1}{\sqrt{2}}[\phi(\mathbf{r}_1)\phi(\mathbf{r}_2) - \phi(\mathbf{r}_2)\phi(\mathbf{r}_1)]\chi_T, \tag{2.1.12}$$

where χ_T is a symmetric triplet spin state (S=1, parallel spins). The difference in energy between singlet and triplet states is given by

$$E_S - E_T = 2\int \phi_1^*(\mathbf{r}_1)\phi_2^*(\mathbf{r}_2)\hat{\mathcal{H}}\phi_1(\mathbf{r}_2)\phi_2(\mathbf{r}_1)d\mathbf{r}_1 d\mathbf{r}_2 = J_{12}, \tag{2.1.13}$$

where $\frac{J_{12}}{2} = \int \phi_1^*(\mathbf{r}_1)\phi_2^*(\mathbf{r}_2)\hat{\mathcal{H}}\phi_1(\mathbf{r}_2)\phi_2(\mathbf{r}_1)d\mathbf{r}_1 d\mathbf{r}_2$ is known as the exchange integral. The contribution of energy of the two electrons due to their spin can be determined to be [9, 10]

$$\hat{\mathcal{H}}^{\text{spin}} = -J_{12}\hat{\mathbf{S}}_1 \cdot \hat{\mathbf{S}}_2, \tag{2.1.14}$$

which is the two electron exchange Hamiltonian. The qualitative effect of this result can be expected to occur between all electron spins in a ferromagnetic material giving

$$\hat{\mathcal{H}} = -\frac{1}{2}\sum_{ij} J_{ij}\hat{\mathbf{S}}_i \cdot \hat{\mathbf{S}}_j, \tag{2.1.15}$$

where the three dimensional spin vector operator $\hat{\mathbf{S}}_i = \frac{\hbar}{2}(\hat{\sigma}_{x,i}, \hat{\sigma}_{y,i}, \hat{\sigma}_{z,i})$ at site i is constructed using the well known Pauli matrices

$$\hat{\sigma}_{x,i} = \begin{pmatrix} 0 & 1 \\ 1 & 0 \end{pmatrix}, \quad \hat{\sigma}_{y,i} = \begin{pmatrix} 0 & -i \\ i & 0 \end{pmatrix}, \quad \hat{\sigma}_{z,i} = \begin{pmatrix} 1 & 0 \\ 0 & -1 \end{pmatrix}. \tag{2.1.16}$$

It is often assumed that ferromagnets contain electrons localised to atoms locked in a crystal structure, and that only nearest neighbour spins have significant interaction. Therefore this is often further simplified by assuming that $J_{ij} = J$ for nearest neighbour spins, and $J_{ij} = 0$ otherwise. When J takes a positive value, the lowest energy state is described by a triplet wavefunction (e.g. 2.1.12), and the spins in the system align with one another to reduce the total energy. If J is given a negative value, the energy of the system is minimised by the anti-alignment of spins, making it a suitable model for the phenomena of antiferromagnetism in which the net magnetisation of ordered magnetic spins is zero. In that case, the coupling between spins is referred to as antiferromagnetic type exchange coupling.

2.1.3 Demagnetising Field

The magnetisation $\mathbf{M}$ of a ferromagnet ends at its surface leading to $\nabla \cdot \mathbf{M} \neq 0$ which, by Gauss's law for magnetism, gives rise to an equal and opposite divergence in $\mathbf{H}$

$$\nabla \cdot \mathbf{H} = -\nabla \cdot \mathbf{M}. \tag{2.1.17}$$

This results in a field that acts to reduce the magnetisation of the ferromagnet according to its geometry, by which the shape of its surface (that acts as the source of the divergence) is defined. Through the minimisation of demagnetising field, this can lead to a preferred direction of magnetisation within the ferromagnet, known as shape anisotropy. For an ellipsoidal ferromagnet, the demagnetising field is uniform, allowing it to be written as

$$\mathbf{H}_d = -\mathcal{N}\mathbf{M}, \tag{2.1.18}$$

where $\mathcal{N}$ is a rank 2 tensor. The contribution to the energy density E_d resulting from the stray field can be written in terms of the magnetisation vector as [9]

$$E_d = \frac{1}{2}\mu_0 \mathbf{M}^{\mathrm{T}} \mathcal{N} \mathbf{M}, \tag{2.1.19}$$

where the superscript T indicates the transpose operation. If the coordinate axes are parallel to the principle axes of the ellipsoid then the demagnetisation tensor can be written as the diagonal 3×3 matrix

$$\mathcal{N} = \begin{pmatrix} N_x & 0 & 0 \\ 0 & N_y & 0 \\ 0 & 0 & N_z \end{pmatrix}, \tag{2.1.20}$$

where the components satisfy the condition $N_x + N_y + N_z = 1$. In the case of an infinite thin film in the xy-plane, the geometry can be identified as a limiting case of the ellipsoidal description, and the diagonal components of the demagnetisation matrix take the values $N_x = N_y = 0$ and $N_z = 1$.

2.1.4 Domains

First proposed by Weiss, [1], a domain is a region within a ferromagnet in which the moments align in a common direction. Within a domain, the magnitude of local magnetisation is equal to the saturisation magnetisation (i.e. the maximum possible value).

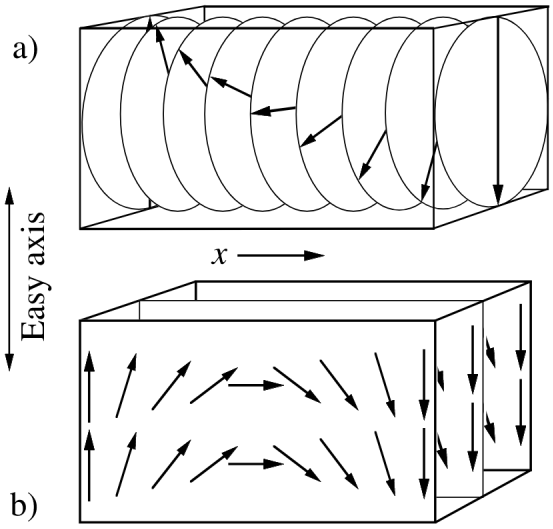

Figure 2.1: Vector representations of the 180° degree rotation of magnetisation across (a) Bloch and (b) Nèel domain walls. Figure reproduced from [11]

The $\nabla \cdot \mathbf{M} \neq 0$ condition that gives rise to the demagnetisation factor of a ferromagnet (discussed in section 2.1.3) leads to a stray field outside the material. To maintain these external fields the system maintains a high energy state. If a path towards a lower energy state exists, the system will reduce its energy through the associated process. One pathway mentioned in section 2.1.3, is the reduction of external fields through modification to the magnetisation direction, introducing a shape anisotropy. In large enough systems another pathway becomes available in the formation of magnetic domains. Domains form when the increase in system energy required to create a domain wall is less than the reduction in energy acheived by the destruction of stray fields. To minimise the exchange energy cost associated with non-aligned spins, a domain wall often occurs cumulatively across multiple moments. Domain walls are known to take one of two forms, known as Bloch walls or Nèel walls, and are differentiated by the plane in which spins rotate within the domain wall. Within the more common Bloch walls, spins rotate in the plane of the domain wall, whereas in Nèel walls, the spins rotate in the plane perpendicular to the wall. The two types of domain wall are shown in figure 2.1.

The existance of magnetic domains is able to explain two important properties of ferromagnetic systems. The first is their capacity for net zero magnetisation at remanence (i.e. zero applied magnetic field). The second is the capability for saturation of some samples by the application of weak magnetic fields. The second property owes its existence to the ability to align spins through the growth of ordered domains through the motion of domain walls, at relatively low energy cost.

2.1.5 Magnetocrystalline Anisotropy

Within a crystal, the magnetisation is found to lie along certain crystallographic axes [10]. This is known as crystalline anisotropy, and is a result of the interaction between the angular momentum of electrons and the crystal field. The crystal field arises from the electrostatic potential which results from the charges associated with crystal lattice points. From the perspective of an electron associated with any one lattice point, the surrounding charge distribution acts to create preferential directions for the orbital angular momentum. In crystals of high symmetry, the crystal field results in multiple equally preferential directions, and as a result the orbital angular momentum is quenched. Due to the requirement for half integer values of the spin angular momentum, the spin cannot be quenched. As a result of spin-orbit interaction, the coupling of spin and orbital terms results in a preferred direction for spins due to the crystal field. This manifests as crystalline anisotropy, and as with shape anisotropy mentioned in section 2.1.3, is usually expressed in terms of the contribution to the energy density E with respect to magnetisation direction. Within cubic (e.g. bcc, fcc) crystal structures this expression is given by [10]

$$E_{\text{mca}} = K_1(u_x^2u_y^2 + u_y^2u_z^2 + u_z^2u_x^2) + K_2u_x^2u_y^2u_z^2, \tag{2.1.21}$$

where $\mathbf{u} = \frac{\mathbf{M}}{M}$ is the direction of magnetisation, and K_1 and K_2 are known as the anisotropy constants. Systems in which the anisotropy can be defined with respect to a single axis (notably hcp crystal structures) are referred to as uniaxial, and the energy density has the dependence [10]

$$E(\theta) = K_1 \sin^2(\theta) + K_2 \sin^4(\theta), \tag{2.1.22}$$

where θ is the angle between magnetisation and the anisotropy axis. When referring to magnetic anisotropy, the directions in which energy is minimised are known as easy directions, and those of maximum energy are known as hard directions.

2.1.6 Interface Anisotropy

At the surface of crystals, and at interfaces between crystals, the symmetry is reduced when compared to bulk. This was shown by Nèel in 1954 to result in an energy density dependence at the surface given by [12]

$$E_s(\theta) = -K_s \cos^2(\theta), \tag{2.1.23}$$

where θ is the angle between magnetisation and anisotropy axis, and the surface anisotropy constant K_s depends on the Miller indices that describe the plane of

the crystal surface. This reduction in symmetry can have significant consequences for the preferred magnetisation direction, particularly in samples where the number of moments at the surface (and/or interfaces) is comparable to the number of moments within the volume. This can be the case for multilayer thin film stacks. In these systems the anisotropy contribution at interfaces dominates over the crystalline anisotropy from the bulk. This often leads to a strong perpendicular magnetic anisotropy (PMA) where the easy direction is perpendicular to the plane of the sample [13].

2.2 Spin Dynamics

This section will show how the dynamics of spin systems are predicted by the Heisenberg model.

2.2.1 Heisenberg Model

The Heisenberg model was introduced in 1928 by Werner Heisenberg to describe the energetics of a ferromagnetic system [2]. This model describes the coupling between spins in a lattice structure along with their interactions with an externally applied magnetic field. The coupling between spins is due to the exchange interaction (discussed in section 2.1.2), which is an electrostatic effect resulting from the quantum mechanical Pauli exclusion principle. The Heisenberg Hamiltonian

$$\hat{\mathcal{H}}_{\text{Heisenberg}} = \hat{\mathcal{H}}_{\text{Zeeman}} + \hat{\mathcal{H}}_{\text{Exchange}}, \tag{2.2.1}$$

describes the total energy of a spin system at the microscopic level, where the energy is reduced by the alignment of spins $\hat{\mathbf{S}}_j$ at each site j with a homogeneous external magnetic field $\mathbf{B}_{ext}$ according to

$$\hat{\mathcal{H}}_{\text{Zeeman}} = -\gamma \sum_j \hat{\mathbf{S}}_j \cdot \mathbf{B}_{\text{ext}} = |\gamma_e| \sum_j \hat{\mathbf{S}}_j \cdot \mathbf{B}_{\text{ext}}, \tag{2.2.2}$$

where the substitution $\gamma = -|\gamma_e|$ has been made since the electron gyromagnetic ratio takes a negative value. The energy is further reduced by the alignment of nearest neighbour spins through the exchange interaction according to

$$\hat{\mathcal{H}}_{\text{Exchange}} = -\frac{J}{2} \sum_{\langle j,k \rangle} \hat{\mathbf{S}}_j \cdot \hat{\mathbf{S}}_k, \tag{2.2.3}$$

where the strength of the coupling is determined by the parameter J, and the angle bracket notation $\langle j, k \rangle$ denotes that the summation takes place only for nearest neighbour spins. Just like any other Hamiltonian, the Heisenberg Hamiltonian can be used to show how the system it describes evolves in time and can be used to derive both its equations of motion (i.e. dynamics) and equilibrium behaviour. Classically the equations of motion can be derived using Hamilton's equations. Quantum mechanically the equations of motion of the spin operators can be determined using the Heisenberg picture of quantum mechanics as

$$\frac{d\hat{\mathbf{S}}}{dt} = \frac{i}{\hbar} \left[\hat{\mathcal{H}}, \hat{\mathbf{S}} \right]. \tag{2.2.4}$$

The Zeeman Hamiltonian (equation 2.2.2) represents the effect of an external magnetic field on the spin system. It is clear from the form of the Hamiltonian that

the energy of the system is minimised when the spins align with the external field. The effect that the field has on the spins is to dictate the average directions of their angular momenta (spin vector). In this way the magnetic field acts as an external reservoir of angular momentum. The exchange term in the Heisenberg Hamiltonian allows for the transfer of angular momentum between the internal spin components of the system. A derivation of the magnetisation dynamics from the Heisenberg Hamiltonian shows only precession of individual spins around an effective field due to the sum of the external field and neighbouring spins. Using the Heisenberg picture of quantum mechanics, the equation of motion is given by,

$$\frac{d\hat{\mathbf{S}}_i}{dt} = \frac{i}{\hbar}\left[\hat{\mathcal{H}}, \hat{\mathbf{S}}_i\right] = \frac{i}{\hbar}\left[\hat{\mathcal{H}}_{\text{Zeeman}}, \hat{\mathbf{S}}_i\right] + \frac{i}{\hbar}\left[\hat{\mathcal{H}}_{\text{Exchange}}, \hat{\mathbf{S}}_i\right]. \tag{2.2.5}$$

The evolution of the spin arising from the Zeeman effect is found by the calculation

$$\begin{aligned}
\left[\hat{\mathcal{H}}_{\text{Zeeman}}, \hat{\mathbf{S}}_i\right] &= -|\gamma_e| \sum_j \sum_{\alpha\neq\beta=x,y,z} B^{\beta}_{\text{ext}} \left[\hat{S}_{j,\beta}, \hat{S}_{i,\alpha}\right] \mathbf{e}_\alpha, \\
&= -i\hbar|\gamma_e| \sum_j \delta_{ij} \sum_{\alpha,\beta,\zeta=x,y,z} B^{\beta}_{\text{ext}} \hat{S}_{i,\zeta} \epsilon_{\alpha\beta\zeta} \mathbf{e}_\alpha, \\
&= i\hbar|\gamma_e|\ \hat{\mathbf{S}}_i \times \mathbf{B}_{\text{ext}},
\end{aligned} \tag{2.2.6}$$

where $\mathbf{e}_\beta$ is the Cartesian unit vector, $\epsilon_{\alpha\beta\zeta}$ is the Levi-Civita symbol defined by [14]

$$\epsilon_{\alpha\beta\zeta} = \begin{cases} +1 & \text{if } \alpha,\beta,\zeta \text{ is an even permutation of } x,y,z, \\ -1 & \text{if } \alpha,\beta,\zeta \text{ is an odd permutation of } x,y,z, \\ 0 & \text{otherwise,} \end{cases} \tag{2.2.7}$$

the summation form of the cross product has been recognised (see appendix A.1), and the spin commutation is expanded as given by appendix equation B.1.4 (this derivation is shown step-by-step in appendix B.1). Similarly, the evolution of the spin arising from the exchange interaction is found by

$$\begin{aligned}
\left[\hat{\mathcal{H}}_{\text{Exchange}}, \hat{\mathbf{S}}_i\right] &= \frac{J}{2} \sum_{\langle j,k\rangle} \sum_{\alpha\neq\beta=x,y,z} \left[\hat{S}_{i,\alpha}, \hat{S}_{j,\beta}\hat{S}_{k,\beta}\right] \mathbf{e}_\alpha \\
&= \frac{J}{2} \sum_{\langle j,k\rangle} \sum_{\alpha,\beta,\zeta=x,y,z} \left(\left[\hat{S}_{i,\alpha}, \hat{S}_{j,\beta}\right] \hat{S}_{k,\beta} + \hat{S}_{j,\beta}\left[\hat{S}_{i,\alpha}, \hat{S}_{k,\beta}\right]\right) \mathbf{e}_\alpha \\
&= \frac{i\hbar J}{2} \sum_{\langle k\rangle_i} \sum_{\alpha,\beta,\zeta=x,y,z} \hat{S}_{k,\beta}\hat{S}_{i,\zeta}\epsilon_{\alpha\beta\zeta}\mathbf{e}_\alpha \\
&\quad + \frac{i\hbar J}{2} \sum_{\langle j\rangle_i} \sum_{\alpha,\beta,\zeta=x,y,z} \hat{S}_{j,\beta}\hat{S}_{i,\zeta}\epsilon_{\alpha\beta\zeta}\mathbf{e}_\alpha \\
&= i\hbar J\ \hat{\mathbf{S}}_i \times \sum_{\langle j\rangle_i} \hat{\mathbf{S}}_j
\end{aligned} \tag{2.2.8}$$

where the angular brackets $\langle\rangle_i$ denote nearest neighbours to the i'th spin site. The spin evolution therefore reduces to a simpler form as

$$\frac{d\hat{\mathbf{S}}_i}{dt} = -|\gamma_e|\hat{\mathbf{S}}_i \times \hat{\mathbf{B}}_{\text{eff}}, \tag{2.2.9}$$

where

$$\hat{\mathbf{B}}_{\text{eff}} = \mathbf{B}_{\text{ext}} + \frac{J}{|\gamma_e|}\sum_{\langle j\rangle_i} \hat{\mathbf{S}}_j, \tag{2.2.10}$$

is the effective field causing the precession of each spin $\hat{\mathbf{S}}_i$. The time-averaged energy of this system remains constant, enforced by the restriction that spins are forbidden from minimising their Zeeman energy by reducing their precession radius and fully aligning with the external field.

2.2.2 Landau-Lifshitz-Gilbert Equation

The Landau-Lifshitz (LL) equation was introduced in 1935 to describe the time evolution of magnetisation in a ferromagnetic system [15]. The LL equation can be used to model the dynamics of microscopic spins, not only being confined to a description of macroscopic magnetisation behaviour. The LL equation is given as,

$$\frac{d\mathbf{S}}{dt} = -\gamma'\left(\mathbf{S} \times \mathbf{B}_{\text{eff}} - |\gamma_e|\eta\mathbf{S} \times (\mathbf{S} \times \mathbf{B}_{\text{eff}})\right) \tag{2.2.11}$$

where

$$\gamma' = \frac{|\gamma_e|}{1 + |\gamma_e|^2\eta^2 S^2}, \tag{2.2.12}$$

(as can be seen in appendix B.2) and the effective field

$$\mathbf{B}_{\text{eff}} = \mathbf{B}_{\text{external}} + \mathbf{B}_{\text{exchange}}, \tag{2.2.13}$$

consists of one part owing to external sources $\mathbf{B}_{\text{external}}$, and another resulting from the exchange interaction $\mathbf{B}_{\text{exchange}}$. The LL equation has two parts. The first part, which contains a single cross product, describes the precessional motion of spins around an effective field described by equation 2.2.10. The second part of the LL equation has two cross products and describes movement of the spin vector towards the effective magnetic field. This movement is known as damping because it reduces the precession radius of the spin. This damping is a dissipative effect because it moves the system towards the equilibrium determined by the Zeeman energy. In 1947, Gilbert re-stated the LL equation in a form where the gyromagnetic factor $|\gamma_e|$ preceding the precession term $\mathbf{S} \times \mathbf{B}$ is independent of the magnitude of the

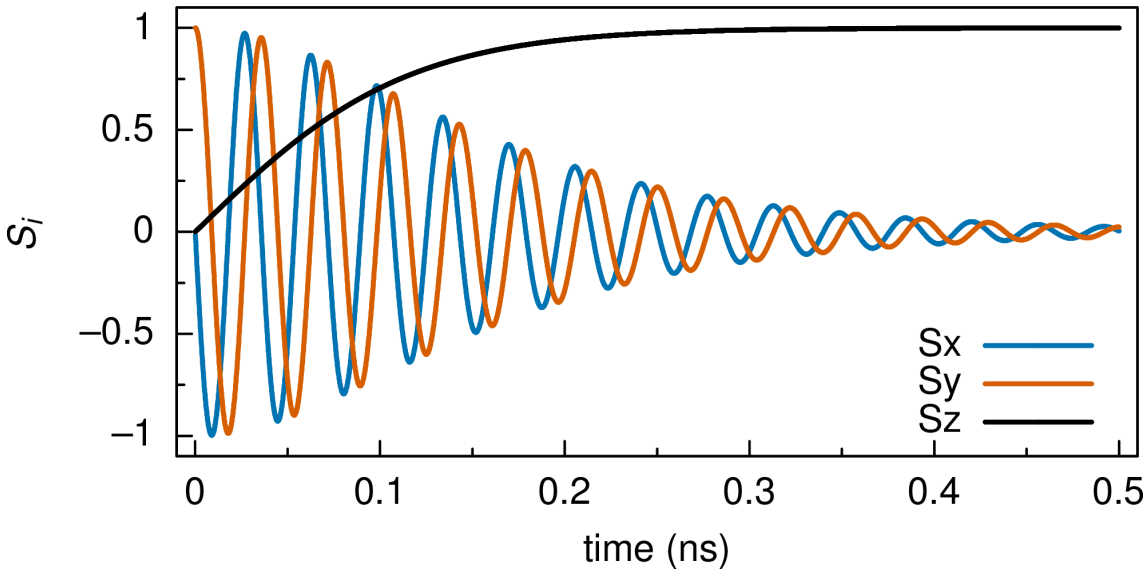

Figure 2.2: Here the time evolution of a single spin is shown. Using VAMPIRE, the LL equation (equation 2.2.11) is simulated for a single spin with initial direction along the y-axis, a magnetic field of 1T applied in the z-axis direction, and a damping constant $|\gamma_e|\eta = 0.05$. The precessional motion is clearly observable in the x-y plane. The damping of the spin is observable in both the reduction in amplitude of x-y precession, and the movement of the spin vector towards +1 in the z-direction. The damping takes place over a longer timescale than the precessional motion due to the sub-unitary value of the damping constant.

damping factor η [16], as

$$\frac{d\mathbf{S}}{dt} = -|\gamma_e| \left(\mathbf{S} \times \mathbf{B}_{\text{eff}} - \eta \mathbf{S} \times \frac{d\mathbf{S}}{dt} \right), \tag{2.2.14}$$

which is known as the Landau-Lifshitz-Gilbert (LLG) equation. As shown in section 2.2.1, the Heisenberg Hamiltonian leads to the precessive part of the LLG but not the damping part. For the Hamiltonian to lead to a damping part, the system must be made open so that the energy of the spin system can be reduced as a whole, by the transfer of energy to other parts of the system or environment not specified by the Heisenberg Hamiltonian. The LLG equation was later extended by Brown [17] to include a temperature dependent stochastic part in the effective magnetic field.

$$\mathbf{B}_{\text{eff}} = \mathbf{B}_{\text{external}} + \mathbf{B}_{\text{exchange}} + \mathbf{B}_{\text{thermal}} \tag{2.2.15}$$

This term represents fluctuations in the system which, analogous to Einstein's theory of Brownian motion, have the same macroscopic source as the damping. The theory underpinning that statement is known as the fluctuation dissiption relation and will be explored more in section 2.3.2. The properties of the stochastic thermal field introduced by Brown are common for thermal noise in the high temperature limit

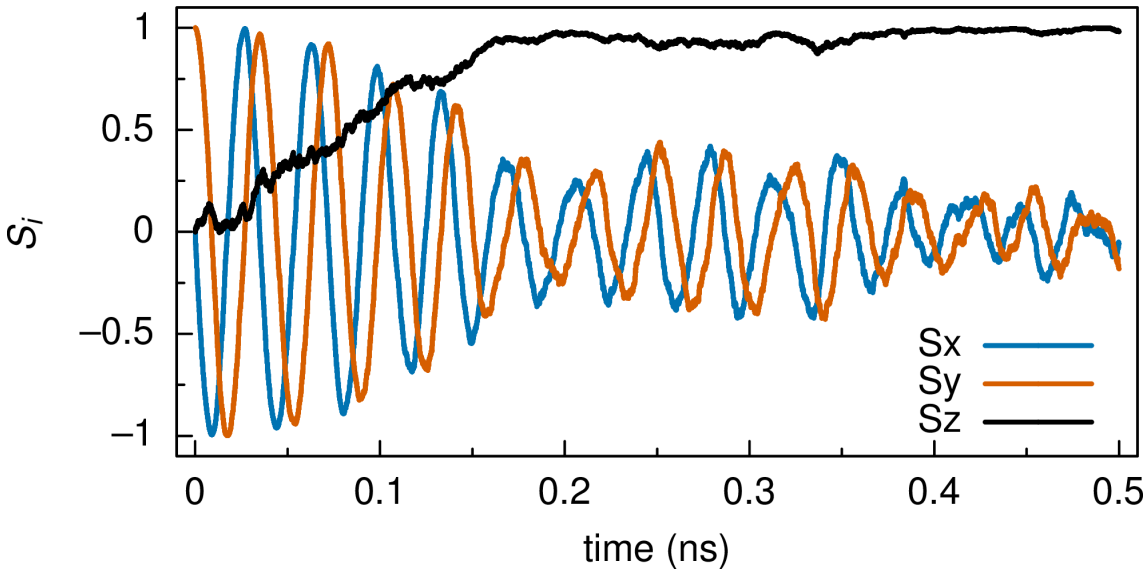

Figure 2.3: Here a spin is simulated in the same manner as in Figure 2.2, but with the stochastic thermal noise described by Brown [17] included as part of the effective magnetic field (equation 2.2.15). Even at the small temperature of 0.01K simulated, the effects of thermal fluctuations on the motion of the spin are evident. Thermal fluctuations not only prevent the system from reaching its mimimum energy state, they also stochastically alter the path of spin direction, and thereby dramatically increase the complexity required by a description of a full ferromagnetic many-body system when considered in conjunction with the exchange interaction coupling between spins.

i.e. white noise, with a mean value of zero,

$$\langle B_{\text{thermal},\alpha} \rangle = 0, \tag{2.2.16}$$

and zero correlation between values at different times,

$$\langle B_{\text{thermal},\alpha}(t) B_{\text{thermal},\beta}(t') \rangle = \mu(T) \delta_{\alpha\beta} \delta(t - t'). \tag{2.2.17}$$

Here $\mu(T)$ is a temperature dependent value which determines the variance and hence magnitude of thermal noise, $\delta_{\alpha\beta}$ and $\delta(t - t')$ are the Kronecker and Dirac delta functions respectively, and $(\alpha, \beta = 1, 2, 3)$ refer to the Cartesian coordinate indices of the magnetic field $\mathbf{B}$. Equation 2.2.14 with the effective field given by equation 2.2.15 is often simply referred to as the LLG equation. To help distinguish this combination from the form without a thermal noise, the form without thermal noise will be referred to as LLG, while the form including the thermal noise with the white noise properties given in equations 2.2.16 and 2.2.17 will be referred to as the Landau-Lifshitz-Gilbert-Brown (LLGB) within this work. A VAMPIRE simulation of a single spin in a magnetic field without thermal noise and with the effect of a white thermal noise included are shown in figures 2.2 and 2.3 respectively.

2.3 Open Quantum Systems

An open quantum system is one where dissipative effects are included in the microscopic description. This is usually achieved by allowing the system to interact with a reservoir that represents the environment of the system. An interaction between the observables of the system and reservoir allows energy to flow between the two. Models of open quantum systems therefore allow the non-conservation of energy of a system, allowing its energy to be reduced to the ground state. On reduction of energy to the ground state, the total energy of the greater system (combined system of interest and reservoir) remains constant, but the energy is dissipated from the system into the reservoir.

In section 2.2.1 the Heisenberg model was examined and found to lead to equations of motion where spins precess around an effective magnetic field, but have no possibility of reducing their precession radius, which would reduce the energy of the system by the minimisation of Zeeman energy. An open quantum system approach will turn out to be useful in the study of this system as it offers a microscopically motivated method for the introduction of dissipation into the model, thereby allowing the precession radius to be reduced.

In this section the Langevin equation will be introduced as an equation of motion representative of an open quantum system. Following from this the fluctuation dissipation theorem, which is a necessary relationship between the dissipative and stochastic components of a physical system, will be discussed. Finally, a Hamiltonian which give rise to the Langevin equation of motion will be outlined.

2.3.1 Langevin Equation

A Langevin equation models how a system evolves under the influence of a stochastic (i.e. random) time dependent force. The random nature of the force requires it to be defined in a statistical rather than a deterministic fashion. The Langevin equation was first introduced in 1908 by Paul Langevin in his description of Brownian motion [18], as a second order differential equation with stochastic force and damping term proportional to velocity.

Here a quantum Langevin equation taking the form of a second order differential equation will be considered, similar to the one introduced by Langevin (although other forms of Langevin equation are possible, notably the LLGB equation in section 2.2.2 which is a first order, non-linear differential equation). The equation considered here describes a damped and stochastically forced particle in one dimension bounded by a potential energy field $\hat{V}(x)$. When $\hat{V}(x)$ varies with position and contains one or more finite minima, it acts as a deterministically decaying dissipative container

for kinetic energy stochastically supplied to a mass M, and can be written as

$$M\frac{d^2\hat{x}}{dt^2} = -2M\gamma\frac{d\hat{x}}{dt} - \frac{\partial\hat{V}(\hat{x})}{\partial\hat{x}} - \hat{F}(t), \tag{2.3.1}$$

where γ is the coefficient of damping. The stochastic force $\hat{F}(t)$ is defined by its time average of zero

$$\langle\hat{F}(t)\rangle = 0, \tag{2.3.2}$$

and by the magnitude and time dependence of its autocorrelation function $\langle\hat{F}(t)\hat{F}(t')\rangle$. For a potential quadratic in position

$$\hat{V} = \frac{1}{2}M\omega^2\hat{x}^2, \tag{2.3.3}$$

the Langevin equation

$$M\frac{d^2\hat{x}}{dt^2} = -2M\gamma\frac{d\hat{x}}{dt} - M\omega^2\hat{x} - \hat{F}(t), \tag{2.3.4}$$

describes a stochastically forced, deterministically damped harmonic oscillator. If the potential is position independent

$$\hat{V} = \text{constant}, \tag{2.3.5}$$

the position of the mass is no longer bounded, and the simple harmonic motion is replaced by the unbounded Brownian motion

$$M\frac{d^2\hat{x}}{dt^2} = -2M\gamma\frac{d\hat{x}}{dt} - \hat{F}(t), \tag{2.3.6}$$

which gives the description of a free particle whose motion is determined by a stochastic force (fluctuations), and a damping effect (dissipations). The motion of the particle in each dimension of the system can be modelled using equation 2.3.6, the motion of a simulated unbounded particle in a two dimensional system is shown in figure 2.4.

2.3.2 Fluctuation Dissipation Theorem

The fluctuation dissipation theorem is a relationship between the stochastic and damping components of a Langevin equation that must be satisfied due to their common source. In his 1905 paper, Einstein pointed out that the source of damping and driving force in the phenomena of Brownian motion is the same, both being due to the interactions of the system of interest (a suspended particle) with its environment (molecules in the fluid) [19]. His observation in that study was that

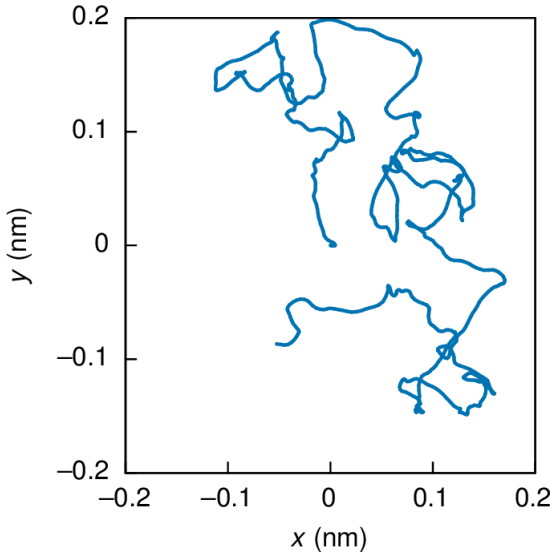

Figure 2.4: Pictured is a simulation of the Brownian motion of a particle with mass $M = 1\text{kg}$. The position and velocity are initialised at $x = y = \frac{\mathrm{d}x}{\mathrm{d}t} = \frac{\mathrm{d}y}{\mathrm{d}t} = 0$, and the motion is determined for 100s with time steps of $\Delta t = 0.1\text{s}$ through equation 2.3.6 (with the operators replaced by scalar quantities, i.e. a classical description). The differential equation is solved using a Python implementation of the 4th order Runge-Kutta method which is used to evaluate the x and y coordinates independently. The stochastic force applied has white noise properties at $T = 300K$, i.e. an expectation value of $\langle F(t)\rangle = 0$ and a temperature dependent autocorrelation function $\langle F(t)F(t')\rangle = Mk_BT\delta(t-t')$ (see appendix A.5).

the conditions required for dynamic equilibrium require a superposition of force on each suspended particle and its process of diffusion (dissipation). By use of this observation, Einstein was able to derive a relationship between macroscopic observables and the microscopic Avogadro's constant, and in the process gave proof for the existence of atoms [20].

The relationship between force and diffusion in Brownian motion was extended to the case of a stochastic force (fluctuations) by Langevin in 1908 [18] (equation 2.3.6). It was later shown that a fluctuation-dissipation relation (FDR) exists for thermal noise in a conductor by Nyquist in 1928 [21], based on Johnson noise [22]. The theory of the FDR was later extended to more general systems by Callen and Welton [23], and expanded on in great detail by Kubo [24].

The fluctuation dissipation relation says that for a linear response system (e.g. the Langevin equation 2.3.1), the imaginary part of the generalised susceptibility $\chi(\omega)$ (see appendix A.3) that describes the response is related to the fluctuations of a variable $\hat{x}$ in the systems equilibrium state through their power spectral density $S_x(\omega)$ as [25].

$$S_x(\omega) = \hbar \mathrm{Im}[\chi(\omega)] \coth\left(\frac{\hbar\omega}{2k_BT}\right), \tag{2.3.7}$$

which reduces to the classical form,

$$S_x(\omega) = \frac{2k_BT}{\omega}\mathrm{Im}[\chi(\omega)], \tag{2.3.8}$$

when $k_BT >> \frac{\hbar\omega}{2}$.

The generalised susceptibility $\chi(\omega)$ works in the frequency, rather than time domain, but ultimately represents the response of the system to forces applied to it at previous times. It is important that a physical description of a linear response system containing both damping and a stochastic force explicitly obeys equation 2.3.7 under all circumstances. Brown's description of a magnetic Langevin equation in his formulation of the LLGB equation [17] attempts to satisfy the FDR in the high temperature limit, but no such attempt is made to guarantee FDR outside of this limit as can be seen by comparison of the variance of the fluctuating variable in Brown's study [17] to the forms for a variable satisfying the fluctuation dissipation relation generally (and by extension having power spectral density given by equation 2.3.7) and in the high temperature limit (with power spectral density given by equation 2.3.8) shown in [25]. The use of this approximation is likely due to the difficulty in describing the properties of thermal noise and damping in magnetisation dynamics, which is itself a result of the difficulty in determining equations of motion inclusive of the required stochastic fluctuations when limited to a closed system such as that described by the Heisenberg model.

2.3.3 Quantum Dissipative Dynamics

In this section, models used to derive the Langevin equation from a microscopic description will be examined and discussed.

A common approach is to use a bath consisting of quantum harmonic oscillators to act as the environment. These quantum harmonic oscillators are similar to their classical counterparts in that they can store system energy through oscillitory motion, but differ in their behaviour in the (lowest energy) ground states. Unlike their classical counterpart, owing to the Heisenberg uncertainty principle quantum harmonic oscillators have ground states with non-zero energy in which the bosonic particles remain in motion. This leads to differences in their behaviour at low temperatures, where significant vibrational motion known as the zero point energy can play a large role in the dynamics of systems to which they are coupled.

The Caldeira-Leggett model [26] is commonly used as an analytically solvable example of dissipation from a system obeying the fluctuation dissipation relation. The microscopic set up is formulated as a Hamiltonian containing four parts, the system of interest, the environment, the coupling of energy between the system and

environment, and an additional 'counter' term

$$\hat{\mathcal{H}}_{\mathrm{CL}} = \hat{\mathcal{H}}_{\mathrm{S}} + \hat{\mathcal{H}}_{\mathrm{R}} + \hat{\mathcal{H}}_{\mathrm{I}} + \hat{\mathcal{H}}_{\mathrm{C}}, \tag{2.3.9}$$

where,

$$\hat{\mathcal{H}}_{\mathrm{S}} = \frac{\hat{p}^2}{2M} + \hat{V}(\hat{x}), \tag{2.3.10}$$

is the system Hamiltonian, with mass M, momentum $\hat{p}$, and a potential $\hat{V}(\hat{x})$,

$$\hat{\mathcal{H}}_{\mathrm{R}} = \sum_n \left(\frac{\hat{p}_n^2}{2m_n} + \frac{1}{2} m_n \omega_n^2 \hat{x}_n^2 \right), \tag{2.3.11}$$

is the reservoir Hamiltonian, consisting of a quantum harmonic oscillators with frequency ω_n

$$\hat{\mathcal{H}}_{\mathrm{I}} = -\hat{x} \sum_n \kappa_n \hat{x}_n, \tag{2.3.12}$$

is a linear coupling between the system coordinates $\hat{x}$ and reservoir coordinates $\hat{x}_n$, and

$$\hat{\mathcal{H}}_{\mathrm{C}} = \hat{x}^2 \sum_n \frac{\kappa_n}{2m_n\omega_n}, \tag{2.3.13}$$

is known as the counter term, which is included to account for a change in the natural frequency of the oscillator due to its coupling to the reservoir. Following [27], we find the equation of motion for the system to be,

$$M\frac{d^2\hat{x}}{dt^2} = -M\int_0^t K(t-t')\frac{d\hat{x(t')}}{dt}dt' - \frac{\partial \hat{V}(\hat{x})}{\partial \hat{x}} - \hat{F}(t), \tag{2.3.14}$$

which is a generalised form of the Langevin equation 2.3.1. By assuming what is known as an Ohmic damping kernel $K(t-t') = 2\gamma\delta(t-t')$ the result simplifies to exactly that result,

$$M\frac{d^2\hat{x}}{dt^2} = -2M\gamma\frac{d\hat{x}}{dt} - \frac{\partial \hat{V}(\hat{x})}{\partial \hat{x}} - \hat{F}(t). \tag{2.3.15}$$

Analysis of this model shows how the fluctuation dissipation relation is satisifed [27], demonstrable from first principles due to its microscopic nature. Due to its success in this regard, the model has found wide usage in theories in the field of quantum thermodynamics [28, 29], where interactions between the system of interest and its environment are of crucial importance. The description provided by the Caldeira-Leggett model contains a reservoir which is introduced as a discrete set, however this is often taken to a continuum limit after the equations of motion (e.g. 2.3.14)

have been determined, and is a requirement for the damping Kernel used to produce 2.3.15 [30]. An alternative framework is provided by the Huttner-Barnett model [31], which achieves many of the same goals as the Caldeira-Leggett model, but starts from a more powerful continuum description of the reservoir. An example of the use of this framework for deriving the dynamics of a quantum harmonic oscillator is given by [30], and this approach will be taken for the reservoir in the magnetic quantum open system described in chapter 4.

2.4 Atomistic Spin Dynamics

Atomistic spin dynamics (ASD) is the name given to a class of magnetic materials simulation softwares that predict the spin evolution of each atom in the crystal structure resulting from the quantum mechanical exchange interaction (discussed in section 2.1.2), often alongside additional factors such as an external field and magnetocrystalline anisotropy (discussed in section 2.1.5). This is often achieved through the simulation of a classical form of the LLGB equation (2.2.14 with the quantum operators replaced by classical spin vectors, and including the white noise stochastic field defined by equations 2.2.16 and 2.2.17).

The use of ASD techniques to simulate three dimensional magnetic systems began in 1969 with simulations of classical Heisenberg ferromagnets [32, 33] by consideration of the exchange interaction between nearest neighbour spins in a simple-cubic lattice with periodic boundary conditions. In 1995, ab-initio ASD techniques were introduced [34, 35], allowing for the determination of spin dynamics within a density-functional-theory framework. Over time a number of groups have developed their own numeric tools for ASD and made them available to the magnetic materials research community. These include the open source softwares VAMPIRE [36] developed at the University of York based on [37, 38], and UppASD [39] developed at Uppsala University based on [40].

ASD has proven to be a useful tool for understanding the behaviour of magnetic materials, finding use in topics including synthetic ferrimagnets [41, 42], ultrafast spin dynamics [43, 44, 45, 46, 47], domain wall motion [48], temperature dependent equilibrium properties [46] and all optical switching [49]. VAMPIRE was used to simulate the single-spin dynamics shown in figures 2.2 and 2.3, and can be used to simulate many-spin structures.

The validity of an ASD method is reliant on the extent to which the equation of motion through which the dynamics are predicted are an accurate description of the dynamics in physical spin systems. Behaviour determined in these systems that does not predict experimental observations is therefore likely to indicate issues with the underlying description. Such issues were identified in [46], where VAMPIRE simulations of the equilibrium magnetisation vs temperature are shown to differ in a qualitative fashion from the phenomenological model of Kuz'min [50] that offers a strong fit to experimental data.

This motivated the study shown in chapter 4, as an attempt to improve the equations of motion used to simulate spin dynamics. In particular, the focus rests on the stochastic thermal magnetic field identified by Brown in his formulation of the LLGB equations 2.2.14, 2.2.16 and 2.2.17. In his introduction of the autocorrelation of thermal noise as a delta function [17], Brown notes that it is the statement of an assumption that the autocorrelation time is assumed to be very short in comparison

with the time scales of spin precession and damping. This is also noted in the description of VAMPIRE given in [36], where it is explained that a more complete description of the microscopic damping mechanism is required for sufficiently short integration timesteps.

The improved microscopic description of the dissipation dynamics in chapter 4 is analogous to the historical path of the Langevin equation (2.3.1), which was introduced as a phenomenological description of Brownian motion [18], and was later described microscopically (see section 2.3.3) through the Caldeira-Leggett model [26] which satisfies the fluctuation dissipation theorem described in [23] under all conditions.

2.5 Synthetic Ferrimagnets

A synthetic ferrimagnet (SFi) is a structure composed of multiple layers, where two of the layers are antiferromagnetically exchange coupled (see section 2.1.2), and the net magnetisation is non-zero. The basic components of an SFi can be seen in figure 2.5. Concepts relevant to the description and understanding of SFi's will be discussed in this section.

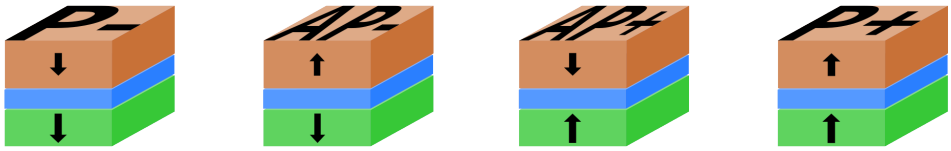

Figure 2.5: The basic components of an SFi structure with perpendicular magnetic anisotropy (PMA) in the four well defined magnetisation configurations. The orange and green layers are ferromagnetic and have moments represented by an arrow. The blue layer is a spacer layer through which an interlayer exchange coupling (IEC) is mediated. Two of the configurations show the moments of the ferromagnetic layers aligned in a parallel (P) fashion. The other two configurations show the ferromagnetic layers aligned in an anti-parallel (AP) fashion.

2.5.1 RKKY (Exchange) Coupling

The Ruderman-Kittel-Kasuya-Yosida (RKKY) interaction is a mechanism by which the exchange effect can occur non locally through a spin current mediated by the conduction electrons of a crystal. This can occur between the spins of localised inner core d-electrons in magnetic transition metals (and also between f-electrons in rare earth metals), and is often exploited in the design and production of SFi's. The effect allows the tuning of a stack so that the strength and type of coupling (ferromagnetic or antiferromagnetic) between magnetic layers - interlayer exchange coupling (IEC) - can be prepared. A full understanding of the effect was the joint work of [51, 52] and [53]. The relevance to SFi's is that a non-magnetic spacer layer placed between ferromagnetic layers can mediate an indirect exhange coupling between them. Changes to the thickness of the spacer layer result in variations in the interlayer exchange coupling (IEC) and the RKKY curve shows the IEC to oscillate between ferromagnetic and antiferromagnetic type with increasing spacer layer thickness [54]. The maximum strength of exchange coupling was shown to

vary systematically with the number of d-electrons in the valence band [55], with the strongest exchange coupling in the 4d transition metals ruthenium (Ru) and rhodium (Rh), along with the 5d transition metal iridium (Ir). Accordingly, the IEC in Ir [42, 56, 57, 58] and Ru [54, 59, 60, 61, 62] spacers has been studied for a number of different systems.

2.5.2 Antiparallel States

In systems with antiferromagnetically coupled layers, the AFM coupling causes the appearance of antiparallel (AP) states within the M-H curves. In the absence of an external field, the layers will align anti-parallel to minimise the energy of the system. If the two layers have a different magnetic moment, this will result in a net moment i.e. ferrimagnetic behaviour. The existence of AP states gives rise to four distinct magnetisation levels within the full hysteresis loops of these samples, two of which are denoted as P (parallel) states which exist at saturation when the magnetisation of layers align, and the other two being the AP states which can be identified at remanence. The four states can be seen in figure 2.5. As shown in [63] the rate of field sweep can effect the type of switching between P and AP states in SFi's.

2.5.3 Positive and Negative Magnetic Remanence

Generally, when a ferrimagnet is saturated and the field is later removed, the resulting remanent state will have the larger moment aligned in the direction of the previously applied field. This is referred to as positive magnetic remanance. Under certain conditions, during the reduction of the saturating field, the larger moment will align anti-parallel to the field, eventually resulting in a negative magnetic remanence at zero applied field. This results from competition between Zeeman, interlayer exchange, and magnetic anisotropy energies as the applied field strength varies, and is qualitatively examined in [64]. As the magnetic moment, interlayer exchange coupling [65] and magnetic anisotropy [66, 67] of the layers are temperature dependent, observations of negative remanence behaviour can depend on the temperature at which an SFi is examined. An example of negative remanence is shown in the range ΔT_{-R} in figure 2.6.

2.5.4 The Compensation Point

The compensation point is the temperature at which the magnetic moments of each layer in the antiferromagnetically exchange coupled structure are equal in magnitude. As such, the magnetic moments cancel out and the total moment is zero i.e. the behaviour is that of an anti-ferromagnet rather than a ferrimagnet. The layer with the larger moment changes either side of the compensation point. The compensation point can be seen in figure 2.6 at T_M where the net magnetic moment

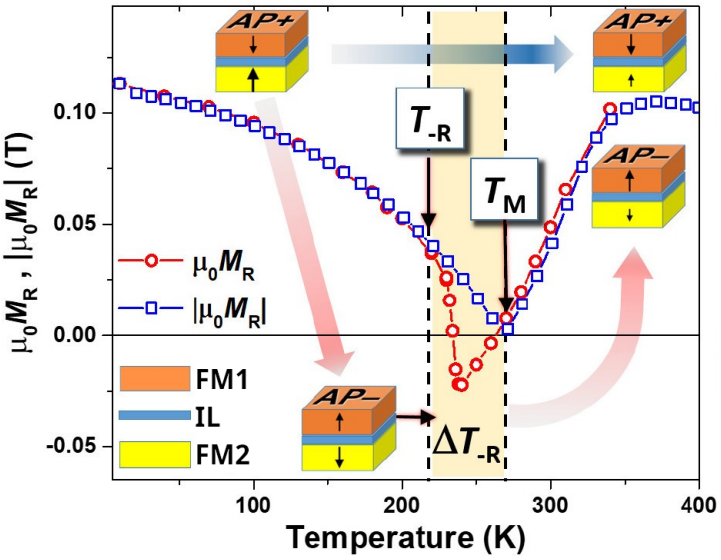

Figure 2.6: An example of remanent magnetisation with respect to temperature for the transition metal synthetic ferrimagnet (SFi) studied in [68]. The SFi is composed of two ferromagnetic layers (FM1 and FM2) separated by a non magnetic interlayer (IL). Negative remanence occurs between the negative remanence temperature T_{-R} and the compensation point T_M. Positive remanence occurs below T_{-R}. The red circles give remanence as calculated from hysteresis loops measured at various temperatures, while the blue squares show how the remanence changes as temperature is increased after preparation of a remanent state at low temperature.

vanishes.

2.6 Optics and Magneto-Optics

Changes to the polarisation of light due to its transmission through a magnetic material or reflection from a magnetic surface can give great insight into its magnetic properties. The capacity of this phenomena for quantitative analysis has given rise to a number of widely used experimental techniques for the study of magnetic materials based on the magneto-optical Kerr effect (MOKE) and the magneto-optical Faraday effect (MOFE). Beyond the experimental techniques used to examine magnetic phenomena, the effect of polarised light on the magnetisation state is of great interest to the study of all optical switching (see section 2.8) and as such, the ability of certain materials to modify the polarisation of a laser beam is used to prepare sources of optical excitation with the properties desired for the study presented in section 5. An explanation of relevant optical and magneto-optical effects will be given following [69].

2.6.1 Polarisation

Linearly polarised light

Owing to the electromagnetic theory of Maxwell, linearly polarised light is classically understood to be a transverse electromagnetic wave, composed of oscillating electric and magnetic field vectors orthogonal to each other and also the direction of wave propagation. In this picture the transverse electric and magnetic fields propagate in phase. It is common to drop references to the magnetic component from discussion of electromagnetic radiation with this implicit understanding. It is also to be understood that in the context of what is written in this section, light refers to any electromagnetic radiation, not only that which falls in the 'visible' range of the electromagnetic spectrum. Light emitted from a source are in general not polarised, and must be polarised through the use of a polarising filter.

Circularly polarised light

Circularly polarised light is where the electric field vector rotates helically around the axis of propagation with a constant radius. The rotation of the electric field vector can occur in either a left handed or right handed fashion as the wave propagates, that is to say light can be either left circularly polarised (LCP) or right circularly polarised (RCP). In each case the circularly polarised light can be thought of as two components of linearly polarised light which are 90° out of phase.

Light in general

More generally, light can be elliptically polarised, where the electric field vector rotates in an elliptical manner in a helical fashion around the axis of propagation.

From the superposition of any two orthogonally polarised light waves with equivalent axis of propagation, and variable amplitudes and phase, all possible polarisations of light can be constructed. This is most often shown in terms of the superposition of either orthogonal linearly polarised waves where the polarisation direction of the two waves are 90° apart, or as the superposition of left and right circularly polarised waves, which are also orthogonal.

A polarising filter is an optical component that allows the transmission of light of only one specific polarisation, while blocking the rest.

2.6.2 Dichroism and Birefringence

Dichroism

Dichroism is the name of the property of some materials where the absorption of polarised light is dependent on the polarisation direction or type. Most relevant to the discussion of all optical switching (see section 2.8) is magnetic circular dichroism (MCD). This phenomena is defined by a different absorption of light in a material depending on its circular polarisation, with the effect occuring as a result of the materials magnetic properties (e.g. magnetisation state).

Birefringence

Birefringence is the name for a property observed in certain materials, where refractive index of linearly polarised light is dependent on the direction of polarisation. That is to say that the speed of light in the material depends on the polarisation. Upon transmisson through a birefringent material, the phase difference between orthogonal linearly polarised waves will be modified. In the case where the orthogonal components retain the same axis of propagation after transmission, this generally results in the introduction of an ellipticity to the polarisation of the beam. Where the orthogonal components do not retain the same axis of propagation, in a phenomenon known as double refraction (shown in figure 2.7), the two components can be measured separately and used to determine the direction of linear polarisation of light. This effect is made use of in optical detectors (e.g. MOKE detectors) in order to observe changes in the polarisation rotation (that result from the reflection of light from the magnetic surface in the case of MOKE).

Circular birefringence is the case when the refractive index of circularly polarised light in a material is dependent on its helicity. By tuning the thickness of the material, a phase difference between the circular components of a (generally elliptically) polarised beam can be introduced, leading to a rotation in the direction of polarisation.

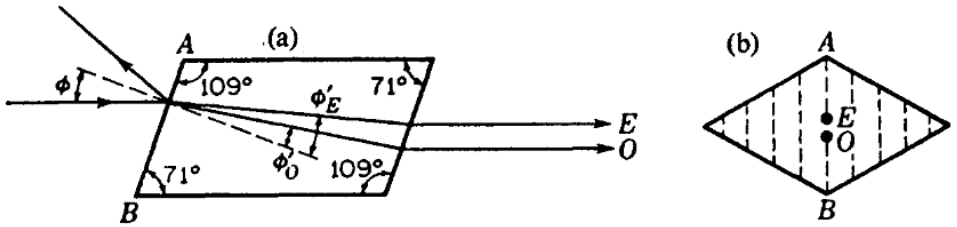

FIGURE 24J
Side and end views of the double refraction of light by a calcite crystal. (a) Cross-section of a principal plane. (b) End view.

Figure 2.7: Double refraction shown for a uniaxial crystal. Uniaxial crystals contain an axis known as the optic axis. A ray of light travelling in the direction of the optic axis does not show double refraction (birefringence). Paths O and E represent ordinary (polarisation perpendicular to the optic axis) and extraordinary (polarisation perpendicular to that of O) rays respectively. Panel (a) shows a side view while panel (b) shows and end view. Figure reproduced from [69]

2.6.3 Magneto Optical Faraday Effect

The magneto optical Faraday effect (MOFE) is the rotation of the polarisation direction of light resulting from its passing through a material containing a magnetic field component parallel to the direction of light propagation. The effect was discovered by Faraday for the transmission of linearly polarised light through glass with a magnetic field applied parallel to the propagation direction of light. The effect can also be seen in transparent magnetic materials, and thin magnetic films for which the thickness is small enough to allow for a detectable transmissive component of the incident light. The rotation of the linear polarisation (θ) due to the MOFE is given by

$$\theta = VBl, \tag{2.6.1}$$

where B is the magnetic field strength in the direction of light propagation, l is the length of the material through which the transmission occurs, and V is a material and wavelength dependent parameter of rotation per unit path per unit field strength, also known as the Verdet constant.

2.6.4 Magneto Optical Kerr Effect

It was later discovered by Kerr that light reflected from a magnetised material will also experience a rotation of its polarisation. This is known as the magneto-optical Kerr effect (MOKE) and is important in the study of optically opaque and strongly reflective materials such as bulk metals. The effect is limited to surface measurements of metals as incident light has a finite penetration depth. The magneto optical Kerr effect acts on the reflected component of incident light, while the magneto op-

tical Faraday effect acts on the transmitted component. Both arise from the same microscopic behaviour and result in a rotation proportional to the magnetisation of the material.

2.6.5 Origin of Magneto Optical Effects

The microscopic origin of MOFE and MOKE are related to the spin-orbit interaction. A rigorous treatment will not be given here as it does not add to the understanding of the study presented. The effect can be understood in simple terms by the interaction between circularly polarised light and the electrons in a material. Right and left circularly polarised light will induce a rotation of the electrons in opposite directions, resulting in orbital angular momentum with opposite signs. This orbital angular momentum interacts with the spins (that are aligned with the magnetisation of the material) resulting in a radius of rotation that differs between the two helicities by an amount proportional to the magnetisation. The difference in rotation radius polarises (separates) electrons of opposite spins in the material, which results in a change in the effective electric permittivity experienced by incoming light of different helicities. This results in a separation of the refractive index of the material for the two helicities, and so linearly polarised light rotates on transmission or reflection in the same manner as explained for circular birefringence.

2.6.6 MOKE Geometries

For an isotropic material, the changes to the (relative) electric permittivity tensor ε_r can be expressed as

$$\varepsilon_r = \frac{n^2}{\mu_r} \begin{pmatrix} 1 & iQ_z & -iQ_y \\ -iQ_z & 1 & iQ_x \\ iQ_y & -iQ_x & 1 \end{pmatrix}, \tag{2.6.2}$$

where n is the refractive index of the material, and Q_x, Q_y and Q_z are the Cartesian components of the Voigt vector, which is a magneto-optical quantity aligned with the magnetic field [9, 70]. The effect on an incoming electromagnetic wave then depends on the direction of magnetisation in the material. When the magnetisation is directed in the z-direction ($|\mathbf{Q}| = Q_Z$), the polar Kerr effect occurs. If the magnetisation lies in the plane of the film, the effect also depends on the plane of the incoming light - if the plane of incidence intersects with the magnetisation direction then the longitudinal Kerr effect occurs, whereas if the plane of incidence is perpendicular to the magnetisation direction the transverse Kerr effect occurs. The three MOKE geometries are shown in figure 2.8. Measurements will contain a superposition of these three effects in the case where magnetisation is not directed

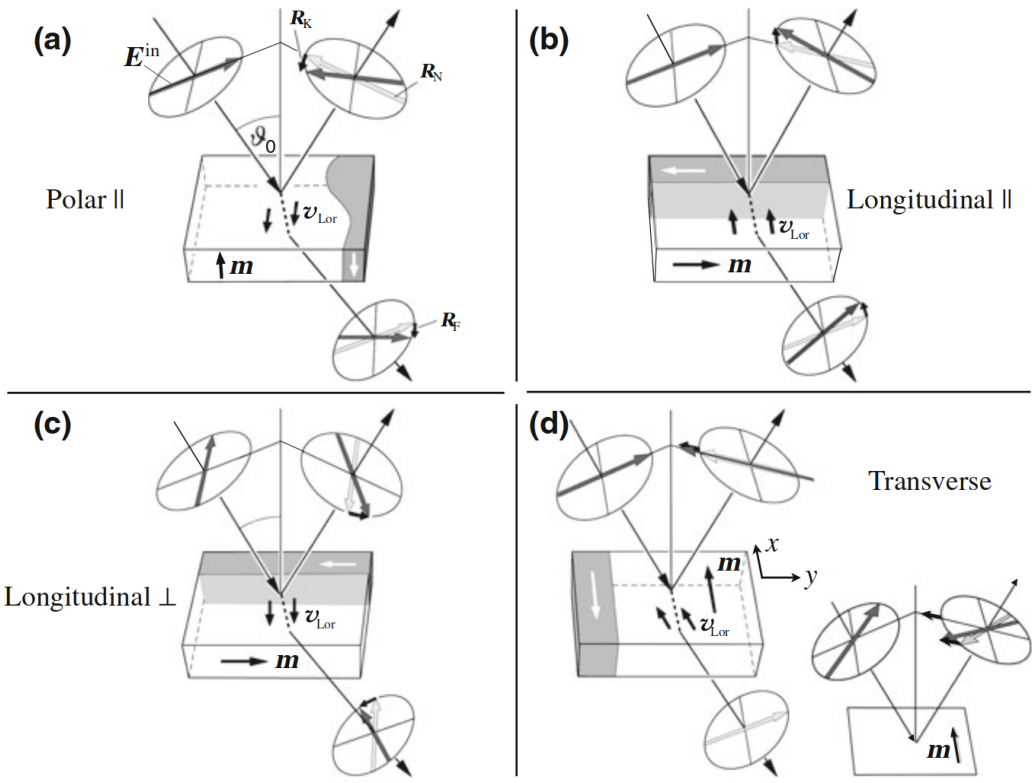

Figure 2.8: A schematic of geometries used for the magneto optical Kerr effect (reflected, $\mathbf{R}_K$) and magneto optical Faraday effect (transmitted, $\mathbf{R}_F$). Panel (a) shows the polar setup, where the sample magnetisation is in the plane of incidence. The longitudinal setup is shown in panels (b) for parallel and (c) for perpendicular magnetisations with respect to the polarisation. The transverse effect, where the magnetisation is perpendicular to the plane of incidence, is shown in panel (d). Figure reproduced from [11, 71].

along any of those three directions, and the incident light is not exactly normal to the surface of the material.

Further to this, Kerr rotation Φ and ellipticity ϵ (resulting from MCD) is also dependent on the polarisation of the incoming beam as per the Fresnel equations. The linear polaration can be separated into two components, the first is referred to as p-polarisation and is the component of polarisation in the plane of incidence of the light. The second component is the s-polarisation, and is the component perpendicular to the plane of incidence. The Kerr rotation and ellipticity is different for the two components as follows. For p-polarised light the rotation is given by

$$\Phi_p = -Re\left(\frac{r_{sp}}{r_{pp}}\right), \tag{2.6.3}$$

and the ellipticity by

$$\epsilon_p = Im\left(\frac{r_{sp}}{r_{pp}}\right), \tag{2.6.4}$$

where $r_{mn} = \frac{E_m^{(r)}}{E_n^{(i)}}$ are ratios of the reflected m component, and incident n component of electric field. For s-polarised light

$$\Phi_s = Re\left(\frac{r_{ps}}{r_{ss}}\right), \tag{2.6.5}$$

and

$$\epsilon_s = Im\left(\frac{r_{ps}}{r_{ss}}\right). \tag{2.6.6}$$

A full treatment of the magneto-optics, including the magneto-optical Faraday effect and application of the theory to multilayer systems can be found in [70].

2.7 Ultrafast Demagnetisation

The field of ultrafast magnetism began in 1996 from the work of Beaurepaire et al. [72]. In that study, a 22nm thick nickel film was excited with 60fs width ultrashort pulses, which was shown to induce a demagnetisation that occurs on a sub-picosecond time scale. This was the first observation of ultrafast (i.e. sub-picosecond) dynamics in magnetic materials and brought forward the question of whether the magnetisation direction may be optically switched. In the same work, ultrafast demagnetisation was explained in a phenomenological fashion through the extension of two temperature models - used to explain the equilibration of the electrons and lattice in metals [73] - to a three temperature model which also allows for the equilibration of the spin system.

2.7.1 Three Temperature model

The three temperature model (3TM) put forward in [72] has seen continued success in explaining ultrafast spin dynamics, such as helicity dependent all optical switching in Co/Pt multilayers [74], and other variations of the two-tempertaure model have been proposed for predictive purposes in AOS, such as that based on an opto-thermal coupling [75]. Therefore it is useful to outline the basic idea of the 3TM. The 3TM consists of three coupled first order differential equations. Each equation corresponds to the time evolution of the temperature of one of the three subsystems being considered. These include the electron temperature T_e, which evolves according to

$$C_e \frac{\mathrm{d}T_e}{\mathrm{d}t} = -G_{el}(T_e - T_l) - G_{es}(T_e - T_s) + P(t), \tag{2.7.1}$$

the lattice temperature T_l which evolves by,

$$C_l \frac{\mathrm{d}T_l}{\mathrm{d}t} = -G_{el}(T_l - T_e) - G_{sl}(T_l - T_s), \tag{2.7.2}$$

and the spin temperature T_s by,

$$C_s \frac{\mathrm{d}T_s}{\mathrm{d}t} = -G_{es}(T_s - T_e) - G_{sl}(T_s - T_l), \tag{2.7.3}$$

where C_e, C_l and C_s are the electron, lattic and spin contributions to the specific heat, G_{el}, G_{es} and G_{sl} are the electron-lattice, electron-spin and spin-lattice interaction constants, and $P(t)$ is the source of the heat introduced to the system through the exciting laser pulse. Together, these three equations describe the transfer of heat between the sub-systems and act as a phenomenological model for ultrafast demagnetisation, offering a good fit to both the experimentally derived electron and spin temperatures (see figure 2.9 from [72]).

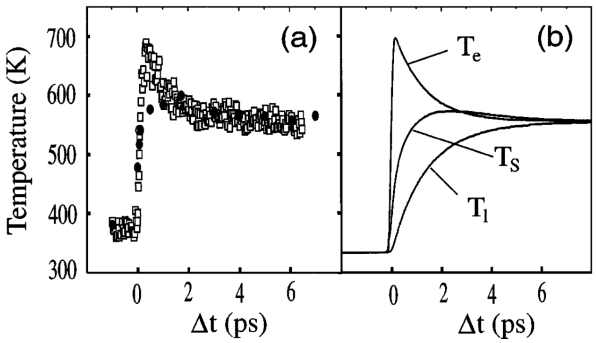

Figure 2.9: A comparison of the experimental demagnetisation data in nickel to values predicted using the three temperature model. Panel (a) shows experimental spin temperature (black circles) and experimental electron temperatures (white squares). Panel (b) shows the spin temperature T_s, electron temperature T_e, and lattice temperature T_l found using the three temerature model. Figure reproduced from [72]

2.7.2 The Microscopic Three Temperature Model

Since its introduction, the three temperature model and extended or modified versions of it have found widespread use in the modelling of ultrafast phenomena in magnetic systems. One popular modification is the microscopic 3TM (M3TM) proposed in [76] which is based on Elliot-Yafet spin-flip scattering of electrons interacting with the crystal lattice, itself facilitated by spin-orbit interactions. The Elliot-Yafet process is the proposed mechanism for the equilibration between electron and spin systems, ultimately leading to ultrafast demagnetisation. In [77], two different types of demagnetisation are shown to result from the M3TM (and then experimentally verified) based on the strength of coupling between electrons and spins. The first (type I) is where there is a strong coupling and occurs in 3d ferromagnets, while the second (type II) with weak coupling occurs in 4f systems such as Gd and Tb. It has been pointed out that these correspond to magnetic systems with itinerant and localised electrons respectively [39].

2.8 All Optical Switching

All optical switching is the reversal of the direction of the magnetisation of a material due to only the effect of incident electromagnetic radiation.

2.8.1 History of All Optical Switching

The first observation of all optical switching in a material with strong perpendicular anisotropy came in 2007 with the helicity dependent all optical switching (HD-AOS) of the RE-TM alloy GdFeCo [78] on the application of 40fs laser pulses. Soon after the effect was shown to be an ultrafast (sub-picosecond) reversal [79]. In 2012 single pulse helicity-indpendent all optical switching (HI-AOS) was observed in GdFeCo [80] showing that circularly polarised light is not a requirement for the effect. This was soon followed by reports of HD-AOS in the RE-TM alloys TbCo [81] and TbFe [82]. In 2014, synthetic ferrimagnets (SFi's) were identified as a promising candidate for AOS, with the criteria for AOS observed from ASD simulations being outlined in [41]. At around the same time it was shown that AOS is not exclusive to ferrimagnetic materials, as HD-AOS was observed in RE/TM multilayers and heterostructures along with transition metal SFi's validating the prediction of AOS in those systems [83]. Shortly after, HD-AOS was also discovered in transition metal Co/Pt and Co/Ni ferromagnetic multilayers, and Pt/Co/Pt trilayer systems [84]. Following on from this AOS of systems were categorised to be either single-pulse or multiple-pulse [85], with single pulse switching generally found in materials containing Gd and strongly associated with HI-AOS, and multiple-pulse switching found in a wider range of ferromagnetic and ferrimagnetic thin films alongside both HI-AOS and HD-AOS behaviour. More recently, in 2020 single pulse AOS was observed in the ferrimagnetic Heusler alloy Mn_2Ru_xGa (MRG) [86], and the multiple pulse switching in a Co/Pt layer was optimised as a dual pulse process in 2022 [87]. Furthermore, AOS was also observed in the 2D van der Waals ferromagnet CrI_3 in 2022 [88], and single pulse AOS has just been observed in the TM spin value structure [Pt/Co]/Cu/[Co/Pt] [89] (2023).

2.8.2 Categorisation of All Optical Switching

Observations of AOS are categorised according to whether the material shows helicity dependent switching, and whether more than a single pulse is required to see switching.

As previously mentioned, initial reports of AOS in the rare earth (RE) alloy GdFeCo were of a single pulse helicity dependent effect [78], but a helicity independent AOS was later shown to be possible [80]. Other materials showing single pulse HI-AOS include the TM/RE SFi Pt/Co/Gd [90], the Heusler alloy MRG [86],

the RE/TM Tb/Co multilayer based ferromagnetic stacks [91] and SFi's containing GdFeCo [92] along with the RE alloy GdTbCo [93].

The other major category is multiple pulse HD-AOS found in Co/Pt multilayers [84, 94, 95], and also seen in the RE/TM ferrimagnetic alloys and multilayers TbCo and Tb/Co alongside Co/Ir/CoNiPtCo/Ir TM SFi heterostructures [83]. The single pulse HI-AOS of a Pt/Co/Pt trilayer is shown in [96], but this result remains an outlier and it is unclear whether it has been successfully replicated.

The first observation of AOS in a magnetic dielectric was for cobalt-substituted yttrium iron garnet (YIG:Co) in 2017, with the mechanism of spin switching proceeding via the precession of the net magnetisation [97]. This is different to the more generally thermal mechanisms for metals discussed in section 2.8.3.

In 2021, multiple pulse HI-AOS was observed for the first time in a material with the structure Ni_3Pt/Ir/Co [68]. This initiated the study of a new class of materials consisting of rare-earth free synthetic ferrimagnets (e.g. the materials studied in chapter 5).

2.8.3 Mechanisms for Switching

In this section an overview for the proposed mechanisms for AOS will be given.

Magnetic Circular Dichroism

(Described in section 2.6.2). The early observations of HD-AOS in GdFeCo [78], when compared with HI-AOS found later [80] show that under certain conditions, helicity can have a significant effect on the resulting behaviour. The source of this helicity dependence was initially thought to be an effective field due to the inverse Faraday effect. Later it was shown that single pulse all optical switching in GdFeCo depends only on the amount of energy absorbed by the system but that the switching threshold is helicity dependent due to the effect of MCD [98]. Therefore it is the MCD effect in GdFeCo which gives rise to observations of AOS through its absorption dependence on circular polarisation and resultant asymmetry in the thermal properties of the pulse incident on the sample, that is to say that it is a helicity dependent thermal mechanism. As both MCD and the inverse Faraday effect (IFE) result from circular polarisation, it can be difficult to distinguish between the effects of each without close examination of the circumstances that result in AOS.

Inverse Faraday Effect

The inverse Faraday effect (IFE) is the generation of a magnetic field in a material resulting from the influence of a circularly polarised light [99]. This is the inverse process of the Faraday effect, where during the interaction between light and material, the magnetisation of the material effects the phase of incoming light. The

first observation of this effect in a nonabsorbing (MCD independent) material was reported in Eu^{+2}:CaF_2 in 1965 [100]. As previously mentioned, early reports of AOS in GdFeCo ascribed the effect to an effective field generated by the IFE in the material. While it subsequently came to light that MCD is the mechanism for the helicity dependence observed in those systems, the IFE model has continued to see use as a mechanism to explain multiple pulse HD-AOS seen in TM multilayer systems [101]. An ab-initio theory of IFE [102] provided evidence that IFE is strongly material and frequency dependent, and also that it induces both spin and orbital magnetisations with different behaviours. That ab-initio theory has been used to explain AOS in FePt nanoparticles [103]. In that study it is stated that the small number of pulses required for AOS indicates that it cannot be solely due to MCD, requiring also IFE. The form of effective magnetic field resulting from IFE was examined in [75], which discusses a field which remains acting on the magnetisation even after the duration of the incident pulse is complete. This is explained as the result of an optothermal and optomagnetic coupling. That study was motivated by the realisation that an extended effective field duration is required, or else the B-field needed to switch the magnetisation on a femtosecond timescale is unphysically high. In 2019 a study was performed on a TM SFi where the helicity dependence (assumed to arise through IFE) can be varied by tuning the thickness of FM layers [104]. This is thought to be the result of modification of the Curie temperature of the layers, with a helicity independence appearing when the Curie temperature different layers are matched.

Compensation point effects

It has been claimed that heating above a compensation point is a condition for AOS in some systems, including the RE-TM alloys GdCo [105] and TbCo [81]. While this appears to be a requirement for those systems, it is far from a general requirement as crossing over the compensation point has been shown not to be a requirement for AOS in GdFeCo [80], and AOS is well established in other ferrimagnetic samples where a compensation point does not exist [82, 106].

Transient ferromagnetic-like state

It was shown in 2011 by element specific XMCD measurements that a precondition for AOS in GdFeCo is the appearance of a transient-ferromagnetic state [107], where for a period of time in the picosecond scale dynamics after optical demagnetisation, the two sublattices briefly align. This leads to switching as the rate of remagnetisation during the realignment differs. As the antiferromagnetic coupling begins to dominate once again, the resulting dynamics direct the magnetisation of the ferrimagnet in a fashion opposite to that existing prior to interaction with the pulse. In 2012, observations of HI-AOS in GdFeCo showed that the reversal could be accounted for as a purely thermal effect [80], which was put down to the transient

FM state. The transient ferromagnetic state is a consequence of angular momentum transfer between sublattices in a ferrimagnet. A general theoretical framework for the dynamics in sublattices was introduced in [108]. That study differentiates between dynamics with exchange coupling and relativistic origins and determines that sublattice dynamics are distinct in the relativistic regime, and strongly coupled in the exchange regime, allowing for the appearance of the transient ferromagnetic state. By extension of that framework, it was shown that AOS of a ferrimagnetic alloy is due to the transfer of angular momentum from TM to RE sublattice [109]. In [110], the transfer of angular momentum was modelled in a microscopic fashion revealing the role of a two-magnon bound state in angular momentum transfer, and the pulse fluence and composition of GdFeCo under which it, and thereby the transient ferromagnetic state and AOS can occur.

Spin current driven

In some synthetic ferrimagnets a spacer layer is positioned between the ferromagnetic layers. The transfer of angular momentum between these layers in AOS can occur during demagnetisaion by means of a spin current. Demagnetisation of a layer causes it to act as the source of a spin angular momentum, which can then flow to the other ferromagnetic layer. The laser pulse induced spin current mechanism was first shown in 2008 to speed up the demagnetisation rate in Co/Pt multilayers [111]. After this, the effect was shown to enhance the magnetisation in the Fe layer of Ni/Ru/Fe [112]. In 2014 the spin current was shown to be a thermally driven effect [113]. In 2018 spin mediated single pulse HI-AOS was demonstrated in the spin valve [Co/Pt]/Cu/GdFeCo [114], in the absense of exchange coupling between [Co/Pt] and GdFeCo layers. The mechanism was further explored in 2020 when GdFeCo/Cu/FM spin valves were studied more generally, and showed that layer Curie temperature and thickness, along with pulse duration, play important roles in the capacity for AOS [115]. In that study, AOS was observed for many FM layer structures and for a significant range of pulse widths between 35fs and 1ps. A deterministic direction of spin current driven single pulse HI-AOS was shown for a range of pulse fluences above the critical fluence in a [Co/Ni]/Co/Cu/Co/Gd stack [116]. The deterministic switching results from the effect of the spin current, hindering switching when [Co/Ni] and Co/Gd are aligned parallel, and assisting it when antiparallel. Above a second fluence threshold the spin current effect is overcome and toggle switching between P and AP states is observed. Recently, spin current was identified as the mechanism in a multiple pulse HI-AOS for the RE free stack Ni_3Pt/Ir/Co [68].

Helicity Dependent Domain Wall Motion

The multiple pulse HD-AOS found in ferromagnetic multilayers takes place in a two part process [85]. In the first part, the sample undergoes a cumulative thermal demagnetisation on the arrival of each pulse. In the second part, the demagnetised region remagnetises in a helicity dependent process. The remagnetisation by subsequent pulses is a helicity dependent cumulative process, and takes many more pulses to occur than the initial demagnetisation (around 10× more pulses in Co thin films [85]). It was shown that the demagnetisation is due to a multiple-domain formation within the area probed, and the remagnetisation was postulated to result from a helicity-dependent domain wall motion resulting from MCD and/or IFE. These dynamics were confirmed in [117], where the demagnetisation process in [Co/Pt] multilayers nucleates domains with a 50nm radius. This is followed by the slower helicity dependent remagnetisation process driven by domain wall propagation with down to 3nm radial growth per pulse, which eventually leads the multiple domains to merge into a single domain. Domain wall propagation was shown to to be driven by a thermal gradient, with motion from cooler to hotter regions leading to the movement of nucleated domains towards the centre of the Gaussian spot, with the helicity dependent growth of domains due to MCD [95]. In [118] the properties of the induced domain wall motion were shown to also depend on domain wall pinning, and IFE was given as an alternative reason for domain wall motion while pointing out that the direction of motion due to MCD is unclear. A recent study explores the domain wall motion through a thermal gradient in greater detail [119].

2.8.4 Criteria for All Optical Switching

Domain and/or laser beam size

In multiple pulse HD-AOS ferromagnetic multilayer systems, it was found that the size of domains formed during cooling after the application of a pulse is critical to the ability to see switching [94]. The criterion for switching was that the size of domains formed should be larger than the laser spot size, else thermal demagnetisation (a multidomain state) will occur. The size of domains in Co/Pt multilayer thin films is strongly dependent on the thickness of the film, with lower thickness films having larger domains as a result of the balance between dipolar and domain wall energy. The number of multilayers or else thickness of layers in a stack can therefore be reduced in certain circumstances in order to meet this criterion. The report of single pulse HD-AOS in Co shown in [96] meets this criterion, further highlighting the importance of the domain size for AOS in ferromagnets.

Pulse Duration

It was initially thought that ultrafast (sub-picosecond) pulses were part of the criteria for AOS, due to a need for a strong non-equilibrum effect on the electrons [78, 120]. However over time a body of evidence has built to suggest that while non-equilibrium processes are important, such a strong non-equilibrium of electrons as earlier estimated is not required, and as such picosecond pulses are also sufficient for AOS [121, 122, 123]. Pulses of width up to 12.5ps are shown to induce AOS in GdFeCo in [122]. Despite this, pulse duration can still play an important role, particularly for multiple pulse switching as shown by [74] for Co/Pt multilayers, where the fluence range for AOS is broadened with increasing pulse duration.

Pulse repetition rate and ambient temperature

For samples showing multiple pulse switching, an increase in the repetition rate corresponds to an increase in the number of pulses interacting with the system in a given time interval, therefore AOS can become more likely for shorter periods of beam exposure, as the cumulative effect of the pulses occurs more quickly. Furthermore, the reduction of time between pulses can have the additional consequence of reducing the ability of the sample to cool, thereby modifying the ambient temperature which itself plays a role in the rate of domain wall motion via the thermal gradient [95]. Ambient temperature also plays a role within ultrafast demagnetisation, being able to significantly affect the demagnetisation dynamics and thereby AOS [124]. This is explained within the framework of the microscopic three temperature model (see section 2.7.2) as a transition from type I to type II dynamics at higher ambient temperatures when thermal equilibration of spins can no longer occur within the time taken for electron-phonon equilibration.

References

[1] Pierre Weiss. L'hypothèse du champ moléculaire et la propriété ferromagnétique. *Journal de Physique Théorique et Appliquée*, 6(1):661–690, 1907.

[2] W. Heisenberg. Zur Theorie des Ferromagnetismus. *Zeitschrift für Physik*, 49(9-10):619–636, September 1928.

[3] G. E. Uhlenbeck and S. Goudsmit. Spinning Electrons and the Structure of Spectra. *Nature*, 117(2938):264–265, February 1926.

[4] Walther Gerlach and Otto Stern. Der experimentelle Nachweis der Richtungsquantelung im Magnetfeld. *Zeitschrift für Physik*, 9(1):349–352, December 1922.

[5] David J. Griffiths. *Introduction to Quantum Mechanics*. Cambridge University Press, Cambridge, United Kingdom, 2nd edition edition, April 2004.

[6] E. Schrödinger. An Undulatory Theory of the Mechanics of Atoms and Molecules. *Physical Review*, 28(6):1049–1070, December 1926.

[7] W. Pauli. Über den Zusammenhang des Abschlusses der Elektronengruppen im Atom mit der Komplexstruktur der Spektren. *Zeitschrift für Physik*, 31(1):765–783, February 1925.

[8] W. Pauli. The Connection Between Spin and Statistics. *Physical Review*, 58(8):716–722, October 1940.

[9] S. Blundell. *Magnetism in Condensed Matter (Oxford Master Series in Physics)*. Oxford University Press, New York, 2001.

[10] Allan H. Morrish. *The Physical Principles of Magnetism*. R. E. Krieger Publishing Company, 1980.

[11] Alex Hubert and Rudolf Schäfer. *Magnetic Domains: The Analysis of Magnetic Microstructures*. Springer Science & Business Media, 3 edition, 2009.

[12] Louis Néel. Anisotropie magnétique superficielle et surstructures d'orientation. *Journal de Physique et le Radium*, 15(4):225–239, 1954.

[13] M. T. Johnson, P. J. H. Bloemen, F. J. A. den Broeder, and J. J. de Vries. Magnetic anisotropy in metallic multilayers. *Reports on Progress in Physics*, 59(11):1409, November 1996.

[14] Kenneth Franklin Riley, Michael Paul Hobson, and Stephen John Bence. *Mathematical Methods for Physics and Engineering: A Comprehensive Guide*. Cambridge University Press, Cambridge, January 1998.

[15] Lev Davidovich Landau and E Lifshitz. On the theory of the dispersion of magnetic permeability in ferromagnetic bodies. *Phys. Z. Sowjet.*, 8:153, 1935.

[16] T.L. Gilbert. Classics in Magnetics A Phenomenological Theory of Damping in Ferromagnetic Materials. *IEEE Transactions on Magnetics*, 40(6):3443–3449, November 2004.

[17] W. Brown. Thermal fluctuation of fine ferromagnetic particles. *IEEE Transactions on Magnetics*, 15(5):1196–1208, September 1979.

[18] Don S. Lemons and Anthony Gythiel. Paul Langevin's 1908 paper "On the Theory of Brownian Motion" ["Sur la théorie du mouvement brownien," C. R. Acad. Sci. (Paris) 146 , 530–533 (1908)]. *American Journal of Physics*, 65(11):1079–1081, November 1997.

[19] Albert Einstein. On the movement of small particles suspended in stationary liquids required by the molecular-kinetic theory of heat. In *The Collected Papers of Albert Einstein*, volume 2, pages 123–134. Princeton University Press, Princeton, New Jersey, 1989.

[20] Umberto Marini Bettolo Marconi, Andrea Puglisi, Lamberto Rondoni, and Angelo Vulpiani. Fluctuation–dissipation: Response theory in statistical physics. *Physics Reports*, 461(4):111–195, June 2008.

[21] H. Nyquist. Thermal agitation of electric charge in conductors. *Physical Review*, 32(1):110–113, 1928.

[22] J. B. Johnson. Thermal agitation of electricity in conductors. *Physical Review*, 32(1):97–109, 1928.

[23] Herbert B. Callen and Theodore A. Welton. Irreversibility and Generalized Noise. *Physical Review*, 83(1):34–40, July 1951.

[24] R Kubo. The fluctuation-dissipation theorem. *Reports on Progress in Physics*, 29(1):306, January 1966.

[25] L. D. Landau and E. M. Lifshitz. *Course of Theoretical Physics Volume 5, Statistical Physics Part 1*. 1980.

[26] A.O Caldeira and A.J Leggett. Quantum tunnelling in a dissipative system. *Annals of Physics*, 149(2):374–456, September 1983.

[27] Heinz Peter Breuer and Francesco Petruccione. Quantum Master Equations. In *The Theory of Open Quantum Systems*, pages 109–218. Oxford University Press, Oxford, January 2010.

[28] B. L. Hu, Juan Pablo Paz, and Yuhong Zhang. Quantum Brownian motion in a general environment: Exact master equation with nonlocal dissipation and colored noise. *Physical Review D*, 45(8):2843–2861, April 1992.

[29] Ken Funo and H. T. Quan. Path integral approach to heat in quantum thermodynamics. *Physical Review E*, 98(1):012113, July 2018.

[30] T. G. Philbin. Quantum dynamics of the damped harmonic oscillator. *New Journal of Physics*, 14, August 2012.

[31] Bruno Huttner and Stephen M. Barnett. Quantization of the electromagnetic field in dielectrics. *Physical Review A*, 46(7):4306–4322, October 1992.

[32] R. E. Watson, M. Blume, and G. H. Vineyard. Spin Motions in a Classical Ferromagnet. *Physical Review*, 181(2):811–823, May 1969.

[33] K. Binder and H. Rauch. Numerische Berechnung von Spin-Korrelationsfunktionen und Magnetisierungskurven von Ferromagnetica. *Zeitschrift für Physik A Hadrons and nuclei*, 219(3):201–215, June 1969.

[34] V. P. Antropov, M. I. Katsnelson, M. van Schilfgaarde, and B. N. Harmon. $\mathit{Ab}\mathit{}\mathit{Initio}$ Spin Dynamics in Magnets. *Physical Review Letters*, 75(4):729–732, July 1995.

[35] V. P. Antropov, M. I. Katsnelson, B. N. Harmon, M. van Schilfgaarde, and D. Kusnezov. Spin dynamics in magnets: Equation of motion and finite temperature effects. *Physical Review B*, 54(2):1019–1035, July 1996.

[36] R. F.L. Evans, W. J. Fan, P. Chureemart, T. A. Ostler, M. O.A. Ellis, and R. W. Chantrell. Atomistic spin model simulations of magnetic nanomaterials. *Journal of Physics Condensed Matter*, 26(10), March 2014.

[37] Ulrich Nowak. Thermally activated reversal in magnetic nanostructures. In *Annual Reviews of Computational Physics IX*, volume Volume 9 of *Annual Reviews of Computational Physics*, pages 105–151. World Scientific, April 2001.

[38] U. Nowak, O. N. Mryasov, R. Wieser, K. Guslienko, and R. W. Chantrell. Spin dynamics of magnetic nanoparticles: Beyond Brown's theory. *Physical Review B*, 72(17):172410, November 2005.

[39] Olle Eriksson, Anders Bergman, Lars Bergqvist, and and Johan Hellsvik. *Atomistic Spin Dynamics: Foundations and Applications*. Oxford University Press, New York, April 2017.

[40] B. Skubic, J. Hellsvik, L. Nordström, and O. Eriksson. A method for atomistic spin dynamics simulations: Implementation and examples. *Journal of Physics: Condensed Matter*, 20(31):315203, July 2008.

[41] Richard F. L. Evans, Thomas A. Ostler, Roy W. Chantrell, Ilie Radu, and Theo Rasing. Ultrafast thermally induced magnetic switching in synthetic ferrimagnets. *Applied Physics Letters*, 104(8):082410, February 2014.

[42] Jade N. Scott. *A Combined Experimental and Computational Study of Ni3Pt/Ir/Co Synthetic Ferrimagnets*. PhD thesis, Queen's University Belfast, July 2020.

[43] Anders Bergman, Björn Skubic, Johan Hellsvik, Lars Nordström, Anna Delin, and Olle Eriksson. Ultrafast switching in a synthetic antiferromagnetic magnetic random-access memory device. *Physical Review B*, 83(22):224429, June 2011.

[44] Satadeep Bhattacharjee, Anders Bergman, Andrea Taroni, Johan Hellsvik, Biplab Sanyal, and Olle Eriksson. Theoretical Analysis of Inertia-like Switching in Magnets: Applications to a Synthetic Antiferromagnet. *Physical Review X*, 2(1):011013, March 2012.

[45] Raghuveer Chimata, Anders Bergman, Lars Bergqvist, Biplab Sanyal, and Olle Eriksson. Microscopic Model for Ultrafast Remagnetization Dynamics. *Physical Review Letters*, 109(15):157201, October 2012.

[46] R. F. L. Evans, U. Atxitia, and R. W. Chantrell. Quantitative simulation of temperature-dependent magnetization dynamics and equilibrium properties of elemental ferromagnets. *Physical Review B*, 91(14):144425, April 2015.

[47] Johan Hellsvik, Johan H. Mentink, and José Lorenzana. Ultrafast cooling and heating scenarios for the laser-induced phase transition in CuO. *Physical Review B*, 94(14):144435, October 2016.

[48] Takayuki Shiino, Se-Hyeok Oh, Paul M. Haney, Seo-Won Lee, Gyungchoon Go, Byong-Guk Park, and Kyung-Jin Lee. Antiferromagnetic Domain Wall Motion Driven by Spin-Orbit Torques. *Physical Review Letters*, 117(8):087203, August 2016.

[49] Matthew O. A. Ellis, Eric E. Fullerton, and Roy W. Chantrell. All-optical switching in granular ferromagnets caused by magnetic circular dichroism. *Scientific Reports*, 6(1):30522, July 2016.

[50] M. D. Kuz'min. Shape of Temperature Dependence of Spontaneous Magnetization of Ferromagnets: Quantitative Analysis. *Physical Review Letters*, 94(10):107204, March 2005.

[51] M. A. Ruderman and C. Kittel. Indirect Exchange Coupling of Nuclear Magnetic Moments by Conduction Electrons. *Physical Review*, 96(1):99–102, October 1954.

[52] Tadao Kasuya. A Theory of Metallic Ferro- and Antiferromagnetism on Zener's Model. *Progress of Theoretical Physics*, 16(1):45–57, July 1956.

[53] Kei Yosida. Magnetic Properties of Cu-Mn Alloys. *Physical Review*, 106(5):893–898, June 1957.

[54] S. S. P. Parkin and D. Mauri. Spin engineering: Direct determination of the Ruderman-Kittel-Kasuya-Yosida far-field range function in ruthenium. *Physical Review B*, 44(13):7131–7134, October 1991.

[55] S. S. P. Parkin. Systematic variation of the strength and oscillation period of indirect magnetic exchange coupling through the 3d, 4d, and 5d transition metals. *Physical Review Letters*, 67(25):3598–3601, December 1991.

[56] A. Dinia, M. Stoeffel, K. Rahmouni, D. Stoeffler, and H. A. M. van den Berg. Exchange coupling and magnetoresistance in Co/Ir multilayers prepared by ion beam sputtering. *Europhysics Letters*, 42(3):331, May 1998.

[57] M. S. Gabor, T. Petrisor, R. B. Mos, M. Nasui, C. Tiusan, and T. Petrisor. Interlayer exchange coupling in perpendicularly magnetized Pt/Co/Ir/Co/Pt structures. *Journal of Physics D: Applied Physics*, 50(46):465004, October 2017.

[58] Qinli Ma, Yufan Li, Young-suk Choi, Wei-Chuan Chen, Shu Jen Han, and C. L. Chien. Spin orbit torque switching of synthetic Co/Ir/Co trilayers with perpendicular anisotropy and tunable interlayer coupling. *Applied Physics Letters*, 117(17):172403, October 2020.

[59] P. J.H. Bloemen, H. W. Van Kesteren, H. J.M. Swagten, and W. J.M. De Jonge. Oscillatory interlayer exchange coupling in Co/Ru multilayers and bilayers. *Physical Review B*, 50(18):13505, November 1994.

[60] Tommy McKinnon, Bret Heinrich, and Erol Girt. Spacer layer thickness and temperature dependence of interlayer exchange coupling in Co/Ru/Co trilayer structures. *Physical Review B*, 104(2):024422, July 2021.

[61] H. J. Waring, Y. Li, C. Moutafis, I. J. Vera-Marun, and T. Thomson. Magnetization dynamics in synthetic ferromagnetic thin films. *Physical Review B*, 104(1):014419, July 2021.

[62] Teng Xu, Jiahao Liu, Xichao Zhang, Qihan Zhang, Heng-An Zhou, Yiqing Dong, Pierluigi Gargiani, Manuel Valvidares, Yan Zhou, and Wanjun Jiang. Systematic Control of the Interlayer Exchange Coupling in Perpendicularly Magnetized Synthetic Antiferromagnets. *Physical Review Applied*, 18(5):054051, November 2022.

[63] R. B. Morgunov, E. I. Kunitsyna, A. D. Talantsev, O. V. Koplak, T. Fache, Y. Lu, and S. Mangin. Influence of the magnetic field sweeping rate on magnetic transitions in synthetic ferrimagnets with perpendicular anisotropy. *Applied Physics Letters*, 114(22):222402, June 2019.

[64] K. Takanashi, H. Kurokawa, and H. Fujimori. A novel hysteresis loop and indirect exchange coupling in Co/Pt/Gd/Pt multilayer films. *Applied Physics Letters*, 63(11):1585–1587, 1993.

[65] S. Schwieger, J. Kienert, K. Lenz, J. Lindner, K. Baberschke, and W. Nolting. Temperature dependence of interlayer exchange coupling. *Journal of Magnetism and Magnetic Materials*, 310(2, Part 3):2301–2303, March 2007.

[66] H. B. Callen and E. Callen. The present status of the temperature dependence of magnetocrystalline anisotropy, and the l(l+1)2 power law. *Journal of Physics and Chemistry of Solids*, 27(8):1271–1285, August 1966.

[67] J. B. Staunton, L. Szunyogh, A. Buruzs, B. L. Gyorffy, S. Ostanin, and L. Udvardi. Temperature dependence of magnetic anisotropy: An ab initio approach. *Physical Review B*, 74(14):144411, October 2006.

[68] Maciej Dąbrowski, Jade N. Scott, William R. Hendren, Colin M. Forbes, Andreas Frisk, David M. Burn, David G. Newman, Connor R. J. Sait, Paul S. Keatley, Alpha T. N'Diaye, Thorsten Hesjedal, Gerrit van der Laan, Robert M. Bowman, and Robert J. Hicken. Transition Metal Synthetic Ferrimagnets: Tunable Media for All-Optical Switching Driven by Nanoscale Spin Current. *Nano Letters*, 21(21):9210–9216, November 2021.

[69] Francis Arthur Jenkins and Harvey Elliott White. *Fundamentals of Optics*. McGraw-Hill College, Auckland, 4th edition edition, June 1976.

[70] J. Zak, E. R. Moog, C. Liu, and S. D. Bader. Universal approach to magneto-optics. *Journal of Magnetism and Magnetic Materials*, 89(1):107–123, September 1990.

[71] Wolfgang Kuch, Rudolf Schäfer, Peter Fischer, and Franz Ulrich Hillebrecht. *Magnetic Microscopy of Layered Structures*, volume 57 of *Springer Series in Surface Sciences*. Springer, Berlin, Heidelberg, 2015.

[72] E. Beaurepaire, J. C. Merle, A. Daunois, and J. Y. Bigot. Ultrafast spin dynamics in ferromagnetic nickel. *Physical Review Letters*, 76(22):4250–4253, May 1996.

[73] S. Anisimov, B. L. Kapeliovich, and T. Perelman. Electron emission from metal surfaces exposed to ultrashort laser pulses. *Journal of Experimental and Theoretical Physics*, August 1974.

[74] G. Kichin, M. Hehn, J. Gorchon, G. Malinowski, J. Hohlfeld, and S. Mangin. From Multiple- to Single-Pulse All-Optical Helicity-Dependent Switching in Ferromagnetic Co/Pt Multilayers. *Physical Review Applied*, 12(2):024019, August 2019.

[75] Zhidong Du, Chen Chen, Feng Cheng, Yongmin Liu, and Liang Pan. Supplementary: Prediction of Deterministic All-Optical Switching of Ferromagnetic Thin Film by Ultrafast Optothermal and Optomagnetic Couplings. *Scientific Reports*, 7(1):13513, October 2017.

[76] B. Koopmans, J. J. M. Ruigrok, F. Dalla Longa, and W. J. M. de Jonge. Unifying Ultrafast Magnetization Dynamics. *Physical Review Letters*, 95(26):267207, December 2005.

[77] T. Roth, A. J. Schellekens, S. Alebrand, O. Schmitt, D. Steil, B. Koopmans, M. Cinchetti, and M. Aeschlimann. Temperature Dependence of Laser-Induced Demagnetization in Ni: A Key for Identifying the Underlying Mechanism. *Physical Review X*, 2(2):021006, May 2012.

[78] C. D. Stanciu, F. Hansteen, A. V. Kimel, A. Kirilyuk, A. Tsukamoto, A. Itoh, and Th. Rasing. All-Optical Magnetic Recording with Circularly Polarized Light. *Physical Review Letters*, 99(4):047601, July 2007.

[79] C. D. Stanciu, A. Tsukamoto, A. V. Kimel, F. Hansteen, A. Kirilyuk, A. Itoh, and Th. Rasing. Subpicosecond Magnetization Reversal across Ferrimagnetic Compensation Points. *Physical Review Letters*, 99(21):217204, November 2007.

[80] T. A. Ostler, J. Barker, R. F.L. Evans, R. W. Chantrell, U. Atxitia, O. Chubykalo-Fesenko, S. El Moussaoui, L. Le Guyader, E. Mengotti, L. J. Heyderman, F. Nolting, A. Tsukamoto, A. Itoh, D. Afanasiev, B. A. Ivanov, A. M. Kalashnikova, K. Vahaplar, J. Mentink, A. Kirilyuk, Th Rasing, and A. V. Kimel. Ultrafast heating as a sufficient stimulus for magnetization reversal in a ferrimagnet. *Nature Communications*, 3, 2012.

[81] Sabine Alebrand, Matthias Gottwald, Michel Hehn, Daniel Steil, Mirko Cinchetti, Daniel Lacour, Eric E. Fullerton, Martin Aeschlimann, and Stéphane Mangin. Light-induced magnetization reversal of high-anisotropy TbCo alloy films. *Applied Physics Letters*, 101(16):162408, October 2012.

[82] Alexander Hassdenteufel, Birgit Hebler, Christian Schubert, Andreas Liebig, Martin Teich, Manfred Helm, Martin Aeschlimann, Manfred Albrecht, and Rudolf Bratschitsch. Thermally Assisted All-Optical Helicity Dependent Magnetic Switching in Amorphous Fe100–xTbx Alloy Films. *Advanced Materials*, 25(22):3122–3128, 2013.

[83] S. Mangin, M. Gottwald, C. H. Lambert, D. Steil, V. Uhlíř, L. Pang, M. Hehn, S. Alebrand, M. Cinchetti, G. Malinowski, Y. Fainman, M. Aeschlimann, and E. E. Fullerton. Engineered materials for all-optical helicity-dependent magnetic switching. *Nature Materials*, 13(3):286–292, February 2014.

[84] C. H. Lambert, S. Mangin, B. S.D.Ch S. Varaprasad, Y. K. Takahashi, M. Hehn, M. Cinchetti, G. Malinowski, K. Hono, Y. Fainman, M. Aeschlimann, and E. E. Fullerton. All-optical control of ferromagnetic thin films and nanostructures. *Science*, 345(6202):1337–1340, September 2014.

[85] Mohammed Salah El Hadri, Michel Hehn, Philipp Pirro, Charles Henri Lambert, Grégory Malinowski, Eric E. Fullerton, and Stéphane Mangin. Domain size criterion for the observation of all-optical helicity-dependent switching in magnetic thin films. *Physical Review B*, 94(6):064419, August 2016.

[86] C. Banerjee, N. Teichert, K. E. Siewierska, Z. Gercsi, G. Y. P. Atcheson, P. Stamenov, K. Rode, J. M. D. Coey, and J. Besbas. Single pulse all-optical toggle switching of magnetization without gadolinium in the ferrimagnet Mn2RuxGa. *Nature Communications*, 11(1):4444, September 2020.

[87] Kihiro T. Yamada, Alexey V. Kimel, Kiran Horabail Prabhakara, Sergiu Ruta, Tian Li, Fuyuki Ando, Sergey Semin, Teruo Ono, Andrei Kirilyuk, and Theo Rasing. Efficient All-Optical Helicity Dependent Switching of Spins in a Pt/Co/Pt Film by a Dual-Pulse Excitation. *Frontiers in Nanotechnology*, 4:765848, 2022.

[88] Maciej Dąbrowski, Shi Guo, Mara Strungaru, Paul S. Keatley, Freddie Withers, Elton J. G. Santos, and Robert J. Hicken. All-optical control of spin in a 2D van der Waals magnet. *Nature Communications*, 13(1):5976, October 2022.

[89] Junta Igarashi, Wei Zhang, Quentin Remy, Eva Díaz, Jun-Xiao Lin, Julius Hohlfeld, Michel Hehn, Stéphane Mangin, Jon Gorchon, and Grégory Malinowski. Optically induced ultrafast magnetization switching in ferromagnetic spin valves. *Nature Materials*, pages 1–6, March 2023.

[90] M. L. M. Lalieu, M. J. G. Peeters, S. R. R. Haenen, R. Lavrijsen, and B. Koopmans. Deterministic all-optical switching of synthetic ferrimagnets using single femtosecond laser pulses. *Physical Review B*, 96(22):220411, December 2017.

[91] L. Avilés-Félix, A. Olivier, G. Li, C. S. Davies, L. Álvaro-Gómez, M. Rubio-Roy, S. Auffret, A. Kirilyuk, A. V. Kimel, Th Rasing, L. D. Buda-Prejbeanu, R. C. Sousa, B. Dieny, and I. L. Prejbeanu. Single-shot all-optical switching of magnetization in Tb/Co multilayer-based electrodes. *Scientific Reports*, 10(1):5211, March 2020.

[92] Jon Gorchon, Charles-Henri Lambert, Yang Yang, Akshay Pattabi, Richard B. Wilson, Sayeef Salahuddin, and Jeffrey Bokor. Single shot ultrafast all optical magnetization switching of ferromagnetic Co/Pt multilayers. *Applied Physics Letters*, 111(4):042401, July 2017.

[93] Wei Zhang, Jun Xiao Lin, Tian Xun Huang, Gregory Malinowski, Michel Hehn, Yong Xu, Stéphane Mangin, and Weisheng Zhao. Role of spin-lattice coupling in ultrafast demagnetization and all optical helicity-independent single-shot switching in Gd1-x-yTbyCox alloys. *Physical Review B*, 105(5):054410, February 2022.

[94] M. S. El Hadri, P. Pirro, C.-H. Lambert, S. Petit-Watelot, Y. Quessab, M. Hehn, F. Montaigne, G. Malinowski, and S. Mangin. Two types of all-optical magnetization switching mechanisms using femtosecond laser pulses. *Physical Review B*, 94(6):064412, August 2016.

[95] U. Parlak, R. Adam, D. E. Bürgler, S. Gang, and C. M. Schneider. Optically induced magnetization reversal in [Co/Pt]N multilayers: Role of domain wall dynamics. *Physical Review B*, 98(21):214443, December 2018.

[96] M. Vomir, M. Albrecht, and J.-Y. Bigot. Single shot all optical switching of intrinsic micron size magnetic domains of a Pt/Co/Pt ferromagnetic stack. *Applied Physics Letters*, 111(24):242404, December 2017.

[97] A. Stupakiewicz, K. Szerenos, D. Afanasiev, A. Kirilyuk, and A. V. Kimel. Ultrafast nonthermal photo-magnetic recording in a transparent medium. *Nature*, 542(7639):71–74, February 2017.

[98] A. R. Khorsand, M. Savoini, A. Kirilyuk, A. V. Kimel, A. Tsukamoto, A. Itoh, and Th. Rasing. Role of Magnetic Circular Dichroism in All-Optical Magnetic Recording. *Physical Review Letters*, 108(12):127205, March 2012.

[99] Hui-Liang Zhang, Yan-Zhong Wang, and Xiang-Jun Chen. A simple explanation for the inverse Faraday effect in metals. *Journal of Magnetism and Magnetic Materials*, 321(24):L73–L74, December 2009.

[100] J. P. van der Ziel, P. S. Pershan, and L. D. Malmstrom. Optically-Induced Magnetization Resulting from the Inverse Faraday Effect. *Physical Review Letters*, 15(5):190–193, August 1965.

[101] T. D. Cornelissen, R. Córdoba, and B. Koopmans. Microscopic model for all optical switching in ferromagnets. *Applied Physics Letters*, 108(14):142405, April 2016.

[102] Marco Berritta, Ritwik Mondal, Karel Carva, and Peter M. Oppeneer. Ab Initio Theory of Coherent Laser-Induced Magnetization in Metals. *Physical Review Letters*, 117(13):137203, September 2016.

[103] R. John, M. Berritta, D. Hinzke, C. Müller, T. Santos, H. Ulrichs, P. Nieves, J. Walowski, R. Mondal, O. Chubykalo-Fesenko, J. McCord, P. M. Oppeneer, U. Nowak, and M. Münzenberg. Magnetisation switching of FePt nanoparticle recording medium by femtosecond laser pulses. *Scientific Reports*, 7(1):4114, June 2017.

[104] Jung-Wei Liao, Pierre Vallobra, Liam O'Brien, Unai Atxitia, Victor Raposo, Dorothée Petit, Tarun Vemulkar, Gregory Malinowski, Michel Hehn, Eduardo Martínez, Stéphane Mangin, and Russell P. Cowburn. Controlling All-Optical Helicity-Dependent Switching in Engineered Rare-Earth Free Synthetic Ferrimagnets. *Advanced Science*, 6(24):1901876, 2019.

[105] A. Mekonnen, M. Cormier, A. V. Kimel, A. Kirilyuk, A. Hrabec, L. Ranno, and Th. Rasing. Femtosecond Laser Excitation of Spin Resonances in Amorphous Ferrimagnetic Gd(1-x)Co(x) Alloys. *Physical Review Letters*, 107(11):117202, September 2011.

[106] M. Beens, M. L. M. Lalieu, A. J. M. Deenen, R. A. Duine, and B. Koopmans. Comparing all-optical switching in synthetic-ferrimagnetic multilayers and alloys. *Physical Review B*, 100(22):220409, December 2019.

[107] I. Radu, K. Vahaplar, C. Stamm, T. Kachel, N. Pontius, H. A. Dürr, T. A. Ostler, J. Barker, R. F. L. Evans, R. W. Chantrell, A. Tsukamoto, A. Itoh, A. Kirilyuk, Th Rasing, and A. V. Kimel. Transient ferromagnetic-like state mediating ultrafast reversal of antiferromagnetically coupled spins. *Nature*, 472(7342):205–208, April 2011.

[108] J. H. Mentink, J. Hellsvik, D. V. Afanasiev, B. A. Ivanov, A. Kirilyuk, A. V. Kimel, O. Eriksson, M. I. Katsnelson, and Th. Rasing. Ultrafast Spin Dynamics in Multisublattice Magnets. *Physical Review Letters*, 108(5):057202, January 2012.

[109] U. Atxitia, T. Ostler, J. Barker, R. F. L. Evans, R. W. Chantrell, and O. Chubykalo-Fesenko. Ultrafast dynamical path for the switching of a ferrimagnet after femtosecond heating. *Physical Review B*, 87(22):224417, June 2013.

[110] J. Barker, U. Atxitia, T. A. Ostler, O. Hovorka, O. Chubykalo-Fesenko, and R. W. Chantrell. Two-magnon bound state causes ultrafast thermally induced magnetisation switching. *Scientific Reports*, 3(1):3262, November 2013.

[111] G. Malinowski, F. Dalla Longa, J. H. H. Rietjens, P. V. Paluskar, R. Huijink, H. J. M. Swagten, and B. Koopmans. Control of speed and efficiency of ultrafast demagnetization by direct transfer of spin angular momentum. *Nature Physics*, 4(11):855–858, November 2008.

[112] Dennis Rudolf, Chan La-O-Vorakiat, Marco Battiato, Roman Adam, Justin M. Shaw, Emrah Turgut, Pablo Maldonado, Stefan Mathias, Patrik Grychtol, Hans T. Nembach, Thomas J. Silva, Martin Aeschlimann, Henry C. Kapteyn, Margaret M. Murnane, Claus M. Schneider, and Peter M. Oppeneer. Ultrafast magnetization enhancement in metallic multilayers driven by superdiffusive spin current. *Nature Communications*, 3(1):1037, September 2012.

[113] Gyung-Min Choi, Byoung-Chul Min, Kyung-Jin Lee, and David G. Cahill. Spin current generated by thermally driven ultrafast demagnetization. *Nature Communications*, 5(1):4334, July 2014.

[114] Satoshi Iihama, Yong Xu, Marwan Deb, Grégory Malinowski, Michel Hehn, Jon Gorchon, Eric E. Fullerton, and Stéphane Mangin. Single-Shot Multi-Level All-Optical Magnetization Switching Mediated by Spin Transport. *Advanced Materials*, 30(51):1804004, 2018.

[115] Junta Igarashi, Quentin Remy, Satoshi Iihama, Grégory Malinowski, Michel Hehn, Jon Gorchon, Julius Hohlfeld, Shunsuke Fukami, Hideo Ohno, and Stéphane Mangin. Engineering Single-Shot All-Optical Switching of Ferromagnetic Materials. *Nano Letters*, 20(12):8654–8660, December 2020.

[116] Youri L. W. van Hees, Paul van de Meugheuvel, Bert Koopmans, and Reinoud Lavrijsen. Deterministic all-optical magnetization writing facilitated by non-local transfer of spin angular momentum. *Nature Communications*, 11(1):3835, July 2020.

[117] R. Medapalli, D. Afanasiev, Dokyun Kim, Y. Quessab, Sergio A. Monotoya, A. Kirilyuk, T. Rasing, A. Kimel, and E. Fullerton. Mechanism of all-optical control of ferromagnetic multilayers with circularly polarized light. *arXiv: Materials Science*, July 2016.

[118] Y. Quessab, R. Medapalli, M. S. El Hadri, M. Hehn, G. Malinowski, E. E. Fullerton, and S. Mangin. Helicity-dependent all-optical domain wall motion in ferromagnetic thin films. *Physical Review B*, 97(5):054419, February 2018.

[119] Umut Parlak, Roman Adam, Daniel E. Bürgler, Tomáš Duchoň, Slavomír Nemšák, Fangzhou Wang, Christian Greb, Sarah Heidtfeld, and Claus M. Schneider. Ferromagnetic domain wall manipulation using optically induced

thermal gradients. *Journal of Magnetism and Magnetic Materials*, 560:169441, October 2022.

[120] K. Vahaplar, A. M. Kalashnikova, A. V. Kimel, S. Gerlach, D. Hinzke, U. Nowak, R. Chantrell, A. Tsukamoto, A. Itoh, A. Kirilyuk, and Th. Rasing. All-optical magnetization reversal by circularly polarized laser pulses: Experiment and multiscale modeling. *Physical Review B*, 85(10):104402, March 2012.

[121] Daniel Steil, Sabine Alebrand, Alexander Hassdenteufel, Mirko Cinchetti, and Martin Aeschlimann. All-optical magnetization recording by tailoring optical excitation parameters. *Physical Review B*, 84(22):224408, December 2011.

[122] J. Gorchon, R. B. Wilson, Y. Yang, A. Pattabi, J. Y. Chen, L. He, J. P. Wang, M. Li, and J. Bokor. Role of electron and phonon temperatures in the helicity-independent all-optical switching of GdFeCo. *Physical Review B*, 94(18):184406, November 2016.

[123] C.S. Davies, T. Janssen, J.H. Mentink, A. Tsukamoto, A.V. Kimel, A.F.G. van der Meer, A. Stupakiewicz, and A. Kirilyuk. Pathways for Single-Shot All-Optical Switching of Magnetization in Ferrimagnets. *Physical Review Applied*, 13(2):024064, February 2020.

[124] B. Koopmans, G. Malinowski, F. Dalla Longa, D. Steiauf, M. Fähnle, T. Roth, M. Cinchetti, and M. Aeschlimann. Explaining the paradoxical diversity of ultrafast laser-induced demagnetization. *Nature Materials*, 9(3):259–265, March 2010.

Chapter 3

Experimental Techniques

3.1 Vibrating Sample Magnetometer

A vibrating sample magnetometer (VSM) device works on the principle of Faraday's law of induction. As shown in figure 3.1, the vibration of a magnetic sample induces a voltage detected by pickup coils, which is used to determine the magnetisation of the sample. A uniform field is applied to the sample by an electromagnet, and the electromotive force induced by the sample is plotted as the output while the input field is swept. The induced voltage is proportional to the magnetic moment of the sample, so comparison to the voltage produced by a reference sample can be used to calibrate the system and determine the moment of the sample under study.

After calibration, the system outputs the magnetic moment in emu, which can be converted to magnetisation in SI units by use of the equivalence of units

$$\frac{\text{moment[emu]}}{\text{volume[cm}^3\text{]}} = 1000[A/m]. \tag{3.1.1}$$

Hence

$$\mu_0 M[mT] = \mu_0 \frac{\text{moment[emu]}}{\text{volume[cm}^3\text{]}} \tag{3.1.2}$$

is used to find the magnetisation of the sample in terms of the known values of magnetic moment and sample volume.

(a)

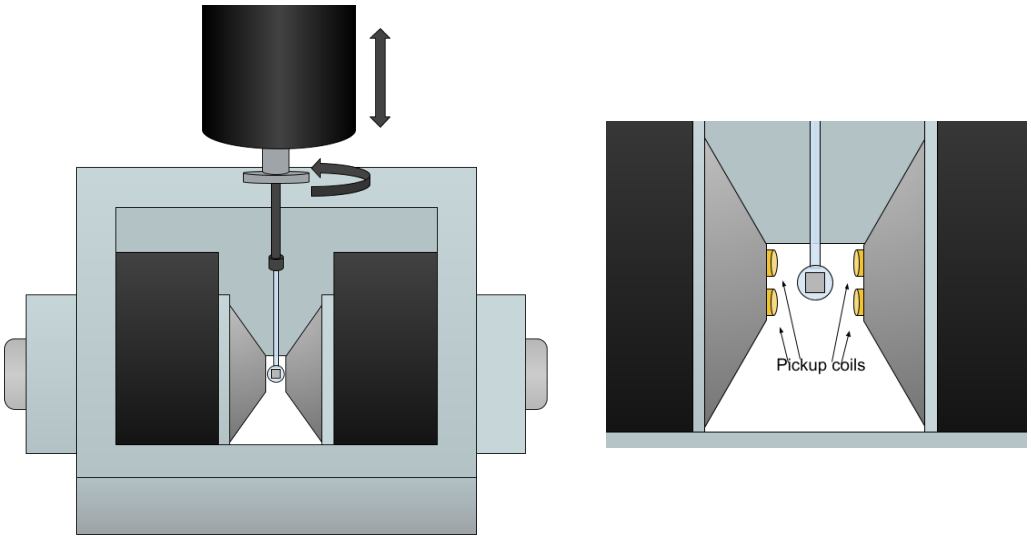

Figure 3.1: A schematic of the vibrating sample magnetometer (VSM) setup. The sample is mounted on a quartz rod between the poles of an electromagnet and pickup coils (shown in the inset) which measure the field induced by the vertical oscillation of the sample.

3.2 Wide Field Kerr Microscopy

Wide field Kerr microscopy is a useful non-destructive technique for the real time imaging of magnetic domain formation and changes to the magnetic state of a local area of a sample at depths of up to 20nm (the penetration depth of light in metallic materials) [1]. Here we use white LED light as a probe, and a dry objective lens, giving a good spatial resolution with the ability to resolve domains as small as 350nm according to the Rayleigh criterion (taking the average wavelength as 550nm, and NA=0.95). The usual limitation of this technique is of the small 20nm probed depth. However this is not a concern in this study as the thickness of the thin films used (table 5.1) are of the order of 20nm. The signal is detected and digitised by a CMOS camera allowing for quantitative analysis.

The setup used in this study, shown in figure 3.2, consists of an Evico Magnetics magneto-optical Kerr microscope & magnometer system, positioned on a mechanically damped optical table, which is used to observe the magnetisation changes in a sample due to either an external field applied by a perpendicular coil, or an ultrafast laser applied to the area of the sample within the field of view.

3.2.1 Wide Field Kerr Microscope Optics

The optics of the microscope in the wide field Kerr microscopy (WFKM) setup are shown in figure 3.3. A brief overview of the experimental optics between the light source and dectector will be given.

Light source

A white LED light source is used to illuminate the sample for the purpose of WFKM. The LED's are housed in the lamp controller, and the light is guided into the WFKM using glass optical fibers. The fiber outputs are arranged in a cross pattern and by choosing the active LED's the Kerr geometry can be defined as shown in [3]. In this study the samples of interest have strong perpendicular magnetic anistropy and therefore pure polar contrast is desired in order to view the changes to out of plane magnetisation. A pure polar contrast can be achieved by a symmetric activation of LED's, with equalised luminous intensity. The LED's can be individually brightened and dimmed within the Evico software to manually ensure equalisation by measurement of intensity in the raw output of the CMOS camera. In all WFKM images shown in chapter 5, the four central LED's are illuminated to give a symmetric incidence of white light on to the sample, corresponding to a polar Kerr contrast that corresponds to the out-of-plane magnetisation of the sample.

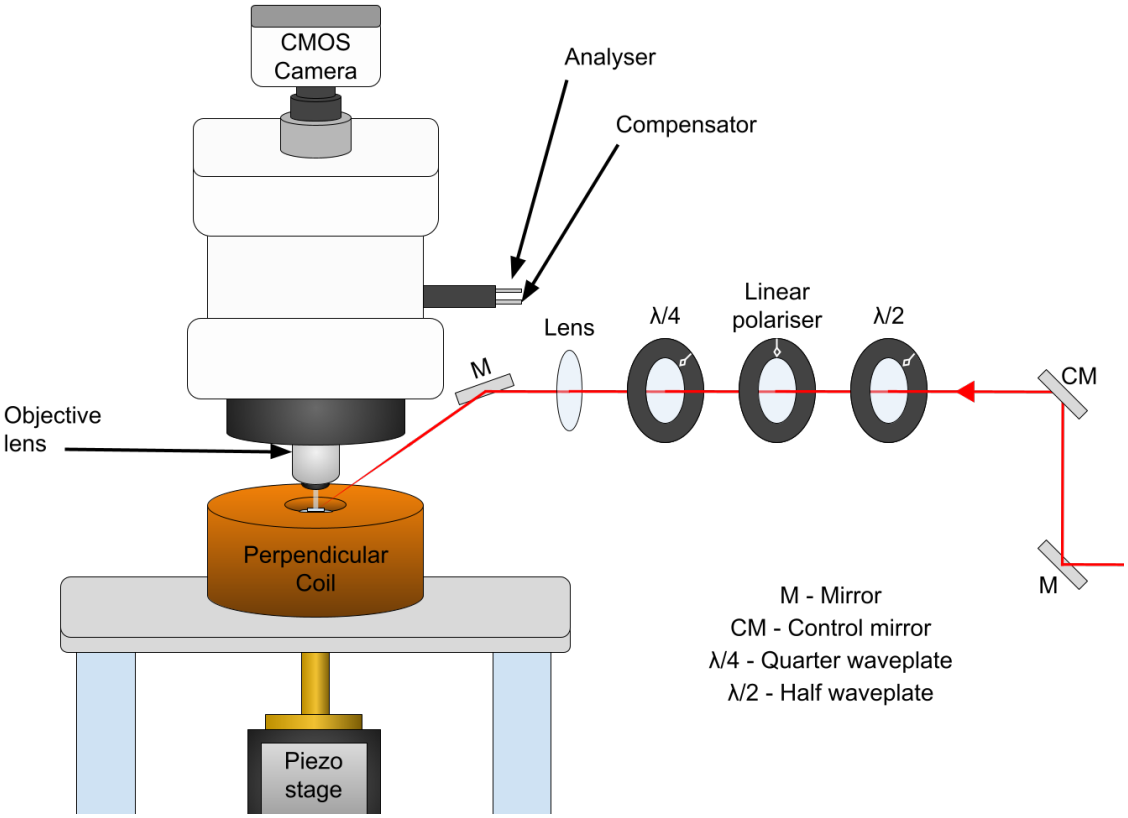

Figure 3.2: A schematic to show the experimental setup of the wide field Kerr microscope (WFKM). The sample is placed beneath the objective lens of the WFKM microscope, on top of a piezo-electric stage and positioned within the perpendicular coil. A laser beam is brought to the sample to study the effect of optical exposure upon the magnetisation. The beam enters at the bottom right, and is brought to the height of the optics using a periscope. The top mirror of the periscope is also used to control the beam position in the camera's field of view. After the periscope, the beam is passed through a half waveplate, linear polariser and quarter waveplate to set the fluence and polarity of the incident beam. A lens after these optics is used to focus the beam onto the sample.

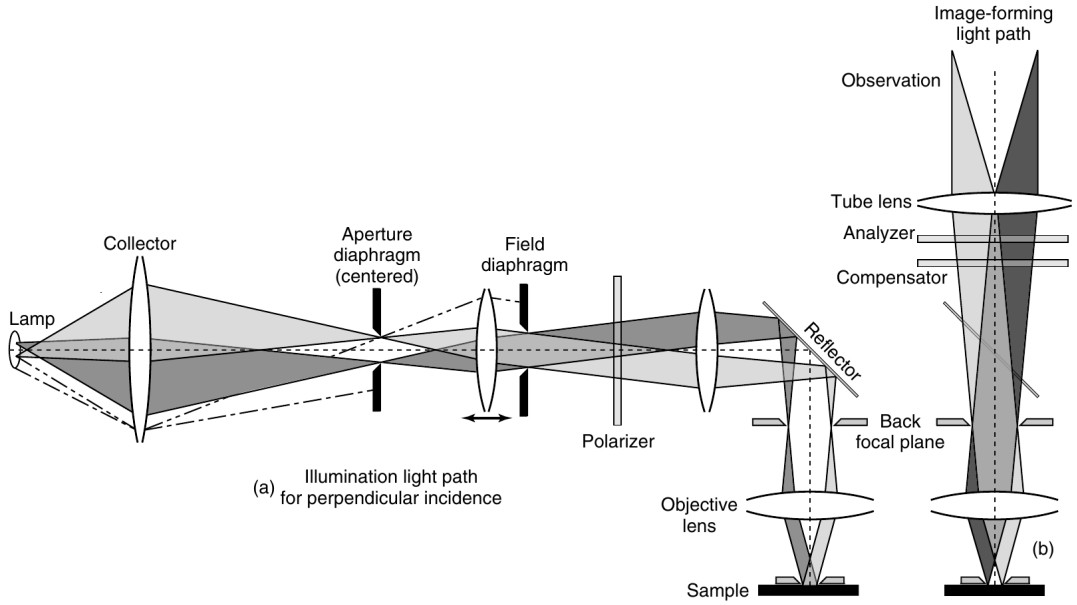

Figure 3.3: This diagram shows the optics of the WFKM. Part (a) shows the path of light from the light source, onto the sample. The light source (i.e. lamp) in the Evico WFKM setup consists of a crossed array of white LED's. The light is polarised and then reflected onto the sample. Part (b) shows the path of the light reflected from the sample before it is captured by the microscope for measurement. The compensator and analyser convert the Kerr rotation into an intensity contrast in the image formed at the output. Figure reproduced from [2].

Polariser

The LED light is linearly polarised within the WFKM before it illuminates the sample. This allows the use of polarising filters to later produce contrast in the image reflected from the sample surface, which varies across the image depending on the polarisation (Kerr) rotation.

Objective lens

An objective lens is then required both to focus the LED light onto the sample, and to gather the light required to produce the microscope image after reflection from the sample. A number of objective lenses can be chosen to mount into the microscope based on the geometrical and magnification requirements of a given experiment. When using the heater or cryogenic stages (section 3.2.2) usage is limited to a long working distance lens, as the space requirements of the vacuum system, in particular the cap above the sample, limits how close the lens can be brought to the sample. Furthermore in the experiments shown, a long working distance lens must be used to allow space for the path of the pump beam. In the majority of WFKM images shown in chapter 5, a 20x magnification long working distance objective lens was used, with the remainder using a 50x magnification long working distance lens.

Compensator

The light collected by the microscope then passes through a compensator and analyser. The action of a compensator is to modify the phase difference between the orthogonal components of light in a variable fashion. In the WFKM setup, the light collected by the objective lens is passed through a compensator which is used to optimise the magnetic contrast by balancing rotation and ellipticity contributions to total intensity.

Analyser

The analyser is the component that converts the Kerr rotation of light reflecting from the sample into an intensity contrast. The compensator is introduced prior to the analyser to make it possible to linearise or otherwise change the ellipticity of the reflected light. The analyser will give maximum contrast when the linear polarisation of one of the domains in the sample is orthogonal to the transmission axis of the analyser, so that light from that domain is brought to extinction, and light from domains of other magnetisation (and hence Kerr rotation) pass through increasingly easily with larger rotations. However, setting the analyser close to extinction will strongly reduce the signal and therefore the setting should be chosen to achieve the optimum balance of contrast and signal intensity for each sample.

CMOS Camera

A complimentary metal-oxide-semiconductor (CMOS) camera is then used to digitise the light signal that passes through the analyser. Pixel binning is set to 2x2 resulting in 960 x 600 pixel images with a readout speed of 130 frames per second. The lateral resolution with this camera and settings when using a 20x/0.5 (magnification/NA) is 1.17µm, which is improved to 469nm when using a 50x/0.8 lens [4].

3.2.2 Heating/Cooling Stage and Controller

For measurements at reduced temperatures a cryostat can be used. Liquid nitrogen is used as a coolant for temperatures down to 80K, and the flow rate is controlled using both a needle valve at the transfer line between dewar and cryostat, and a magnetic proportion valve at the nitrogen outflow. Measurements at temperatures up to 875K are possible when using the heating stage. Both heating and cooling stages operate under a $< 10^{-5}$ mbar vacuum using a Pfeiffer HiCube 30 Eco pump and are temperature stabilised using a CryoVac TIC 500 PID controller. The sample is mounted onto a copper plate using silver paste which is placed onto the sample holder of the stage and fixed in place with a threaded ring to ensure good thermal conductivity. A tube with glass window is screwed in over the sample and used

to close the space required to hold a vacuum at the sample position. The vacuum and cooling systems introduce large vibrational modes to the setup owing to their pivoted nature and vacuum tube connections. These vibrations are limited as far as possible by the use of cable ties to fix the position of electrical wires, and a spring support for the stage in order to couple the motion of the stage to the mechanically damped table.

3.2.3 Piezo Stage

Mechanical stabilisation is critical for the use of the difference-imaging procedure. A piezo-electric stage is used to further limit both vibrations and larger scale drift of the sample (due to thermal instability) during measurement. A reference image is provided to the piezo controller, and a sample defect or some other feature in the image is identified and chosen as a reference area. When stabilisation is activated, the piezo stage will move the sample to align the feature with its position in the reference image, and can travel up to 40µm from the central position horizontally or vertically (or some combination of the two). The piezo stage can also be controlled through the Evico software to change the position of the sample. This can be used to repeatably prepare the position at which the sample is exposed to the beam, with higher accuracy of both position and rate than when controlling the position of the beam using the mirrors shown in figure 3.3.

3.2.4 Perpendicular Coil

A magnetic field is used to prepare magnetisation states for optical exposure, to form domains for imaging, and for hysteresis measurements (section 3.2.8). A perpendicular coil with 104mT maximum field was used despite its low maximum field because of the lack of remanent field. Observations of AOS require no applied field during optical exposure, and to remove the potential for small biasing fields it becomes critical that the field from the coil vanishes when the power to the coil is removed. An input voltage to field calibration for the perpendicular coil was performed by another group member using a Lakeshore 421 gaussmeter when it was first used in the setup.

3.2.5 Pump Beam Optics

An ultrafast laser is used to pump the magnetisation dynamics in experiments searching for AOS. A brief overview of the experimental optics between the laser source and dectector will be given.

Laser system

An ultrafast Monaco laser with 1035nm wavelength and output power set to 1.1W fluence was used. This system has variable pulse width, with a 280fs lower bound, and repetition rate between 10kHz and 1MHz. An optical parametric amplifier can be used to vary the wavelength, however only the unmodified 1035nm output was used here.

Sweeping mirror

A mirror prior to the half waveplate is used to direct the beam through the set of four optical components before the final mirror directing the beam to the sample. This mirror was used to sweep the beam owing to its convenient location next to the computer workstation used to control the WFKM software. A basic check was performed to confirm that the travel range is sufficient to avoid clipping of the beam. A power meter located in the beam path after the quarter waveplate ($\lambda/4$ in figure 3.2) reported no drop in power for changes in the direction of the beam corresponding to movements of the focused beam position across the full field of view of a $20\times$ magnification long working distance lens.

Half waveplate and linear polariser

A linear polariser is used to prepare the beam with p-polarisation. A half waveplate immediately prior is used in combination with the polariser to attenuate the beam to a desired power value with 5mW uncertainty, measured using a power meter placed between the quarter waveplate and focussing lens. The power values corresponding to different half waveplate settings were checked daily and required minimal updating indicating a high stability of the Monaco laser output power, although it is important to note that daily beam drift was common and required daily mirror re-alignment into the setup.

Quarter waveplate

A quarter waveplate preceding the focusing lens is used to set the circular polarisation. It should be noted that due to the grazing incidence of light onto the sample the polarisation of light reflected from the sample is elliptical, not completely circular [5].

Focusing lens

Once set with the correct polarisation the beam is focused on to the sample with a spot size that is small when compared to the field of view of the microscope. A lens with variable position along the beam path is used to focus the beam onto the

sample. The spot size can be modified (i.e. focused and defocused) by changing the position of the lens along the beam path.

Beam profiling

A beam profiler was set up at the position of the sample in order to determine the spatial profile of the focused beam. The beam spot size was found to have 116.4µm $1/e^2$ width (average diameter of the elliptical shape).

3.2.6 Signal Generator

A signal generator can be used to control the number of beam pulses applied to the sample. It is used in all static beam measurements, and in measurements where the repetition rate is set to 1MHz. Since one ultrafast pulse occurs every 1µs, setting a square trigger signal for Nµs, results in N pulses applied to the sample.

3.2.7 Image Processing

The raw contrast of the WFKM signal is often found to be weak. In order to improve the contrast, background removal is commonly used. To do this, a background (reference) image is taken of the sample in a monodomain state. That image is then subtracted from later images as the magnetisation changes. This results in an image free from sample defects, in the best case showing purely magnetic contrast. In practice, resulting images in the polar MOKE setup can have additional contrast due to MOFE in the objective lens (often appearing as a field dependent signal offset), and any displacement of the sample will result in clear contrast due to defects in the sample. Despite best efforts to reduce sample displacement using a piezoelectric stage mentioned in section 3.2.3, displacements can still occur. In such instances, the displacement between images can be removed in postprocessing through the use of scale-invariant feature transform (SIFT) alignment [6, 7]. This technique is available as a preinstalled plugin for the Fiji image analysis software [8, 9]. It works by overlappping images with the background image through feature matching. This can be done before performing the background subtraction manually, as opposed to using the automated process offered by the Evico WFKM software. Averaging over a number of images can further improve image contrast and the background subtraction procedure can be applied to averaged background and measurement images for best results. The number of images averaged in measurement images varies throughout the figures shown in chapter 5, but is usually 16 for domain and optical exposure measurements, and 2 for images used to form hysteresis loops. In order to understand the results of optical exposure measurements, the magnetisation states corresponding to certain contrasts should be well understood. To do this two main procedures to quantify the contrast between states have been used. The first

is to use the WFKM setup to perform hysteresis measurements with the background removal procedure applied, and to take the difference in contrast before and after switching events in order to quantify the contrast change required to confirm a given event. The second procedure is to use a bias field combined with optical exposure to write to a (background removed) monodomain state, and use the line profiling procedure in ImageJ [9] to determine the contrast change at the domain wall. Once quantified, changes to contrast due to beam exposure can be compared in order to determine whether switching or demagnetisation occurs. Once the difference between states is known and the states within images have been identified, images can be prepared for presentation by applying post process contrasting to the images. In ideal cases, the contrast between domains is large enough that two Gaussian peaks can be resolved in the image histograms. It is then trivial to determine the contrast procedure, as a good contrast can be achieved by limiting the colour range between the average values of the two peaks. When the peaks cannot be resolved, best judgement of the level of contrasting is used.

3.2.8 Hysteresis Measurement

Hysteresis loops can be obtained by taking images as the magnetic field is swept. The images used are raw measurement images without background removal. The average contrast of the entire 960x600 pixel images is determined using ImageJ [9]. First the loop is closed by determining the difference between the start and end of the loop and subtracting a line from the data with gradient calculated from the range of average contrast and number of field values. Next a quadratic function is fit to the entire data set using gnuplot [10]. The quadratic is removed from the contrast measurements and a state which should take constant value is identified from the resulting loop. A line is fit to that section of the loop and the line fit is removed from the entire data set resulting in the kind of loop seen in this work. The background removal steps along with an example hysteresis loop are shown in figure 3.4.

3.2.9 State Preparation

For certain experiments the specifics of the magnetic field history can have a large influence on the resulting measurments. In order to repeatably prepare a state under repeatable conditions a Python 3 script was produced to automate the process of changing the magnetic field. The script makes use of the 'pyautogui' library to set an applied field and wait for a specified amount of time before advancing. This script was later extended to make use of the piezo stage, so that domain walls could be repeatedly prepared before exposure, and to position the (beam on the) sample at repeatable locations for static beam measurements. Scripts (shown in appendix

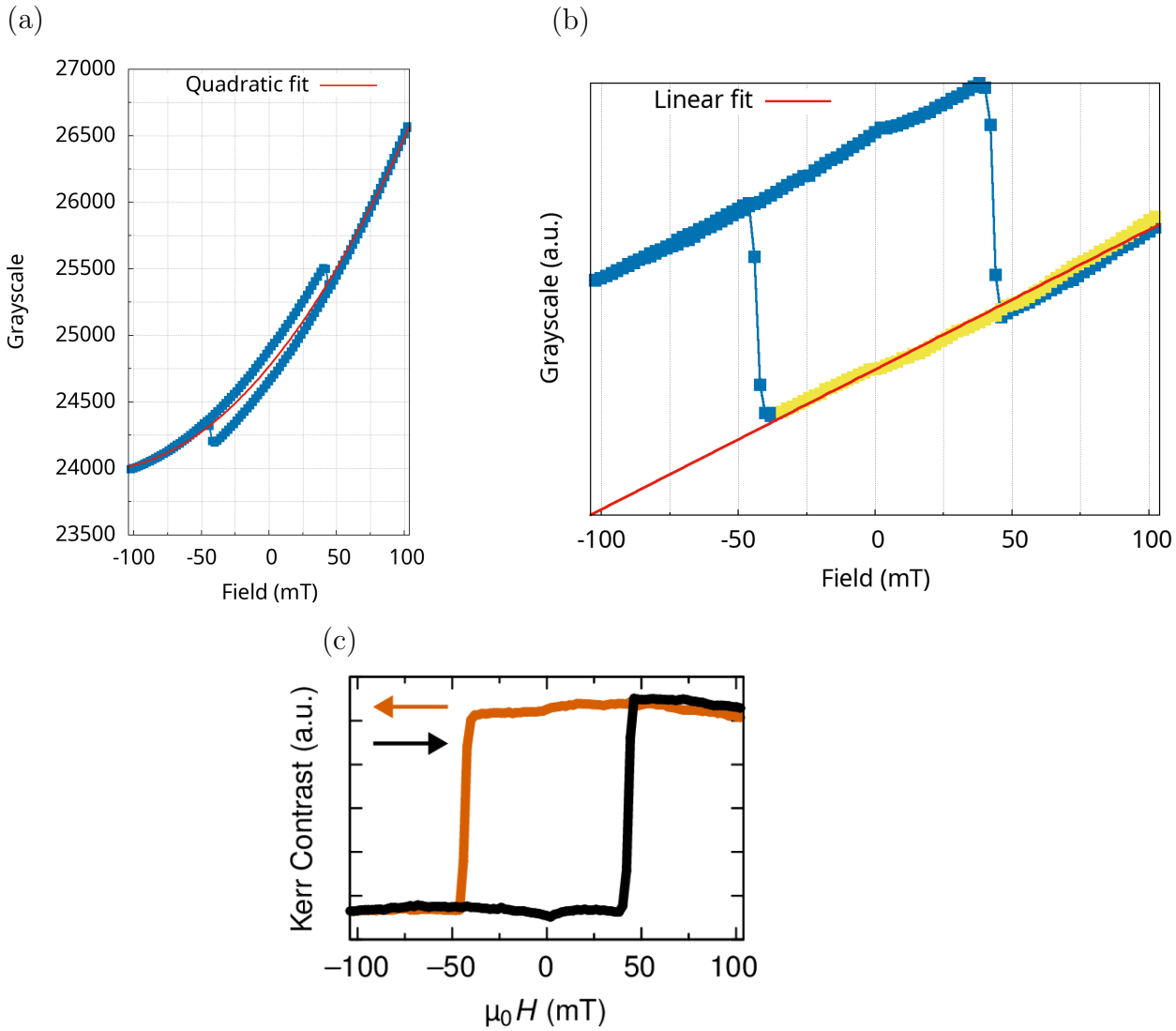

Figure 3.4: A visual outline of the background removal used to produce hysteresis loops from WFKM data. The blue squares in panel (a) show the average (16 bit integer) grayscale value determined from each WFKM image taken as the magnetic field is swept from +104mT to -104mT and then back to +104mT. The red line in (a) shows a quadratic fit to the entire set of grayscale values, which is then removed from the data shown in panel (b). In that panel a set of data shown as yellow squares are chosen to take a linear fit (red line) which in turn is removed from the grayscale values resulting in the loop shown in panel (c), in which the y-axis has also been inverted to match with conventional hysteresis loop plots in which maximum magnetic signal correspond to maximum applied field and vice versa.

C.1) were based on the use of pyautogui presented in [11].

3.3 Time-Resolved Magneto Optical Kerr Effect

The time resolved dynamics shown in this work were measured with the following setup, shown in figures 3.5 and 3.6.

3.3.1 Laser System

The ability to observe ultrafast phenomena depends critically on the choice of laser system, as the temporal resolution is limited by the pulse duration of pump and probe pulses. In order to generate ultrashort pulses a Coherent Reg-A 9040 Ti:Sapphire amplifier is used to optically amplify seed pulses from a Coherent Vitara-T ultrashort pulse Ti:Sapphire Oscillator. Both oscillator and amplifier are pumped by a Coherent Verdi V18 diode-pumped solid-state (continuous wave) laser [12], which outputs a 532nm wavelength beam of up to 18W output power. The output of the Verdi is set to 16W and is split into separate 5.3W and 10.7W beams using a beamsplitter. These two beams are routed to pump the oscillator and amplifier respectively. The nominally 800nm wavelength and $<$ 20fs width pulses from the Vitara are streched in a separate unit before being routed to the Reg-A amplifier, where a chirped-pulse amplification technique is used to generate amplified pulses with 100kHz repetition rate. These pulses are then passed back into the pulse compressor unit to once again obtain ultrafast pulses with 50fs width and average power of approximately 600mW. The laser setup is shown in figure 3.5.

After recompression, the beam is passed through a beamsplitter where the beam is split into pump and probe paths. In the following sections, the different components that interact with the pump and probe beams as they take a path through the setup will be discussed.

3.3.2 Pump Path

Delay stage

For time-resolved pump-probe measurements, a tunable delay is introduced between the pump and probe beams so that the effects induced by the pump can be measured at different times before, during and after a pump pulse interacts with the probed region of the sample. To introduce this tunable delay, a Newport IMS600CCHA motorised linear stage is placed within the pump beam path. A retroreflector mounted on the stage can be positioned with a travel range of 600mm to increase or decrease the path length of the pump beam by a total of 1200mm, while the path length of the probe remains constant. This corresponds to delay times of up to 4ns. The minimum incremental motion of the stage is 0.2µm, corresponding to 7fs resolution. The stage is used in the pump path rather than the probe path to avoid fluctuations in signal at the detector which would be strongly affected by flutuations in the probe

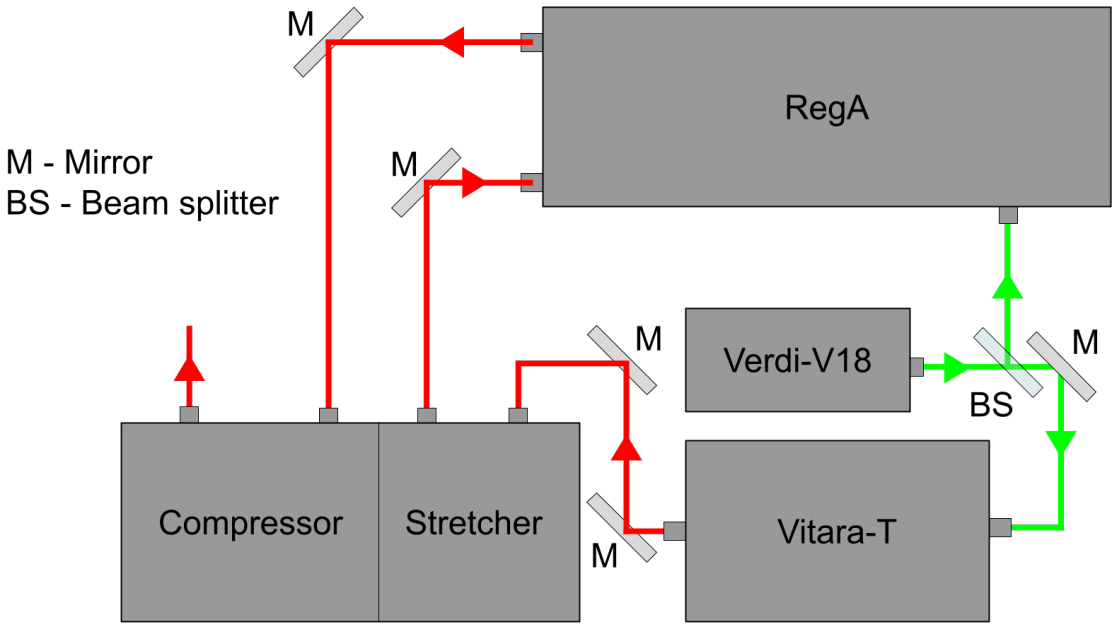

Figure 3.5: This schematic shows the laser system setup used for TR-MOKE. The Verdi-V18 acts as a pump for both the Vitata-T oscillator and RegA amplifier, and its 512nm output is split between the two. The 800nm Vitara-T ultrashort pulse output is temporally streched before being used to seed the RegA. The RegA amplifies the power of the beam, and its output is sent to the compressor to reduce the pulse width back to an ultrashort value. The output from the compressor is used in the TR-MOKE experiment as shown in figure 3.6

path due to vibrations in the mechanical stage. Once the pump and probe beams are overlapped, the full range of the delay stage must be tested to ensure that beam overlap remains constant.

Chopper

An optical modulator is required to improve the signal to noise ratio. When used with the LIAs, this repetitive signal can be extracted (see section 3.3.4), with a strong improvement to the signal to noise ratio. Here a Thorlabs MC1000 Optical Chopper is used with a 10 slot blade. A frequency of 520Hz was found to be suitable for measurement.

3.3.3 Probe Path

Optical Parameteric Amplifier

After the beam is split, the part of the beam used for magnetisation probing is first passed through an optical parametric amplifier (OPA), which contains a second harmonic generation unit used to halve the wavelength from 800nm to 400nm. In this way the measurements constitute a two-colour pump-probe experiment.

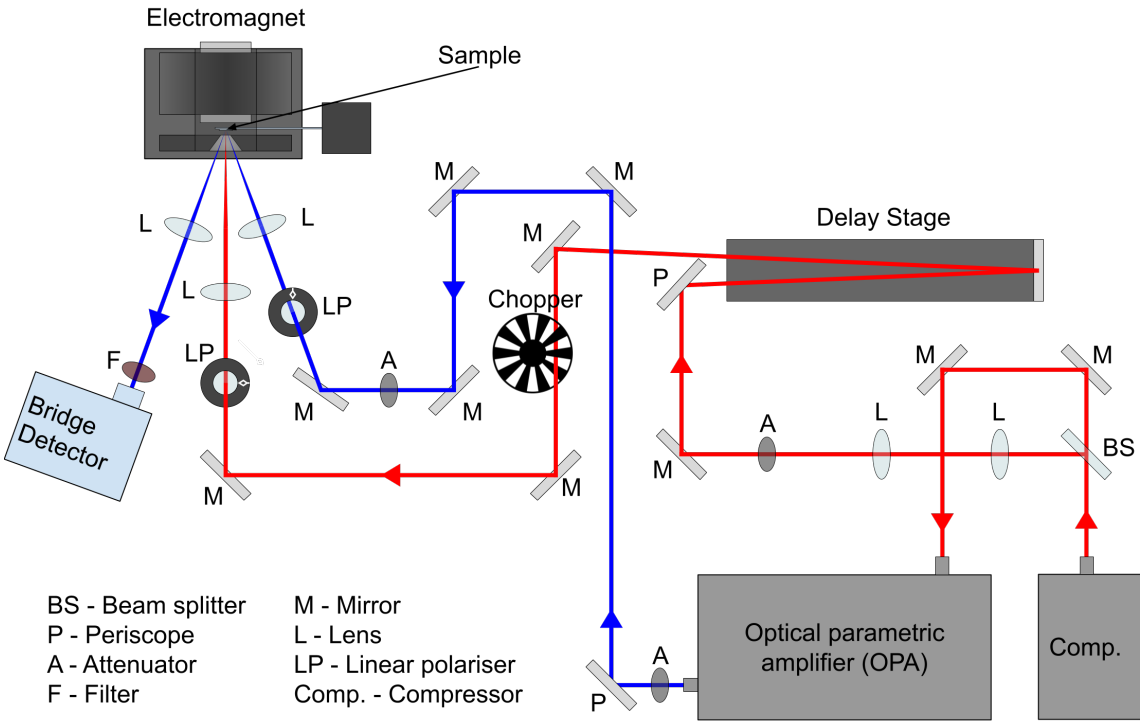

Figure 3.6: Schematic of the optical setup of the TR-MOKE experiment. The output from the compressor (see figure 3.5) is split between a pump (red line) and probe (blue line) beam. The pump beam is passed through a delay stage to allow for control of temporal overlap and delay between the two beam paths. It is then modulated at 520Hz frequency by an optical chopper, set at a horizontal linear polarisation and focused onto the sample by a lens. The probe is transformed into a 400nm beam using the second harmonic generation unit within an OPA, set to vertical polarisation and reflected from the sample. The reflection from the sample is then directed into the bridge detector. The sample is positioned in between the poles of an electromagnet, so a field can be applied during measurments. The geometry of the polar electromagnet can be seen in this figure.

Polariser

The probe beam is s-polarised using a linear polariser before illuminating the sample at a 15° angle of incidence, which allows for both polar and longitudinal MOKE components in the signal which have greater relevance for ultrafast demagnetisation (with a polar electromagnet) and precession measurements (with a longitudinal electromagnet) respectively.

Filter

Immediately prior to the detector is a filter used to attenuate light at 800nm which may scatter from the sample towards the detector. This can greatly improve the signal to noise ratio under certain reflection conditions.

Detector

The reflection of the probe from the sample is passed into a bridge detector which uses a Glan-Thompson polarising beamsplitter to separate the beam into orthogonally polarised components. Those components are directed into separate photodiode detectors resulting in voltage signals A and B. The electric circuit of the detector transforms these signals into two more signals, $A - B$ and $A + B$ which are sensitive to rotations of linear polarisation, and intensity changes of the beam respectively. Owing to the magneto optical Kerr effect, changes in $A - B$ are proportional to changes in the magnetisation of the sample in the probed region, while the $A + B$ reading is proprtional to the laser source power and changes to the sample reflectivity. Before measurements begin, it is important to null the detector by rotating it until the A-B signal is zeroed.

3.3.4 Lock-in Amplifier

The signal in TR-MOKE measurements is very small compared to background noise, therefore AMETEK lock in amplifiers (LIA) are used to determine the signal occuring at the 520Hz reference frequency set by the pump modulator. The sensistivity of the LIA is set manually, and the output reading is a percentage of this value. Furthermore, the LIA reports the root mean square value of the sinusoidal signal rather than a peak to peak value. For those reasons the voltage (V) in volts corresponding to static beam measurements is recovered by

$$V_{A-B} = \text{LIA signal} \times \frac{\text{LIA sensitivity}}{100} \times \frac{\pi}{\sqrt{2}}. \tag{3.3.1}$$

3.3.5 Demagnetisation Signal

This signal can be converted into a demagnetisation signal if a static (non-pumped) MOKE loop is taken with the same average A+B level. In the example of a square loop, the difference in A-B readings between the two saturated states is twice the expected change in signal for the sample to be fully demagnetised from its saturated state. In TR-MOKE measurements where the sample is saturated between applications of the pump beam owing to a continuously applied saturation field, the percentage demagnetisation (D) can be determined by

$$D = 100 \times \frac{V_{A-B}}{\text{half loop height}}. \tag{3.3.2}$$

3.3.6 Kerr Rotation Signal

Kerr rotation signal can be determined for a given A+B by the calibration of changes in A-B for a known amount of rotation. Such a rotation can be performed by mechanical rotation of the detector, as this is geometrically equivalent to a rotation of the linearly polarised signal entering the detector.

3.3.7 Setting the Beam Fluence

A beam profiler was used at the sample position to determine the $1/e^2$ width of the pump and probe beams (shown in figure 3.7). The ratio of pump to probe sizes ranged between 2:1 and 3:1, as is best practice to ensure continued overlap over the course of an experiment (overlap might otherwise be lost due to beam drift). The following formula can be used to convert between power (P) and peak fluence (F)

$$F[\text{mJ/cm}^2] = 100 \times \frac{2 \times P[\text{mW}]}{R[\text{MHz}] \times A[\mu\text{m}^2]}, \tag{3.3.3}$$

where R is the pulse repetition rate, and $A = \pi\left(\frac{D}{2}\right)$ is the area of the beam where D is the $1/e^2$ width (diameter) of the beam in µm. The factor of 100 in equation 3.3.3 is for conversion of units, while the factor of 2 is to convert from average fluence of a Gaussian beam to the peak value at the beam centre.

The fluence of the pump beam is critical to the dynamics it will induce. In order to control the beam fluence, a neutral density wheel (variable) attenuator prior to the delay stage was used in combination with a power meter, to set the average power as desired. From the average power, the beam fluence can be determined by equation 3.3.3. The selection of probe power must be sufficient to avoid large fluctuations in signal due to noise received by the detector, but small enough that it does not give rise to any dynamics that would be picked up during the measurement. Two neutral density wheel attenuators located after the OPA were used to achieve

(a) (b)

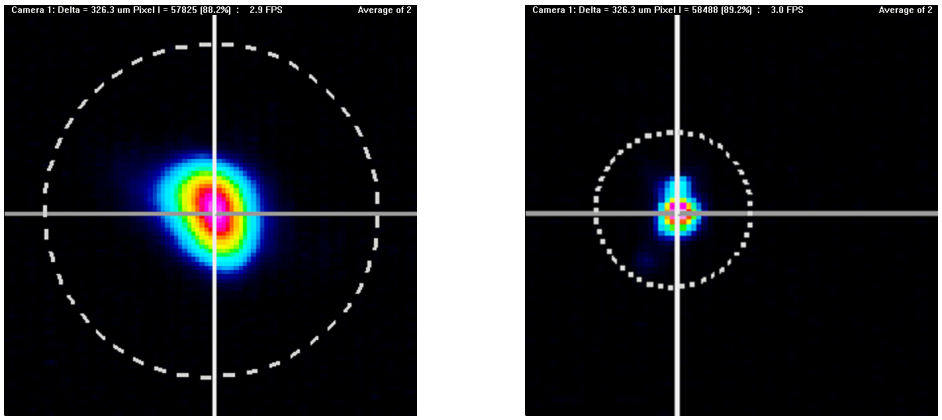

Figure 3.7: Beam profiles in the TR-MOKE setup taken at the position of the sample using a beam profiler camera. Panel (a) shows the pump beam with 102.5µm $1/e^2$ width. Panel (b) shows the probe beam with 39µm $1/e^2$ width.

this, and care was taken to limit the DC A+B reading across all measurements to approximately 500mV.

3.3.8 Electromagnet

Depending on the behaviour under examination, a different electromagnet was used in order to apply the field to the sample in a particular direction. In demagnetisation measurements, a polar electromagnet is used to apply a field out-of-plane with respect to the sample. At the time that most demagnetisation measurements were made, no Hall probes were available to measure the applied field during experiments. Instead a Lakeshore 421 gaussmeter was used to calibrate the magnetic field relative to the applied input voltage to the electromagnet, as shown in figure 3.8. Owing to remanent magnetisation in the electromagnet, along with reduction in applied field due to electromagnet heating, there is some level of uncertainty in this calibration. However, this is not of critical importance for demagnetisation measurements, as the purpose of the field in these measurements is to remagnetise the sample between measurements.

For precession measurements a longitudinal electromagnet was used to apply a field in the plane of the sample. In anticipation of these measurements, F.W. Bell GH-604 Hall probes were purchased. By the time that these measurements were performed, the Hall probes had arrived and could be implemented into the setup to measure the field during time resolved measurements, therefore the field settings shown for precession measurements have superior certainty. This is critical for precession measurements as through the Larmor precession formula, the magnitude of applied field is proportional to the precession frequency. Calibrations for these probes are shown in figure 3.9.

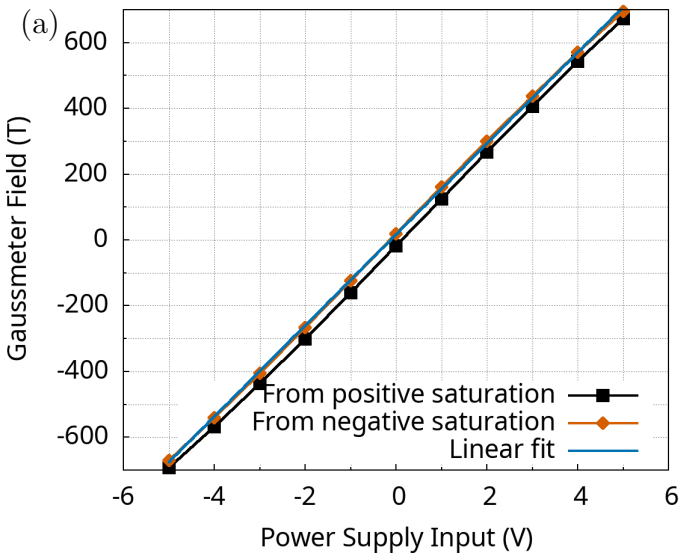

Figure 3.8: A calibration for the polar electromagnet used in the TR-MOKE setup. The fitting parameters for the line fit (blue line) to the data collected from positive saturation (orange diamonds) are used to interpolate the field applied in measurements shown in section 5.4.1.

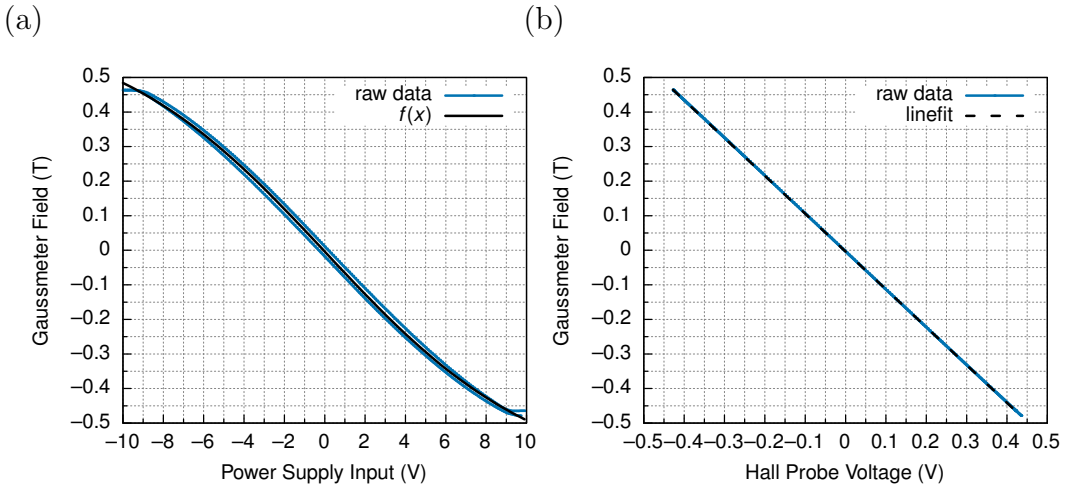

Figure 3.9: Calibrations for the longitudinal electromagnet used in the TR-MOKE setup. Panel (a) shows the calibration between input voltage and resulting field measured using a gaussmeter. A sigmoid function is fit to the data (black line). Panel (b) shows the gaussmeter field as the voltage in the reference Hall probe varies. The black dashed line is a line fit to the calibration, and is used to determine the fields produced by the longitudinal electromagnet in section 5.4.2

.

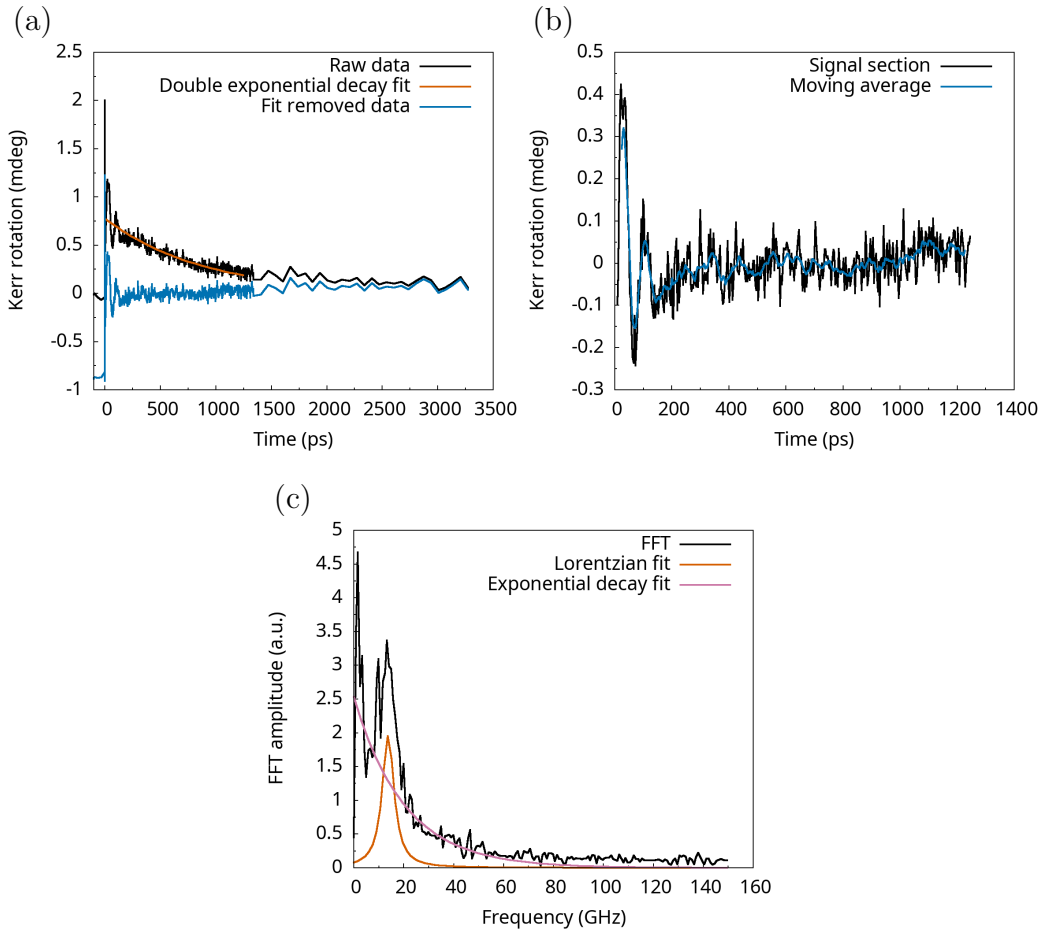

Figure 3.10: Panel (a) shows an example of time-resolved data containing a precession signal (black), a fit of equation 3.3.4 to the signal (orange), and the full signal with the fit removed. Panel (b) shows the section from which the double exponenetial fit was removed (black), and a ten-point moving average (blue). Panel (c) shows the FFT of the ten-point moving average (black) and the two terms on the right hand side of equation 3.3.5 fit to that FFT (orange and pink).

3.3.9 Precession Parameter Extraction

A Python script was written to extract the precession frequency from TR-MOKE measurements. First a double exponential background is removed from the data as shown in 3.10(a). That is the function

$$f(t) = A_1 e^{-t/\tau_1} + A_2 e^{-t/\tau_2} \tag{3.3.4}$$

was fit to the signal after 6ps (and up to a variable point where the time delay between measurements points is constant) to obtain the fitting parameters A_1, A_2, τ_1 and τ_2. The resulting best fit is taken from the raw signal. As shown in 3.10(b), the 10 point moving average is determined for the same time range of the background removed signal in order to smoothen the curve. The fftpack fast Fourier transform (FFT) from the scipy (scientific python) library is then applied to the smoothed and background removed data to convert the signal to the frequency domain. Assuming

the precession signal is strong, the frequency domain signal is expected to show a Lorentzian peak at the precession frequency, shown in 3.10(c). Any offset (non zero average) in the signal to which the FFT was applied will cause a 0Hz, quickly decaying peak in the frequency domain data. To capture the properties of the Lorentzian peak associated with the precession, it must be separated from this decaying signal. To do so, the function

$$f(\omega) = A_3 e^{-\omega/\omega_3} + \frac{A_4}{(\omega - \omega_0)^2 + \omega^2 \lambda^2} \tag{3.3.5}$$

is fit to the data, (with the term on the left fitting an exponential decay, and the term on the right fitting a Lorentzian peak). For a successful fit to the FFT, the extracted parameters A_4, ω_0 and λ, correspond to the strength, frequency and damping strength of the precession behaviour respectively.

3.4 X-ray Magnetic Circular Dichroism

X-ray magnetic circular dichroism is a useful technique for element resolved measurements of magnetisation. This makes it a useful technique for understanding the behaviour of synthetic ferrimagnet samples studied in chapter 5, where the two ferromagnetic layers are composed of elemental cobalt and nickel-platinum multilayers respectively, allowing the magnetisation of the two layers to be probed independently. This elemental resolution results from the tuning of X-ray energy to the energy required to excite core electrons to the valence band, and the use of circularly polarised X-rays to allow for magnetic sensitivity. The technique is described in detail in [13] and [14]. Measurements were performed at the ALS facility which uses a third-generation synchotron light source, and can be configured for fluorescence yield detection or total electron yield detection.

3.5 Microcoil Magneto Optical Setup

To test the capability of microcoil devices to switch magnetic samples, a setup was designed to allow for both transmission and reflection geometry measurements of magneto-optical signal. A schematic of this setup is shown in figure 3.11. Like in the setups shown in sections 3.2 and 3.3, the reflection geometry measurements make use of the magneto optical Kerr effect. For samples that allow the transmission of a large proportion of light, the detector can be repositioned to collect the transmitted light, making use of the magneto optical Faraday effect to determine the magnetic behaviour of the sample.

In this setup both the polar electromagnet and microcoil provide a field perpendicular to the plane of the sample. The sample itself is attached to the microcoil. For reflective geometry measurements, the beam passes twice through the microcoil hole, and the sample is necessarily facing towards the device.

Similar to the detector describe in section 3.3, the incoming beam is first separated into orthogonal polarisation componenents. Optical fibers then couple these components to the A and B inputs of an external Thorlabs 'PDB150A' balanced amplified photodetector. This device is capable of high speed measurements of polarisation rotations (i.e. $A-B$) with switchable transimpedance gain settings. Increasing the gain of the detector results in a corresponding reduction in the bandwidth, i.e. the signal magnitude can be increased at the expense of the ability to observe phenomena that occur at faster speed. The possible settings (of transimpedance gain[Ω]/bandwidth[MHz]) are $10^3/150$, $10^4/50$, $10^5/5$, $10^6/0.3$ and $10^7/0.1$. Ideally the detector should be set to have the maximum gain that is able to accurately resolve the time required to switch the sample by passing current pulses through the microcoil. It is important to note that the gain is reduced by a factor of two into a 50Ω load [15]. This is important with regards to the RIGOL 'DS1302CA' oscilloscope used to observe the voltage waveform resulting from the magneto optical response, for which the input resistance can be set as either 50Ω or $1M\Omega$. When set to 50Ω, the signal output by the PDB150A detector must be multiplied by a factor of two to allow proper comparison to the height of MOKE (or MOFE) loops and thereby determine the switching percentage due to a microcoil pulse.

Measurements made using the RIGOL oscilloscope can be set to take the average of 256 traces. The measurements shown in chapter 6 were taken in this average aquisition mode to reduce the effect of random noise.

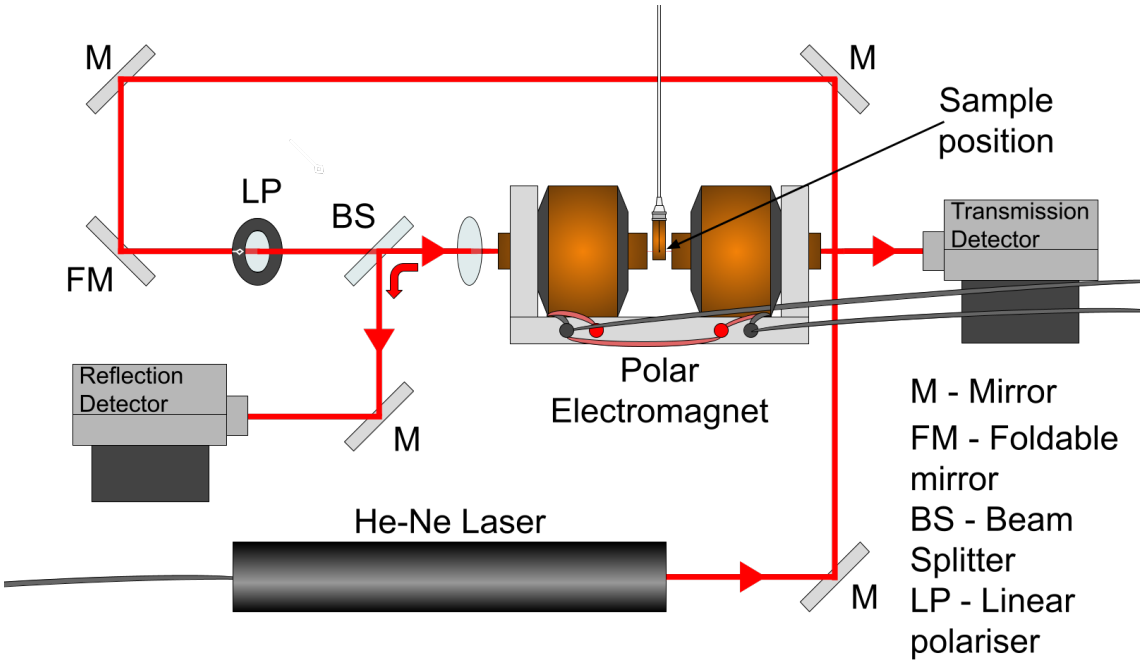

Figure 3.11: This schematic shows the setup used to perform magneto-optical testing of microcoil devices. The linear polariser, polar electromagnet and beam splitter were previously set up for use in spectroscopic MOKE experiments with a monochromated white light source. To avoid disruption of that setup, a foldable mirror has been used to allow for the introduction of the 633nm continuous wave output of a He-Ne laser into the setup. The linear polariser is used to set the beam to a horizontal polarisation before passing through a beam splitter. Upon first entry to the beamsplitter, the beam is split into two components. Only the non reflected component has been shown in this schematic. This beam is then passed into a lens which focuses the beam onto the sample. The sample is attached to the microcoil, which is fixed in position between the poles of a polar electromagnet. The position of the bridge detector is modified depending on whether the magneto optical Faraday effect (MOFE) or magneto optical Kerr effect (MOKE) is being measured. When using MOFE, the detector is placed behind the electromagnet so that the component of the beam transmitted through the sample is measured. For MOKE measurements the component of the beam reflected from the sample is passed back through the beam splitter. The detector is positioned so that the part of the beam reflected upon second entry to the beamsplitter is measured.

References

[1] Wolfgang Kuch, Rudolf Schäfer, Peter Fischer, and Franz Ulrich Hillebrecht. *Magnetic Microscopy of Layered Structures*, volume 57 of *Springer Series in Surface Sciences*. Springer, Berlin, Heidelberg, 2015.

[2] Rudolf Schäfer. Investigation of Domains and Dynamics of Domain Walls by the Magneto-optical Kerr-effect. In *Handbook of Magnetism and Advanced Magnetic Materials*. John Wiley & Sons, Ltd, 2007.

[3] I. V. Soldatov and R. Schäfer. Selective sensitivity in Kerr microscopy. *Review of Scientific Instruments*, 88(7):073701, July 2017.

[4] Evico Magnetics. *User Instruction for Evico Magnetics Combined Overview / High-Resolution Kerr Microscope & Magnetometer*.

[5] Grant R. Fowles. *Introduction to Modern Optics*. Dover Publications, New York, 2nd edition edition, June 1989.

[6] D.G. Lowe. Object recognition from local scale-invariant features. In *Proceedings of the Seventh IEEE International Conference on Computer Vision*, volume 2, pages 1150–1157 vol.2, September 1999.

[7] David G. Lowe. Distinctive Image Features from Scale-Invariant Keypoints. *International Journal of Computer Vision*, 60(2):91–110, November 2004.

[8] Johannes Schindelin, Ignacio Arganda-Carreras, Erwin Frise, Verena Kaynig, Mark Longair, Tobias Pietzsch, Stephan Preibisch, Curtis Rueden, Stephan Saalfeld, Benjamin Schmid, Jean-Yves Tinevez, Daniel James White, Volker Hartenstein, Kevin Eliceiri, Pavel Tomancak, and Albert Cardona. Fiji: An open-source platform for biological-image analysis. *Nature Methods*, 9(7):676–682, July 2012.

[9] Curtis T. Rueden, Johannes Schindelin, Mark C. Hiner, Barry E. DeZonia, Alison E. Walter, Ellen T. Arena, and Kevin W. Eliceiri. ImageJ2: ImageJ for the next generation of scientific image data. *BMC Bioinformatics*, 18(1):1–26, December 2017.

[10] Thomas Williams and Colin Kelley. *Gnuplot 5.4 An Interactive Plotting Program*. http://www.gnuplot.info/docs_5.4/Gnuplot_5_4.pdf, September 2022.

[11] Albert Sweigart. *Automate the Boring Stuff with Python: Practical Programming for Total Beginners*. No Starch Press, San Francisco, Calif, 1st edition edition, May 2015.

[12] Coherent. Verdi V-Series. Datasheet, 2021.

[13] Gerrit van der Laan and Adriana I. Figueroa. X-ray magnetic circular dichroism—A versatile tool to study magnetism. *Coordination Chemistry Reviews*, 277–278:95–129, October 2014.

[14] J. Stöhr. X-ray magnetic circular dichroism spectroscopy of transition metal thin films. *Journal of Electron Spectroscopy and Related Phenomena*, 75:253–272, December 1995.

[15] Thorlabs. Operation Manual Thorlabs Instrumentation PDB100 Series Balanced Amplified Photodetectors PDB110, PDB120, PDB130, PDB140, PDB145, PDB150 Version 1.3, 2007.

Chapter 4

Dissipative Magnetisation Dynamics

4.1 Introduction

In this section, the Heisenberg picture of quantum mechanics will be used to determine the equation of motion for an extended quantum Heisenberg model of a ferromagnet in a manner similar to that shown in section 2.2.1. The extention to the model is an inclusion of a continuum environment of quantum harmonic oscillators, and a generalised coupling between the spins of the ferromagnetic system, and the displacement of the oscillator enviroment, allowing a dissipative pathway through which energy can flow to and from the system of spins. Using this approach, it will be shown that the extended model satisfies the fluctuation dissipation theorem (see section 2.3.2) for any form of coupling, and that the Landau-Lifshitz-Gilbert-Brown equation (see section 2.2.2) is recovered as the equation of motion for a particular 'Ohmic' form of coupling. A 'Lorentzian' form of coupling will then be explored and shown to approximate LLGB dynamics under common experimental conditions, while having more physically realistic properties than the Ohmic type. The consequences of this Lorentzian form of coupling will then be explored in further detail for a semi-classical single spin system using numerical techniques.

Prior work on derivation of the equations of motion for spin dynamics starting from microscopic (i.e. quantum mechanical) descriptions was shown by Antropov et. al. in 1995 [1], and was used to consider finite temperature effects in 1996 [2] through the use of a classical bath. In 2003, Rebei and Parker developed a model of spin dynamics from microscopic principles using a path-integral formalism [3] and couple the spin to a quantum bath in satisfaction of the fluctuation dissipation relation in a manner similar to the approach taken in what follows.

4.2 Derivation

4.2.1 Extended Heisenberg Model

The quantum Heisenberg model (equation 2.2.1) contains Zeeman interactions between spins $\hat{\mathbf{S}}_j$ and an external field $\mathbf{B}_{\text{ext}}$, and exchange interactions between nearest neighbour spins $\hat{\mathbf{S}}_j$ and $\hat{\mathbf{S}}_k$. Through alignment of the spins with one another and the external field, the energy of the system is reduced. In this section the Hamiltonian of the quantum Heisenberg model will be referred to as the system Hamiltonian $\hat{\mathcal{H}}_{\text{S}}$, written explicitly as

$$\hat{\mathcal{H}}_{\text{S}} = -|\gamma_e| \sum_j \hat{\mathbf{S}}_j \cdot \mathbf{B}_{\text{ext}} - \frac{J}{2} \sum_{\langle j,k \rangle} \hat{\mathbf{S}}_j \cdot \hat{\mathbf{S}}_k. \tag{4.2.1}$$

As shown in section 2.2.1 this model does not allow for dissipative effects. In order to rectify this, an open quantum system approach is taken. The Hamiltonian of the open quantum system is given by

$$\hat{\mathcal{H}} = \hat{\mathcal{H}}_{\text{S}} + \hat{\mathcal{H}}_{\text{R}} + \hat{\mathcal{H}}_{\text{Int}}, \tag{4.2.2}$$

where the reservoir is modelled as a continuum of harmonic oscillators following in the approach laid out by Huttner and Barnett [4] discussed in section 2.3.3, leading to

$$\hat{\mathcal{H}}_{\text{R}} = \sum_j \int_0^\infty \mathrm{d}\omega' \left[\frac{\hat{\mathbf{P}}^2_{j,\omega'}}{2} + \frac{\omega'^2 \hat{\mathbf{X}}^2_{j,\omega'}}{2} \right], \tag{4.2.3}$$

which describes a continuous frequency reservoir at each lattice site j, where $\hat{\mathbf{P}}_{j,\omega'}$ and $\hat{\mathbf{X}}_{j,\omega'}$ are three-dimensional momentum and displacement operators of the reservoir oscillator with frequency ω'. The interaction between spin system and the reservoir is given by

$$\hat{\mathcal{H}}_{\text{Int}} = |\gamma_e| \sum_j \int_0^\infty \mathrm{d}\omega' C_{j,\omega'} \hat{\mathbf{S}}_j \cdot \hat{\mathbf{X}}_{j,\omega'}. \tag{4.2.4}$$

That is to say that a bath of harmonic oscillators is coupled through their displacement $\hat{\mathbf{X}}_{j,\omega'}$ (i.e. distance from the position of minimum potential energy that defines the quantum harmonic oscillator, and unlike it's classical counterpart does not collapse to zero at low temperatures - see section 2.3.3) to the spins $\hat{\mathbf{S}}_j$ of the lattice, through their direction by means of a dot product component, with coupling strength C_ω. It is important to note that the coupling is in general a rank two tensor contracted with the spin an reservoir indices, but for simplicity here considered only as an scalar, avoiding the complexity of coupling between perpendicular components

of spin and displacement. A description of this kind is able to allow for the flow of both Zeeman energy and angular momentum of spins to the total energy and angular momentum of the oscillator bath respectively (and vice versa). In addition, this form of Hamiltonian allows for the transfer of angular momentum between spins and environment, which is a requirement for spin damping as alluded to in section 2.3.

To describe the complete motion of the system using the Heisenberg approach, the effects of each of the three Hamiltonian components $\hat{\mathcal{H}}_{\mathrm{S}}$, $\hat{\mathcal{H}}_{\mathrm{R}}$ and $\hat{\mathcal{H}}_{\mathrm{Int}}$, on the generalised coordinates $\hat{\mathbf{S}}_i$, $\hat{\mathbf{X}}_{i,\omega}$ and the generalised momentum $\hat{\mathbf{P}}_{i,\omega}$ must be considered. This done in the Heisenberg picture of quantum mechanics [5], in which the evolution of quantum mechanical operators without any explicit time dependence is given by

$$\frac{\mathrm{d}\hat{A}}{\mathrm{d}t} = \frac{i}{\hbar}\left[\hat{\mathcal{H}}, \hat{\mathbf{A}}\right]. \tag{4.2.5}$$

Considering the dependencies of each component of the total Hamiltonian, and their commutation properties, the calculations of the equations of motion can be reduced to the spin evolution

$$\frac{\mathrm{d}\hat{\mathbf{S}}_i}{\mathrm{d}t} = \frac{i}{\hbar}\left[\hat{\mathcal{H}}_{\mathrm{S}} + \hat{\mathcal{H}}_{\mathrm{Int}}, \hat{\mathbf{S}}_i\right], \tag{4.2.6}$$

the evolution of oscillator displacement

$$\frac{\mathrm{d}\hat{\mathbf{X}}_{i,\omega}}{\mathrm{d}t} = \frac{i}{\hbar}\left[\hat{\mathcal{H}}_{\mathrm{R}}, \hat{\mathbf{X}}_{i,\omega}\right], \tag{4.2.7}$$

and the evolution of oscillator momentum

$$\frac{\mathrm{d}\hat{\mathbf{P}}_{i,\omega}}{\mathrm{d}t} = \frac{i}{\hbar}\left[\hat{\mathcal{H}}_{\mathrm{R}} + \hat{\mathcal{H}}_{\mathrm{Int}}, \hat{\mathbf{P}}_{i,\omega}\right]. \tag{4.2.8}$$

The time evolution of harmonic oscillator positions is found in the Heisenberg picture by the calculation of

$$\left[\hat{\mathcal{H}}_{\mathrm{R}}, \hat{\mathbf{X}}_{i,\omega}\right] = \sum_j \int_0^\infty \mathrm{d}\omega' \frac{1}{2}\left[\hat{\mathbf{P}}^2_{j,\omega'}, \hat{\mathbf{X}}_{i,\omega}\right], \tag{4.2.9}$$

where

$$\left[\hat{\mathbf{P}}^2_{j,\omega'}, \hat{\mathbf{X}}_{i,\omega}\right] = \sum_{\alpha=x,y,z}\left[\hat{P}^2_{j,\omega',\alpha}, \hat{X}_{i,\omega,\alpha}\right]\mathbf{e}_\alpha, \tag{4.2.10}$$

can be reduced using both the commutation identity

$$\left[\hat{\mathbf{A}}\hat{\mathbf{B}}, \hat{\mathbf{C}}\right] = \hat{\mathbf{A}}\left[\hat{\mathbf{B}}, \hat{\mathbf{C}}\right] + \left[\hat{\mathbf{A}}, \hat{\mathbf{C}}\right]\hat{\mathbf{B}}, \tag{4.2.11}$$

and the commutator of position and momentum

$$\left[\hat{\mathbf{X}}_{i,\omega}, \hat{\mathbf{P}}_{j,\omega'}\right] = i\hbar\delta_{ij}\delta(\omega' - \omega), \tag{4.2.12}$$

to

$$\left[\hat{\mathbf{P}}^2_{j,\omega'}, \hat{\mathbf{X}}_{i,\omega}\right] = -2i\hbar\delta_{ij}\delta(\omega' - \omega)\sum_{\alpha=x,y,z}\hat{P}_{j,\omega',\alpha}\mathbf{e}_\alpha = -2i\hbar\delta_{ij}\delta(\omega' - \omega)\hat{\mathbf{P}}_{j,\omega'}, \tag{4.2.13}$$

which gives the displacement evolution of harmonic oscillators as

$$\frac{\mathrm{d}\hat{\mathbf{X}}_{i,\omega}}{\mathrm{d}t} = \hat{\mathbf{P}}_{i,\omega}. \tag{4.2.14}$$

Following a similar calculation the reservoir contribution to momentum evolution is given as,

$$\frac{i}{\hbar}\left[\hat{\mathcal{H}}_{\mathrm{R}}, \hat{\mathbf{P}}_{i,\omega}\right] = -\omega^2\hat{\mathbf{X}}_{i,\omega}. \tag{4.2.15}$$

To complete the momentum evolution, its commutation with the interaction term in the Hamiltonian must be considered

$$\left[\hat{\mathcal{H}}_{\mathrm{Int}}, \hat{\mathbf{P}}_{i,\omega}\right] = -|\gamma_e|\sum_j\int_0^\infty \mathrm{d}\omega' C_{j,\omega'}\sum_{\alpha=x,y,z}\hat{S}_{j,\alpha}\left[\hat{X}_{j,\omega',\alpha}, \hat{P}_{i,\omega,\alpha}\right]\mathbf{e}_\alpha, \tag{4.2.16}$$

so

$$\left[\hat{\mathcal{H}}_{\mathrm{Int}}, \hat{\mathbf{P}}_{i,\omega}\right] = -i\hbar|\gamma_e|C_{i,\omega}\hat{\mathbf{S}}_i, \tag{4.2.17}$$

and therefore the momentum equation of motion for the Harmonic oscillators is

$$\frac{\mathrm{d}\hat{\mathbf{P}}_{i,\omega}}{\mathrm{d}t} = -\omega^2\hat{\mathbf{X}}_{i,\omega} + |\gamma_e|C_{i,\omega}\hat{\mathbf{S}}_i. \tag{4.2.18}$$

Finally, the motion of the spin due to the interaction Hamiltonian must also be considered

$$\left[\hat{\mathcal{H}}_{\mathrm{int}}, \hat{\mathbf{S}}_i\right] = -|\gamma_e|\sum_j\int_0^\infty \mathrm{d}\omega' C_{j,\omega'}\sum_{\alpha\neq\beta=x,y,z}\hat{X}_{j,\omega',\beta}\left[\hat{S}_{j,\omega',\beta}, \hat{S}_{i,\omega',\alpha}\right]\mathbf{e}_\alpha, \tag{4.2.19}$$

using

$$\sum_{\alpha\neq\beta=x,y,z}\left[\hat{S}_{j,\omega',\beta}, \hat{S}_{i,\omega',\alpha}\right] = i\hbar\delta_{ij}\sum_{\alpha\neq\beta\neq\zeta=x,y,z}\epsilon_{\alpha\beta\zeta}\hat{S}_{j,\omega',\zeta}\mathbf{e}_\alpha, \tag{4.2.20}$$

and

$$\mathbf{A} \times \mathbf{B} = \sum_{i,j,k=1}^{3} \epsilon_{ijk} A_j B_k \mathbf{e}_i, \tag{4.2.21}$$

gives

$$\left[\hat{\mathcal{H}}_{\text{Int}}, \hat{\mathbf{S}}_i\right] = i\hbar|\gamma_e|\hat{\mathbf{S}}_i \times \int_0^\infty \mathrm{d}\omega' C_{i,\omega'} \hat{\mathbf{X}}_{i,\omega'}, \tag{4.2.22}$$

which, when combined with the equations of motion found in section 2.2.1, leads to the spin evolution

$$\frac{\mathrm{d}\hat{\mathbf{S}}_i}{\mathrm{d}t} = -|\gamma_e|\hat{\mathbf{S}}_i \times \hat{\mathbf{B}}_{\text{eff}}, \tag{4.2.23}$$

where

$$\hat{\mathbf{B}}_{\text{eff}} = \mathbf{B}_{\text{ext}} + \frac{\mathcal{J}}{|\gamma_e|} \sum_{\langle j \rangle_i} \hat{\mathbf{S}}_j + \int_0^\infty \mathrm{d}\omega' C_{i,\omega'} \hat{\mathbf{X}}_{i,\omega'}. \tag{4.2.24}$$

Therefore, the time evolution of the system is given by the dependent equations of motion for the spin evolution (equation 4.2.23), and the displacement (equation 4.2.14) and momentum (4.2.18.) evolution of the frequency continuum of harmonic oscillators at sites i.

4.2.2 Reducing the Equations of Motion

In order to solve for the motion of spins in the system, the three equations of motion should be reduced to a single one by substitution. The derivative of equation 4.2.14 is equal to equation 4.2.18, leading to

$$\frac{\mathrm{d}^2\hat{\mathbf{X}}_{i,\omega}}{\mathrm{d}t^2} = -\omega^2 \hat{\mathbf{X}}_{i,\omega} + |\gamma_e| C_{i,\omega} \hat{\mathbf{S}}_i. \tag{4.2.25}$$

This is a second order differential equation in position with respect to time (specifically the harmonic oscillator with frequency ω) at site i, with a forcing function proportional to $\hat{\mathbf{S}}_i$, the spin at site i through the coupling constant $C_{i,\omega}$. In the case where the forcing function is zero, i.e. no coupling between spins and harmonic oscillators, the solution to the equation

$$\frac{\mathrm{d}^2\hat{\mathbf{X}}_{i,\omega}}{\mathrm{d}t^2} + \omega^2 \hat{\mathbf{X}}_{i,\omega} = 0, \tag{4.2.26}$$

is most suitably given in terms of the bosonic ladder operators, $\hat{\mathbf{a}}_{i,\omega} = \sqrt{\frac{\omega}{2\hbar}}\hat{\mathbf{X}}_{i,\omega} - \frac{i}{\sqrt{2\hbar\omega}}\hat{\mathbf{P}}_{i,\omega}$, and $\hat{\mathbf{a}}^\dagger_{i,\omega} = \sqrt{\frac{\omega}{2\hbar}}\hat{\mathbf{X}}_{i,\omega} + \frac{i}{\sqrt{2\hbar\omega}}\hat{\mathbf{P}}_{i,\omega}$, the annihilation and creation operators

respectively. These operators obey the commutation relation

$$\left[\hat{\mathbf{a}}_{i,\omega}, \hat{\mathbf{a}}^{\dagger}_{j,\omega'}\right] = \delta_{ij}\delta(\omega' - \omega), \tag{4.2.27}$$

which means that the annihilation and creation operators corresponding to different spin sites commute, as do those for the same spin site but with different frequencies, but those at the same spin site and frequency do not. The physical significant of this commutation relation is an asymmetry in the capacity for creation and annihilation of bosons [6]. Due to this relation, the time evolution of the ladder operators can be evaluated as follows. Starting with an alternate form of the harmonic reservoir

$$\hat{\mathcal{H}}_{\mathrm{R}} = \sum_j \int_0^{\infty} \mathrm{d}\omega' \left(\frac{\hat{\mathbf{P}}^2_{j,\omega'}}{2} + \frac{\omega'^2 \hat{\mathbf{X}}^2_{j,\omega'}}{2} \right) = \sum_j \int_0^{\infty} \mathrm{d}\omega' \hbar\omega' \left(\hat{\mathbf{a}}^{\dagger}_{j,\omega'} \hat{\mathbf{a}}_{j,\omega'} + \frac{1}{2} \right), \tag{4.2.28}$$

and using equation 4.2.5, the time evolution of ladder operators can be shown to be

$$\frac{\mathrm{d}\hat{\mathbf{a}}_{i,\omega}}{\mathrm{d}t} = \frac{i}{\hbar}\left[\hat{\mathcal{H}}_{\mathrm{R}}, \hat{\mathbf{a}}_i\right] = -i\omega\hat{\mathbf{a}}_{i,\omega}, \tag{4.2.29}$$

and,

$$\frac{\mathrm{d}\hat{\mathbf{a}}^{\dagger}_{i,\omega}}{\mathrm{d}t} = \frac{i}{\hbar}\left[\hat{\mathcal{H}}_{\mathrm{R}}, \hat{\mathbf{a}}^{\dagger}_i\right] = i\omega\hat{\mathbf{a}}^{\dagger}_{i,\omega} \tag{4.2.30}$$

which can be used to show that

$$\hat{\mathbf{X}}_{i,\omega} = \sqrt{\frac{\hbar}{2\omega}} \left(\hat{\mathbf{a}}_{i,\omega} e^{-i\omega t} + \hat{\mathbf{a}}^{\dagger}_{i,\omega} e^{i\omega t} \right), \tag{4.2.31}$$

is the homogeneous solution to equation 4.2.26. This is the solution for a non forced harmonic oscillator, and can be extended to the solution for a forced harmonic oscillator by consideration of the Greens function. Using the Greens function approach [7] to forced (inhomogeneous) differential equations, this can be extended to solve for equation 4.2.25 as

$$\frac{\mathrm{d}^2\mathbf{G}(t-t')}{\mathrm{d}t^2} + \omega^2\mathbf{G}(t-t') = \delta(t-t'). \tag{4.2.32}$$

Using the fundamental property of the Dirac delta function it is found that

$$\mathcal{L}\int \mathbf{G}(t-t')f(t')\mathrm{d}t' = \int \delta(t-t')f(t')\mathrm{d}t' = f(t), \tag{4.2.33}$$

where $\mathcal{L} = \frac{\mathrm{d}^2}{\mathrm{d}t^2} + \omega^2$ is a linear differential operator, so that if

$$\hat{\mathbf{X}}_{i,\omega} = |\gamma_e| \int \mathbf{G}(t-t')C_{i,\omega}\hat{\mathbf{S}}_i(t')\mathrm{d}t' + \sqrt{\frac{\hbar}{2\omega}}\left(\hat{\mathbf{a}}_{i,\omega}e^{-i\omega t} + \hat{\mathbf{a}}^\dagger_{i,\omega}e^{i\omega t}\right), \quad (4.2.34)$$

then equation 4.2.25 is satisfied. By substitution into the effective field, the equation of motion of the spins is given by equation 4.2.23, where the effective field is

$$\hat{\mathbf{B}}_{\text{eff}} = \mathbf{B}_{\text{ext}} + \frac{\mathcal{J}}{|\gamma_e|}\sum_{\langle j\rangle_i}\hat{\mathbf{S}}_j + \int_0^\infty \mathrm{d}\omega' C^2_{i,\omega'}\int \mathbf{G}(t-t')\hat{\mathbf{S}}_i(t')\mathrm{d}t' + \int_0^\infty \mathrm{d}\omega' C_{i,\omega'}\sqrt{\frac{\hbar}{2\omega'}}\left(\hat{\mathbf{a}}_{i,\omega'}e^{-i\omega' t} + \hat{\mathbf{a}}^\dagger_{i,\omega'}e^{i\omega' t}\right). \quad (4.2.35)$$

The specific Green's function is defined according to the differential equation 4.2.32, which must be solved to determine its form. Starting with a general sinusoidal solution

$$\mathbf{G}(t-t') = A\sin(\omega(t-t')) + B\cos(\omega(t-t')), \quad (4.2.36)$$

the boundary conditions are set by the requirement to satisfy causality in a physical system. In order to satisfy this and remain a continuous function, the Green's function must vanish at $t' = t$ setting $B = 0$. Therefore the time derivative of the Greens function can be written as

$$\frac{\mathrm{d}\mathbf{G}(t-t')}{\mathrm{d}t} = \omega A\cos(\omega(t-t')), \quad (4.2.37)$$

with boundary condition at $t' = t$ of $\frac{\mathrm{d}\mathbf{G}(t-t')}{\mathrm{d}t} = \omega A$. By infinitesimal integration of 4.2.32 about the delta position

$$\int_{t-\epsilon}^{t+\epsilon}\frac{\mathrm{d}^2\mathbf{G}(t-t')}{\mathrm{d}t^2}\mathrm{d}t' + \int_{t-\epsilon}^{t+\epsilon}\omega^2\mathbf{G}(t-t')\mathrm{d}t' = \int_{t-\epsilon}^{t+\epsilon}\delta(t-t')\mathrm{d}t = 1. \quad (4.2.38)$$

In the limit of $\varepsilon \to 0$

$$\int_{t-\epsilon}^{t+\epsilon}\omega^2\mathbf{G}(t-t')\mathrm{d}t' = 0, \quad (4.2.39)$$

and therefore by equivalence of the terms on the left and right of equation 4.2.38

$$\frac{\mathrm{d}\mathbf{G}}{\mathrm{d}t}(\epsilon) - \frac{\mathrm{d}\mathbf{G}}{\mathrm{d}t}(-\epsilon) = 1, \quad (4.2.40)$$

which is satisfied by the Heaviside step function

$$\frac{\mathrm{d}\mathbf{G}(t'=t)}{\mathrm{d}t} = \Theta(t-t'), \quad (4.2.41)$$

and therefore the Green's function is given by

$$\mathbf{G}(t-t') = \frac{\Theta(t-t')}{\omega}\sin(\omega(t-t')). \tag{4.2.42}$$

The effective field is therefore given by substitution of equation 4.2.42 into 4.2.35 as

$$\begin{aligned}\hat{\mathbf{B}}_{\text{eff}} = \mathbf{B}_{\text{ext}} + \frac{\mathcal{J}}{|\gamma_e|}\sum_{\langle j\rangle_i}\hat{\mathbf{S}}_j \\ + \int_0^\infty \mathrm{d}\omega' C_{i,\omega'}^2 \int \frac{\Theta(t-t')}{\omega}\sin(\omega(t-t'))\hat{\mathbf{S}}_i(t')\mathrm{d}t' + \hat{\mathbf{b}}_i(t).\end{aligned} \tag{4.2.43}$$

4.2.3 Properties of the Effective Field

The effective field can be rewritten in terms of its thermodynamically important quantities

$$\hat{\mathbf{B}}_{\text{eff}} = \mathbf{B}_{\text{ext}} + \frac{\mathcal{J}}{|\gamma_e|}\sum_{\langle j\rangle_i}\hat{\mathbf{S}}_j + \int_{-\infty}^{t} K(t-t')\hat{\mathbf{S}}_i(t')\mathrm{d}t' + \hat{\mathbf{b}}_i(t), \tag{4.2.44}$$

where

$$K(t-t') = \int_0^\infty \mathrm{d}\omega' \frac{C_{i,\omega'}^2}{\omega'}\sin(\omega'(t-t')), \tag{4.2.45}$$

is the memory kernel through which the dynamics takes a non-Markovian form as it couples the effective field driving the spin motion to the history of the spin, and

$$\hat{\mathbf{b}}_i(t) = \int_0^\infty \mathrm{d}\omega' C_{i,\omega'}\sqrt{\frac{\hbar}{2\omega'}}\left(\hat{\mathbf{a}}_{i,\omega'}e^{-i\omega' t} + \hat{\mathbf{a}}_{i,\omega'}^\dagger e^{i\omega' t}\right), \tag{4.2.46}$$

is the stochastic thermal field.

The relationship between the coupling function and the memory kernel in the frequency space can be shown using the inverse Fourier transform (appendix equation A.2.2) [8]. In the frequency domain, the memory kernel is given by

$$\tilde{K}(\omega) = \mathrm{Re}[\tilde{K}(\omega)] - i\mathrm{Im}[\tilde{K}(\omega)] = \int_{-\infty}^{\infty} K(\tau)e^{-i\omega\tau}d\tau, \tag{4.2.47}$$

where τ is the delay $t-t'$. By taking the inverse Fourier transform and identifying the odd and even parts of the quantity $K(\tau)$ by considering the complex conjugate of $\tilde{K}(\omega)$, it can be shown that a $K(\tau)$ odd in τ takes the form

$$K(\tau) = \frac{i}{\pi}\int_{-\infty}^{\infty}\mathrm{Im}[\tilde{K}(\omega)]e^{i\omega\tau}\mathrm{d}\omega, \tag{4.2.48}$$

where the complex exponential can be separated into real and imaginary parts by

Euler's formula $e^{ix} = \cos(x) + i\sin(x)$

$$K(\tau) = \frac{i}{\pi}\int_{-\infty}^{\infty} \mathrm{Im}[\tilde{K}(\omega)]\left(\cos\left(\omega\tau\right) + i\sin\left(\omega\tau\right)\right)\mathrm{d}\omega, \tag{4.2.49}$$

and by the reduction of imaginary terms can be written as

$$K(\tau) = \int_{-\infty}^{\infty} \frac{\mathrm{Im}[\tilde{K}(\omega)]}{\pi}\left(-i\cos\left(\omega\tau\right) + \sin\left(\omega\tau\right)\right)\mathrm{d}\omega, \tag{4.2.50}$$

which is evaluated differently depending on whether $\mathrm{Im}[\tilde{K}(\omega)]$ is odd or even in ω. For the time domain expression to be real valued, this term must be odd, and as such it is evaluated as

$$K(\tau) = \int_{0}^{\infty} \frac{\mathrm{Im}[\tilde{K}(\omega)]}{\pi}\sin\left(\omega\tau\right)\mathrm{d}\omega, \tag{4.2.51}$$

which when compared with equation 4.2.45 shows the dissipative part of the memory kernel to be

$$\mathrm{Im}[K(\omega)] = \frac{\pi C_{i,\omega}^2}{2\omega}. \tag{4.2.52}$$

Now lets examine more closely the properties of the stochastic field $\hat{\mathbf{b}}_i(t)$. From equation 4.2.46

$$\hat{\mathbf{b}}_i(t) = \int_0^{\infty} \mathrm{d}\omega C_{i,\omega}\sqrt{\frac{\hbar}{2\omega}}\left(\hat{\mathbf{a}}_{i,\omega}e^{-i\omega t} + \hat{\mathbf{a}}_{i,\omega}^{\dagger}e^{i\omega t}\right), \tag{4.2.53}$$

the ladder operators increase and decrease the energy level of the harmonic oscillators, and obey the commutation relation given in equation 4.2.27. Like any quantum ladder operators, their meaning is only clear in a statistical sense, and the same is therefore true of the field $\hat{\mathbf{b}}_i(t)$, an indication of its stochastic nature. The second moment of $\hat{\mathbf{b}}_i(t)$ is given by its autocorrelation function, which characterises its memory of its value at previous times. In order to calculate the autocorrelation of the stochastic thermal field, the expectation value of the quantity with a delayed copy of itself is taken (see appendix A.5 and equation A.5.1). Using the property

$$\langle\hat{\mathbf{a}}_{i,\omega}\hat{\mathbf{a}}_{j,\omega'}\rangle = \langle\hat{\mathbf{a}}_{j,\omega}\hat{\mathbf{a}}_{i,\omega'}\rangle = \langle\hat{\mathbf{a}}_{i,\omega}^{\dagger}\hat{\mathbf{a}}_{j,\omega'}^{\dagger}\rangle = \langle\hat{\mathbf{a}}_{j,\omega}^{\dagger}\hat{\mathbf{a}}_{i,\omega'}^{\dagger}\rangle = 0, \tag{4.2.54}$$

the autocorrelation is given as

$$\begin{aligned}&\langle\hat{\mathbf{b}}_i(t)\hat{\mathbf{b}}_j(t')\rangle = \\ &\int_0^{\infty}\mathrm{d}\omega\int_0^{\infty}\mathrm{d}\omega'\delta_{ij}\hbar\frac{C_{i,\omega}C_{j,\omega'}}{2\sqrt{\omega\omega'}}\left(\langle\hat{\mathbf{a}}_{i,\omega}\hat{\mathbf{a}}_{j,\omega'}^{\dagger}\rangle e^{i(\omega't'-\omega t)} + \langle\hat{\mathbf{a}}_{i,\omega}^{\dagger}\hat{\mathbf{a}}_{j,\omega'}\rangle e^{-i(\omega't'-\omega t)}\right),\end{aligned} \tag{4.2.55}$$

which by use of equation 4.2.27 reduces to

$$\langle \hat{\mathbf{b}}_i(t)\hat{\mathbf{b}}_j(t')\rangle = \int_0^\infty \mathrm{d}\omega\hbar\frac{C_{i,\omega}^2}{2\omega}\left(\langle 1+\hat{\mathbf{a}}_{i,\omega}^\dagger\hat{\mathbf{a}}_{i,\omega'}\rangle e^{-i\omega(t-t')} + \langle\hat{\mathbf{a}}_{i,\omega}^\dagger\hat{\mathbf{a}}_{i,\omega'}\rangle e^{i\omega(t-t')}\right), \quad (4.2.56)$$

and similarly

$$\langle \hat{\mathbf{b}}_j(t')\hat{\mathbf{b}}_i(t)\rangle = \int_0^\infty \mathrm{d}\omega\hbar\frac{C_{i,\omega}^2}{2\omega}\left(\langle 1+\hat{\mathbf{a}}_{i,\omega}^\dagger\hat{\mathbf{a}}_{i,\omega'}\rangle e^{i\omega(t-t')} + \langle\hat{\mathbf{a}}_{i,\omega}^\dagger\hat{\mathbf{a}}_{i,\omega'}\rangle e^{-i\omega(t-t')}\right) \quad (4.2.57)$$

When considering quantum behaviour where physical quantities do not necessariliy commute, it is important to distinguish the (Hermitian) symmetrised autocorrelation,

$$\frac{\langle \hat{\mathbf{b}}_i(t)\hat{\mathbf{b}}_j(t') + \hat{\mathbf{b}}_j(t')\hat{\mathbf{b}}_i(t)\rangle}{2} = \int_{-\infty}^\infty \mathrm{d}\omega\hbar\frac{C_{i,\omega}^2}{2\omega}\langle 1+2\hat{\mathbf{a}}_{i,\omega}^\dagger\hat{\mathbf{a}}_{i,\omega'}\rangle e^{-i\omega(t-t')}. \quad (4.2.58)$$

From quantum mechanics [6], the term $\hat{\mathbf{a}}^\dagger\hat{\mathbf{a}}$ is the number operator for the Bose-Einstein distribution, which for a non degenerate system such as a continuum of harmonic oscillators, has the form

$$\langle\hat{\mathbf{a}}_{i,\omega}^\dagger\hat{\mathbf{a}}_{i,\omega'}\rangle = \langle\hat{n}_{i,\omega}\rangle\delta(\omega'-\omega) = \frac{1}{e^{\frac{\hbar\omega}{k_BT}}-1}\delta(\omega'-\omega), \quad (4.2.59)$$

from which the inner product on the right hand side of equation 4.2.58 is calculated to be

$$\langle 1+2\hat{\mathbf{a}}_{i,\omega}^\dagger\hat{\mathbf{a}}_{i,\omega'}\rangle = \coth\left(\frac{\hbar\omega}{2k_BT}\right)\delta(\omega'-\omega). \quad (4.2.60)$$

By substitution of equations 4.2.52 and 4.2.60 into equation 4.2.58, the autocorrelation is given by

$$\frac{\langle \hat{\mathbf{b}}_i(t)\hat{\mathbf{b}}_j(t') + \hat{\mathbf{b}}_j(t')\hat{\mathbf{b}}_i(t)\rangle}{2} = \int_{-\infty}^\infty \mathrm{d}\omega\mathrm{Im}[\tilde{K}(\omega)]\hbar\coth\left(\frac{\hbar\omega}{2k_BT}\right)e^{-i\omega(t-t')} \quad (4.2.61)$$

which through the Wiener-Khinchin theorem (discussed in appendix A.5) shows the symmetrised power spectral density to be

$$\tilde{P}(\omega) = \hbar\mathrm{Im}[K(\omega)]\coth\left(\frac{\hbar\omega}{2k_BT}\right), \quad (4.2.62)$$

indicating by comparison to the formulation by Kubo [8] that the fluctuation dissipation theorem (equation 2.3.7) is satisfied for the dynamics predicted by the

Heisenberg-Langevin equation (from 4.2.44 and 4.2.23)

$$\frac{\mathrm{d}\hat{\mathbf{S}}_i}{\mathrm{d}t} = -|\gamma_e|\hat{\mathbf{S}}_i \times \left[\mathbf{B}_{\mathrm{ext}} + \frac{\mathcal{J}}{|\gamma_e|}\sum_{\langle j\rangle_i}\hat{\mathbf{S}}_j + \int_{-\infty}^{t} K(t-t')\hat{\mathbf{S}}_i(t')\mathrm{d}t' + \hat{\mathbf{b}}_i(t)\right], \quad (4.2.63)$$

for any choice of coupling function. However, similar to the symmetrisation of autocorrelation, the spin dynamics must also be Hermitian leading to

$$\frac{\mathrm{d}\hat{\mathbf{S}}_i}{\mathrm{d}t} = -\frac{|\gamma_e|}{2}\hat{\mathbf{S}}_i \times \left[\mathbf{B}_{\mathrm{ext}} + \frac{\mathcal{J}}{|\gamma_e|}\sum_{\langle j\rangle_i}\hat{\mathbf{S}}_j + \int_{-\infty}^{t} K(t-t')\hat{\mathbf{S}}_i(t')\mathrm{d}t' + \hat{\mathbf{b}}_i(t)\right] + h.c., \quad (4.2.64)$$

where h.c. indicates the Hermitian conjugate of the prior term.

4.2.4 Obtaining the LLG equation

Equation 4.2.64 is a general formula for the spin dynamics containining a free parameter in the form of the memory kernel $K(t-t')$ and undefined autocorrelation behaviour for the stochastic thermal field operator $\hat{\mathbf{b}}_i(t)$. To determine a predictive dynamical equation (i.e. define the properties of these two parameters), the coupling $C_{i,\omega'}$ between spins and oscillators must be chosen. When the coupling between a system and a harmonic oscillator reservoir is linear in frequency, it is referred to as 'Ohmic' [9]. Here the dynamics resulting from an Ohmic coupling will be determined, and shown to result in Landau-Lifshitz-Gilbert-Brown dynamics outlined in section 2.2.2. Taking a coupling between spins and oscillators linear in the frequency of harmonic oscillators

$$C_{i,\omega'}^{\mathrm{Ohm}} = \Lambda\omega', \quad (4.2.65)$$

where Λ is the coefficient in the linear relationship, gives the time domain kernel from equation 4.2.45 as

$$K^{\mathrm{Ohm}}(t-t') = \Lambda^2\int_0^\infty \mathrm{d}\omega'\omega'\sin(\omega'(t-t')), \quad (4.2.66)$$

which can be rewritten in the form

$$K^{\mathrm{Ohm}}(t-t') = \Lambda^2\frac{\mathrm{d}}{\mathrm{d}t}\int_0^\infty \mathrm{d}\omega'\cos(\omega'(t-t')), \quad (4.2.67)$$

$$K^{\mathrm{Ohm}}(t-t') = \frac{\Lambda^2}{2}\frac{\mathrm{d}}{\mathrm{d}t}\int_0^\infty \mathrm{d}\omega'\left[e^{i\omega'(t-t')} + e^{-i\omega'(t-t')}\right], \quad (4.2.68)$$

$$K^{\mathrm{Ohm}}(t-t') = \frac{\Lambda^2}{2}\frac{\mathrm{d}}{\mathrm{d}t}\int_{-\infty}^{\infty}\mathrm{d}\omega' e^{i\omega'(t-t')}. \tag{4.2.69}$$

Applying the inverse Fourier transform to move from the frequency to the time domain, noting that the sum of plane waves of all frequncies is a delta function located at $t' = t$

$$K^{\mathrm{Ohm}}(t-t') = \frac{\Lambda^2\pi}{2}\frac{\mathrm{d}\delta(t-t')}{\mathrm{d}t}. \tag{4.2.70}$$

Substituting this expression into the effective field (equation 4.2.44)

$$\hat{\mathbf{B}}_{\mathrm{eff}} = \mathbf{B}_{\mathrm{ext}} + \frac{\mathcal{J}}{|\gamma_e|}\sum_{\langle j\rangle_i}\hat{\mathbf{S}}_j + \frac{\Lambda^2\pi}{2}\int_{-\infty}^{t}\frac{\mathrm{d}\delta(t-t')}{\mathrm{d}t}\hat{\mathbf{S}}_i(t')\mathrm{d}t' + \hat{\mathbf{b}}_i(t), \tag{4.2.71}$$

and using the product rule of differentiation

$$\frac{\mathrm{d}\delta(t-t')}{\mathrm{d}t}\hat{\mathbf{S}}_i(t') = \frac{\mathrm{d}\delta(t-t')\hat{\mathbf{S}}_i(t')}{\mathrm{d}t} - \delta(t-t')\frac{\mathrm{d}\hat{\mathbf{S}}_i}{\mathrm{d}t}, \tag{4.2.72}$$

the effective field is found to be

$$\hat{\mathbf{B}}_{\mathrm{eff}} = \mathbf{B}_{\mathrm{ext}} + \frac{\mathcal{J}}{|\gamma_e|}\sum_{\langle j\rangle_i}\hat{\mathbf{S}}_j + \frac{\Lambda^2\pi}{2}\int_{-\infty}^{t}\frac{\mathrm{d}\delta(\mathrm{t}-\mathrm{t}')\hat{\mathbf{S}}_{\mathrm{i}}(\mathrm{t}')}{\mathrm{d}t}\mathrm{d}t' - \Lambda^2\pi\frac{\mathrm{d}\hat{\mathbf{S}}_i}{\mathrm{d}t} + \hat{\mathbf{b}}_i(t). \tag{4.2.73}$$

Taking in to account that the full quantum spin evolution is a Hermitian equation of motion (equation 4.2.64), it is found that the cross product of $\hat{\mathbf{S}}_i$ with the third term on the right hand side of equation 4.2.73, vanishes because the cross product is an anti-Hermitian operator. Therefore this term is dropped from the effective field with no modification to the resultant dynamics

$$\hat{\mathbf{B}}_{\mathrm{eff}} = \mathbf{B}_{\mathrm{ext}} + \frac{\mathcal{J}}{|\gamma_e|}\sum_{\langle j\rangle_i}\hat{\mathbf{S}}_j - \frac{\Lambda^2\pi}{2}\frac{\mathrm{d}\hat{\mathbf{S}}_i}{\mathrm{d}t} + \hat{\mathbf{b}}_i(t). \tag{4.2.74}$$

The spin equation of motion now takes the form of the LLG equation, with the spin derivative taking the form of damping, and an additional field characterised by its composition in terms of harmonic oscillator ladder operators. To separate and make clear the damping part of the motion, the term containing the time derivative of spin can be removed from the effective field term giving the spin evolution as

$$\frac{\mathrm{d}\hat{\mathbf{S}}_i}{\mathrm{d}t} = -\frac{|\gamma_e|\hat{\mathbf{S}}_i}{2}\times\left[\hat{\mathbf{B}}_{\mathrm{eff}} - \frac{\Lambda^2\pi}{2}\frac{\mathrm{d}\hat{\mathbf{S}}_i}{\mathrm{d}t}\right] + h.c., \tag{4.2.75}$$

If

$$\Lambda = \sqrt{\frac{2\eta}{\pi}} \tag{4.2.76}$$

then the spin dynamics is given by the Landau-Lifshitz-Gilbert equation,

$$\frac{\mathrm{d}\hat{\mathbf{S}}_i}{\mathrm{d}t} = -\frac{|\gamma_e|}{2}\left(\hat{\mathbf{S}}_i \times \hat{\mathbf{B}}_{\text{eff}} - \eta\hat{\mathbf{S}}_i \times \frac{\mathrm{d}\hat{\mathbf{S}}_i}{\mathrm{d}t}\right) + h.c., \tag{4.2.77}$$

where the effective field is,

$$\hat{\mathbf{B}}_{\text{eff}} = \mathbf{B}_{\text{ext}} + \frac{\mathcal{J}}{|\gamma_e|}\sum_{\langle j\rangle_i}\hat{\mathbf{S}}_j + \hat{\mathbf{b}}_i(t), \tag{4.2.78}$$

containing the thermal magnetic field $\hat{\mathbf{b}}_i(t)_i(t)$, which has properties characterised by the power spectral density which can be calculated using equations 4.2.52 and 4.2.62 giving

$$\tilde{P}^{\text{Ohm}}_{\text{qu}}(\omega) = \eta\hbar\omega\,\coth\left(\frac{\hbar\omega}{2k_BT}\right), \tag{4.2.79}$$

which reduces at high temperature ($k_BT >> \frac{\hbar\omega}{2}$) to the classical form

$$\tilde{P}^{\text{Ohm}}_{\text{cl}}(\omega) = 2\eta k_BT, \tag{4.2.80}$$

which is the frequency independent white noise introduced by Brown [10] into the LLGB equation which is traditionally used in simulations of magnetic materials to represent thermal fluctuations (see section 2.2.2).

4.2.5 Beyond LLG Dynamics

As mentioned in section 4.2.4, LLG dynamics results from the case where the coupling function takes a linear dependence on frequency. However, in reality there can be no coupling between system and reservoir at infinitely high frequencies, as that would imply that the system can respond infinitely quickly, which is an unphysical description. Therefore an alternative description of the coupling function must be found, that can still capture the well established behaviour of LLG dynamics under classical and more importantly experimental conditions, but reduces to zero at high frequencies. The simplest way to model a more physically realistic behaviour is to continue with Ohmic coupling, but choose a cutoff frequency, above which the coupling function is set to zero. This involves making the function discontinuous, but does at least solve the issue with high frequency oscillation behaviour. In a more complex fashion, it is possible to solve the issue by choosing a continuous coupling function which also reduces to zero in the limit

$$\lim_{\omega'\to\infty} C_{i,\omega'} \to 0. \tag{4.2.81}$$

One way to achieve this is to choose the coupling function in a way such that the damping kernel takes a Lorentzian form. This is satisfied by the function

$$C_{i,\omega}^{\mathrm{Lor}} = \sqrt{\frac{2A\Gamma}{\pi}}\sqrt{\frac{\omega^2}{(\omega_0^2+\omega^2)^2+\omega^2\Gamma^2}}, \tag{4.2.82}$$

where A, Γ and ω_0 represent the magnitude, bandwidth and resonance frequency of coupling respectively. Substituting the coupling function 4.2.82 into 4.2.52 shows the imaginary component of the frequency domain memory kernel to be

$$\mathrm{Im}[\tilde{K}(\omega)] = A\frac{\Gamma\omega}{(\omega_0^2-\omega^2)^2+\omega^2\Gamma^2}. \tag{4.2.83}$$

Using the Kramers-Kronig relations (appendix equation A.4.14), the real part of the susceptibility can be shown to be

$$\mathrm{Re}[\tilde{K}(\omega)] = A\frac{(\omega_0^2-\omega^2)}{(\omega_0^2-\omega^2)^2+\omega^2\Gamma^2}. \tag{4.2.84}$$

Therefore the complex susceptibility is given by the Lorentian form

$$\tilde{K}(\omega) = \frac{A}{(\omega_0^2-\omega^2)+i\omega\Gamma}. \tag{4.2.85}$$

Through the use of the Fourier transform, this can be used to derive the memory kernel in the time domain

$$K^{\mathrm{Lor}}(t-t') = \Theta(t-t')Ae^{-\frac{\Gamma(t-t')}{2}}\frac{\sin\left(\sqrt{\omega_0^2-\frac{\Gamma^2}{4}}(t-t')\right)}{\sqrt{\omega_0^2-\frac{\Gamma^2}{4}}}, \tag{4.2.86}$$

from which it becomes clear that $\Gamma/2$ is the kernel decay rate. Substitution of equation 4.2.83 into 4.2.62 shows the power spectral density to be

$$\tilde{P}_{\mathrm{qu}}^{\mathrm{Lor}}(\omega) = \frac{A\Gamma\hbar\omega}{(\omega_0^2-\omega^2)^2+\omega^2\Gamma^2}\coth\left(\frac{\hbar\omega}{2k_BT}\right). \tag{4.2.87}$$

4.2.6 Comparison of Ohmic and Lorentzian Coupling

To understand the implications of a Lorentzian type coupling between spins and harmonic oscillators shown in section 4.2.5 on the physical behaviour of magnetic spin systems, here it will be shown how by a considered selection of the parameters A, Γ and ω_0 that characterise the Lorentzian coupling, the behaviour of the system can either approximate the memoryless Ohmic system described in section 4.2.4, or alternatively a system with memory of the previous dynamics and coloured noise.

In order to appropriately compare the results of Ohmic and Lorentzian coupling,

the damping factor η should be kept the same between equations 4.2.77, and 4.2.64. The deviations of the Lorentzian dynamics from the Ohmic dynamics is determined by consideration of the integral term in equation 4.2.64. By Taylor expansion of $\hat{\mathbf{S}}_i(t)$ around $t' = t$, the integral can be written as

$$\int_{-\infty}^{t} K(t-t')\hat{\mathbf{S}}_i(t')\mathrm{d}t' = \sum_{m=1}^{\infty} \kappa_m \partial_t^m \hat{\mathbf{S}}_i(t), \tag{4.2.88}$$

where

$$\kappa_m = \frac{(-1)^m}{m!} \int_0^{\infty} \tau^m K(\tau)\mathrm{d}\tau, \tag{4.2.89}$$

assuming that the dynamics have been running longer than the kernel decay time. Noting that only a time derivative of spin to the first order contributes to the Ohmic spin dynamics (equation 4.2.77), it is seen that $\kappa_1^{\mathrm{Ohm}} = -\eta$ corresponds to the damping parameter, and all other coefficients are zero. For Lorentzian dynamics, all coefficients (where $m > 0$) are non zero and given by [11]

$$\kappa_1^{\mathrm{Lor}} = \frac{(-1)^m A}{\omega_0^{2(m+1)}\sqrt{\omega_0^2 - \frac{\Gamma^2}{4}}} \mathrm{Im}\left[\left(\frac{\Gamma}{2} + i\sqrt{\omega_0^2 - \frac{\Gamma^2}{4}}\right)^{m+1}\right]. \tag{4.2.90}$$

The first coefficient can then be determined and matched to the first coefficient of Ohmic dynamics as the first order damping behaviour, giving

$$\eta = \frac{A\Gamma\omega_L^2}{\omega_0^4}, \tag{4.2.91}$$

when the dynamics are written in terms of unit-free variables. Here, $\omega_L = |\gamma_e||\mathbf{B}_{\mathrm{ext}}|$ is the Larmor frequency at which the spins would precess in a field composed of only an external component $\mathbf{B} = \mathbf{B}_{\mathrm{ext}}$.

The two sets of parameters considered for the Lorentzian coupling function are shown in table 4.1. Parameter Set 1 is chosen to have a resonant frequency ω_0 much larger than ω_L Alternatively, parameter Set 2 is chosen to have a resonant frequency comparable to ω_L.

Figure 4.1 shows that for parameter Set 1 in panel (a), the Lorentzian coupling function $C_{i,\omega}^{\mathrm{Lor}}$ is well approximated by the Ohmic (LLG) coupling function $C_{i,\omega}^{\mathrm{Ohm}}$ in the range of frequencies comparable to ω_L. Alternatively, panel (b) shows that for parameter Set 2, Ohmic coupling is a poor approximation to the Lorentzian form with resonant frequency comparable to the Larmor frequency. These qualities feed through to 4.2 which shows the memory kernel in the frequency space. For parameter Set 1, the imaginary component takes an approximately linear form within the relevant frequency range, comparable to the Ohmic memory kernel given

Parameters	Set 1	Set 2
ω_0	$7\omega_L$	$1.4\omega_L$
Γ	$5\omega_L$	$0.5\omega_L$
A	$10\omega_L$	$0.16\omega_L$
$\eta = \frac{A\Gamma\omega_L^2}{\omega_0^4}$	0.0208	0.0208

Table 4.1: A table showing the two sets of parameters used to plot the red and black lines in figures 4.1, 4.2, 4.3, 4.4 and 4.5 relating to the Lorentzian type coupling.

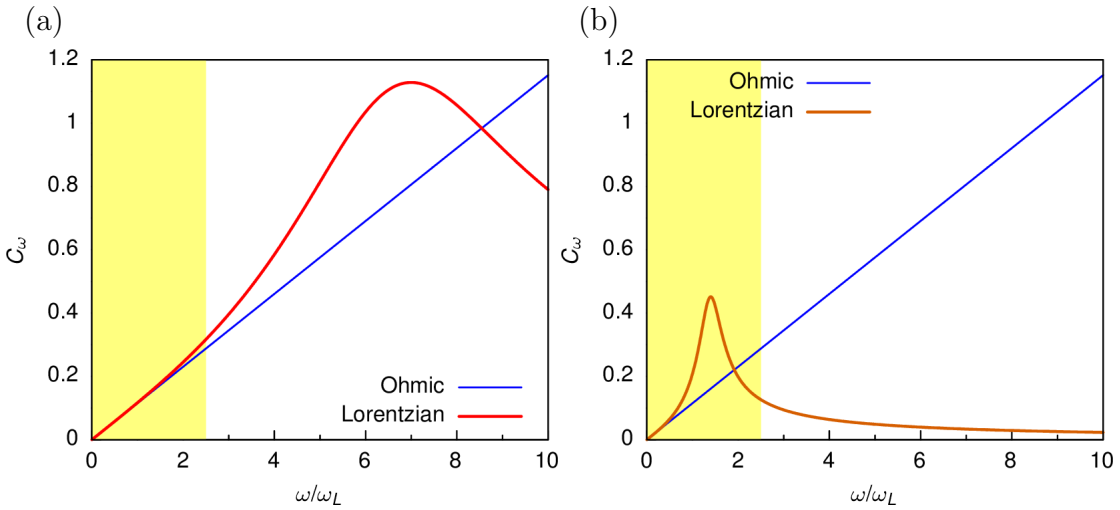

Figure 4.1: A comparison between the Ohmic and Lorentzian type coupling functions as a function of frequency. The blue lines show the Ohmic coupling function in equation 4.2.65 with η=0.0208. In panel (a) the red line shows the Lorentzian coupling function in equation 4.2.82 using the parameters in the 'Set 1' column of table 4.1, while in panel (b) the orange line shows Lorentzian coupling with parameters in the 'Set 2' column. The frequency range shaded yellow indicates typical spin dynamics frequencies.

by equations 4.2.52 and 4.2.65. For parameter set two, the imaginary parts of the Ohmic and Lorentzian memory kernels diverge significantly. Figure 4.3 shows the memory kernel in the time domain, which for parameter Set 1 in panel (a) is close to instantaneous (i.e. limited memory), while for Set 2 in panel (b), the memory persists over the timescale of several ω_L^{-1} (i.e. precessions). Figure 4.4 shows the power spectral density at 200K. In panel (a) for parameter Set 1, both quantum and classical Ohmic spectra offer a good approximation to the Lorentzian behaviour at frequencies comparable to the Larmor frequency. In panel (b) for parameter Set 2, neither offer a good approximation for the character of the coloured noise. Figure 4.5 shows the power spectral density at 1K. In panel (a) for parameter Set 1, the quantum Ohmic spectra offers a good approximation to the Lorentzian behaviour, while the classical Ohmic (white noise) fails to approximate the behaviour in all but the lowest frequencies, demonstrating the importance of quantum noise

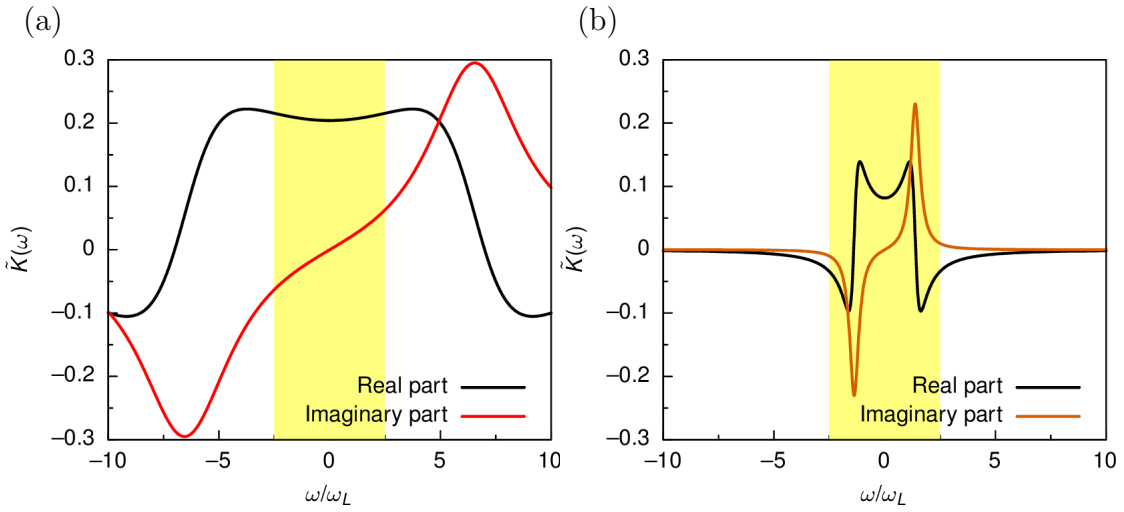

Figure 4.2: Lorentzian memory kernels as a function of frequency. The black lines show the real part of the kernel as given in equation 4.2.84, while the red and orange lines show the imaginary part as given in equation 4.2.83. In panel (a) the parameters in the 'Set 1' column of table 4.1 are used, while in panel (b) the parameters used are given in the 'Set 2' column. The frequency range shaded yellow indicates typical spin dynamics frequencies.

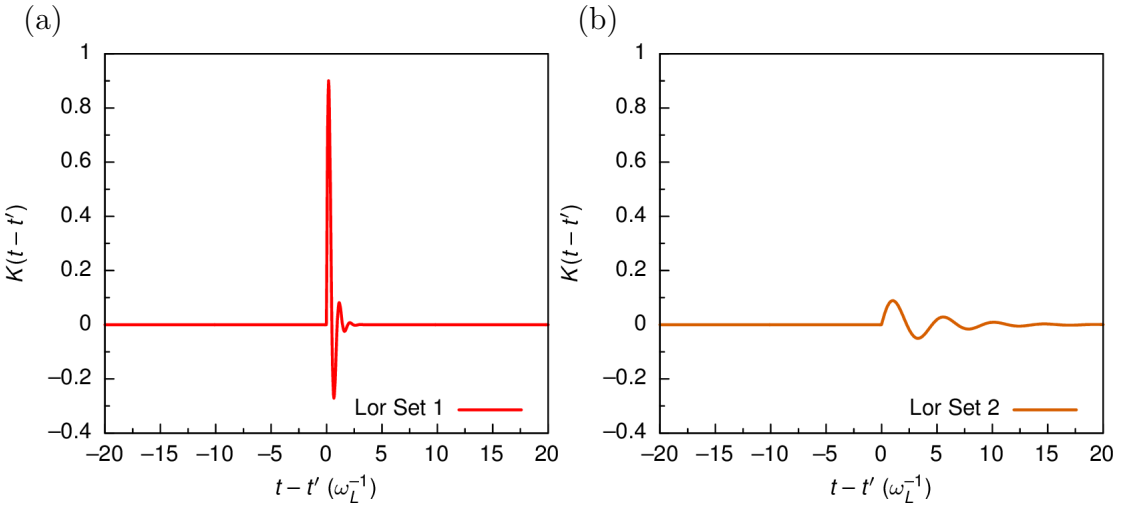

Figure 4.3: Lorentzian memory kernels as a function of time as given in equation 4.2.86. In panel (a) the parameters in the 'Set 1' column of table 4.1 are used, representing a very short memory that approximates the memoryless nature of Ohmic coupling. In panel (b) the parameters used are given in the 'Set 2' column, giving rise to a memory that lasts for many precessions.

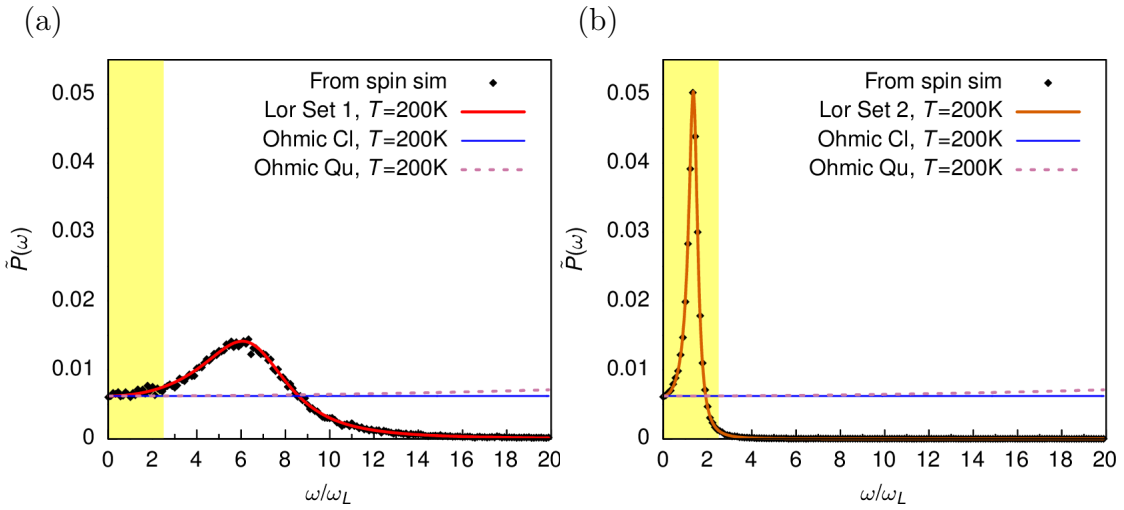

Figure 4.4: A comparison between the Ohmic and Lorentzian type power spectral density (PSD) functions at T=200K. The solid blue and pink dashed lines in both parts show the classical and quantum Ohmic PSD function in equations 4.2.80 and 4.2.79 respectively with $\eta = 0.0208$. The red line in panel (a) shows the Lorentzian PSD in equation 4.2.87 using the parameters in the 'Set 1' column of table 4.1, while in panel (b) the orange line shows the Lorentzian PSD when the parameters in the 'Set 2' column are used. The black diamonds show the average PSD of 50000 samples of noise generated using 4.2.103 with the Lorentzian kernel given in equation 4.2.85. The PSD is determined by the inverse Fourier transform of the autocorrelation of coloured noise using code shown in appendix C.2. The frequency range shaded yellow indicates typical spin dynamics frequencies.

at low temperatures. In panel (b) for parameter Set 2, again neither offer a good approximation for the character of the coloured noise.

4.2.7 Single Spin Simulations

In this section simulations of the dynamics of a single spin predicted by the results outlined earlier in this chapter will be shown and compared. Python functions used to generate the data plotted in this section can be found in appendix C.2.

In order to simulate the dissipative single spin dynamics, we substitute the effective field resulting from the memory kernel $K(t-t')$ and magnetic noise $\hat{\mathbf{b}}_i(t)_i$ (equation 4.2.44) into the spin evolution $\frac{\mathrm{d}\hat{\mathbf{S}}_i}{\mathrm{d}t}$ (equation 4.2.23), resulting in

$$\frac{\mathrm{d}\hat{\mathbf{S}}(t)}{\mathrm{d}t} = -|\gamma_e|\hat{\mathbf{S}}(t) \times \left[\mathbf{B}_{\mathrm{ext}} + \int_{-\infty}^{t} K(t-t')\hat{\mathbf{S}}(t')\mathrm{d}t' + \hat{\mathbf{b}}(t)\right]. \tag{4.2.92}$$

This can be re-written in a classical form as

$$\frac{\mathrm{d}\mathbf{S}(t)}{\mathrm{d}t} = -|\gamma_e|\mathbf{S}(t) \times \left[\mathbf{B}_{\mathrm{ext}} + \mathbf{V}(t) + \mathbf{b}(t)\right], \tag{4.2.93}$$

where $\mathbf{V}(t) = \int_{-\infty}^{t} K(t-t')\mathbf{S}(t')\mathrm{d}t'$, and the quantum mechanical spin $\hat{\mathbf{S}}(t)$ and stochastic field $\hat{\mathbf{b}}(t)$ operators are replaced by classical spin $\mathbf{S}(t)$ and stochastic field

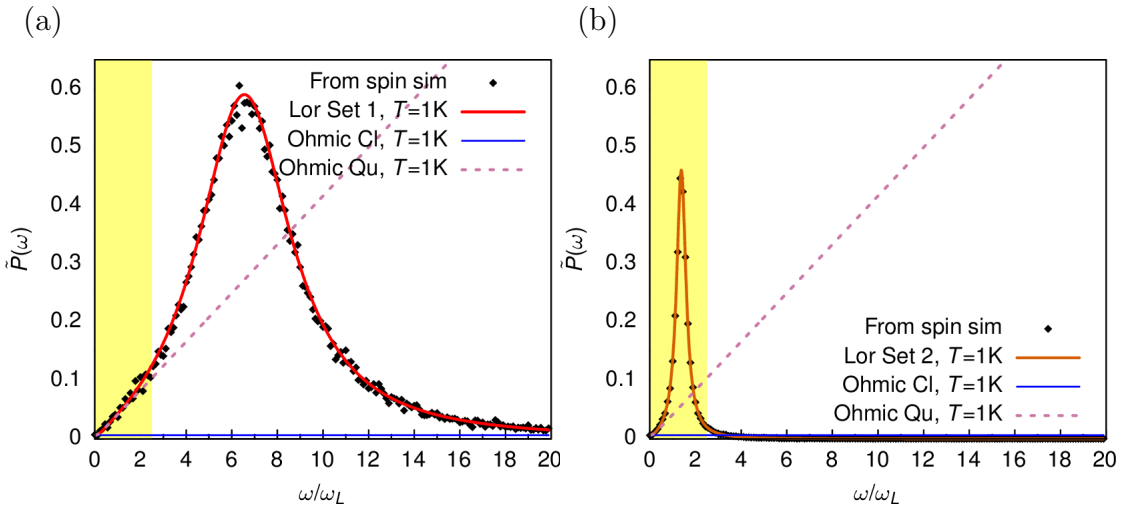

Figure 4.5: A comparison between the Ohmic and Lorentzian type power spectral density (PSD) functions at T=1K. The solid blue and pink dashed lines in both parts show the classical and quantum Ohmic PSD function in equations 4.2.80 and 4.2.79 respectively with $\eta = 0.0208$. The red line in panel (a) shows the Lorentzian PSD in equation 4.2.87 using the parameters in the 'Set 1' column of table 4.1, while in panel (b) the orange line shows the Lorentzian PSD when the parameters in the 'Set 2' column are used. The black diamonds show the average PSD of 50000 samples of noise generated using 4.2.103 with the Lorentzian kernel given in equation 4.2.85. The PSD is determined by the inverse Fourier transform of the autocorrelation of coloured noise using code shown in appendix C.2. The frequency range shaded yellow indicates typical spin dynamics frequencies.

$\mathbf{b}(t)$ vectors. In order to numerically integrate the equation we must consider the time dependence of $\mathbf{V}(t)$. To do this we define

$$\mathbf{W}(t) = \frac{\mathrm{d}\mathbf{V}(t)}{\mathrm{d}t} \tag{4.2.94}$$

and choose the initial values $\mathbf{V}(t_0) = 0$ and $\mathbf{W}(t_0) = 0$. To continue, we consider a variable $\mathbf{Z}(t)$ constructed as the differential equation

$$\mathbf{Z}(t) = \frac{\mathrm{d}\mathbf{W}(t)}{\mathrm{d}t} + \Gamma\mathbf{W}(t) + \omega_0^2\mathbf{V}(t), \tag{4.2.95}$$

which by substitution of equation 4.2.94 becomes

$$\mathbf{Z}(t) = \frac{\mathrm{d}^2\mathbf{V}(t)}{\mathrm{d}t^2} + \Gamma\frac{\mathrm{d}\mathbf{V}(t)}{\mathrm{d}t} + \omega_0^2\mathbf{V}(t). \tag{4.2.96}$$

Writing $\mathbf{V}(t)$ in terms of the frequency domain memory kernel

$$\mathbf{V}(t) = \frac{1}{2\pi}\int_{-\infty}^{t}\mathbf{S}(t')\mathrm{d}t'\int_{\infty}^{\infty}\tilde{K}(\omega)e^{i\omega(t-t')}\mathrm{d}\omega, \tag{4.2.97}$$

shows the first time derivative to be

$$\frac{\mathrm{d}\mathbf{V}(t)}{\mathrm{d}t} = i\omega\mathbf{V}(t), \tag{4.2.98}$$

and the second time derivative to be

$$\frac{\mathrm{d}^2\mathbf{V}(t)}{\mathrm{d}t^2} = -\omega^2\mathbf{V}(t). \tag{4.2.99}$$

This leads to an expression for $\mathbf{Z}(t)$ in terms of $\mathbf{V}(t)$ of

$$\mathbf{Z}(t) = \left(\omega_0^2 - \omega^2 + i\Gamma\omega\right)\mathbf{V}(t), \tag{4.2.100}$$

so that through substitution of $\mathbf{V}(t)$ (equation 4.2.97) and the Lorentzian $\mathbf{K}(\omega)$ (equation 4.2.85)

$$\mathbf{Z}(t) = A\int_{-\infty}^{t}\mathbf{S}(t')\mathrm{d}t'\,\frac{1}{2\pi}\int_{-\infty}^{\infty}e^{i\omega(t-t')}\mathrm{d}\omega = A\mathbf{S}(t), \tag{4.2.101}$$

and by rearranging 4.2.95 the expression for the evolution of $\mathbf{W}(t)$ is found to be

$$\frac{\mathrm{d}\mathbf{W}(t)}{\mathrm{d}t} = -\Gamma\mathbf{W}(t) - \omega_0^2\mathbf{V}(t) + A\mathbf{S}(t). \tag{4.2.102}$$

The stochastic field vector $\mathbf{b}(t)$ required to simulate the dissipative dynamics must have statistics which obey the quantum fluctuation dissipation theorem (equation 2.3.7). The noise generation algorithm described by Schmidt et. al. [12] can be used to generate coloured noise from a desired power spectral density, meeting the requirement if equation 4.2.62 is used for this purpose. The stochastic field can therefore be generated according to

$$b_\alpha = \int_{-\infty}^{\infty}\mathrm{d}t' F(t-t')\xi_\alpha(t'), \tag{4.2.103}$$

for the $\alpha = x, y, z$ components of the vector, where ξ_α is white noise generated through a normal Gaussian distribution centred at 0, and $F(t-t')$ is the Fourier transform of the square root of the ratio of the previously derived power spectrum $\tilde{P}(\omega)$ (equation 4.2.62) to spin length S_0

$$F(t-t') = \frac{1}{2\pi}\int_{-\infty}^{\infty}\mathrm{d}\omega\sqrt{\frac{\tilde{P}(\omega)}{S_0}}e^{-i\omega(t-t')}, \tag{4.2.104}$$

where S_0 allows for the simulation of macrospins (where multiple electrons contribute to the spin under study), and acts to scale the magnitude of fluctuations so that spins of a smaller length respond more strongly to individual fluctuations. This equation can be implemented using a fast Fourier transform algorithm. The set of coupled first order differential equations 4.2.93, 4.2.94 and 4.2.102 can now be solved to simulate the single spin dynamics with a Lorentzian kernel. These dynamics are referred to as semi-classical, as the noise takes a quantum character through its power spectral density.

To simulate the dynamics predicted by an Ohmic coupling function, a classical form of equation 4.2.77 is used instead. This is the the LLG equation

$$\frac{\mathrm{d}\mathbf{S}}{\mathrm{d}t} = -|\gamma_e| \left(\mathbf{S} \times \mathbf{B}_{\text{eff}} - \eta \mathbf{S} \times \frac{\mathrm{d}\mathbf{S}}{\mathrm{d}t} \right), \tag{4.2.105}$$

where

$$\mathbf{B}_{\text{eff}} = \mathbf{B}_{\text{ext}} + \mathbf{b}(t), \tag{4.2.106}$$

and equations 4.2.103 and 4.2.104 are once again used to generate the noise, but this time the power spectral density $\tilde{P}(\omega)$ used is the high temperature approximation given by 4.2.80 (i.e. for comparison to a Lorentzian kernel, the LLGB dynamics will be simulated). The LLG equation can be readily converted into the Landau-Lifshitz equation following [10, 13] and evaluated by numerical integration of

$$\frac{\mathrm{d}\mathbf{S}}{\mathrm{d}t} = \gamma' \mathbf{S} \times \mathbf{B}_{\text{eff}} - \lambda \mathbf{S} \times (\mathbf{S} \times \mathbf{B}_{\text{eff}}), \tag{4.2.107}$$

where $\gamma' = \frac{|\gamma_e|}{1+|\gamma_e|^2 \eta^2 |\mathbf{S}|^2}$ and $\lambda = \gamma' |\gamma_e| \eta |\mathbf{S}|$. This equation is fully classical, and has been used to simulate the dynamics for the figures showing Ohmic single-spin dynamics that follow.

In what follows, simulations of the dynamics of a single spin according to the theories presented will be shown. To recap, the semi-classical dynamics of a single spin will be simulated according to equation 4.2.93 using thermal noise generated with power spectral density given by equation 4.2.87. This will be compared with the classical dynamics of a single spin which will be simulated according to equation 4.2.107 with thermal noise power spectral density given by equation 4.2.80. As in the previous figures, the results are shown at temperatures of T =1K and T =200K. Results will be shown for spin lengths of $S_0 = 1\hbar/2$ and $S_0 = 200\hbar/2$. All simulations are performed with an external field of $B_z = 10T$. In figure 4.6, the top row of panels show a sample of single spin s_z (red line) and s_x (green line) dynamics predicted using the semi-classical Lorentzian dynamics with parameter Set 1 with (a) temperature $T = 1K$ and spin length $S_0 = 1\hbar/2$, and (b) $T = 200K$ and $S_0 = 200\hbar/2$. The bottom row of panels show a sample of single spin s_z (orange line) and s_x (pink line) dynamics predicted using Lorentzian dynamics with parameter Set 2 with (c) $T = 1K$ and $S_0 = 1\hbar/2$, and (d) $T = 200K$ and $S_0 = 200\hbar/2$. In all panels, a sample of single spin s_z (blue line) dynamics predicted using the classical Ohmic dynamics with damping parameter, temperature and spin length corresponding to the Lorentzian plots is also shown for comparison. It is clear that low temperature has strong effect on the dynamics predicted by the Lorentzian coupling, when compared to the Ohmic case. This is to be expected, as the power spectral density of the quantum mechanical stochastic fluctuations remains finite at

absolute zero in contrast to the classical result, in which the PSD and by extension magnitude of noise is directly proportional to temperature. The finite noise in Lorentzian systems at absolute zero is due to quantum zero point fluctuations. At higher temperature, the Lorentzian dynamics for Set 1 are almost equivalent to those predicted by the LLGB equation. For parameter Set 2, the memory effect has a significant effect on the dynamics at both temperatures, and the rapid drop in PSD within the range of frequencies comparable to ω_L (see figures 4.4 and 4.5) result in a smoother dynamics as high frequency fluctuations do not contribute to the dynamics.

Figure 4.7 shows the ensemble averaged spin relaxation dynamics averages over 500 samples. Panel (a) shows low temperature, small spin length dynamics, and makes clear that the quantum noise at low temperature has a strong negative effect on the capability of the spin to align with the external field. Panel (b) shows that at high temperatures, the quantum character of the reservoir can be neglected. In addition to this, it becomes clear that the damping predicted by the Lorentzian coupling with parameter Set 2, is significantly stronger than that predicted by the LLG equation.

Figure 4.8 shows the average value of equilibrated spins resulting from numerical integration of equation 4.2.93 as a function of temperature. The plotted values are determined from data generated at different temperatures in the same manner as that shown in figure 4.7, and as such take the same general shape. The data is fit in gnuplot using the function

$$f(t) = \langle s_{z,f} \rangle \left(1 - e^{-\frac{t}{\tau}}\right) \tag{4.2.108}$$

to determine the equilibrated z-component of spin $\langle s_{z,f} \rangle$ and the time constant τ. In panel (a) where $S_0 = \hbar/2$, the average alignment of the spin to the external field at equilbrium is shown to be much lower for a quantum reservoir than with a classical reservoir for temperatures in the proximity of absolute zero. This is due to the quantum zero point noise which prevents the spin from aligning with the external field at low temperatures, whereas in the classical case the fluctuations vanish at 0K. In panel (b) it is seen that the character of noise has neglible effect on the equilibrium when $S_0 = 200\hbar/2$, indicating that the quantum zero point noise has little effect on the equilibrium state of spins with a large spin length. Figure 4.9, shows how the time constant τ varies with temperature for (a) spin length $S_0 = 1\hbar/2$ and (b) $S_0 = 200\hbar/2$. In all cases other than for the Set 2 Lorentzian dynamics with $S_0 = 1\hbar/2$, it is clear that the rate at which equilibrium is achieved increases with temperature. This is because the dynamics of the system are sampled more quickly owing to the larger fluctuations which change the spin direction by larger amounts within the same period of time. At low temperatures for $S_0 = 1\hbar/2$ shown in panel (b), the equilibration times of the three dynamics

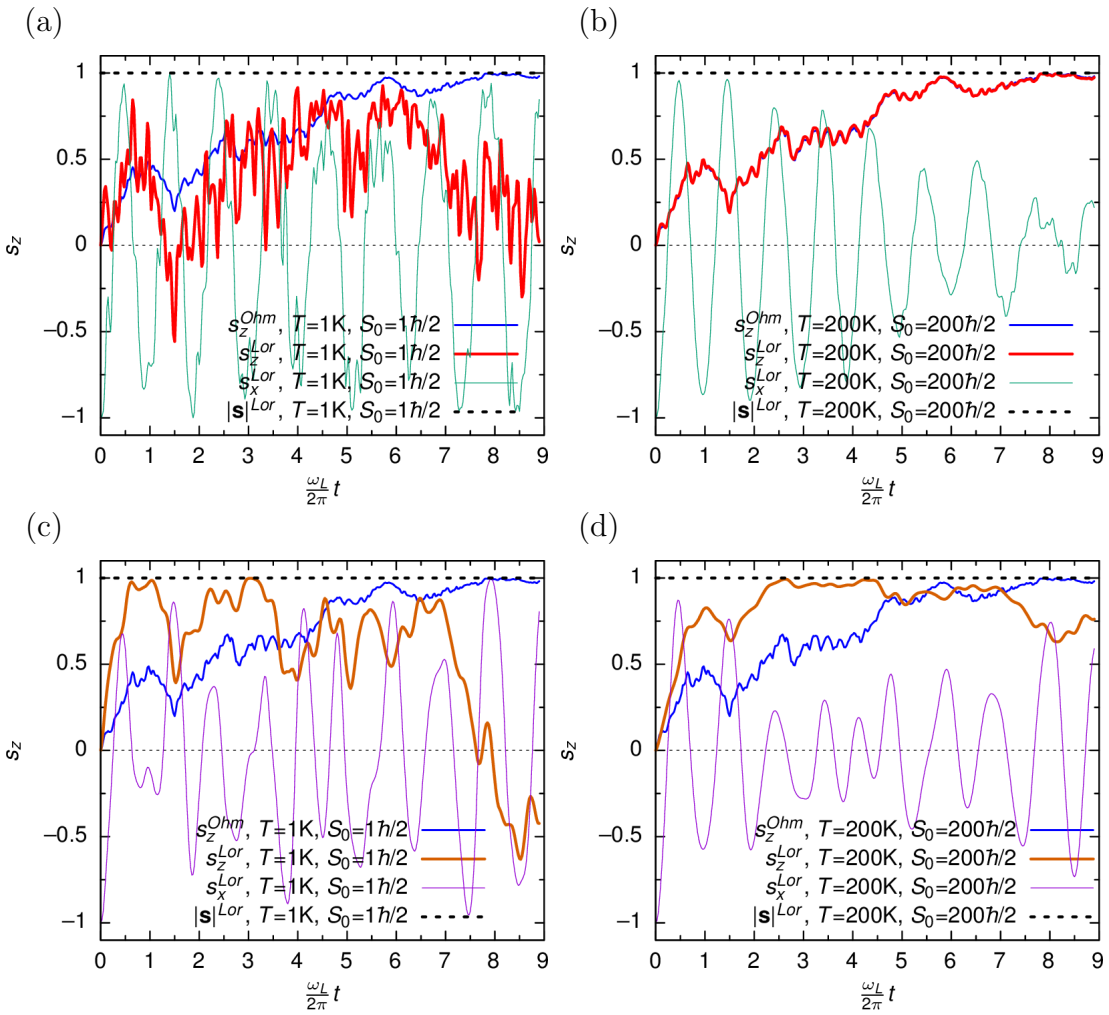

Figure 4.6: Samples of the dynamics of a single spin in a $B_z = 10T$ external field predicted by equation 4.2.93. The red and green lines in panels (a) and (b) show the s_z and s_x dynamics respectively when using the Lorentzian coupling function C_ω^{Lor} and Lorentzian parameter Set 1 (given in table 4.1). The orange and pink lines in panels (c) and (d) show Lorentizian s_z and s_x dynamics respectively with parameter Set 2. In all panels the blue line shows the s_z dynamics predicted by the Ohmic coupling function (through equation 4.2.107) with $\eta = 0.0208$ and using a white noise with power spectral density given by equation 4.2.80. The absolute spin value $|\mathbf{s}| = \sqrt{s_x^2 + s_y^2 + s_z^2}$ is plotted using a black-dashed line. Panels (a) and (c) show the dynamics for a spin length of $S_0 = 1\hbar/2$ at temperature $T = 1K$, whereas panels (b) and (d) show the dynamics when $S_0 = 200\hbar/2$ and $T = 200K$. To aid comparison, in all calculations shown, the same samples of Gaussian noise $\boldsymbol{\xi}$ are used through equation 4.2.103 to generate noise with statistics appropriate to the spin length, temperature and Lorentzian parameters for each direction of $\mathbf{s}$.

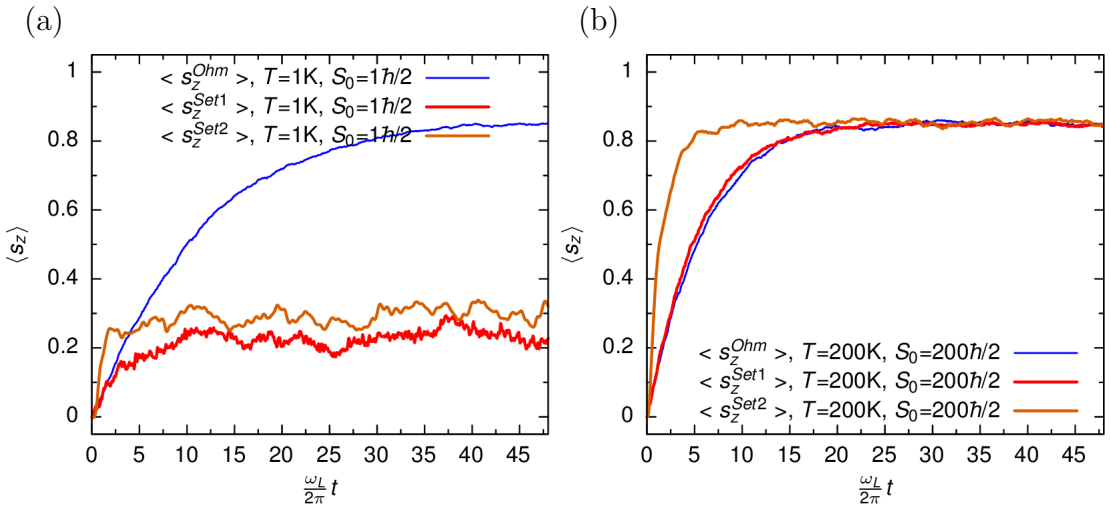

Figure 4.7: Ensemble averaged $\langle s_z \rangle$ relaxation dynamics of 500 traces of a single spin in a $B_z = 10T$ external field. The red and orange lines shows the dynamics according to equation 4.2.93 with the Lorentzian coupling function C_ω^{Lor} for parameter Set 1 and Set 2 respectively in table 4.1. The blue line shows the $\langle s_z \rangle$ dynamics with the Ohmic coupling function (through equation 4.2.107) applied, using a white noise thermal field with power spectral density given by equation 4.2.80 with $\eta = 0.0208$. Panel (a) shows the dynamics for a spin length of $S_0 = 1\hbar/2$ at temperature $T = 1K$, whereas panel (b) uses $S_0 = 200\hbar/2$ and $T = 200K$.

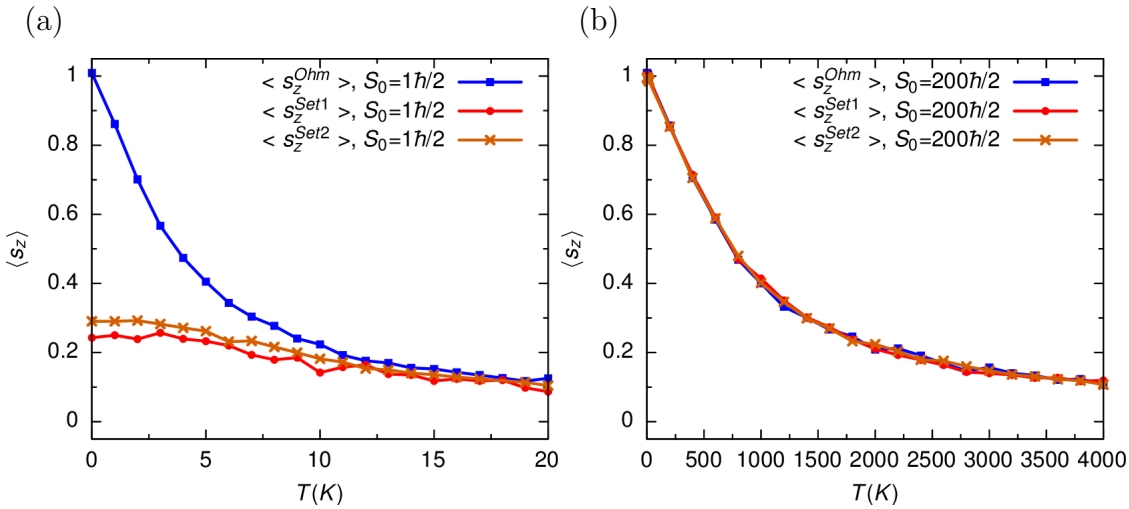

Figure 4.8: Equilibrated $\langle s_z \rangle$ vs temperature T for a single spin in a $B_z = 10T$ external field. The plotted points show the $\langle s_z \rangle$ value after equilibration determined by fitting equation 4.2.108 to the ensemble average of single spin dynamics determined for 48 precessions after initiation of the spin direction in the xy-plane. The ensemble consists of 500 samples of the dynamics per plotted point. The red circles and orange crosses show the value predicted by equation 4.2.93 with the Lorentzian coupling function C_ω^{Lor} (equation 4.2.82) for parameter Set 1 and Set 2 in table 4.1 respectively. The blue squares show the values predicted by the Ohmic coupling function with $\eta = 0.0208$ through 4.2.107 using a white noise thermal field characterised by the power spectral density 4.2.80. In panel (a) the spin length is $S_0 = 1\hbar/2$ while in panel (b) the spin length is $200\hbar/2$.

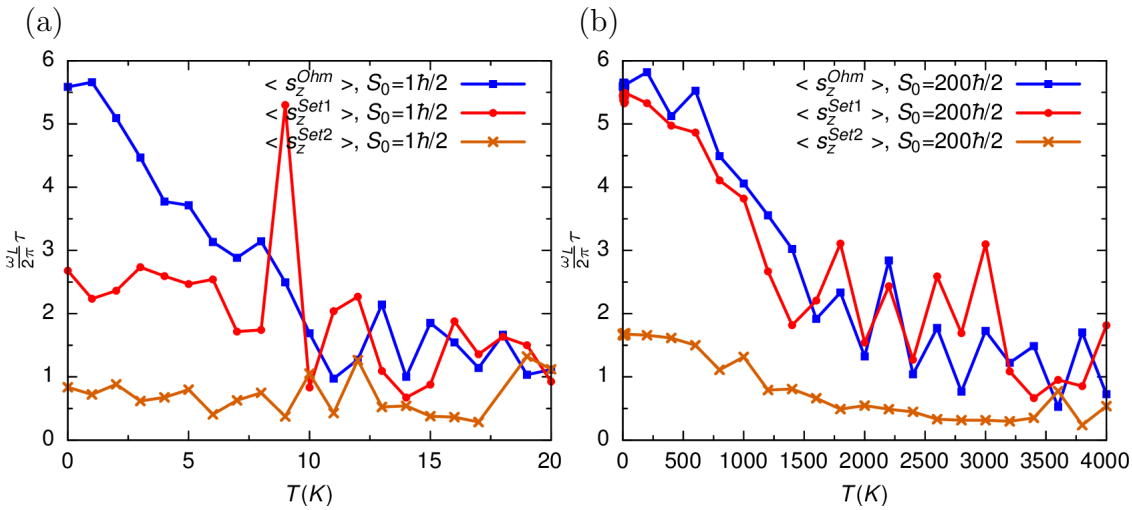

Figure 4.9: Time constant of equilibration τ vs temperature T for a single spin in a $B_z = 10T$ external field. The plotted points show the number of precessions that occur in the time τ that it takes for the average spin direction to reach 63.2% of its equilibrated value after initiation in the xy-plane. The value is determined by fitting equation 4.2.108 to the ensemble average of single spin dynamics determined for 48 precessions after initiation of the spin direction in the xy-plane. The ensemble consists of 500 samples of the dynamics per plotted point. The red circles and orange crosses show the value predicted by equation 4.2.93 with the Lorentzian coupling function C_ω^{Lor} (equation 4.2.82) for parameter Set 1 and Set 2 in table 4.1 respectively. The blue squares shows the values from the average of 500 samples of the dynamics using an Ohmic coupling function with classical noise. In panel (a) the spin length is $S_0 = 1\hbar/2$ while in panel (b) the spin length is $200\hbar/2$.

show different rates, with Set 2 Lorentzian dynamics occuring most quickly, Set 1 dynamics occuring approximately three times more slowly, and Ohmic dynamics occuring slowest, taking approximately six times more slowly than for Set 2. This indicates that the quantum zero point noise plays some role in the equilibration rate. However in panel (b) the equilibration rate of Ohmic and Set 1 dynamics are equivalent, occuring three times more slowly than for Set 2. This is because the fluctuations experienced in Set 2 dynamics are of lower frequency, and the damping process is therefore less likely to be impeded by a large impulse counter to the equilibrium state as the system traverses towards it.

4.3 Discussion

As discussed in section 2.4, the work discussed in this chapter was motivated by the inability of atomistic spin dynamics (ASD) software to describe the magnetisation vs temperature curves measured experimentally, which can be accurately described by the analytical curves of Kuz'min [14]. It was pointed out by Evans et. al., that simulations utilising the LLGB equation do not result in the correct experimentally reproducable magnetisation vs temperature behaviour of elemental ferromagnets [15], and are also unable to recover the ultrafast demagnetisation behaviour of nickel shown in [16]. Within that work, the use of a temperature rescaling method was demonstrated to recover the correct behaviour from ASD. This method works to recover the experimental behaviour by countering an overestimation in the simulated thermal fluctuations thought to results from the classical (as opposed to quantum) nature of their inclusion, but lacks a microscopic motivation for the approach taken or clear reasoning as to why the specific form of temperature mapping between simulated and experimental behaviour is so successful.

The VAMPIRE ASD software used in that study takes the approach outlined by Brown [10] to simulate the Landau-Lifshitz-Gilbert (LLG) equation, with a stochastic thermal field introduced into the effective magnetic field, which is motivated by Brown through the fluctuation dissipation theorem, and outlined using a Langevin dynamics approach. In order to simulate correct physical behaviour, Langevin equations must obey the fluctuation dissipation relation (section 2.3.2) due to the fact that the source of thermal noise forces and damping is the same. Whilst the Landau-Lifshitz-Gilbert-Brown (LLGB) approach taken by commonly used ASD softwares does contain both damping and stochastic field terms, the precise relationship between the two is not explicitly considered. Instead, it is assumed that the stochastic field has a completely random white noise profile (equation 2.2.17) [17, 2, 18, 19, 20, 21, 22]. This limits the description to one where the thermal force at a given time is completely uncorrelated with the thermal force at any other time. In actuality, this is an unphysical description, but under many conditions (particularly at high temperatures where the timescale of noise correlations become neglible) acts as a good approximation to the actual behaviour which necessarily requires the use of a coloured noise. A byproduct of this approximation is a significant reduction in computational requirements, although it sacrifices a full description of interaction with the environment at time scales small enough for those autocorrelations to be non-neglible.

The approximation made to the dynamics is a simplification that can be expected to lead to discrepancies between experimental and numeric studies under specific circumstances. In the case of ultrafast demagnetisation, the dynamics occur on a femtosecond timescale. The demagnetisation itself is a sub-picosecond phe-

nomena [16], while remagnetisation and precession dynamics occur on the timescale of picoseconds (see section 5.4.2). In ordinary circumstances, the damping of a ferromagnetic system takes place over a much longer time scale than the precession, and therefore either dynamic process can be considered independently of the other during simulations. However, during ultrafast demagnetisation the effect of damping on the time evolution of the systems magnetisation will have a large effect over the subsequent dynamics, and therefore indicates a possible reason for the failure of ASD to simulate this effect [15] (without the inclusion of the temperature rescaling method previously mentioned) as being due to a poor approximation to the true dynamics that satisfies the fluctuation dissipation relation.

There has been interest in the nature of the stochastic thermal field prior to the work shown here (and in the associated work [11]). Previously it has been noted that the stochastic thermal field should have a quantum distribution. Through such a consideration it has been possible to partially reproduce experimental magnetisation vs temperature curves [23, 24, 25, 26]. However, these models fail to capture the non-zero quantum fluctuations of the Bose-Einstein distribution at 0K. This is equivalent to a failure to properly consider the implications of the commutation properties of the quantum bosonic creation and annihilation operators which give rise to the stochastic thermal magnetic field in equation 4.2.46. Judged from the viewpoint of this work, the form of power spectral density enforced in those works is equivalent to that which would be recovered in assuming that the fluctuation dissipation theorem relates the power spectral density to the memory kernel through the non-symmetrised autocorrelation of the thermal field (equation 4.2.57), as opposed to the symmetrised form (equation 4.2.58). That approach misses the quantum ground state contribution of $\hbar\omega/2$, which acts as a stochastic force on the spin system even in proximity to absolute zero temperature. As shown in figure 4.3, a quantum distribution leads to a coloured noise characterised by the memory of previous dynamics (i.e. they have a non-Markovian nature). A previous work has considered the effects of coloured noise on spin dynamics [27], but the fluctuation dissipation theorem is not shown to hold generally, and quantum effects (e.g. zero point fluctuations) are not considered.

Unlike those works, the theory presented in this chapter provides a framework in which the fluctuation disspation relation is automatically met through the reservoir extension to the microscopic (i.e. quantum Heisenberg) model. While the model of spin dynamics presented will always satisfy the fluctuation dissipation relation, it does not always lead to the Landau-Lifshitz-Gilbert form of spin dynamics. This allows for the exploration of alternative, but still potentially physical spin dynamics that deviate from the widely confirmed and accepted LLG model. Historically it has been difficult to deviate from the LLG formalism of spin dynamics due to its dominant ability to explain experimental observations, the lack of alternative de-

scriptions, and a lack of computing power to simulate more complex models. With this new thermodynamically constrained quantum formalism of the dynamics, it should be possible to determine the conditions under which the LLG model fails, and give alternative equations of motion that better describe spin systems under those conditions, overcoming many of the obstacles to a deeper understanding of magnetic systems.

Though the work presented allows the description of more general spin dynamics, certain assumptions and approximations have been made in the presentation of the resultant equations of motion. For example, in this work only the effects of the generalised spin dynamics on a single spin has been considered. This avoids the complexities involved with the many-body problem of keeping track of exchange contribution between large numbers of spins in the lattice. Only the effect of an externally applied magnetic field, and the thermal contribution to the motion of spin are accounted for. Another simplification made is that the numerics of a semi-classical spin were shown rather than for a fully quantum system, allowing the equations of motion to be simulated according to classical numerical methods. In the future it may be possible to apply some of the recent advances in quantum numerics, such as the hierarchical equations of motion approach [28] and/or time-evolving matrix product operators method [29] to efficiently simulate the full non-Markovian quantum dynamics resulting from the Lorentzian coupling proposed. The complexity increases further if a many quantum spin system is considered due to the presence of spin entanglement at low temperatures [30, 31]. To simulate a system beyond a limited number of spins will require advanced quantum numerical algorithms such as the density-matrix renormalization group approach [32] in order to determine realistic approximate solutions. Furthermore, the environment being considered as a reservoir of quantum harmonic oscillators, can only provide a bosonic environment, while a fully generalised treatment of the environment should also consider fermionic modes and will require additional methods of treatment such as that of non-Markovian quantum state diffusion [33] and/or the reaction coordinate mapping approach [34]. A further simplification made is the reduction of the more general tensor coupling quantity $\mathcal{C}_{j,\omega'}$ in the interaction Hamiltonian to an isotropic scalar quantity $C_{j,\omega'}$. This is a reasonable assumption to make for most systems, but is broken in certain transition metal thin films [35] where the Gilbert damping is anisotropic owing to interfacial spin-orbit coupling. It would be possible to account for that anisotropy by retaining the tensor character of the coupling function.

For the choice of an Ohmic coupling constant (i.e. linear in frequency), it is possible to recover Landau-Lifshitz-Gilbert-Brown dynamics. When taking this approach it is found that the fluctuation and dissipation dynamics are Markovian, in that they are not influenced by the historic state of the system. However, consideration of the quantum noise power spectra for the Ohmic coupling case reveals the choice to be

unphysical, as for a physical process, the integrated power spectral density must result in a finite value [36]. This problem is solved by considering Lorentzian type coupling, which can be tuned to have similar properties by appropriate choice of the resonant frequency. Because the coupling reduces to zero in the high frequency limit, this type of coupling is a superior approximation to physically realistic behaviour. While other choices of coupling function could be chosen with this same property (e.g. Gaussian), for the special Lorentzian choice, numerical integration is made easier. For example, in equation 4.2.102, the memory effect can be absorbed in to the ordinary differential equation without having to integrate across the entire history for every advance in time.

It has recently been shown that the form of coupling function is suggested by the experimentally measurable density of states, and well modelled by the Lorentzian framework outlined here [37]. Despite this, significant work will be required in the development of numerical methods (in both classical, but particularly in the quantum mechanical description) before the simulation of bulk magnetic systems can be performed.

4.4 Summary

In this chapter a general quantum spin dynamics equation has been outlined, and shown to predict the precession of spins in a magnetic field, along with a damping that satisfies the full quantum fluctuation dissipation theorem. Specific forms of spin dynamics can be found by choice of a coupling factor $C_{j,\omega'}$ between the spin system and harmonic oscillator reservoir, and two choices and their resulting dynamics were shown. For an Ohmic coupling, the dynamics were shown to reduce to the Landau-Lifshitz-Gilbert-Brown dynamics, while a Lorentzian choice also approximates LLGB dynamics in the high temperature and high resonance frequency limit, which is representative of common experimental systems where the precession is slow in comparison with the fluctuations that result from interaction with the environment. The Lorentzian choice leads to a non-Markovian (memory driven) dynamics and a coloured noise stochastic field which result in behaviour more difficult to solve analytically or numerically than the LLGB case. Despite this it has been possible to perform simulations of a single spin coupled to the (bosonic) harmonic oscillator environment, and thereby identify a significant effect on the dynamics and equilibrium state at low temperatures due to quantum zero point fluctuations.

References

[1] V. P. Antropov, M. I. Katsnelson, M. van Schilfgaarde, and B. N. Harmon. $\mathit{Ab}\mathit{}\mathit{Initio}$ Spin Dynamics in Magnets. *Physical Review Letters*, 75(4):729–732, July 1995.

[2] V. P. Antropov, M. I. Katsnelson, B. N. Harmon, M. van Schilfgaarde, and D. Kusnezov. Spin dynamics in magnets: Equation of motion and finite temperature effects. *Physical Review B*, 54(2):1019–1035, July 1996.

[3] A. Rebei and G. J. Parker. Fluctuations and dissipation of coherent magnetization. *Physical Review B - Condensed Matter and Materials Physics*, 67(10):14, 2003.

[4] Bruno Huttner and Stephen M. Barnett. Quantization of the electromagnetic field in dielectrics. *Physical Review A*, 46(7):4306–4322, October 1992.

[5] Stephen M. Barnett and P. M. Radmore. *Methods in Theoretical Quantum Optics*. Oxford University Press, New York, 1 edition, 1997.

[6] David J. Griffiths. *Introduction to Quantum Mechanics*. Cambridge University Press, Cambridge, United Kingdom, 2nd edition edition, April 2004.

[7] Kenneth Franklin Riley, Michael Paul Hobson, and Stephen John Bence. *Mathematical Methods for Physics and Engineering: A Comprehensive Guide*. Cambridge University Press, Cambridge, January 1998.

[8] R Kubo. The fluctuation-dissipation theorem. *Reports on Progress in Physics*, 29(1):306, January 1966.

[9] T. G. Philbin. Quantum dynamics of the damped harmonic oscillator. *New Journal of Physics*, 14, August 2012.

[10] W. Brown. Thermal fluctuation of fine ferromagnetic particles. *IEEE Transactions on Magnetics*, 15(5):1196–1208, September 1979.

[11] J. Anders, C. R. J. Sait, and S. A. R. Horsley. Quantum Brownian motion for magnets. *New Journal of Physics*, 24(3):033020, March 2022.

[12] Julian Schmidt, Alex Meistrenko, Hendrik van Hees, Zhe Xu, and Carsten Greiner. Simulation of stationary Gaussian noise with regard to the Langevin equation with memory effect. *Physical Review E*, 91(3):032125, March 2015.

[13] T.L. Gilbert. Classics in Magnetics A Phenomenological Theory of Damping in Ferromagnetic Materials. *IEEE Transactions on Magnetics*, 40(6):3443–3449, November 2004.

[14] M. D. Kuz'min. Shape of Temperature Dependence of Spontaneous Magnetization of Ferromagnets: Quantitative Analysis. *Physical Review Letters*, 94(10):107204, March 2005.

[15] R. F. L. Evans, U. Atxitia, and R. W. Chantrell. Quantitative simulation of temperature-dependent magnetization dynamics and equilibrium properties of elemental ferromagnets. *Physical Review B*, 91(14):144425, April 2015.

[16] E. Beaurepaire, J. C. Merle, A. Daunois, and J. Y. Bigot. Ultrafast spin dynamics in ferromagnetic nickel. *Physical Review Letters*, 76(22):4250–4253, May 1996.

[17] A. Lyberatos, D. V. Berkov, and R. W. Chantrell. A method for the numerical simulation of the thermal magnetization fluctuations in micromagnetics. *Journal of Physics: Condensed Matter*, 5(47):8911, November 1993.

[18] José Luis García-Palacios and Francisco J. Lázaro. Langevin-dynamics study of the dynamical properties of small magnetic particles. *Physical Review B - Condensed Matter and Materials Physics*, 58(22):14937–14958, 1998.

[19] Ulrich Nowak. Classical Spin Models. In *Handbook of Magnetism and Advanced Magnetic Materials*, pages 832–850. John Wiley & Sons, Ltd, 2007.

[20] R. F.L. Evans, W. J. Fan, P. Chureemart, T. A. Ostler, M. O.A. Ellis, and R. W. Chantrell. Atomistic spin model simulations of magnetic nanomaterials. *Journal of Physics Condensed Matter*, 26(10), March 2014.

[21] Olle Eriksson, Anders Bergman, Lars Bergqvist, and and Johan Hellsvik. *Atomistic Spin Dynamics: Foundations and Applications*. Oxford University Press, New York, April 2017.

[22] Johan Hellsvik, Danny Thonig, Klas Modin, Diana Iuşan, Anders Bergman, Olle Eriksson, Lars Bergqvist, and Anna Delin. General method for atomistic spin-lattice dynamics with first-principles accuracy. *Physical Review B*, 99(10):104302, March 2019.

[23] Joseph Barker and Gerrit E. W. Bauer. Semiquantum thermodynamics of complex ferrimagnets. *Physical Review B*, 100(14):140401, October 2019.

[24] C. H. Woo, Haohua Wen, A. A. Semenov, S. L. Dudarev, and Pui-Wai Ma. Quantum heat bath for spin-lattice dynamics. *Physical Review B*, 91(10):104306, March 2015.

[25] Lars Bergqvist and Anders Bergman. Realistic finite temperature simulations of magnetic systems using quantum statistics. *Physical Review Materials*, 2(1):013802, January 2018.

[26] S. V. Halilov, H. Eschrig, A. Y. Perlov, and P. M. Oppeneer. Adiabatic spin dynamics from spin-density-functional theory: Application to Fe, Co, and Ni. *Physical Review B*, 58(1):293–302, July 1998.

[27] U. Atxitia, O. Chubykalo-Fesenko, R. W. Chantrell, U. Nowak, and A. Rebei. Ultrafast Spin Dynamics: The Effect of Colored Noise. *Physical Review Letters*, 102(5):057203, February 2009.

[28] Akihito Kato and Yoshitaka Tanimura. Hierarchical Equations of Motion Approach to Quantum Thermodynamics. In Felix Binder, Luis A. Correa, Christian Gogolin, Janet Anders, and Gerardo Adesso, editors, *Thermodynamics in the Quantum Regime: Fundamental Aspects and New Directions*, Fundamental Theories of Physics, pages 579–595. Springer International Publishing, Cham, 2018.

[29] A. Strathearn, P. Kirton, D. Kilda, J. Keeling, and B. W. Lovett. Efficient non-Markovian quantum dynamics using time-evolving matrix product operators. *Nature Communications*, 9(1):3322, December 2018.

[30] M. C. Arnesen, S. Bose, and V. Vedral. Natural Thermal and Magnetic Entanglement in the 1D Heisenberg Model. *Physical Review Letters*, 87(1):017901, June 2001.

[31] Guo-Feng Zhang and Shu-Shen Li. Thermal entanglement in a two-qubit Heisenberg XXZ spin chain under an inhomogeneous magnetic field. *Physical Review A*, 72(3):034302, September 2005.

[32] U. Schollwöck. The density-matrix renormalization group. *Reviews of Modern Physics*, 77(1):259–315, April 2005.

[33] Mi Chen and J. Q. You. Non-Markovian quantum state diffusion for an open quantum system in fermionic environments. *Physical Review A*, 87(5):052108, May 2013.

[34] Philipp Strasberg, Gernot Schaller, Neill Lambert, and Tobias Brandes. Nonequilibrium thermodynamics in the strong coupling and non-Markovian regime based on a reaction coordinate mapping. *New Journal of Physics*, 18(7):073007, July 2016.

[35] L. Chen, S. Mankovsky, S. Wimmer, M. a. W. Schoen, H. S. Körner, M. Kronseder, D. Schuh, D. Bougeard, H. Ebert, D. Weiss, and C. H. Back. Emergence of anisotropic Gilbert damping in ultrathin Fe layers on GaAs(001). *Nature Physics*, 14(5):490–494, May 2018.

[36] Shlomo Engelberg. *Random Signals and Noise: A Mathematical Introduction*. CRC Press, Florida, 1 edition, October 2006.

[37] S. Nemati, C. Henkel, and J. Anders. Coupling function from bath density of states. *Europhysics Letters*, 139(3):36002, July 2022.

Chapter 5

Synthetic Ferrimagnets

5.1 Introduction

Transition metal (TM) synthetic ferrimagnets (SFi's) have gained interest for their potential as media for all optical switching (AOS) magnetic recording applications due to their low cost and highly tunable magnetic properties. Recent work identified Ni_3Pt/Ir/Co as one such material showing helicity independent all optical switching (HI-AOS) over a broad temperature range [1]. Here the properties of the related transition metal SFi [Ni/Pt]/Ir/Co and reference samples of its constituent ferromagnetic [Ni/Pt] and Co layers will be examined through the use of wide field Kerr microscopy (WFKM), X-ray magnetic circular dichroism (XMCD), vibrating sample magnetometry (VSM), superconducting quantum interference device (SQUID) magnetometry and time-resolved magneto optical Kerr effect pump-probe measurements. In this chapter reference samples of the component layers of Ni_3Pt alloy and [Ni/Pt] multilayer samples will be examined, and the results compared with those for a [Ni/Pt] based SFi.

In the WFKM measurements shown in this chapter, the polar coil shown in figure 3.2 was used to ensure a true remanence state when the supplied voltage is removed. This is not the case for the Evico perpendicular electromagnet which retains a remanent field when the voltage is removed. The polar coil is limited to a field of 104mT which can otherwise be far surpassed through the use of the perpendicular electromagnet which can supply up to 600mT in a geometry suited to optical pumping experiments. Details of the WFKM measurements are given in section 3.2 and result in images showing magnetic contrast in the surface of a material. The evidence for AOS in a material can be determined by comparison of the change in optically induced magnetic contrast to that seen when switching events are initiated by the use of an applied magnetic field. Therefore an understanding of the field induced Kerr signal is a prerequisite to understanding the effect of optical excitation.

The SQUID measurements shown in this chapter were performed by Dr. Jade

Scott at Queens University Belfast (QUB).

The XMCD measurements shown were taken at the Advanced Light Source on beamtime van der Laan - ALS-DXR-0056 (September 2021). The measurements were performed remotely by David G. Newman, Jade N. Scott and Mąciej Dąbrowski, with the on-site assistance of Alpha T. N'Diaye, Christoph Klewe and Padraic Shafer.

The samples studied using these methods are shown in table 5.1. These samples were sputter deposited at a pressure of 10^{-3} Torr in an Ar^{+} environment at room temperature by the group at QUB onto either c-plane sapphire (Al_2O_3) or silicon (Si/SiO2) wafer substrates. The multilayer structure of [Ni/Pt] improves the perpendicular magnetic anisotropy (PMA) compared to the previously studied Ni_3Pt alloy, allowing the entire deposition process to take place at RT. The Ni_3Pt layer required deposition at elevated temperature in order to retain a strong PMA, leading to a two stage growth process, which in the samples shown here, is simplified to a single stage continuous sputtering. Compared to the SFi based on an alloyed layer, the antiferromagnetic type interlayer exchange coupling (IEC) mediated by the Ir is enhanced, which is thought to be a requirement for achieving AOS with fewer laser pulses [2]

Sample name	Substrate	Composition (thickess in nm)
Cobalt reference	Si/SiO2	Ta(5)/Ir(3)/Co(1)/Ir(3)/Ta(4)
Ni_3Pt alloy	Si/SiO2	Ta(5)/Ni_3Pt(11)/Ta(9)
Ni/Pt Reference A	Al_2O_3	Pt(5)/6x[Ni(0.6)/Pt(0.3)]/Pt(5)
Ni/Pt Reference B	Al_2O_3	Pt(5)/6x[Ni(0.6)/Pt(0.25)]/Pt(5)
SFi Sample A	Al_2O_3	Pt(5)/5x[Ni(0.6)/Pt(0.3)]/Ni(0.6)/Ir(0.4)/Co(0.8)/Ir(3)
SFi Sample B	Al_2O_3	Pt(5)/5x[Ni(0.6)/Pt(0.25)]/Ni(0.6)/Ir(0.4)/Co(0.8)/Ir(3)

Table 5.1: A table to show the substrate and stack of samples studied in chapter 5.

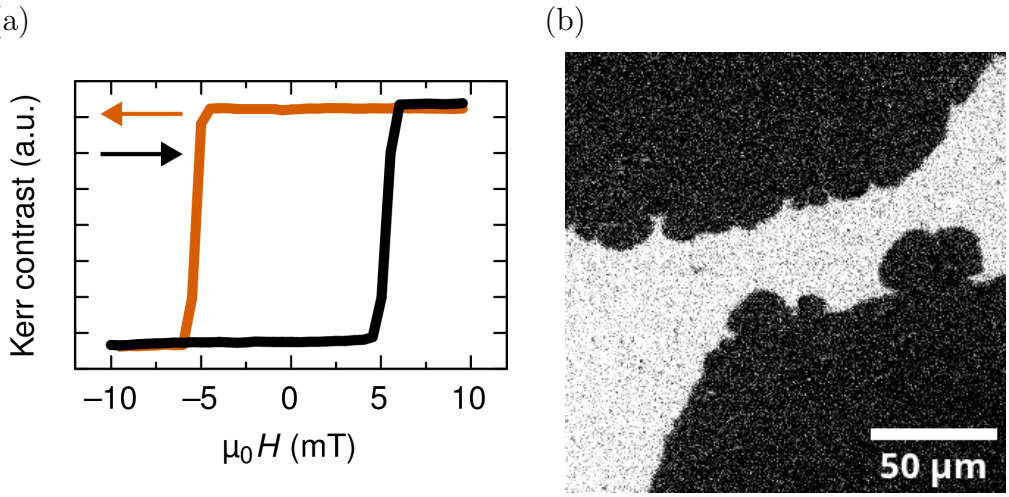

Figure 5.1: Wide field Kerr microscope (WFKM) data of the Co reference layer at room temperature. Part (a) shows the hysteresis loop determined from the average greyscale value of WFKM images taken as the applied field is swept from positive to negative (orange curve) and then from negative to positive (black curve) in the out-of-plane direction. Part (b) shows a WFKM image in which domains form at the switching field (approximately 5.5mT).

5.2 Characterisation

In order to interpret the results of optical exposure of the SFi samples, it will be important to understand the magnetic properties of the samples and their constituent ferromagnetic layers. Each of the samples in table 5.1 were studied using a number of magnetic characterisation techniques, and the results of those studies are shown in what follows.

5.2.1 Cobalt Layer

For comparison with the full SFi stack, a single cobalt reference layer was examined with stack composition given by Si/SiO2/Ta(5nm)/Ir(3nm)/Co(1nm)/Ir(3nm)/Ta(4nm). Similar thin cobalt layers were used not only for the Ni/Pt multilayer SFi stacks, but also for the Ni_3Pt alloy SFi stacks, allowing further comparison.

Figure 5.1 shows the room temperature characterisation of the cobalt layer using WFKM techniques. Panel (a) shows the hysteresis loop of the cobalt layer determined through the analysis of WFKM data and shows a square loop, indicating the sample will remain saturated at remanence in the out-of-plane direction with small coercivity of approximately 5.5mT. In panel (b) the domains coloured in black are shown to have size on the order of 100μm, with domain walls that take an appearance reminiscent of splattered ink.

Figure 5.2 shows VSM data from the cobalt reference layer at room temperature. In panel (a) the field is applied out-of-plane giving rise to a square loop. In this panel, the magnetisation is poorly sampled, as can be seen by comparison to figure 5.1b

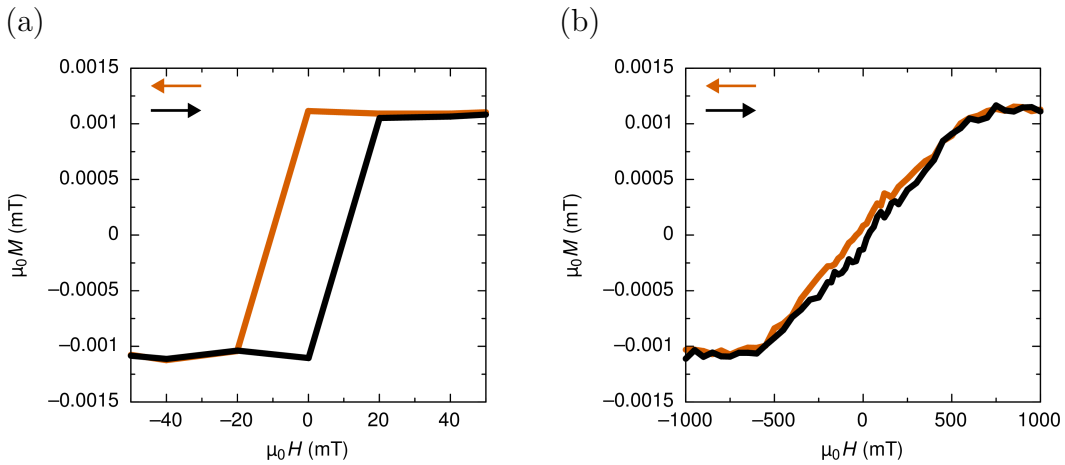

Figure 5.2: Vibrating Sample Magnetometer (VSM) M vs. H loops of the Co reference layer with the **H** field applied out-of-plane (a) and in-plane (b) with respect to the sample. The black curve tracks the path of the magnetisation as the applied field is swept from negative to positive, and the orange curve tracks the subsequent reverse field sweep .

which shows that the 20mT step between points is too large to capture the correct shape of the hysteresis, and therefore it is not possible to identify the precise value of coercive field. Despite this it is clear that the saturation field is less than 20mT. The saturation magnetisation of the cobalt layer can be seen to be approximately 1.1×10^{-3} mT. In panel (b) the field is applied in-plane. The in-plane saturation field is on the order of 600mT, significantly greater than the out-of-plane saturation field. Furthermore in-plane magnetisation is lost at remanence indicating a strong PMA.

5.2.2 Ni_3Pt Alloy

In order to aid comparison with the Ni_3Pt alloy based synthetic ferrimagnets reported in [1], a Ni_3Pt reference layer was characterised. The full stack of this reference sample is given by Si/SiO2/Ta(5nm)/Ni_3Pt(11nm)/Ta(9nm).

Figure 5.3 shows the room temperature characterisation of the Ni_3Pt layer using WFKM techniques. Panel (a) shows the hysteresis loop of the layer determined through the analysis of WFKM data and shows a square loop, indicating the sample will remain saturated at remanence in the out-of-plane direction with coercivity of approximately 28mT. In panel (b) the domains coloured in white are shown to have size on the order of 20 µm. The domains are not completely solid in colour, showing fine features in proximity to the domain walls.

Figure 5.4 shows RT VSM data for the Ni_3Pt reference layer. In panel (a) the field is applied out-of-plane giving rise to a square loop with 20mT coercivity. The moment of the thin film can be seen to be approximately 10^{-4} emu. In panel (b) the field is applied in-plane. The in-plane saturation field is on the order of 800mT, significantly greater than the out-of-plane saturation field of 30mT. The net in-plane

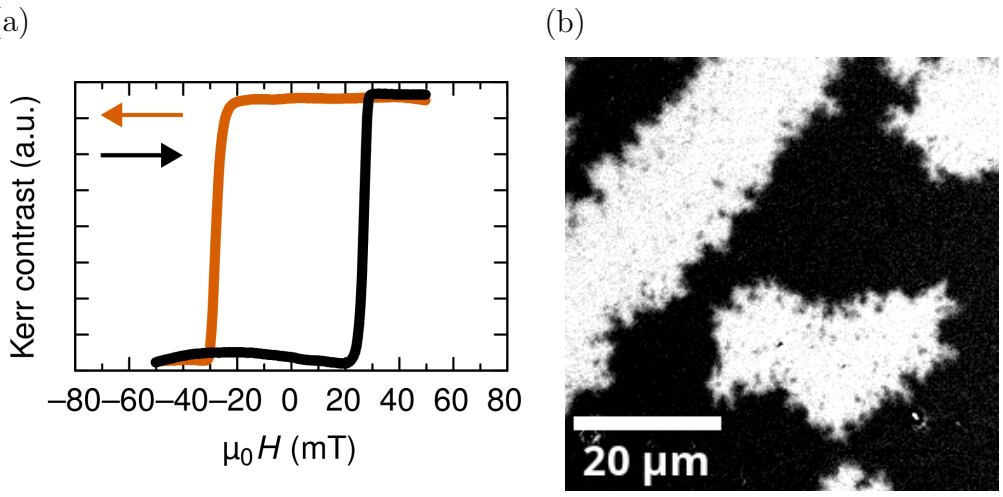

Figure 5.3: WFKM data for the Ni_3Pt reference layer at room temperature. Part (a) shows the hysteresis loop determined from the average greyscale value of WFKM images taken as the applied field is swept from positive to negative (orange curve) and then from negative to positive (black curve) in the out-of-plane direction . Part (b) shows a WFKM image in which domains form at the switching field (approximately 28mT).

moment is lost at remanence indicating a strong perpendicular magnetic anisotropy (PMA). The coercivity appears slightly different between the two methods, as the switching event measured using VSM appears to occur over the course of 20mT starting at 10mT and ending at 30mT, whereas the switching occurs over a shorter range of approximately 10mT from between 20mT to 30mT for the WFKM data.

5.2.3 Ni/Pt Multilayer

Similar to the cobalt reference layer, two Ni/Pt multilayer stacks were produced in order to better understand the properties of the constituent layer of the full SFi stack without the influence of the antiferromagnetic type interlayer exchange coupling. The two stacks studied correspond in layer thicknesses to the Ni/Pt multilayers (that act as one of the two ferromagnetic layers) in the full SFi stacks. The full stack of these reference samples are given by: Ni/Pt Reference A - Al_2O_3/Pt(5nm)/ 6x[Ni(0.6nm)/Pt(0.3nm)]/Pt(5nm) and Ni/Pt Reference B - Al_2O_3/Pt(5nm)/ 6x[Ni(0.6nm)/Pt(0.25nm)]/Pt(5nm).

In figure 5.5, the room temperature WFKM loops and domains of Ni/Pt Reference A are shown. Panel (a) shows the hysteresis of the multilayer which has a very small stauration field of about 2mT, takes a wasp-waisted shape, and has a neglible remanent magnetisation at RT. The domains shown in panel (b) are very small, and cannot be seen with a 20x magnification lens. The image shown in this panel was taken with a 50x objective lens which is a high enough magnification to resolve the domains. The domains themselves take a striped pattern with size on the order of 1μm.

Figure 5.6 shows the VSM loops at room temperature. In panel (a) where the

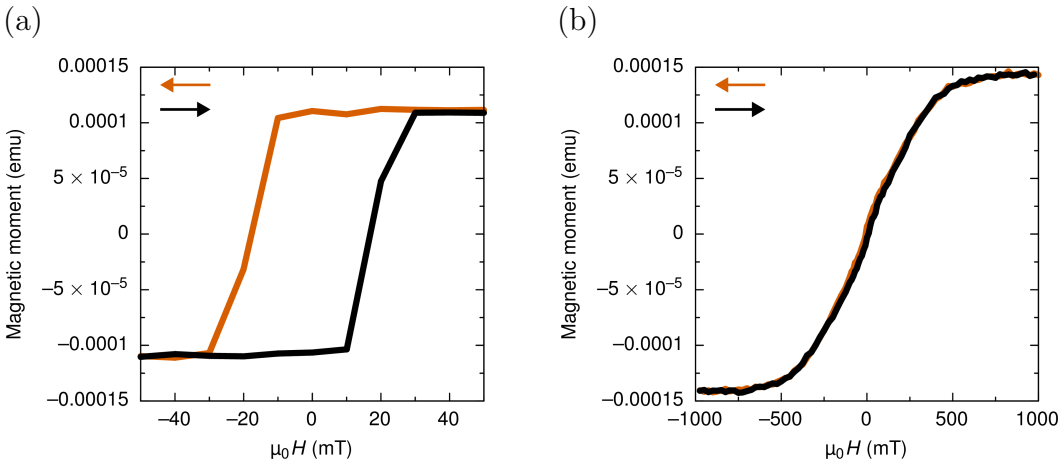

Figure 5.4: VSM magnetic moment vs. H loops of the Ni_3Pt reference layer with the **H** field applied out-of-plane (a) and in-plane (b) with respect to the sample. The black curve tracks the path of the magnetisation as the applied field is swept from negative to positive, and the orange curve tracks the subsequent reverse field sweep.

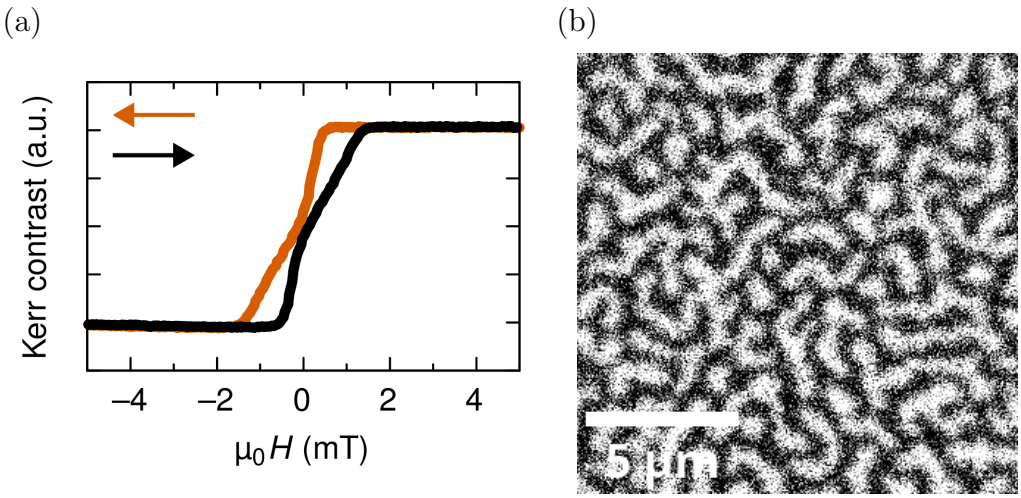

Figure 5.5: WFKM data for [Ni/Pt] (Reference A) multilayer at room temperature. Part (a) shows the hysteresis loop determined from the average greyscale value of WFKM images taken as the applied field is swept from positive to negative (orange curve) and then from negative to positive (black curve) in the out-of-plane direction. Panel (b) shows a WFKM image in which domains form at remanence after the removal of a saturating field.

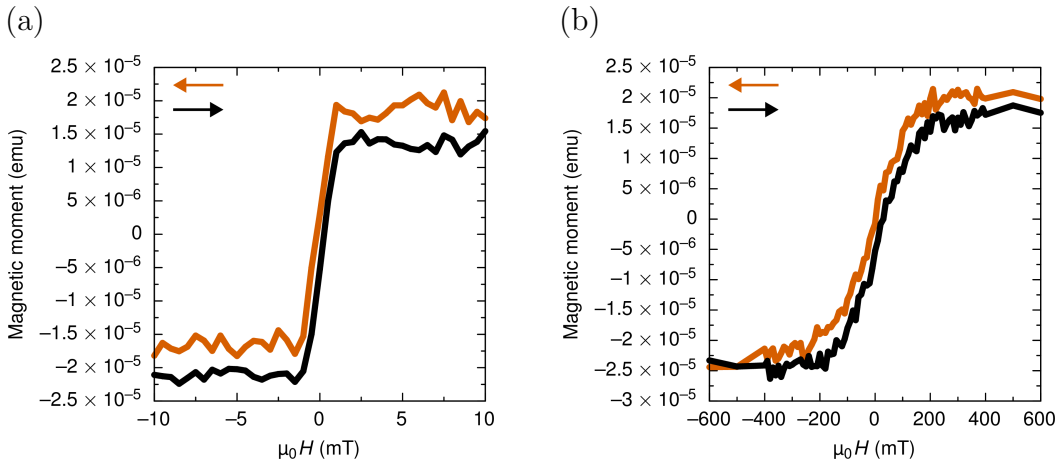

Figure 5.6: VSM magnetic moment vs. H loops of the [Ni/Pt] (Reference A) multilayer with the **H** field applied out-of-plane (a) and in-plane (b) with respect to the sample. The black curve tracks the path of the magnetisation as the applied field is swept from negative to positive, and the orange curve tracks the subsequent reverse field sweep.

field is applied out-of-plane, the saturation field is approximately 2mT and there is neglible remanent magnetisation similar to the WFKM data. However, the wasp-waisted shape of the loop cannot be seen here. In panel (b) the field is applied in-plane, showing an in-plane saturation field of about 400mT. As this is far greater than the out-of-plane saturation field the sample has a strong perpendicular magnetic anisotropy, however at remanence it appears to demagnetise, not retaining any significant magnetisation.

The demagnetisation of Ni/Pt Reference A at room temperature is contrasted with that of Ni/Pt Reference B, seen in figure 5.7. In panel (a) a square out-of-plane loop is shown indicating saturation out-of-plane at remanence, with a small coercive field of approximately 3mT, comparable in magnitude to the coercive field in the cobalt reference layer. The domains shown in panel (b) take a black colour due to the strong Kerr contrast, and have size of the order of 100µm, which is similar to that of the domains in the cobalt reference layer.

The VSM data for Ni/Pt Reference B is shown in figure 5.8. Panel (a) shows the out-of-plane hysteresis, confirming the observations from the WFKM loop. In panel (b) the in-plane loop shows a saturation field of about 300mT, comparable to that found for Ni/Pt Reference A. Similar to the other in-plane loops there is no net remnant magnetic moment, and the saturation field is far greater than in the out-of-plane loop indicating strong PMA.

The effect of temperature on the properties of the Ni/Pt multilayer is explored in figures 5.9 and 5.10. Figure 5.9 highlights that as the temperature is increased, the coercive field decreases until the coercivity reaches zero at around 335K and the sample loses its remnant magnetisation. At the even higher temperature of 340K the coercivity remains zero, but the saturation field begins to increase. The behaviour of Ni/Pt Reference B at 330K (figure 5.9d) appears similar to Ni/Pt Reference A at

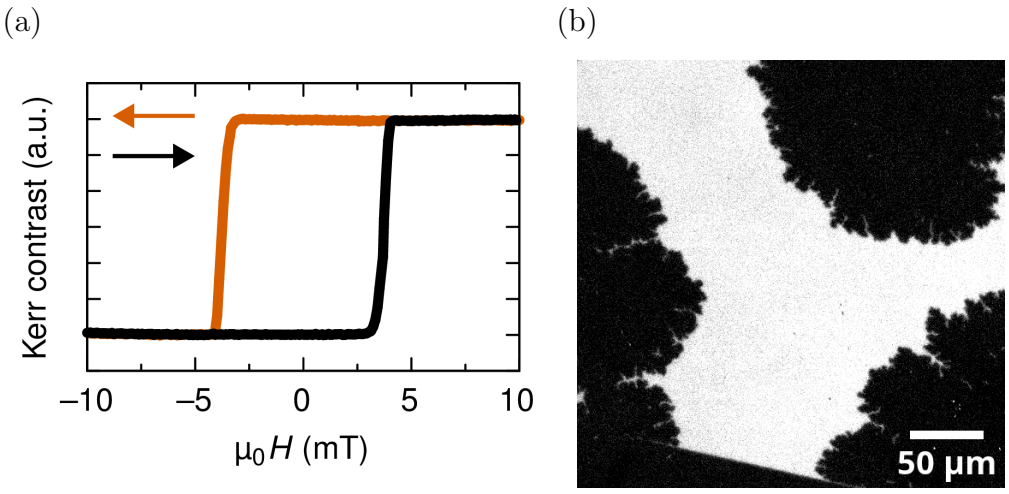

Figure 5.7: WFKM data for [Ni/Pt] (Reference B) multilayer at room temperature. Part (a) shows the hysteresis loop determined from the average greyscale value of WFKM images taken as the applied field is swept from positive to negative (orange curve) and then from negative to positive (black curve) in the out-of-plane direction. Part (b) shows a WFKM image in which domains form at the switching field (approximately 3mT).

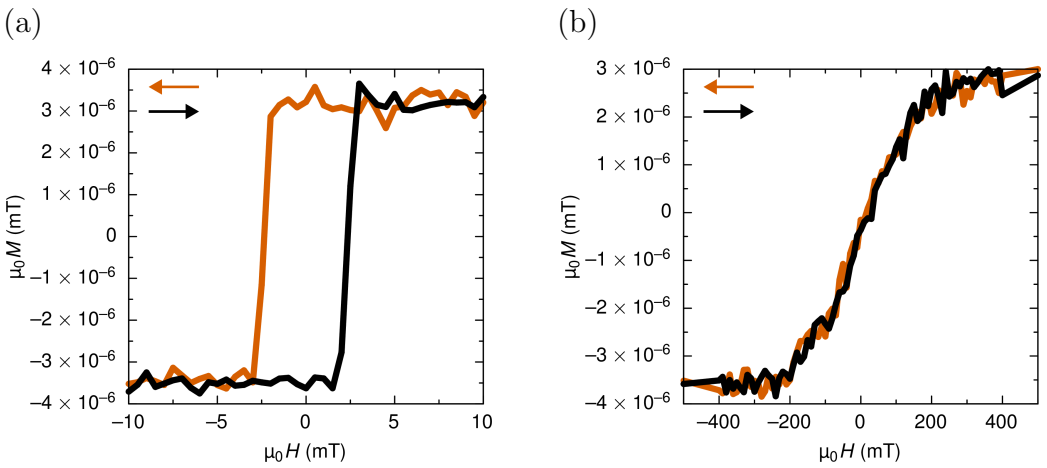

Figure 5.8: VSM M vs. H loops of the [Ni/Pt] (Reference B) multilayer with the **H** field applied out-of-plane (a) and in-plane (b) with respect to the sample. The black curve tracks the path of the magnetisation as the applied field is swept from negative to positive, and the orange curve tracks the subsequent reverse field sweep.

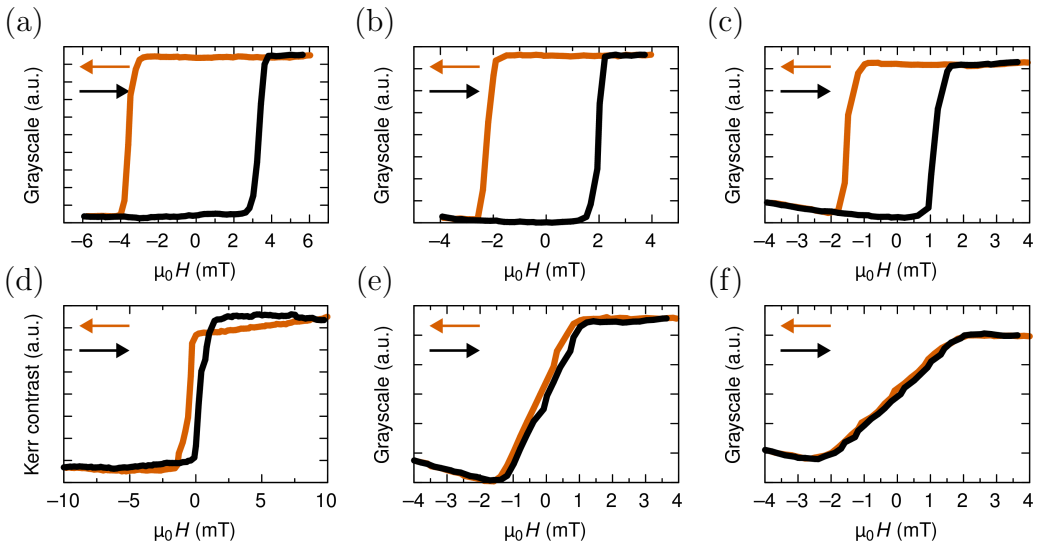

Figure 5.9: Loops determined from the average greyscale value in WFKM images of the [Ni/Pt] (Reference B) multilayer surface at (a) 300K, (b) 310K, (c) 320K, (d) 330K, (e) 335K and (f) 340K. The orange curve shows how the greyscale changes as the applied field is swept from positive to negative, and the black curve shows the subsequent reverse sweep.

room temperature (figure 5.5a), seeming to show a wasp-waist with 2mT saturation field, although this is difficult to confirm due to a non-linear drift in the image contrast.

In figure 5.10 the structure of domains is shown to change significantly with temperature. In panels (a,b,c), the images were taken at temperature 300K, 310K and 320K respectively. At 300K the domains take a solid colour in an ink splattered globule pattern. At 310K those domains are no longer solid, showing fractures at the domain walls. At 320K those fractures spread all the way through the structure of the globule, although the globules themselves have a comparable size to those at 300K. At 330K in panel (d) the structure of the domains changes dramatically as the globules no longer appear. Instead small domains with size on the order of 10μm fill the area independently of defects, which at lower temperatures acted as a barrier to the growth of the globules. The contrast is also significantly reduced. Just 2K above this at 332K in panel (e) the size of domains decreases even further to be of the order of 1μm with a further reduction in contrast. At 335K in panel (f), there is no visible domain structure when using the 20x objective lens, similar to the domains at room temperature in Ni/Pt Reference A.

5.2.4 [Ni/Pt]/Ir/Co Synthetic Ferrimagnet

In this section the SFi samples of interest for purposes of AOS will be examined.

Two synthetic ferrimagnets composed of cobalt and Ni/Pt multilayers FM layers, coupled antiferromagnetically through an iridium layer, were chosen for study based on their negative remanence (NR) behaviours. In a previous study [1],

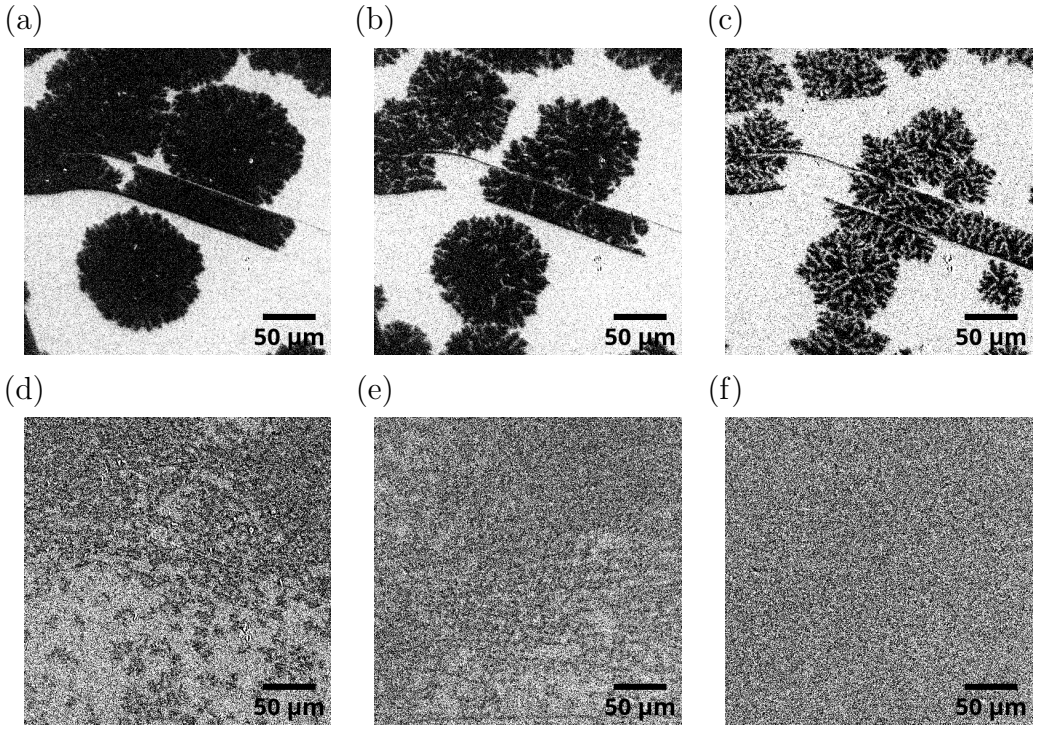

Figure 5.10: Domains formed at the switching event in [Ni/Pt] (Reference B) multilayer imaged using WFKM at (a) 300K, (b) 310K, (c) 320K, (d) 330K, (e) 332K and (f) 335K.

Ni_3Pt SFi's were found to show AOS below the negative remanence temperature (NRT), so here the properties of the stacks above and below T_{-R} are examined, particularly at temperature close to NRT. The full stack of the two samples are: Sample A - Pt(5nm)/5x[Ni(0.6nm)/Pt(0.3nm)]/Ni(0.6nm)/Ir(0.4nm)/Co(0.8nm)/Ir(3nm) and Sample B - Pt(5nm)/5x[Ni(0.6nm)/Pt(0.25nm)]/Ni(0.6nm)/Ir(0.4nm)/Co(0.8nm)/Ir(3nm) and can be seen in figure 5.11.

The NR regime exists between two critical temperatures. The lower bound is the negative remanence temperature T_{-R}, and the upper bound is the well known ferrimagnetic compensation point where the moments of the two FM layers cancel out. Within this regime, NR occurs because it is more energetically favourable to switch the ferromagnetic layer with the larger moment to achieve antiparallel alignment as the appied field is decreased towards remanence. This is shown for SFi samples A and B by plotting superconducting quantum interference device (SQUID) magnetometer measurements of the remanent magnetisation against temperature in figures 5.12 and 5.13 respectively.

The red curve is obtained from hysteresis measurements performed at each temperature, while the blue curve measures the magnetisation value at remanenence as the temperature is raised. In the case of the red curve, within the NR regime, the net remanent magnetisation of the sample is anti-aligned to the direction of a previously saturating field.

The multilayer structure of the [Ni/Pt] layers allows for the magnetic properties of these SFi's to be tuned as desired. In particular, the thickness of the platinum lay-

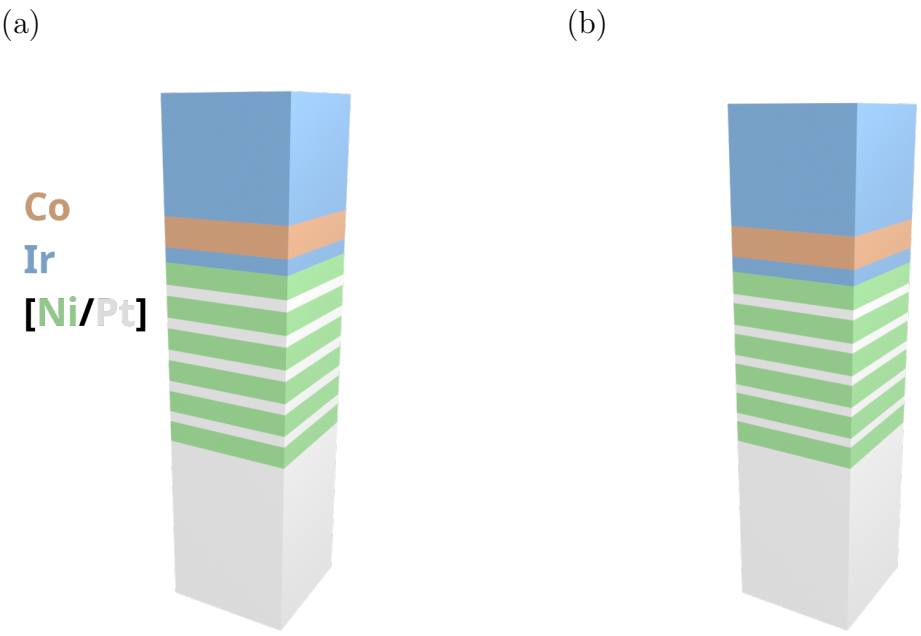

Figure 5.11: Visual representation of the stack structure of the synthetic ferrimagnets studied in chapter 5. Panel (a) shows SFi sample A and panel (b) shows SFi sample B. Both images show a cuboid cut of the thin film structure with blue Ir, orange Co, green Ni and grey Pt layers.

ers within the multilayers has a large influence on the negative remanence (T_{-R}), and magnetic compensation (T_M) temperatures. These critical temperatures increase as the Pt layer thickness decreases, as can be seen by comparing figures 5.12 and 5.13. The negative remanence temperature rises from T^A_{-R}=289K to T^B_{-R}=326K, and the compensation temperature rises from T^A_M=310K to T^B_M=343K when the thickness of platinum layers is reduced by 0.05nm between the two samples.

In each case the width of the negative remanence temperature regime $\Delta T_{-R} = T_M$-T_{-R} is a significantly smaller range than found in Ni_3Pt based SFi's with the example given in that study having $\Delta T_{-R} \approx 50$K, whereas for the present samples $\Delta T^A_{-R} = 21$K and $\Delta T^B_{-R} = 17$K.

Figure 5.14 shows the individual hysteresis loops for the coupled Co and [Ni/Pt] layers in SFi Sample A, measured using XMCD at temperatures (a) below and (b) within the negative remanence regime. Likewise, figure 5.15 shows the same for Sample B. In both samples, at temperatures above T_{-R} the cobalt undergoes a single switching event and the [Ni/Pt] layer switching event takes place before, rather than after reaching remanence when coming from a saturated state. This occurs as a result of a temperature dependence of the magnetic anisotropy in the two layers. At the field associated with P to AP state switching, the reduction in interlayer exchange energy given by an AP alignment is greater than the reduction in Zeeman energy favoured by a P alignment. Above T_{-R}, the anisotropy barrier of the larger (Ni/Pt) moment, but not the smaller (Co) moment can be overcome. Therefore the system can minimise its exchange energy, but is unable to reach the

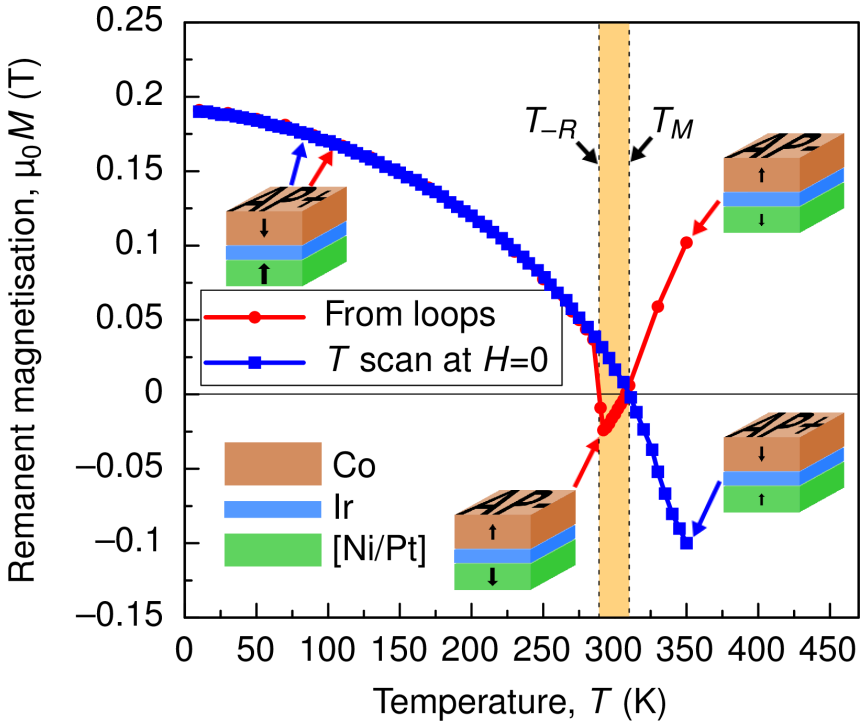

Figure 5.12: The remanent magnetisation of SFi Sample A as a function of temperature determined from SQUID magnetometry. The red circles give the remanence as calculated from a hysteresis loop taken at different temperatures, whereas the blue squares show how the remanence changes when increasing the temperature after preparing the remanent state at 10K. The negative remanence regime, highlighted in orange, falls between $T^A_{-R} = 289$K and $T^A_M = 310$K. The relevant antiferromagnetic type of alignment $\mathbf{AP}^+$ or $\mathbf{AP}^-$, is indicated for each region.

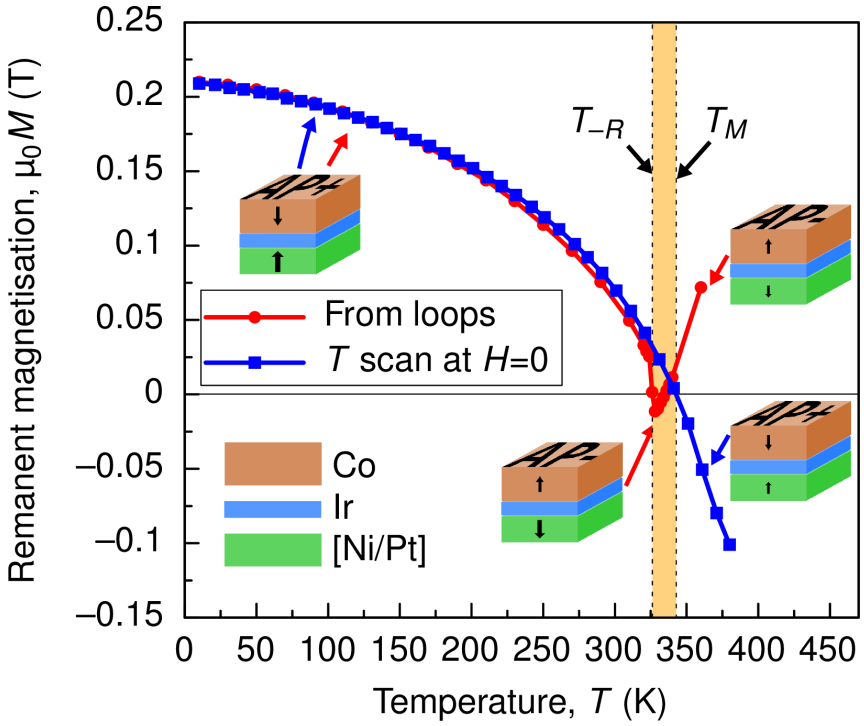

Figure 5.13: The remanent magnetisation of SFi Sample B as a function of temperature determined from SQUID magnetometry. The red circles give the remanence as calculated from a hysteresis loop taken at different temperatures, whereas the blue squares show how the remanence changes when increasing the temperature after preparing the remanent state at 10K. The negative remanence regime, highlighted in orange, falls between $T^B_{-R} = 326$K and $T^B_M = 343$K. The relevant antiferromagnetic type of alignment $\mathbf{AP}^+$ or $\mathbf{AP}^-$, is indicated for each region.

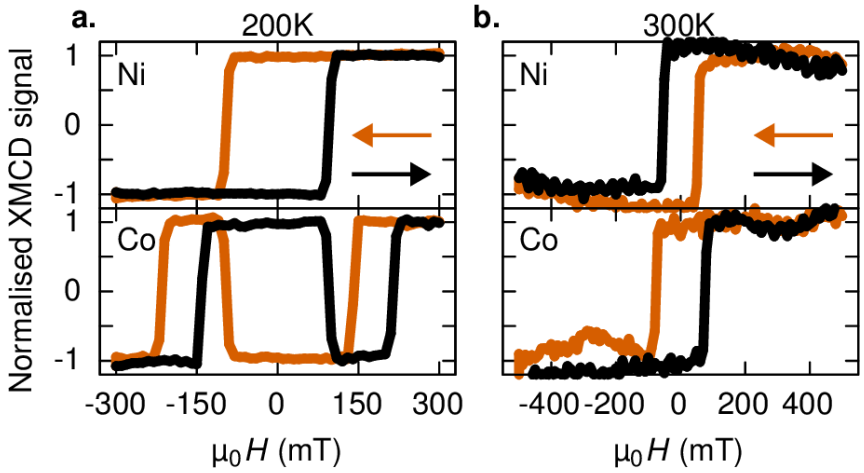

Figure 5.14: Element specific XMCD measurements of SFi Sample A that show hysteresis loops measured at the nickel and cobalt X-ray absorption edges at (a) 200K and (b) 300K. In each plot, the black coloured line shows the effect of the magnetic field swept in the positive direction, while the orange line shows a negative direction sweep.

true energy minimum state as the Co layer cannot reverse its direction to further reduce the Zeeman energy [3]. Below T_{-R} the cobalt layer has multiple switching events because both Zeeman and exchange energy can be reduced at each switching event, due to the smaller anisotropy barrier for Co.

The difference in magnetisation behaviour below and within ΔT^{A}_{-R} is highlighted further in Figure 5.16, the loops in which show the net magnetisation in SFi Sample A both below and above T_{-R} in panels (a) and (b) respectively, as determined from the magnetic contrast in WFKM images of a 0.2mm^2 area of the thin film. By comparison of these with Figure 5.14, it is possible to infer the available equilibrium states for these samples (i.e. the direction of layer moments), and the field history required to form them. WFKM images of the domains that form during switching events are shown beneath the loops in panels (c-g).

Slightly below T^{A}_{-R} at 285K, when moving from positive (+104mT) to negative (-104mT) saturation, the first switching event is $\mathbf{P}^{+}\rightarrow\mathbf{AP}^{+}$ at +78mT. The next event to occur is $\mathbf{AP}^{+}\rightarrow\mathbf{AP}^{-}$ at -67mT. In event $\mathbf{AP}^{-}\rightarrow\mathbf{P}^{-}$ the magnetisation is again saturated at -101mT.

Above T^{A}_{-R}, within the negative remanence regime, $\mathbf{P}^{+}\rightarrow\mathbf{AP}^{-}$i occurs at +71mT, leading to the negative remanence behaviour when the field is removed. Event $\mathbf{AP}^{-}\rightarrow\mathbf{P}^{-}$ occurs at -90mT and is equivalent in magnetic layer switching behaviour to the case below T_{-R}.

Events $\mathbf{P}^{+}\rightarrow\mathbf{AP}^{+}$ and $\mathbf{AP}^{+}\rightarrow\mathbf{AP}^{-}$, (which are a cobalt layer switching event and AP reversal respectively) have large comparably sized domains which are about 100 µm in width. Small domains with widths of tens of µm nucleate during the cobalt layer switch in $\mathbf{AP}^{-}\rightarrow\mathbf{P}^{-}$ and even smaller domains with width on the order of 1 µm nucleate as the nickel-platinum layer switches in $\mathbf{P}^{+}\rightarrow\mathbf{AP}^{-}$.

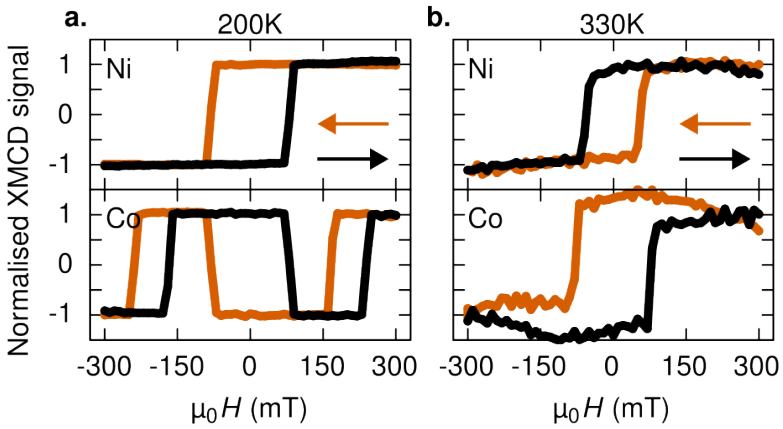

Figure 5.15: Element specific XMCD measurements of SFi Sample B that show hysteresis loops measured at the nickel and cobalt X-ray absorption edges at (a) 200K and (b) 330K. In each plot, the black coloured line shows the effect of the magnetic field swept in the positive direction, while the orange line shows a negative direction sweep.

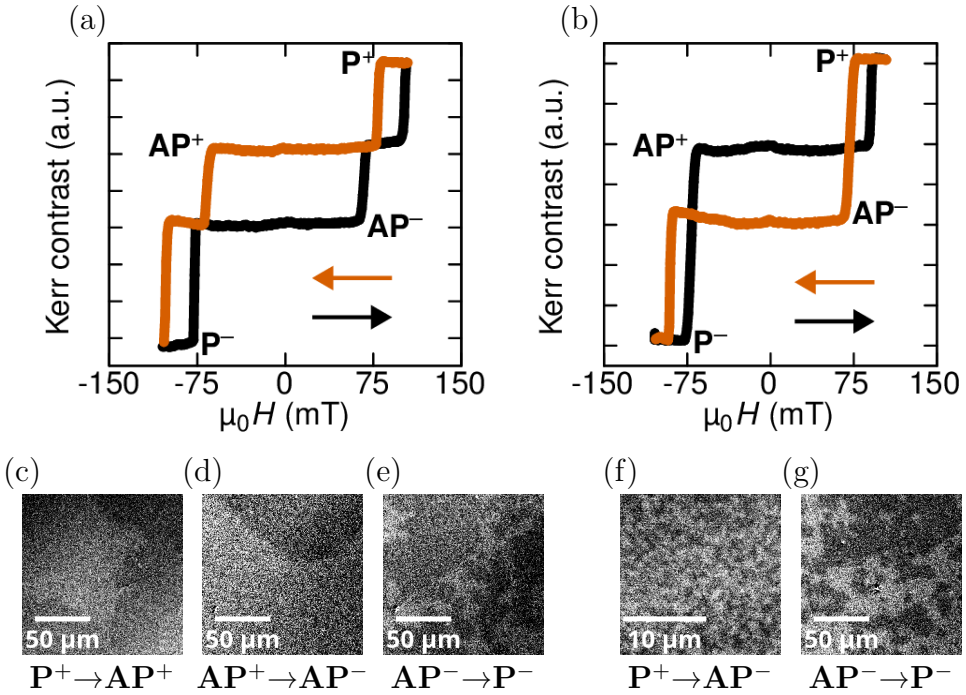

Figure 5.16: Hysteresis loops from Sample A determined from the magnetic contrast during WFKM measurements at (a) 285K and (b) 293K which are respectively below and above the negative remanence temperature T_{-R}^{A} for the locally imaged region. In the bottom row WFKM images representative of each switching event are displayed, showing the formation of large domains for (c) $\mathbf{P^+}\rightarrow\mathbf{AP^+}$ and (d) $\mathbf{AP^+}\rightarrow\mathbf{AP^-}$, smaller domains in (e,g) $\mathbf{AP^-}\rightarrow\mathbf{P^-}$, and miniscule domains in (f) $\mathbf{P^+}\rightarrow\mathbf{AP^-}$. In each image, the domains that form are darker than the background.

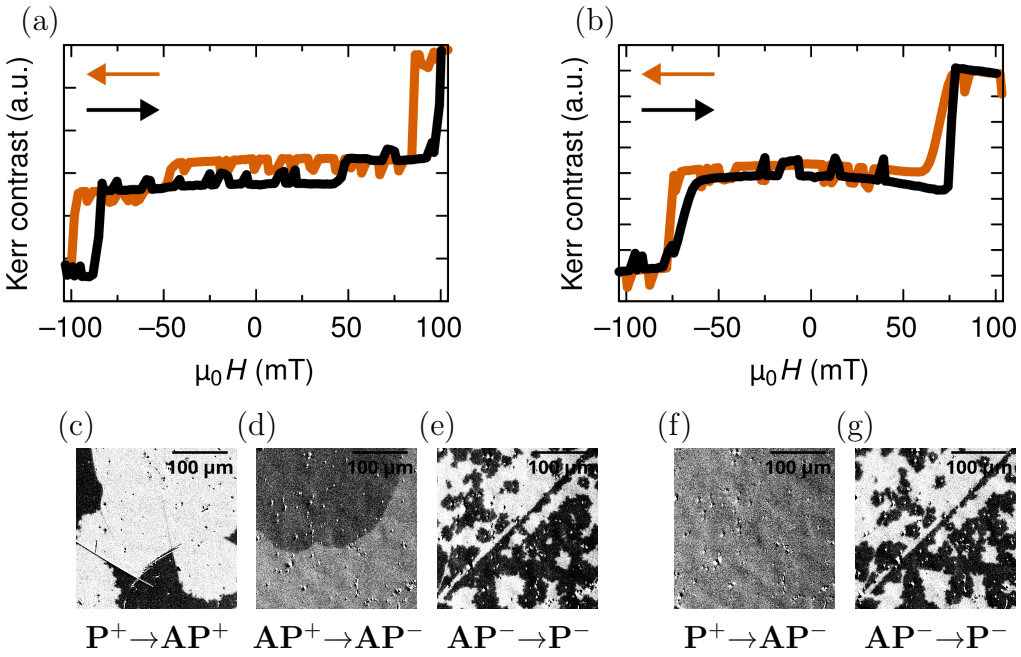

Figure 5.17: Hysteresis loops from Sample B determined from the magnetic contrast during WFKM measurements at (a) 320K and (b) 335K which are respectively below and above the negative remanence temperature T_{-R}^{A} for the locally imaged region. In the bottom row WFKM images representative of each switching event are displayed, showing the formation of large domains for (c) $\mathbf{P}^{+}\rightarrow\mathbf{AP}^{+}$ and (d) $\mathbf{AP}^{+}\rightarrow\mathbf{AP}^{-}$, smaller domains in (e,g) $\mathbf{AP}^{-}\rightarrow\mathbf{P}^{-}$, and a lack of visible domains in (f) $\mathbf{P}^{+}\rightarrow\mathbf{AP}^{-}$. In each image, the domains that form are darker than the background.

Figure 5.17 shows the loops and domain formation for Sample B within and below ΔT_{-R}^{B}. Although the loop in (b) does not appear to indicate negative remanence through the Kerr contrast value, the reduction to two rather than three switching events indicates that the measurements are performed within ΔT_{-R}^{B}. Therefore this figure indicates much the same thing in SFi Sample B at the transition to negative remanence, as figure 5.16 does for Sample A.

As negative remanence behaviour has been shown to destroy the capability for AOS behaviour, the behaviour at the transition has been studied in further detail. In figure 5.18 the temperature of Sample A was brought to $T = 289.5$K, in close proximity to the negative remanence temperature $T_{-R}^{A} = 289$K (figure 5.12). In each panel, the time delay between each WFKM image taken is different, leading to a different field sweep rate in each case. In panel (a) which has the longest delay of 0.8 seconds between each image, comparison with figure 5.16 shows that the resulting loop has the same character as loops taken below T_{-R}^{A}. In contrast to this, in panel (d) which has the shortest delay of 0.1 seconds, the resulting loop shows negative remanence behaviour. The intermediate delays of 0.4 and 0.2 seconds in panels (b) and (c) respectively, show that the resulting net remanence in an imaged area can be tuned as desired by choice of field sweeping rate.

From closer examination of the images taken to form these loops, it is possible to explain this phenomenon. In figure 5.19 half of a loop at $T = 289.5$K with Δt

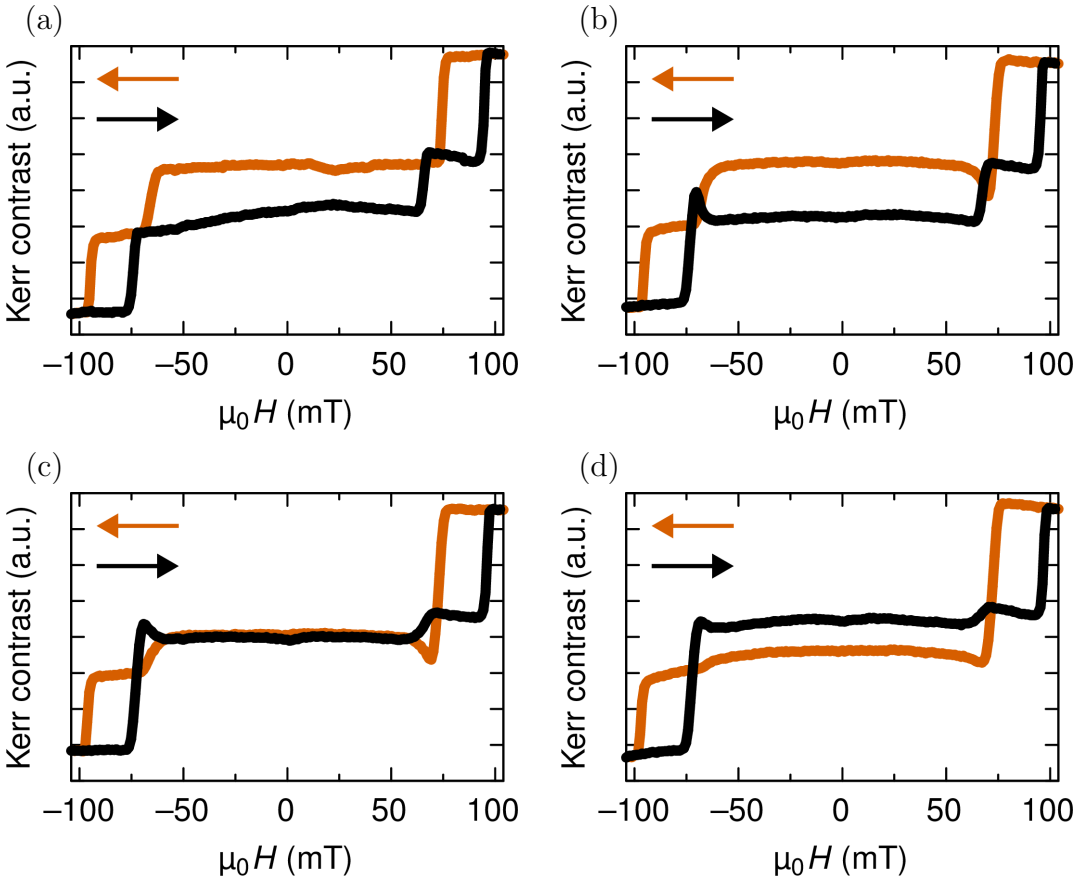

Figure 5.18: WFKM loops from SFi Sample A at T=289.5K. In each case the time delay Δt between subsequent images when incrementing the field differs. In panel (a) there is a $\Delta t = 0.8$s delay, for (b) $\Delta t = 0.4$s, (c) $\Delta t = 0.2$s and in (d) $\Delta t = 0.1$s.

= 0.2s is shown to give a similar loop to figure 5.18(b), in that the first switching event when coming from saturation towards remanence appears to head from $\mathbf{P}^+$ to $\mathbf{AP}^-$, but then rebounds to $\mathbf{AP}^+$. This indicates an initial preference for the state shown at negative remanence, followed by a reversal of moments in both layers to result in the type of state shown at positive remanence. The domains imaged at different points within the field sweep are shown in a column on the right hand side, showing a monodomain state before the event initiates (field H_1), with domains only starting to become visible at field H_2 after the large change in contrast which implies $\mathbf{P}^+ \rightarrow \mathbf{AP}^-$. At H_3 and H_4 those domains grow in size and by comaprison to the loop can be seen to give the $\mathbf{AP}^+$ contrast. However, the rate at which the domains grow rapidly slows as the field is decreased, and at H_5 just above remanence the domains are shown to be not significantly larger than in H_4. At remanence no domain wall motion is detected and the domains are locked in place.

The rapid slow down of domain growth is what allows panels (b) and (c) in figure 5.18 to show an intermediate net remanence behaviour, as the loops show the average across the domains in both the $\mathbf{AP}^-$ and $\mathbf{AP}^+$ states.

Figure 5.20 explores the slow down of the domain growth at various temperatures. In order to do this, first a temperature is set and the sample is saturated. Each panel shows a different temperature. Next the field is changed from saturation at 104mT to the field shown on the x-axis. A timer is started as the field is changed and domains begin to grow across the area viewed under the microscope. The timer is stopped once the field of view is completely covered by those domains. These measurements represent the rate at which the domains seen in figure 5.19 grow at different fields.

In order to reduce human error as much as possible, the field is set and the timer are started programmatically. The timer is stopped manually once the domains visually fill out the region of interest and therefore is still subject to human error. In order to account for this, the average of a number of measurements is made, represented by the error bars present in figure 5.20.

The measurements at different fields show that for each temperature there is an optimal field at which the rate of domain growth occurs at the fastest rate, above and below which the rate of growth is slower. In order to compare these across temperatures a quadratic function is fit (orange curve) to the data, and the x and y corrdinates of the quadratic minima are extracted and plotted in figures 5.21(a) and 5.21(b) respectively.

From those extracted parameters, the optimal switching field vs temperature can be well fit by a linear relationship as seen in panel (a). Panel (b) shows that the time it takes for the domains to fill the field of view rises exponentially with temperature. Given that these domains are shown to give rise to the positive remanence behaviour in figures 5.18 and 5.19, it is possible to conclude that measured values of the

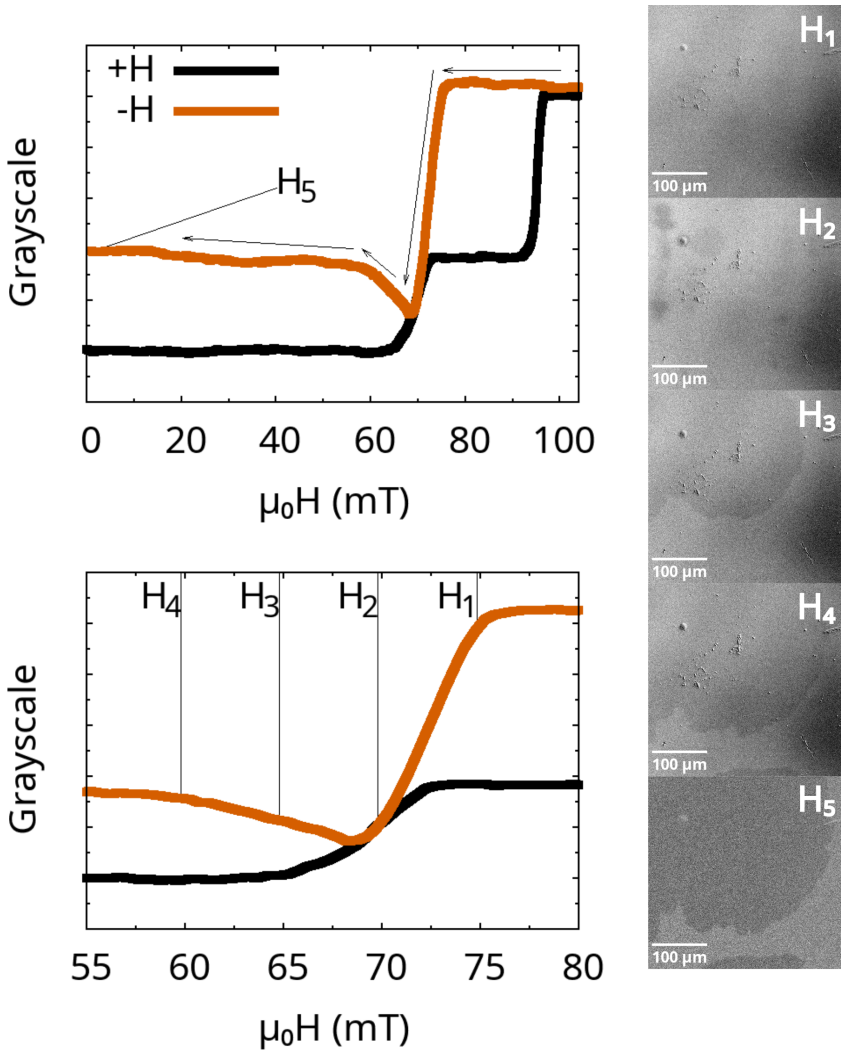

Figure 5.19: WFKM plots of a half loop at 190K$\approx T^A_{-R}$ in SFi Sample A shown for the full field range (top) and close to the switching event (bottom). WFKM images of the sample at various points in the loop are shown in a column on the right hand side, with their locations at $H_1 = 74.8$mT, $H_2 = 69.7$mT, $H_3 = 64.7$mT, $H_4 = 59.7$mT and $H_5 = 0.5$mT marked on the loops.

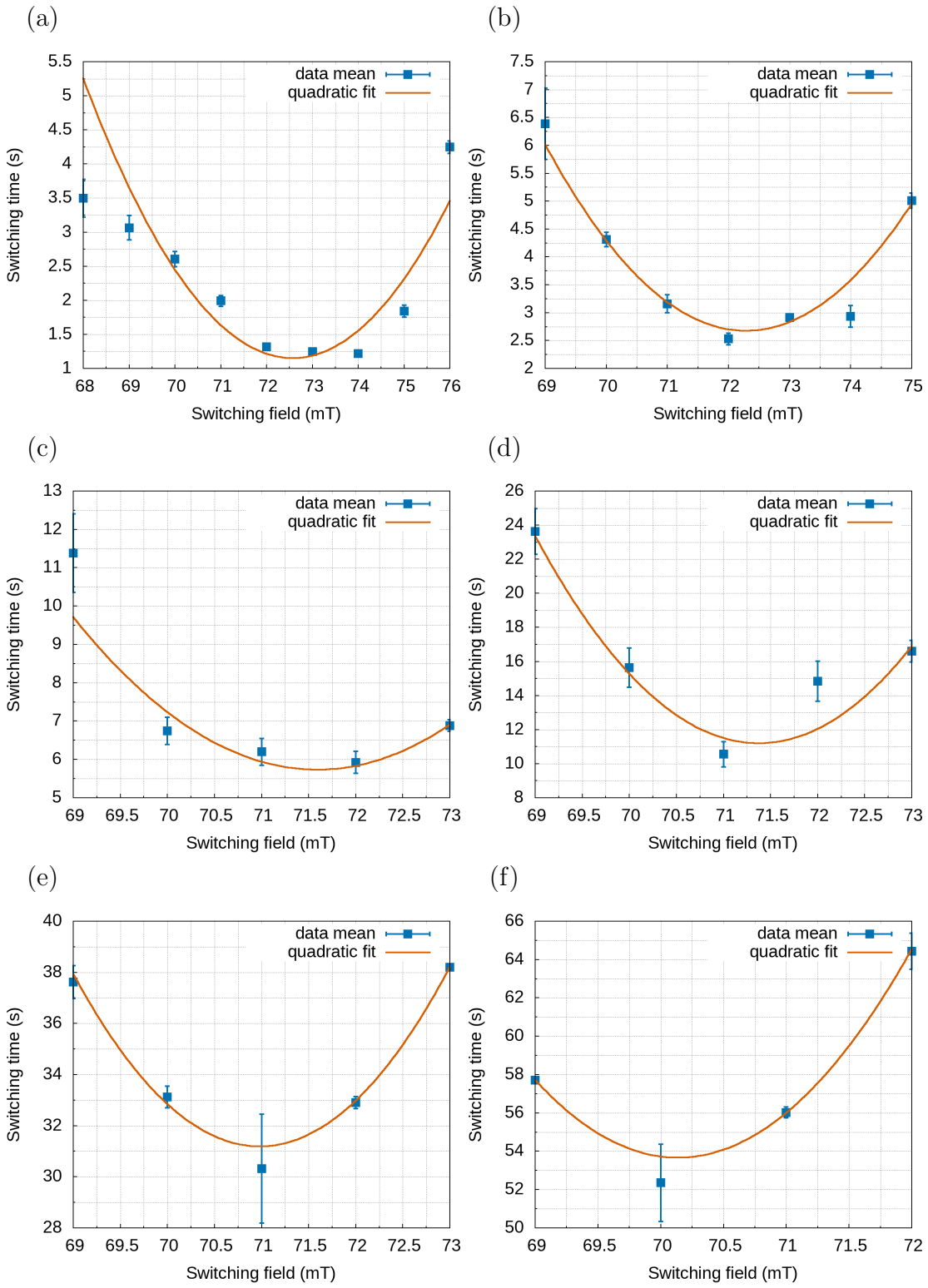

Figure 5.20: The time required for the domains shown in figure 5.19 to fill the imaged area is plotted against the applied out-of-plane field for temperatures (a) 288K, (b) 289K, (c) 290K, (d) 291K, (e) 292K, (f) 293K. The measurements and associated error bars are plotted in blue, and a quadratic fit is shown in orange.

negative remanence temperature in these samples can be expected to vary according to the rate at which the field is swept when the hysteresis is measured. This is one reason why different measurement techniques may lead to small variations in the T_{-R} reported.

As shown by panel (f) of figures 5.16 and 5.17, the domain evolution during the $\mathbf{P}^+ \rightarrow \mathbf{AP}^-$ transition is difficult to observe due to the small domains which form during the event. In figure 5.16(f) a 50x magnification objective lens was required to see the domains for $\mathbf{P}^+ \rightarrow \mathbf{AP}^-$, whereas for other switching events a 20x lens was sufficient. In figure 5.17 all domain images were taken with the 20x lens, and the domains cannot be seen for $\mathbf{P}^+ \rightarrow \mathbf{AP}^-$ at this scale. The domains that form in figure 5.19 occur during an $\mathbf{AP}^- \rightarrow \mathbf{AP}^+$event (i.e. during an antiparallel reversal), and $\mathbf{P}^+ \rightarrow \mathbf{AP}^-$ is again very difficult to detect within the WFKM images (taken using a 20x lens). This implies that event $\mathbf{P}^+ \rightarrow \mathbf{AP}^+$in figure 5.16 (due to the close proximity to T^A_{-R}), is the $\mathbf{P}^+ \rightarrow \mathbf{AP}^- \rightarrow \mathbf{AP}^+$ behaviour seen in figure 5.19, and that the WFKM image for $\mathbf{P}^+ \rightarrow \mathbf{AP}^+$ shown in figure 5.16 shows equivalent domains to $\mathbf{AP}^+ \rightarrow \mathbf{AP}^-$, with unresolvable $\mathbf{P}^+ \rightarrow \mathbf{AP}^-$also forming within the event. The large difference in contrast and changes to the domain shapes between images of $\mathbf{P}^+ \rightarrow \mathbf{AP}^+$ and $\mathbf{AP}^+ \rightarrow \mathbf{AP}^-$ shown in figure 5.17 indicate that panel (c) shows does not show the behaviour seen in figure 5.19, indicating that the smaller moment switches without the prior switching of the larger moment at this temperature in this sample.

Comparison to the XMCD data in figure 5.14 shows $\mathbf{P}^+ \rightarrow \mathbf{AP}^-$ to be a nickel-platinum multilayer reversal, and in the domains of the Ni/Pt multilayer reference samples shown in figures 5.5 and 5.10, it can be seen that close to the negative remanence temperatures in their corresponding SFi stacks, the domains of those reference layers collapse in size and contrast. Therefore it is reasonable to conclude that between fields H_1 and H_2 in figure 5.19, the change in contrast without the appearance of domains is due to the reversal of the Ni/Pt multilayer.

With this understanding, a re-examination of the domains observed below T^A_{-R} in figures 5.16(c) and (d) adds weight to the explanation that the $\mathbf{P}^+ \rightarrow \mathbf{AP}^+$ event shown in (c) is the combination of $\mathbf{P}^+ \rightarrow \mathbf{AP}^-$ followed by $\mathbf{AP}^- \rightarrow \mathbf{AP}^+$. The entirety of this event could happen on a timescale undetectable with the default 0.2 second time step Δt in WFKM imaging, as by extrapolation of the trends shown in figure 5.21 an antiparallel reversal $\mathbf{AP}^- \rightarrow \mathbf{AP}^+$could be expected to occur in as little as 0.12 seconds as $\mu_0 H$ passes 74mT.

The explicit formulae used to fit the data in figures 5.21(a) and (b) are

$$\mu_0 H = mT + c, \tag{5.2.1}$$

and

$$t_{\min} = ae^{bT} \tag{5.2.2}$$

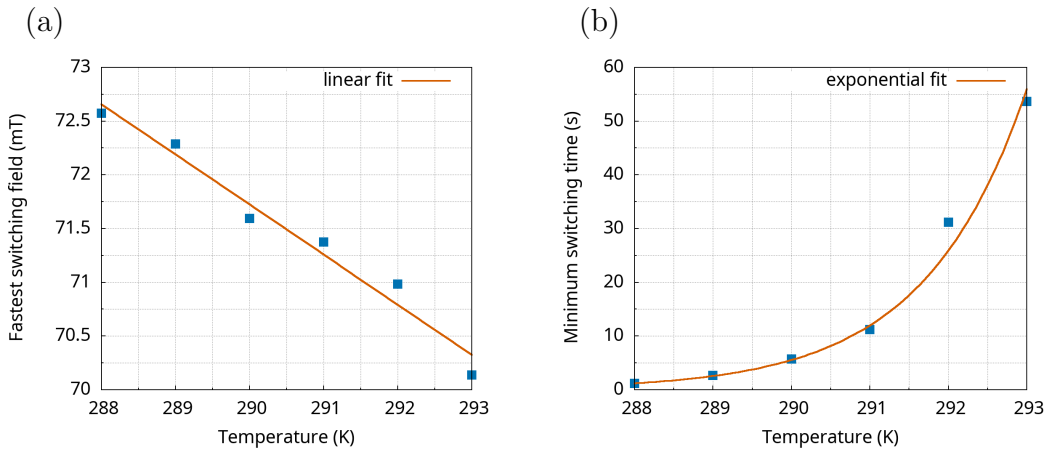

Figure 5.21: The parameters extracted from the quadratic fits in figure 5.20 are plotted here as a function of temperature. In panel (a) the field at which the quadratic takes a minimum is plotted as a function of temperature. In panel (b) the time corresponding to the field at which the quadratic takes a minimum is plotted as a function of temperature. The blue squares are the extracted parameters, while the orange curves show a best fit to the data with a linear funtion in (a) and an exponential function in (b).

respectively, where T is the sample temperature, $t_{\min}$ is the minimum switching time, and m, c, a and b are fitting parameters. Using the unweighted fitting procedure provided by gnuplot 5.4.6, which uses an implementation of the nonlinear least-squares Marquardt-Levenberg algorithm [4, 5, 6], to fit to the data points results in the values $m = -0.466$, $c = 207$, $a = 3.34 \times 10^{-97}$ and $b = 0.772$.

Figure 5.22 shows the hysteresis loops at a range of temperatures between 325K and 350K taking the sample from positive remanence in panels (a) 325K, (b) 330K and (c) 335K, to another example of the behaviour seen in figure 5.19 in (d) 337K, then to negative remanence in (e) 338K, including collapsed AP state contrast in (f) 340K and (g) 345K, and finally to above the compensation temperature in (h) 350K where the sample again shows positive remanence. The loop in (h) and to some extent (g) show a drawn out rotation of the Ni/Pt moment towards saturation.

In these loops, the negative remanence temperature appears to be at around 337K, which is significantly above the $T_{-R}^{B} = 326$K result found using SQUID measurements (figure 5.13), and it also at least 2K greater than found in the WFKM data presented in figure 5.17. The difference between WFKM data sets is easily explained as being due to variations in the local properties of the different areas being imaged on the sample. However, the discrepancy between the loacl WFKM measurements and global SQUID measurements is more difficult to explain unless either there can be drastic variations in sample properties between different regions, or there is some level of significant inaccuracy in the measured temperature for one or both techniques.

Some level of variation was seen in the properties of the samples across different areas, but nothing drastic enough to suggest that to be the only explanation.

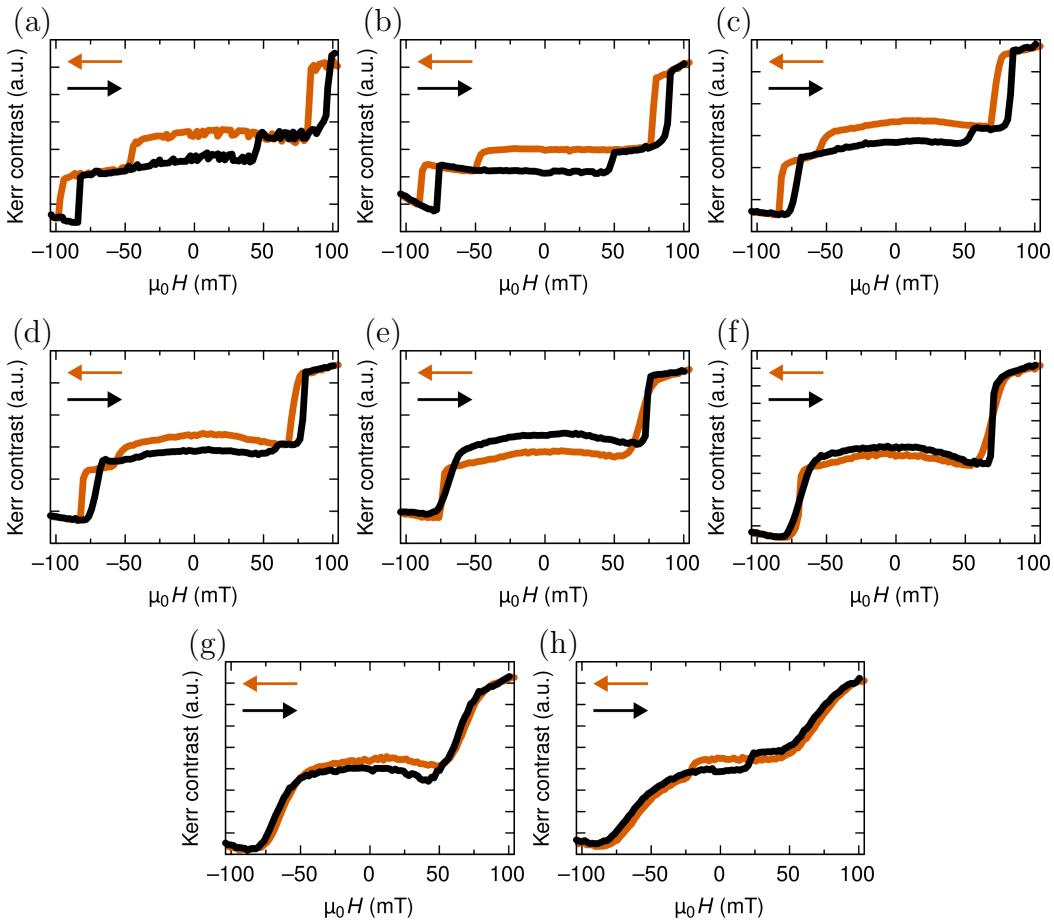

Figure 5.22: WFKM loops for Sample B at temperatures (a) 325K, (b) 330K, (c) 335K, (d) 337K, (e) 338K, (f) 340K, (g) 345K, and (h) 350K.

Therefore, the result shows the importance of calibrating the temperature sensors according to the behaviour of an appropriate calibration sample with easily observable emergent properties at known temperatures. As the WFKM heater stage was only set up recently it has not yet been possible to establish a suitable sample and perform a calibration of the type described. Rather, the sensor calibration provided by the manufacturer of the Kerr system has been relied upon, on the assumption that it can report a sufficiently accurate reading for the purpose of this study.

5.3 Optically Pumped Wide Field Kerr Measurements

In this section, the results of exposing SFi samples to a pulsed laser source will be examined. The results of such exposure are usually classified as either thermal demagnetisation or all optical switching. All optical switching is taken to be a solid spot or stripe of switched region. Pure thermal demagnetisation has an equal amount of area in the switched and non switched state. Areas that are not fully switched but show greater proportion of switched area are referred to as partially switched.

5.3.1 Requirements for AOS

Before AOS was observed in these [Ni/Pt] based SFi's, many measurements were performed in order to understand the conditions required. In what follows, the most enlightening of those measurements will be shown in order to establish the reasons behind the choice of parameters used in the next section.

In order to see any optically induced magnetisation behaviour, the beam fluence must be above a critical threshold. In figure 5.23, the result of different fluences is explored in SFi Sample A at 73K. In panel (a) the 5.8mJ/cm^2 fluence is below the threshold, as scanning the beam from top to bottom resulted in only a small switched area in the position exposed initially. The reason for an effect in this area above any other is likely due to the greater period of time for which that area was exposed (as it takes time for the user to move from opening the shutter to begin rotating the mirror to sweep the beam), increasing the likelihood that a fluctuation in the beam fluence can overcome the critical threshold. Similar behaviour is seen in (b) 6.2mJ/cm^2 and (c) 6.6mJ/cm^2, although increasingly large areas are switched each time. At 7.0mJ/cm^2 shown in panel (d) the fluence is above the critical threshold, and owing to a combination of the beam parameters and temperature, a beam of this fluence is enough to result in thermal demagnetisation.

Figure 5.24 again shows Sample A. Here the 6.8mJ/cm^2 fluence in panel (a) is just above the critical threshold and owing to the balance of beam parameters and temperature, the effect of beam exposure is all optical switching of the region swept by the beam. Continuing to increase the beam fluence in (b) 7.5mJ/cm^2 shows a similar effect. In panel (c) 8.3mJ/cm^2 the increase in fluence increases the width of the switched region. In (d) 9.0mJ/cm^2 the increase in fluence leads to a partial switching rather than full AOS, and in (e) 9.8mJ/cm^2 the level of switching is reduced further to the point that it makes more sense to refer to it simply as a thermal demagnetisation. Overall this figure shows that for parameters which lead to AOS there is an upper limit to the fluence at which it can occur, before thermal

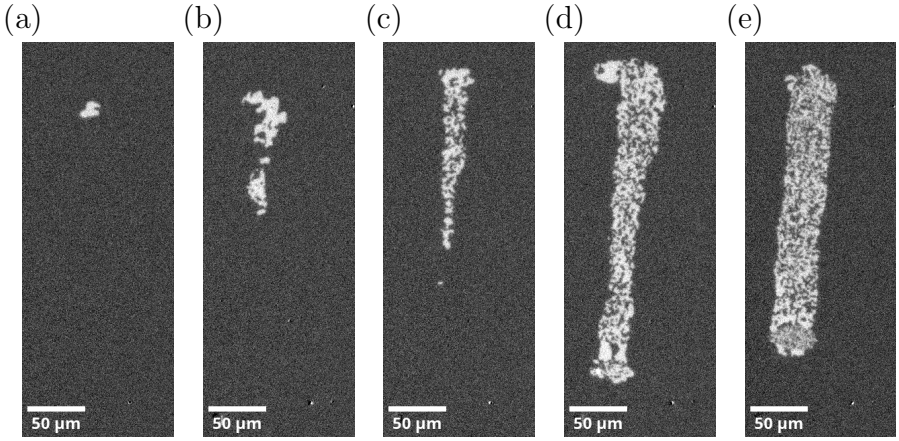

Figure 5.23: The effect of pulse fluence on optical exposure in SFi Sample A in the remanence state at 73K. The 1035nm, 280fs, RCP pulses occur at a repetition rate of 10kHz. Between panels, the fluence is varied such that (a) 5.8mJ/cm^2, (b) 6.2mJ/cm^2, (c) 6.6mJ/cm^2, (d) 7.0mJ/cm^2, (e) 7.3mJ/cm^2. Light and dark grey coloured regions are $\mathbf{AP}^+$ and $\mathbf{AP}^-$ states respectively. In each image the beam was swept from top to bottom at a rate of approximately 150µm/s.

demagnetisation is instead observed. Therefore, when searching for AOS the ideal situation is to set a fluence sufficiently above the threshold enough that fluctuations will not bring the fluence beneath the threshold, but otherwise as close to the critical threshold as possible.

The effect of temperature on the effect of optical exposure was examined in SFi Sample A, as shown in figure 5.25. In each panel, prior to optical exposure the region of the sample to be examined was prepared in the same way. The method of preparation is to first saturate the sample with a -104mT out of plane field, followed by a reduction to -10mT, at which the bias field was used to assist switching as a beam was applied to the left hand side of the imaged area. In each panel, once exposed to the 5.6mJ/cm^2 LCP beam the beam was first of all swept from left to right across the upper region at a rate of approximately 150µm/s across the domain wall. Next, the beam was blocked and the sample moved upwards using the piezoelectric stage. The beam polarisation was changed to right circularly polarised, and the beam swept from right to left back across the domain wall. In each case the pulse repetition rate and width were kept constant at 10kHz and 280fs respectively. Change from LCP to RCP moves the position of beam exposure slightly to the right. In each case, exposure to the beam resulted in thermal demagnetisation with domains of different sizes. In panels (a), (b) and (c) at 72K, 120K and 160K respectively the exposed regions demagnetise with domains forming in a mostly disconnected fashion, with domain size being between approximately half and one times the size of the demagnetised spots. In panels (d), (e) and (f) at 210K, 250K and 290K respectively, the procedure to prepare the state with a saturation field and bias field results in the inversion of contrast. Particularly in (d) and (e), the result of beam exposure leads to a preferance for the light coloured $\mathbf{AP}^+$ state, although

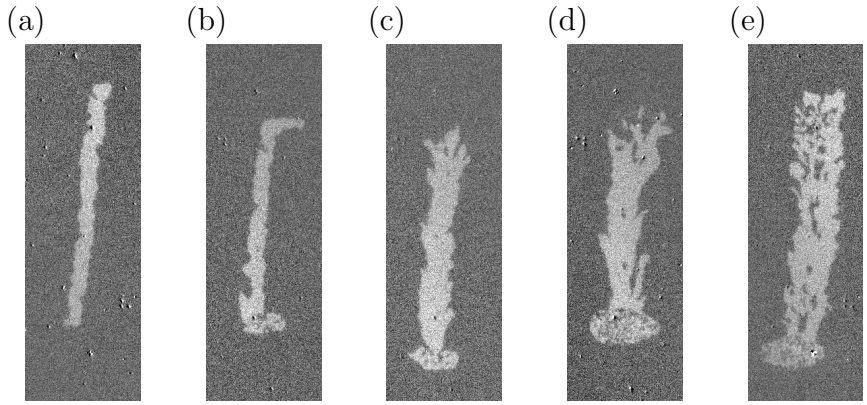

Figure 5.24: The effect of pulse fluence on optical exposure in SFi Sample A in the remanence state at 250K. The 1035nm, 2500fs, LCP pulses occur at a repetition rate of 250kHz. Between panels, the fluence is (a) 6.8mJ/cm^2, (b) 7.5mJ/cm^2, (c) 8.3mJ/cm^2, (d) 9.0mJ/cm^2, (e) 9.8mJ/cm^2. Light and dark grey coloured regions are $\mathbf{AP}^+$ and $\mathbf{AP}^-$ states respectively. In each image the beam was swept from top to bottom at a rate of approximately 150µm/s.

there remains no clear helicity dependence. The reason behind this preference will be explored in the discussion of figures 5.28 and 5.29. The domains formed on the right hand side at higher temperatures appear more connected and are generally larger in size. As the negative remanence temperature is approached, the contrast between the two antiparallel states falls significantly. This is to be expected due to the proximity to the magnetic compensation temperature where the moment of the ferromagnetic layers equal one another, and the net signal from antiparallel layers is expected to vanish (assuming each layer has the same Kerr rotation). Panels (b) and (c) show areas previously demagnetised at a position in the bottom centre (which arise due to the closing of the shutter on the beam used to create the domain wall with a bias field during preparation) are switched more consistently than those in an AP state. This effect is explored further in figure 5.38.

Figures 5.26 and 5.27, show the effect of pulse repetition rate on Sample A at temperature 72K and 250K respectively. In each case the preparation procedure before exposure is the same as that described for figure 5.25, as is the sequence of exposure events. With increasing repetition rate, the size of domains formed is seen to increase, and the resulting effect of the exposure is a better connection between the domains to form a stripe. As in figure 5.25 the results at 72K show similar behaviour in each AP state, whereas at 250K there is a clear preference for the light AP state. At higher rep rates, the effect of demagnetisation is suppressed, while the ability to pull domain walls is heightened. In panels 5.27(e) and (g), a thin switched region longer than 50µm is formed, primarily through the domain wall pulling mechanism.

Figure 5.28 shows the strong effect of historical fields on SFi Sample A at 250K. In each panel, a -104mT out of plane field was used to prepare the left hand side with darker contrast as the $\mathbf{AP}^-$ state. The right hand side with lighter contrast was

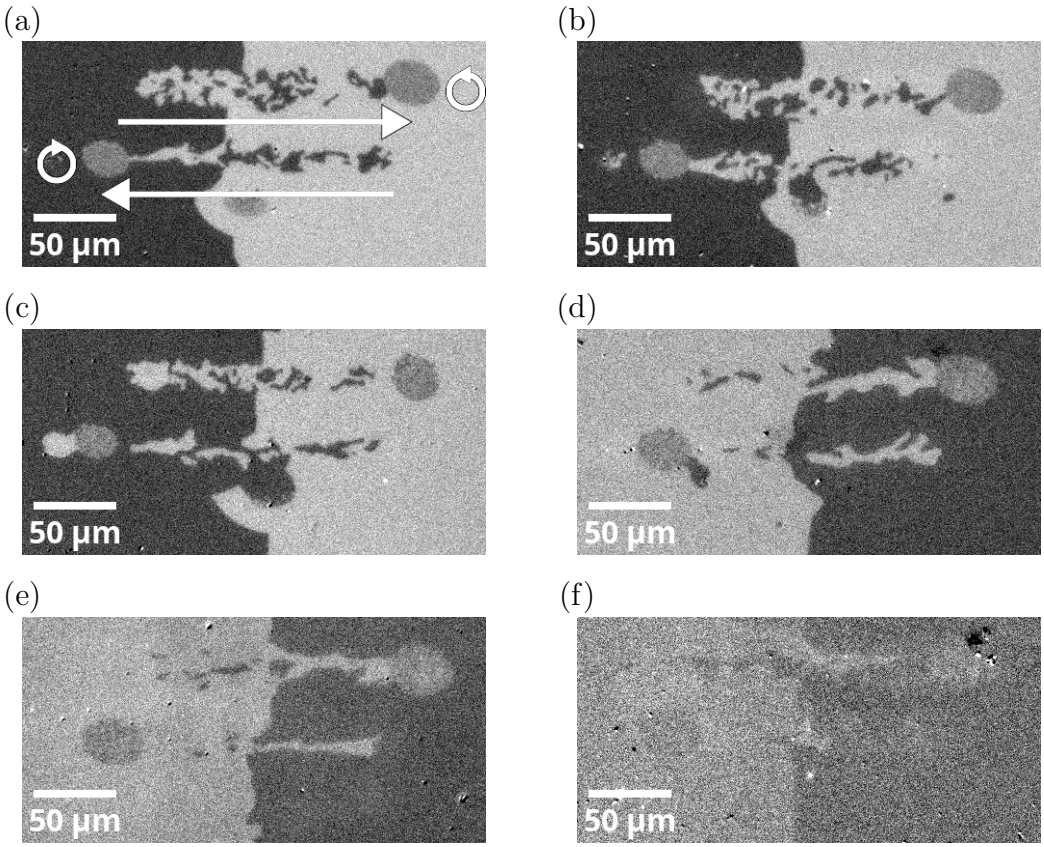

Figure 5.25: Effect of temperature on optical exposure in SFi Sample A. The 1035nm wavelength beam was set with a repetition rate of 10kHz, pulse width of 280fs and fluence of 5.6mJ/cm^2. The temperature in each panel is (a) 72K, (b) 120K, (c) 160K, (d) 210K, (e) 250K and (f) 290K. Each image shows three colours, darkest and lightest grey are AP states, elliptical regions of a middle grey value are at the location where the sweep path ends and the laser shutter closed. In each image, an LCP beam was swept from left to right at the top, and an RCP beam was swept from right to left below that. In all cases the beam was swept at a speed of approximately 150 µm/s.

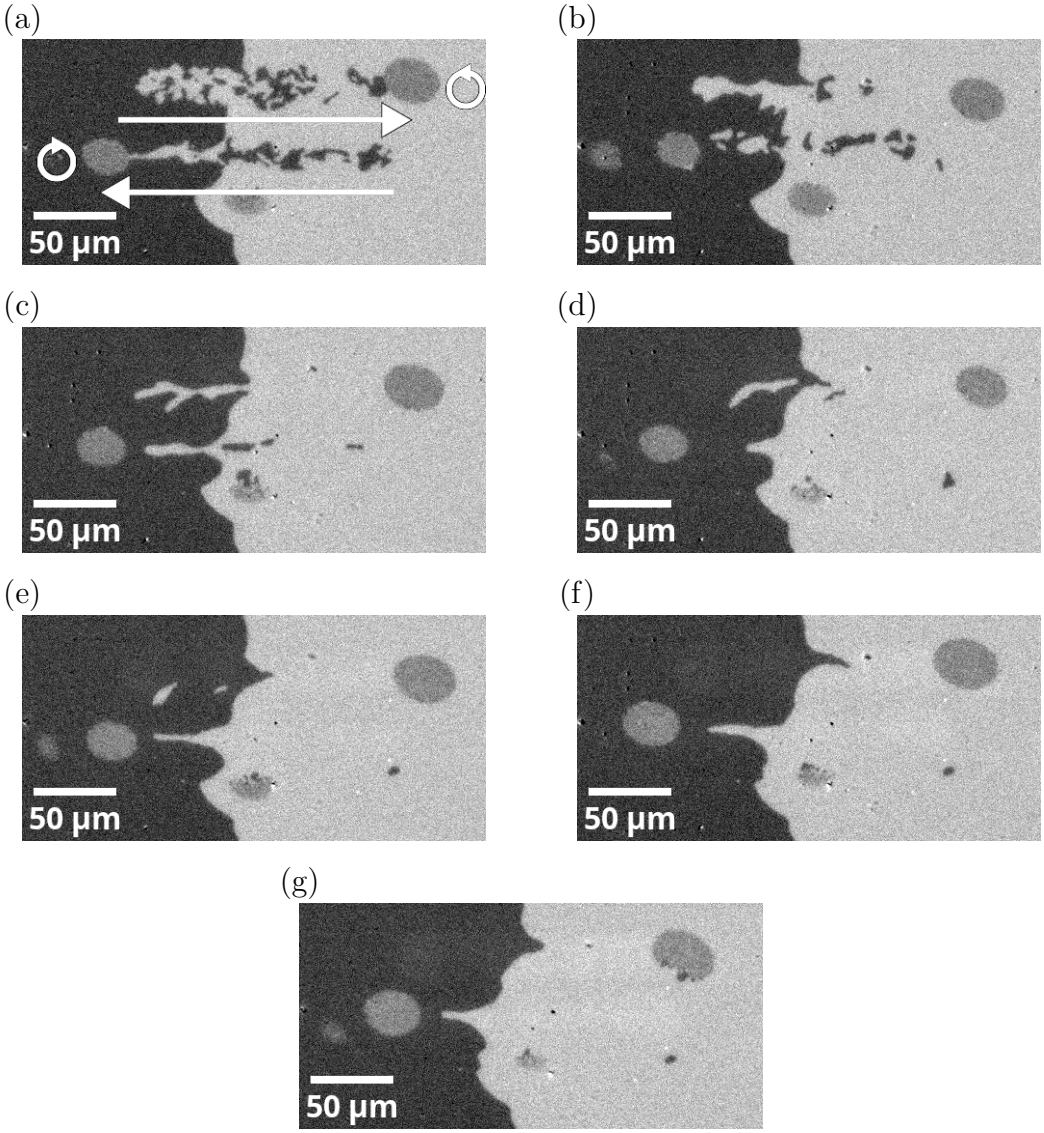

Figure 5.26: Effect of pulse repetition rate on optical exposure in SFi Sample A at 72K. The 1035nm wavelength beam was set with a pulse width of 280fs and fluence of 5.6mJ/cm^2. The repetition rate in each panel is (a) 10kHz, (b) 25kHz, (c) 50kHz, (d) 100kHz, (e) 250kHz, (f) 500kHz and (g) 1000kHz. Each image shows three colours, darkest and lightest grey are AP states, elliptical regions of a middle grey value are at the location where the sweep path ends and the laser shutter closed. In each image, an LCP beam was swept from left to right at the top, and an RCP beam was swept from right to left below that. In all cases the beam was swept at a speed of approximately 150 µm/s.

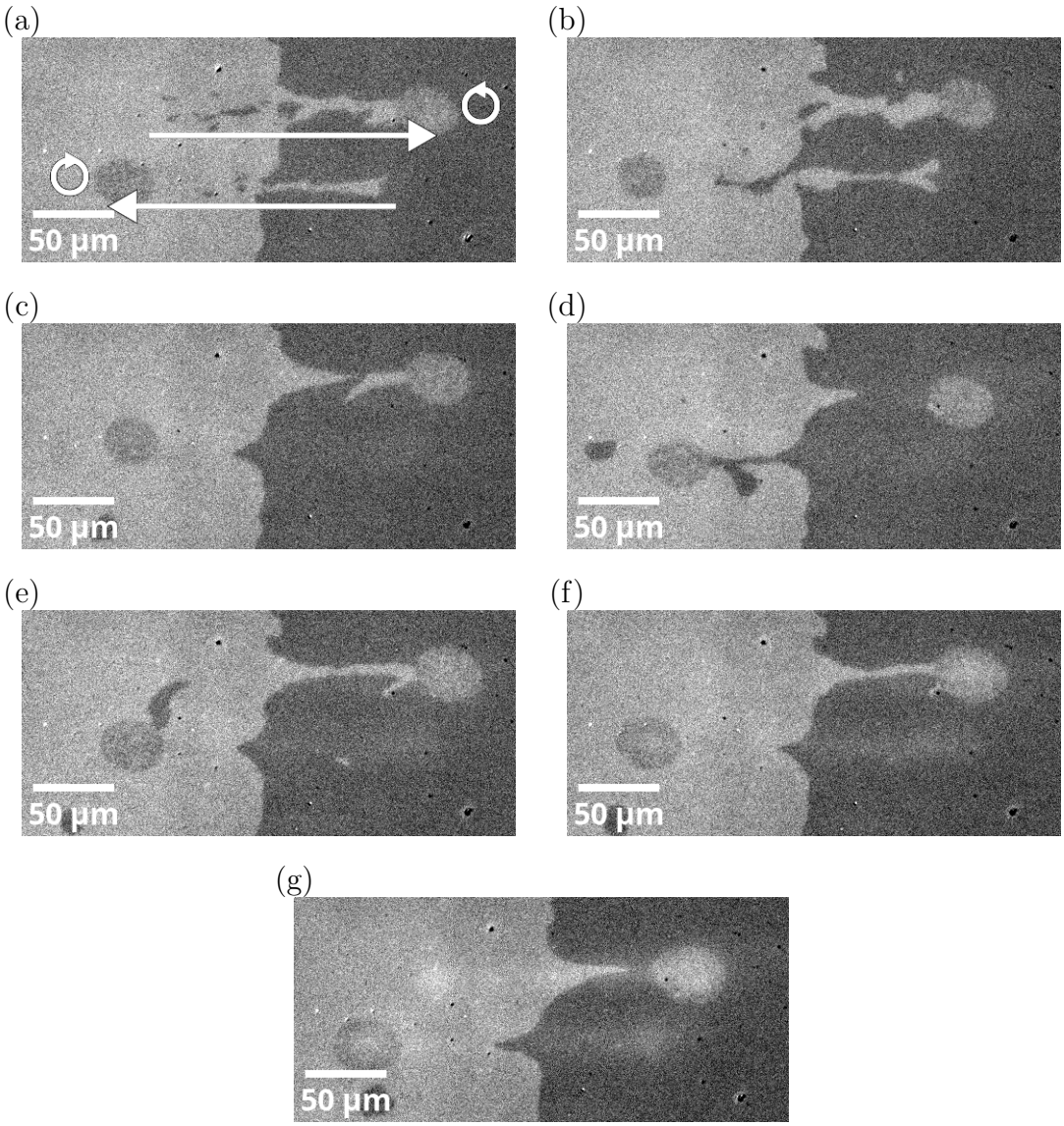

Figure 5.27: Effect of pulse repetition rate on optical exposure for Sample A at 250K. The 1035nm wavelength beam was set with a pulse width of 280fs and fluence of 5.6mJ/cm^2. The repetition rate in each panel is 10kHz, (b) 25kHz, (c) 50kHz, (d) 100kHz, (e) 250kHz, (f) 500kHz and (g) 1000kHz. Each image shows three colours, darkest and lightest grey are AP states, elliptical regions of a middle grey value are at the location where the sweep path ends and the laser shutter closed. In each image, an LCP beam was swept from left to right at the top, and an RCP beam was swept from right to left below that. In all cases the beam was swept at a speed of approximately 150 µm/s.

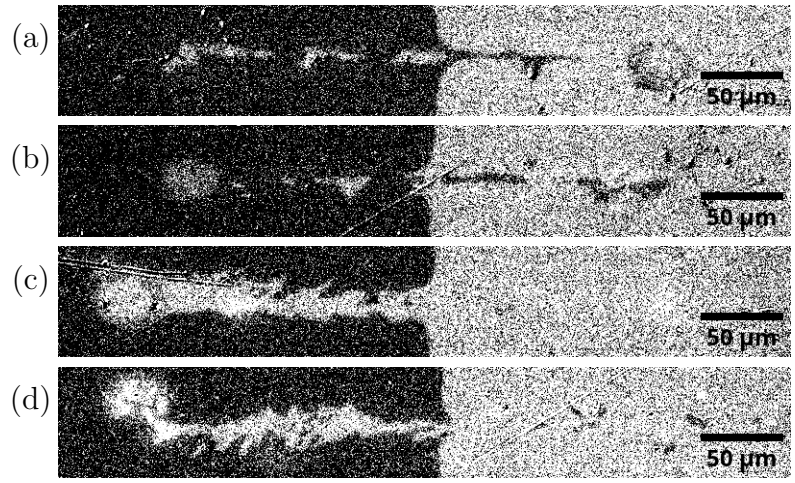

Figure 5.28: The effect of a historical field on optical exposure in SFi Sample A at 250K. In panels (a) and (b) a 10mT bias field in direction opposite to the prior saturation field is applied before exposure to the beam at remanence. In panels (c) and (d) the field is taken directly from saturation to remanence prior to exposure. The beam used in each case has a pulse repetition rate of 1MHz, pulse width of 280fs, fluence of 4.9mJ/cm^2 and 1035nm wavelength.

prepared into $\mathbf{AP}^+$using a -10mT bias field. In panels (a) and (b), in between the application of the -10mT biasing field and the removal of applied field, a positive direction 10mT field was applied to the sample. Whereas in panels (c) and (d), the field was removed directly after the -10mT bias. In panels (a) and (c), the 4.9 mJ/cm^2 fluence, beam was scanned from left to right with a LCP 260mW, 280fs, 1MHz beam. In panels (b) and (d), the beam was scanned from right to left with an otherwise equivalent RCP beam. In both cases exposure to the beam is at remanence, with the only difference in setup being the +10mT field applied immediately prior to remanence in panels (a) and (b). The results show that the historical field has a strong effect on the demagnetisation effects on each AP state. With no historical field, there is a partial switching of the dark contrast $\mathbf{AP}^-$ state, with no significant switching or demagnetisation of the light contrast $\mathbf{AP}^+$ state. However, the application of the historical bias field results in a demagnetisation of both AP states, with no significant dependence on the AP state under exposure. In each case the effect seen is helicity independent.

The historical field effect has been studied further in figure 5.29. Here the background has been prepared in the $\mathbf{AP}^+$ state through the application of a +104mT field, and the historic field before exposure to the beam differs in each panel. In panel (a) the field is taken directly to 0mT and the result of beam exposure is a strong partial switching, in (b) a -5mT field is applied before beam exposure at 0mT and the switching percentage drops from strong partial switching to a thermal demagnetisation in (c), (d) and (e) the historical fields are 10mT, 20mT and 30mT respectively, and show similar demagnetisation as in (b). Further increasing

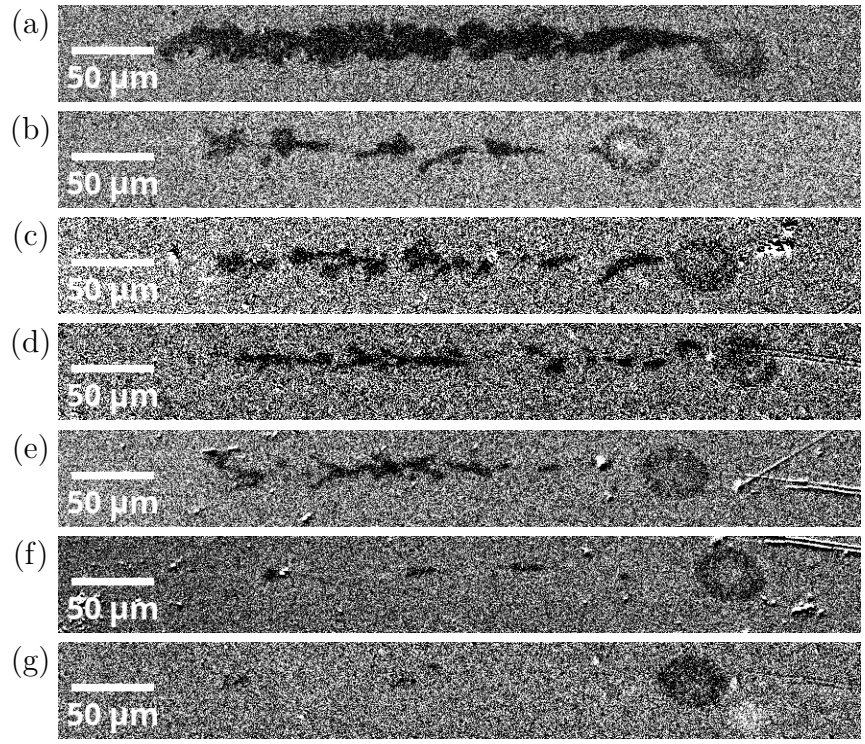

Figure 5.29: The effect of a historical field on optical exposure in SFi Sample A at 250K for various historical fields. The historical field is given by (a) 0mT, (b) 5mT, (c) 10mT, (d) 20mT, (e) 30mT, (f) 40mT and (g) 50mT. In each panel, the laser is pulsed at a 1000kHz repetition rate with pulses of 280fs width and 4.9mJ/cm^2 fluence.

the magnitude of historical field in (f) at 40mT and (g) at 50mT causes the ability switch or demagnetise to be lost almost entirely.

To help understand the reason for this historical field dependence, a WFKM loop for SFi Sample A at 250K is shown in figure 5.30. The first thing to note is that at this temperature, the polar coil cannot generate enough field to saturate the sample (i.e. bring it to the parralel P state) between measurements, and is only sufficient to return the sample to the desired AP state. A second observation, relevant to the behaviour seen in figures 5.28 and 5.29 is that there is a small change in Kerr contrast when sweeping the field past remanence when coming from the maximum field.

This change in contrast moves the signal closer towards net zero magnetisation at the AP level and raises questions as to what about the magnetic state changes at this drop and why it affects the response to optical exposure so strongly.

Re-examination of figure 5.16 shows a small bump at 0mT appearing both below and above, and yet near to T^A_{-R} at temperatures where the 104mT field is enough to bring the sample into the P state, indicating that the historical field effect is still present.

The main implication for the historical field effect with regards to AOS, is that any intentional or unintentional application of a field even if later removed may

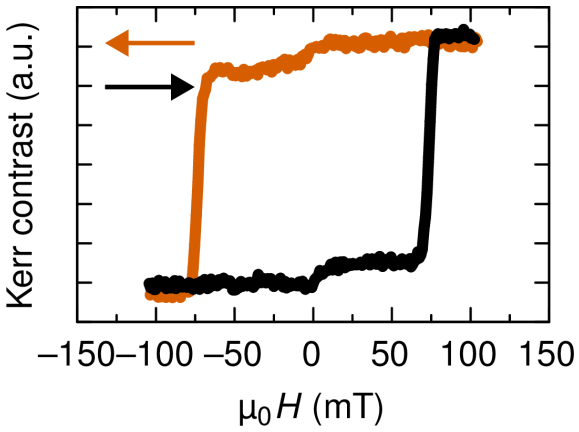

Figure 5.30: WFKM loop of SFi Sample A at 250K.

have a strong effect on the ability to observe AOS in these systems. The effect of wavelength remains unexplored for this class of materials.

5.3.2 Swept beam AOS

For many systems showing AOS, the beam can give rise to thermal demagnetisation at the high fluence central position of beam exposure and switching in an outer ring where the fluence is lower. By sweeping the beam position across the sample, switching from the outer ring takes precedence over length of the exposed stripe and thermal demagnetisation is seen only at position where beam exposure is ended [7, 8, 9]. This effect becomes particularly important in (multiple pulse) HD-AOS where a swept beam can be a requirement for full switching [10]. In $[Co/Pt]_N$ multilayers, the effect of the rate of beam sweep has been studied [11] and shown to give a higher (multiple pulse HD-AOS) switching percentage for lower sweeping speed. Sweeping of the beam was found to be an important factor in the optical switching of nickel-platinum multilayer based SFi's in this study, resulting in more consistent observation of HI-AOS.

For the images presented in what follows, the sample is first saturated with a 104mT out of plane field using the polar coil and then brought directly to remanence, and as such the behaviour presented is an all-optical effect. Once prepared, the sample is exposed to the pump laser, and swept quickly across the surface by rotation of the plane of a mirror.

In figure 5.31 AOS between AP states is shown in SFi Sample A at 289K. This temperature was chosen in order to balance the desire for high temperature with that for a strong contrast. For pulses of 2500fs width and 250kHz reptition rate, the fluence of 8.6mJ/cm^2 was found to be just above the critical threshold. The results show no clear helicity dependence, although for panels (a) and (d) it appears that the fluctuations in the beam fluence have brought it beneath the critical threshold for potions of the scan, resulting in sections of unswitched material. Above T^A_{-R} when HI-AOS no longer occurs, changes to the magnetic contrast resulting from

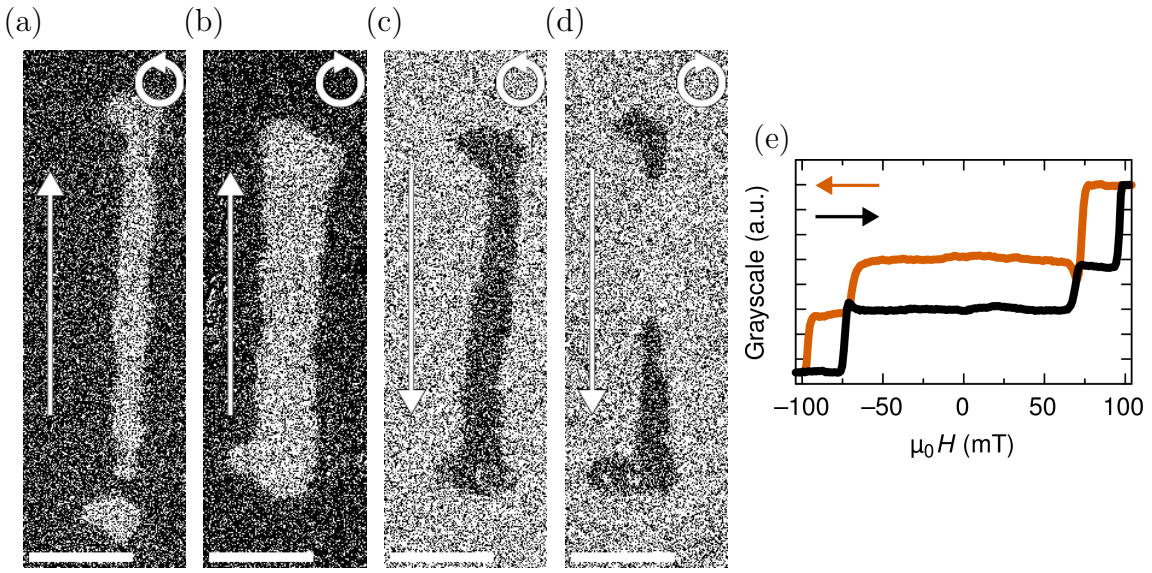

Figure 5.31: HI-AOS between AP states in SFi Sample A at 289K using (a,c) LCP and (b,d) RCP polarised light of fluence 8.6mJ/cm^2, 2500fs pulse width and 250kHz pulse reptition rate. Parts (a) and (b) show magnetic contrast change from $\mathbf{AP}^-$ to $\mathbf{AP}^+$ SFi states, whereas (c) and (d) show the reverse. In each case the beam is swept at a rate of approximately 150µm/s. Scale bars in the bottom left show a 50µm length. Panel (e) shows the WFKM hysteresis loop at 289K.

laser exposure become neglible.

In figure 5.32 AOS is shown in SFi Sample B at 330K. Panels (a), (b) and (c) show the result of exposure to a 116µm $1/e^2$ width, 1035nm wavelength pulsed beam with fluence (a) 2.4 mJ/cm^2 and (b,c) 3.4 mJ/cm^2, 280fs pulse width and 1MHz pulse repetition rate for (a) LP, (b) LCP and (c) RCP beams. The fluence for this image is slightly above the threshold for optically induced magnetisation changes with the parameters detailed. As the ability to switch is independent of the polarisation of the beam, the results indicate a helicity independent switching. For these representative images, the temperature of 330K was chosen to take the sample as close to the negative remanence temperature as possile while remaining below the negative temperature regime, as it was found that AOS is more easily obtained at higher temperatures. Panels (d), (e) and (f) show the same measurements performed for the opposite AP state (i.e. the reverse field history) and indicate no significant difference in the capacity for switching in the reverse direction. Above T^B_{-R} HI-AOS does not occur, and changes to the magnetic contrast resulting from laser exposure instead indicate thermal demagnetisation.

Figure 5.33 shows another example of AOS in SFi Sample B at 300K. In this image, the pulse width used is 10ps, two orders of magnitude larger than that used in figure 5.32 and the fluence has been raised to compensate for the increased threshold fluence of longer pulses. The results show no significant change to the AOS observed indicating that pulse width is not of major significance in AOS of Ni/Pt based SFi's.

Contrary to SFi's with a Ni_3Pt alloy base layer, there has been no observation of

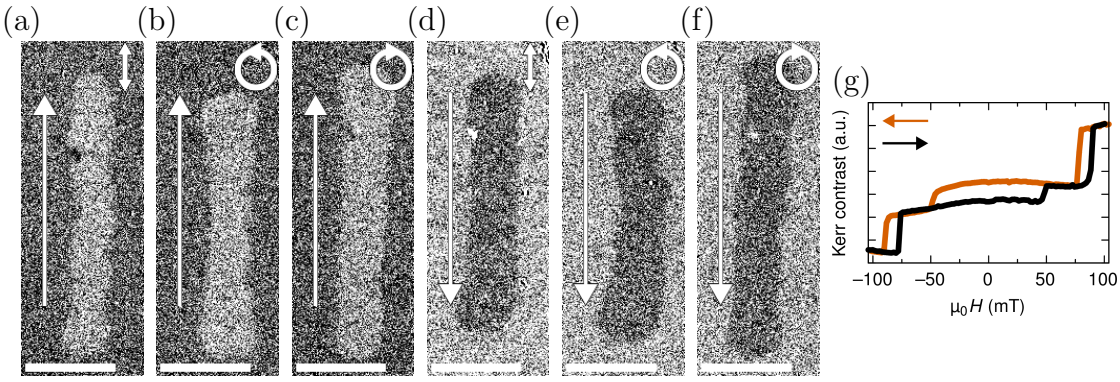

Figure 5.32: HI-AOS between AP states in SFi Sample B at 330K using (a,d) LP light of fluence 2.4mJ/cm^2, (b,e) LCP and (c,f) RCP polarised light of fluence 3.4mJ/cm^2, 1035nm wavelength, 280fs pulse width and 1MHz pulse reptition rate. Parts (a,b,c) show magnetic contrast change from $\mathbf{AP}^-$ to $\mathbf{AP}^+$ SFi states due to beam exposure, whereas (d,e,f) show the reverse. In each case the beam is swept at a rate of approximately 150µm/s. Scale bars in the bottom left shows a 50µm length. Panel (g) shows the WFKM hysteresis loop at 330K.

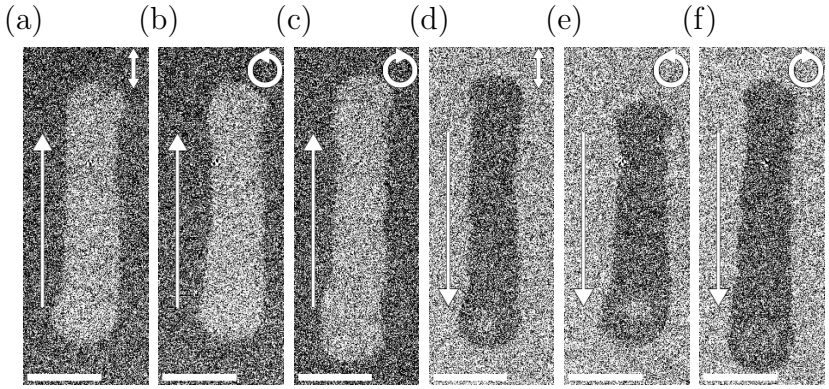

Figure 5.33: HI-AOS between AP states in SFi Sample B at 330K using (a,d) LP light of fluence 3.0mJ/cm^2, (b,e) LCP and (c,f) RCP polarised light of fluence 4.1mJ/cm^2, 1035nm wavelength, 10ps pulse width and 1MHz pulse reptition rate. Parts (a,b,c) show magnetic contrast change from $\mathbf{AP}^-$ to $\mathbf{AP}^+$ SFi states due to beam exposure, whereas (d,e,f) show the reverse. In each case the beam is swept at a rate of approximately 150µm/s. Scale bars in the bottom left shows a 50µm length.

toggle switching for these systems. The left hand column of figure 5.34 shows AOS in SFi Sample B resulting from a 4.7mJ/cm^2 beam swept from top to bottom at a rate of approximately 150µm/s. This is followed in the right hand column by a similar beam sweep from left to right, over the initially switched region, and shows that at the intersection of the swept regions, there is no return to the initial AP state. It is important to note that the unidirectional switching is not a permanent effect, as a new monodomain, with optically switchable remanent state can be prepared using an external magnetic field.

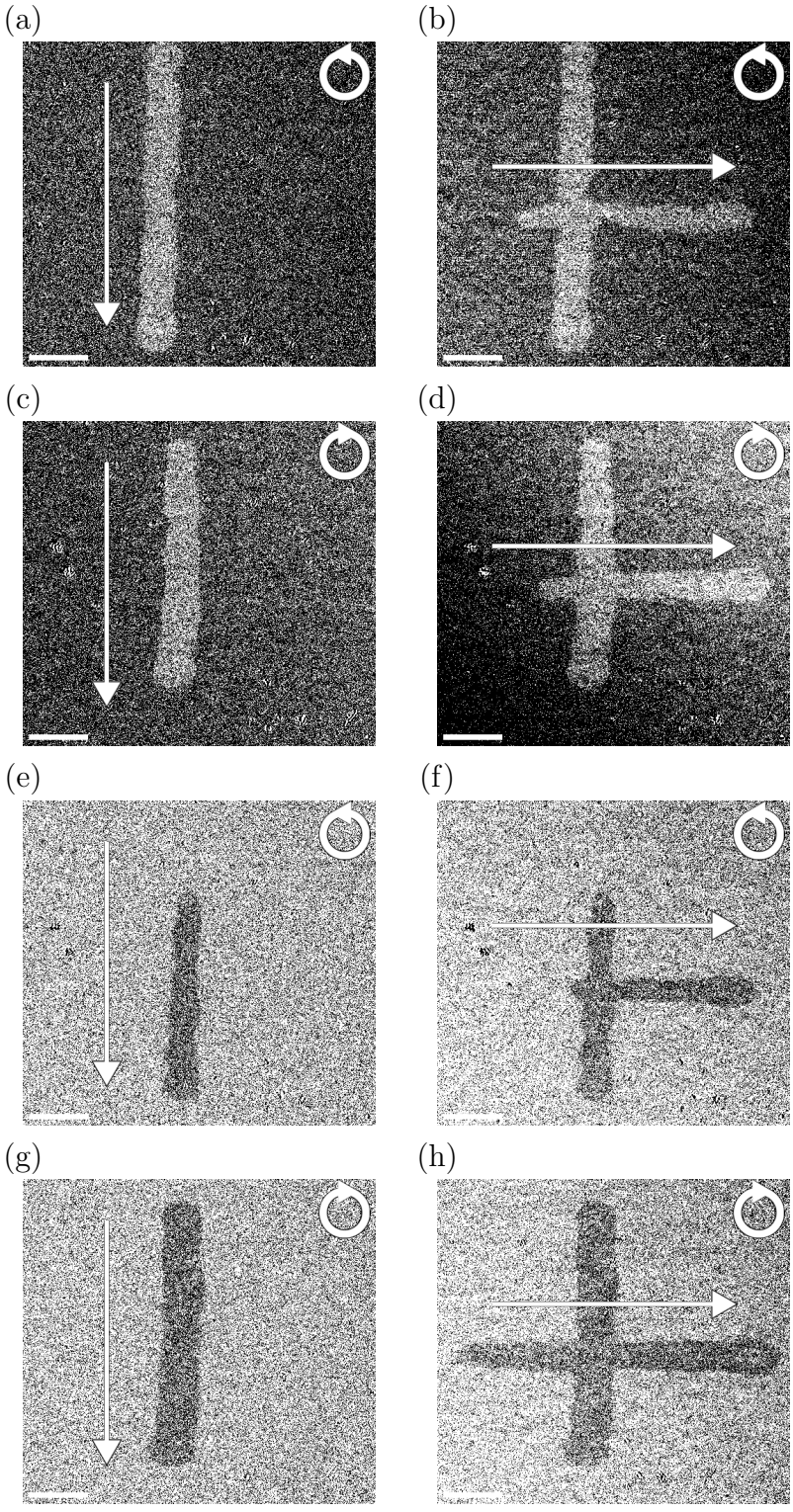

Figure 5.34: Images of Sample B at 330K showing an initial vertical scan (left column) of a 1035nm, 10ps, 1MHz beam with fluence 4.7mJ/cm^2, followed by a horizontal scan with the same parameters (right column) through the vertically swept region. Each row shows the following beam helicity and background state, (a,b) LCP on $\mathbf{AP}^-$, (c,d) RCP on $\mathbf{AP}^-$, (e,f) LCP on $\mathbf{AP}^+$ and (g,h) RCP on $\mathbf{AP}^+$. The swept regions show AOS but the reverse is not found at the interesection of the two scans, indicating a single direction of switching which cannot be rewritten in an all optical fashion. Scale bars in the bottom left shows a 50µm length.

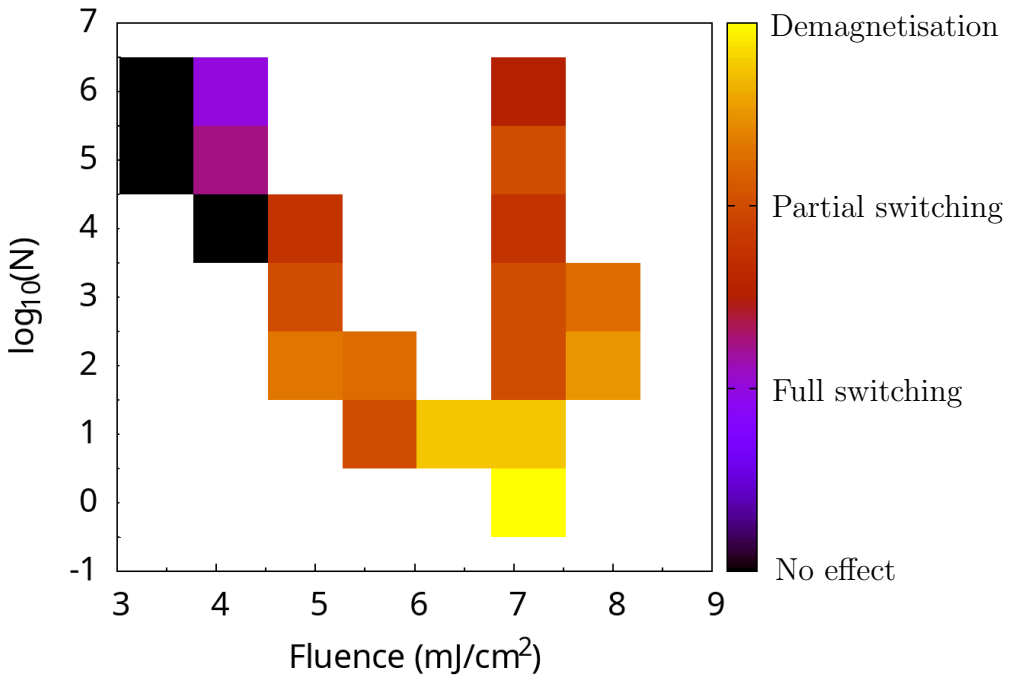

Figure 5.35: A matrix to display the known fluence and number of pulses required for all optical switching at temperature 330K in Sample B using a static beam with pulse width of 10ps, pulse repetition rate of 1MHz and 1035nm wavelength. Determination is based on the average behaviour of four measurements, one for each AP state and circular polarisation of the beam.

5.3.3 Static Beam Measurements

In addition to AOS acheived by scanning the laser beam across the surface, AOS was also observed in both samples with a beam kept at a constant position.

Figure 5.35 shows a matrix of the effects of static beam switching for given pulse fluence and number of pulses applied at a 1MHz rep rate. The colour of each point is determined by the average of four measurements - one for each AP state and polarisation. If no effect is found in any of the four measurements then a black square is assigned. Otherwise each measurements is given a value 1 for full switching, 2 for partial switching and 3 for demagnetisation, and the average across the images which show an effect for the given parameters is taken. The resulting average is converted back into the corresponding colour in the scale and shown in the figure. From this figure it can be seen that AOS occurs just above the threshold fluence (at $\approx$4.1mJ/cm^2) for large ($N \geq 10^5$) numbers of pulses. As can be seen for smaller number ($10 < N < 1000$) of pulses, increasing the fluence does not lead to an improvement in the switching ability. At fluence 7.1mJ/cm^2, there were no observations of (full) AOS. This indicates that the case for observing single pulse switching in these samples is unlikely with the material stacks considered, and that the number of pulses required for switching is comparable to that found for Ni_3Pt based SFi's.

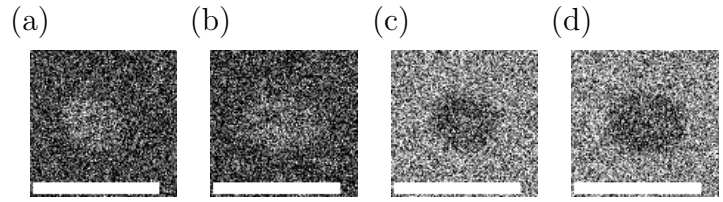

Figure 5.36: Static beam HI-AOS in SFi Sample B at 330K using 10^5 pulses of (a,c) LCP and (b,d) RCP polarised light of fluence 4.1mJ/cm^2, 1035nm wavelength, 10ps pulse width and 1MHz pulse reptition rate. Parts (a) and (b) show magnetic contrast change from $\mathbf{AP}^-$ to $\mathbf{AP}^+$ SFi states, whereas (c) and (d) show the reverse. Scale bars in the bottom left show a 50µm length.

In figure 5.36 the results for static beam switching in SFi Sample B at 330K are shown for 10^5 pulses with 4.1mJ/cm^2 fluence, 10ps pulse width and 1MHz pulse reptition rate are shown as an example of the static beam data collected. For this set, three of the images (shown in panels (a), (c) and (d)) show clear AOS as determined by the change in contrast as compared to the effect of a change in contrast induced by an exposure to a continuous beam with a 5mT bias field. The other spot shows partial demagnetisation according to the same analysis. Therefore the colour matrix shown in figure 5.35 takes a purple colour at those parameters to indicate that three in four measurements showed full switching, while the remaining showed partial switching.

Figure 5.37 shows static beam exposure in SFi Sample A at 250K for a range of pulse numbers with parameters 7.1mJ/cm^2 fluence, 2.5ps pulse width and 1MHz pulse repetition rate. The contrast in these images is strong and more obvious in meaning than the measurements in SFi Sample B at 330K, making them possible to compare and analyse visually. These measurements show a range of behaviour. When only a single pulse is applied, there is no effect on the contrast observed. For 10 pulses only the LCP beam shows demagnetisation. With 10^2 pulses three out of four show demagnetisation. For 10^3, and 10^4 all images show demagnetisation. For 10^5 pulses the LCP beam applied to an $\mathbf{AP}^+$ state shows an example of partial switching, with the left part of the ellipse showing greater contrast than the right half, indicating switching on the left and demagnetisation on the left. A RCP beam applied to $\mathbf{AP}^+$ does not give any effect, which is assumed to be an outlier. Applications of 10^5 pulses to an $\mathbf{AP}^-$ state gave demagnetisation in both cases. For 10^6 pulses three of four measurements show switching, with RCP applied to $\mathbf{AP}^+$ showing demagnetisation.

Figure 5.38, shows static beam thermal demagnetisation split into a two step process. In the first step, 100 pulses of a high fluence are applied to positions in this sample which have been prepared into specific AP states. The result of these pulses is to demagnetise the exposed locations in a homogeneous fashion, introducing a third greyscale contrast to the image since no domains are visible within these demagnetised ellipses.

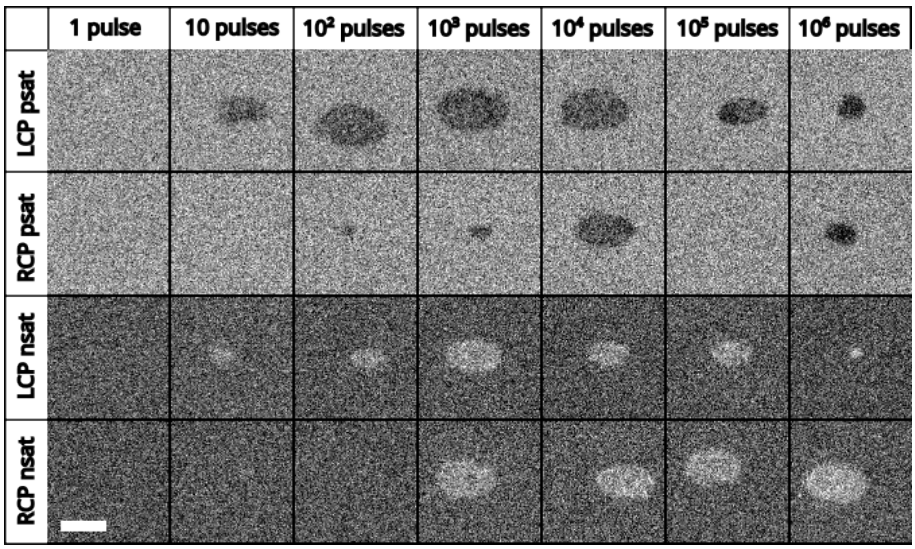

Figure 5.37: Optical exposure of SFi Sample A at 250K using a static beam. The number of 2500fs width, 7.1mJ/cm^2 fluence pulses is varied by factors of ten for each circular polarisation and AP state. The label 'nsat' refers to preparation of the sample in the $\mathbf{AP}^-$ state prior to optical exposure, while 'psat' refers to preparation in the $\mathbf{AP}^+$ state. A scalebar in the bottom left shows a distance of 20µm.

In the second step, a varied number of lower fluence pulses are applied to the sample. At the chosen fluence of 3.4mJ/cm^2 no change is found to the magnetisation state of the exposed regions as the fluence threshold for the specific conditions is not met. Regardless, the effect of this second step is generally an increase in the size of the domains within the exposed regions. It is clear that the size of these domains increases with the number of pulses, indicating a cumulative process of remagnetisation induced by a temperature somewhere between the ambient temperature of the sample, and the Curie temperature.

This result helps to understand why in general, the ability to see AOS is far easier when sweeping the beam, rather than keeping the beam static, since temperatures corresponding to the lower fluence will be applied to the initially demagnetised position as the outer parts of the Gaussian beam are subsequently swept across the central demagnetised spot. It also explains why in figures 5.26 and 5.27, a higher repetition rate leads to larger domains, which is because at higher rates, a larger number of pulses will be applied as the beam is swept, increasing the size of these domains further than for smaller rates. This also explains our observation that sweeping the beam more slowly leads to better AOS results.

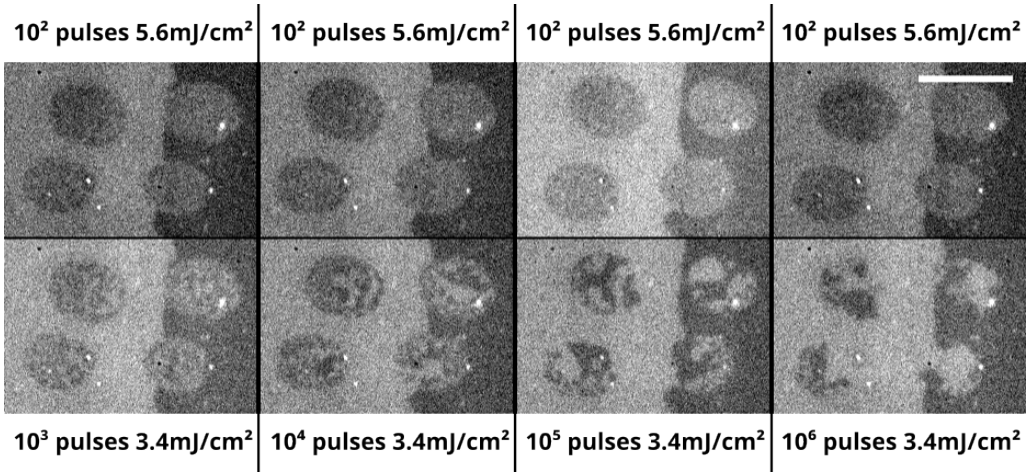

Figure 5.38: A two step process performed at 250K where Sample A is first exposed to a beam with high fluence (5.6mJ/cm^2 shown in the top row), followed by a beam with lower fluence (3.4mJ/cm^2 shown in the bottom row) at the same locations. Each column from left to right has an additional order of magnitude of pulses in the second step starting with 10^3 and reaching up to 10^6. In each image, the background is separated into to halves by a domain wall, with $\mathbf{AP}^+$on the left hand side and $\mathbf{AP}^-$on the right. The two exposed regions at the top of each image are pulsed with LCP light, while the bottom two are exposed with RCP light. In each case, the beam has a 1000kHz repetition rate of pulses with 280fs width. A scalebar at the top right shows a 50µm length.

5.4 Time Resolved Magneto Optical Kerr Effect

In order to better understand the mechanisms by which AOS occurs, the ultrafast magnetisation dynamics of the cobalt reference layer, Ni/Pt Referance A and SFi Sample B were measured using time-resolved pump probe MOKE measurements described in section 3.3.

As shown in section 5.3.3, AOS in these samples requires on the order of 10^6 pulses. As a remagnetisation field is constantly applied during the measurements made in this section, only effects of a single initial pulse on the sample, set by the field applied to either a saturated, or in the case of SFi's an AP state, is observed, and therefore any direct observation of switching behaviour is unlikely to be found here. Regardless of this, TR-MOKE is a useful technique to understand how the system responds to optical pulses on a picosecond timescale, and can add to the understanding of how the AOS mechanism may occur.

5.4.1 Demagnetisation

Figure 5.39 shows the sub-picosecond demagnetisation of the cobalt reference layer with varied fluence. The maximum demagnetisation is achieved with a fluence upper limit of 11.3mJ/cm^2. Beyond that, the time required to remagnetise rises from the order of a few picoseconds to over 100ps. This is likely to be due to an increase in the time required for the heat deposited into the probed area of the sample to disperse.

Figure 5.40 shows that the demagnetisation of the cobalt layer is not significantly effected by the magnitude of field applied.

Figure 5.41 shows that the nickel platinum Reference A multilayer has a significantly lower fluence requirement of 3.8mJ/cm^2 to achieve full demagnetisation, compared to the cobalt layer. Figure 5.42 shows that beyond 58mT the demagnetisation of nickel platinum Reference A multilayer is unaffected by the out-of-plane field applied to remagnetise it. At small fields, the time taken to remagnetise increases significantly. In panel (c) of figure 5.42, the reduction from 58mT to 4.5mT results in an approximate doubling of the remagnetisation time from 1ns to 2ns. This could be a result of a loss of PMA in this layer at higher temperatures (similar to that seen for Reference B in figure 5.9), resulting in the magnetisation lying in the plane of the sample.

A comparison of the picosecond scale dynamics of the cobalt and nickel platinum (A) reference samples is shown in figure 5.43. The rate of demagnetisation is seen to be 2.6 times faster for the Ni/Pt layer. This meets the requirement of different demagnetisation rates for each layer required for the AOS mechanism of spin current transfer between ferromagnetic layers [1, 12].

The ultrafast demagnetisation of SFi samples can depend on whether the mag-

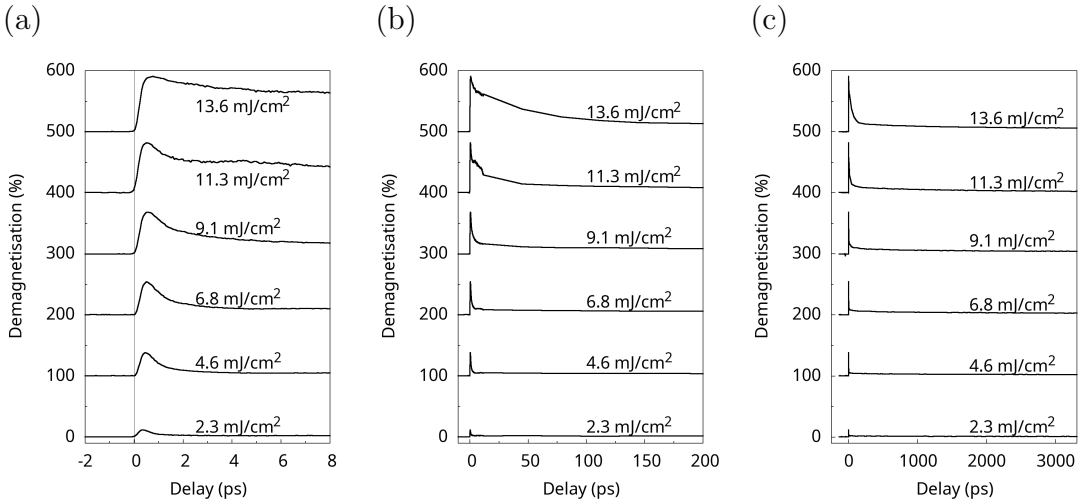

Figure 5.39: Time-resolved magneto optical Kerr effect (TR-MOKE) pump-probe measurements of cobalt reference layer with a 326mT out of plane applied field and varied fluence. Between the panels shown, the signal is shown on a time scale of (a) 8ps, (b) 200ps, (c) 3ns. The demagnetisaton percentage is based upon comparison of the signal magnitude to the height of the static MOKE hysteresis loop measured in the same setup. The experiment setup is shown in figure 3.6 and uses a pulsed laser source with 100kHz rep rate, 50fs pulse width, 800nm wavelength pump pulse and 400nm probe pulse.

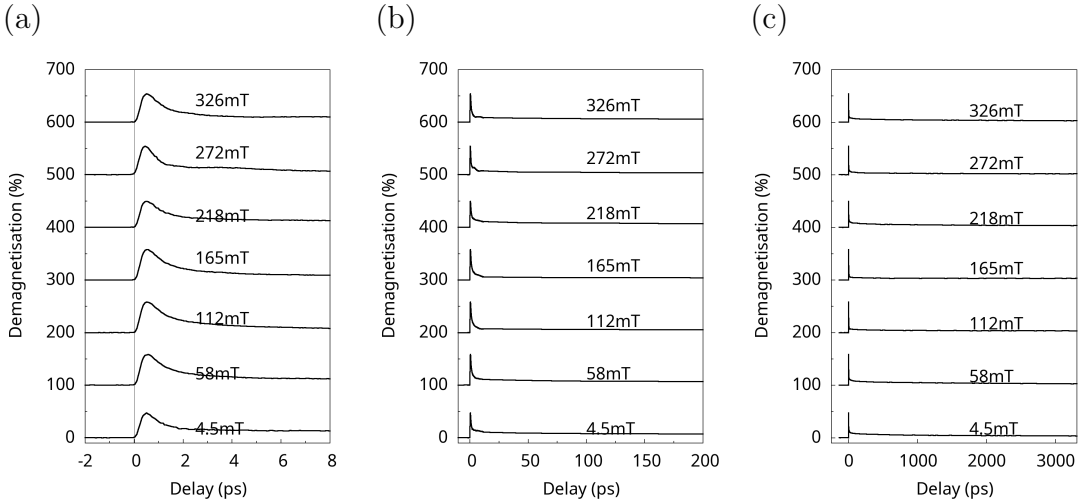

Figure 5.40: TR-MOKE pump-probe measurements of cobalt reference layer with a pump fluence 6.8 mJ/cm^2 and varied out of plane field. Between the panels shown, the signal is shown on a time scale of (a) 8ps, (b) 200ps, (c) 3ns. The demagnetisaton percentage is based upon comparison of the signal magnitude to the height of the static MOKE hysteresis loop measured in the same setup. The experiment setup is shown in figure 3.6 and uses a pulsed laser source with 100kHz rep rate, 50fs pulse width, 800nm wavelength pump pulse and 400nm probe pulse.

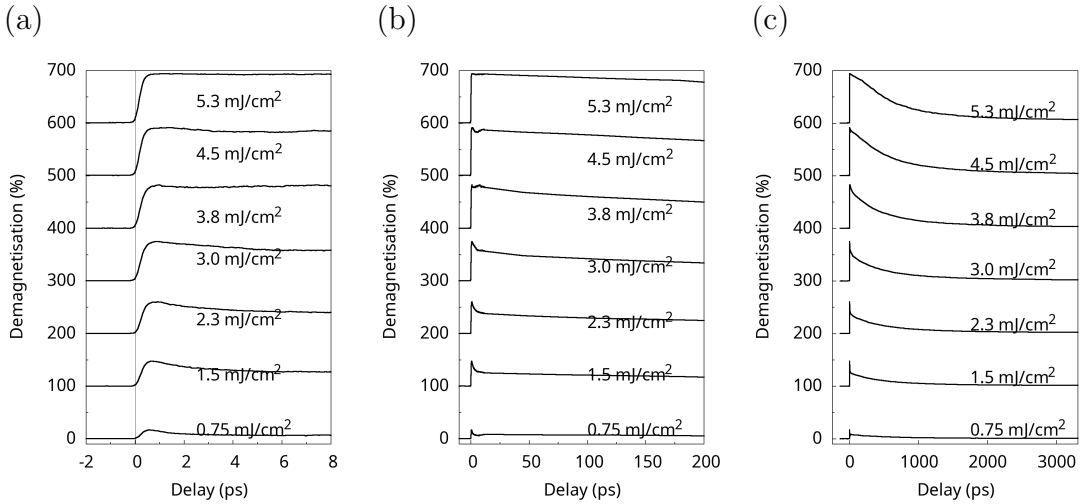

Figure 5.41: TR-MOKE pump-probe measurements of Ni/Pt A reference layer with a 326mT out of plane applied field and varied fluence. Between the panels shown, the signal is shown on a time scale of (a) 8ps, (b) 200ps, (c) 3ns. The demagnetisaton percentage is based upon comparison of the signal magnitude to the height of the static MOKE hysteresis loop measured in the same setup. The experiment setup is shown in figure 3.6 and uses a pulsed laser source with 100kHz rep rate, 50fs pulse width, 800nm wavelength pump pulse and 400nm probe pulse.

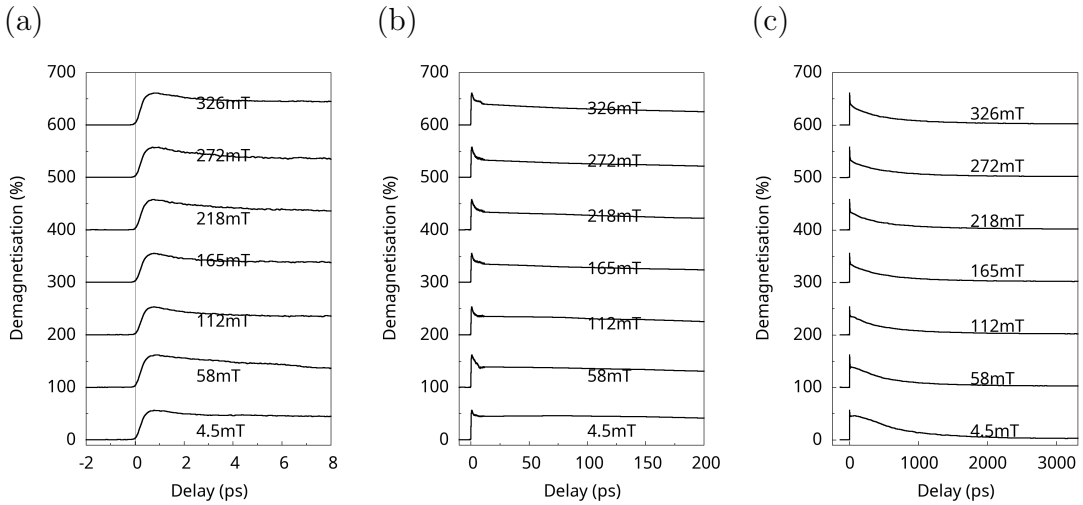

Figure 5.42: TR-MOKE pump-probe measurements of Ni/Pt A reference layer with a pump fluence 2.3 mJ/cm^2 and varied out of plane field. Between the panels shown, the signal is shown on a time scale of (a) 8ps, (b) 200ps, (c) 3ns. The demagnetisaton percentage is based upon comparison of the signal magnitude to the height of the static MOKE hysteresis loop measured in the same setup. The experiment setup is shown in figure 3.6 and uses a pulsed laser source with 100kHz rep rate, 50fs pulse width, 800nm wavelength pump pulse and 400nm probe pulse.

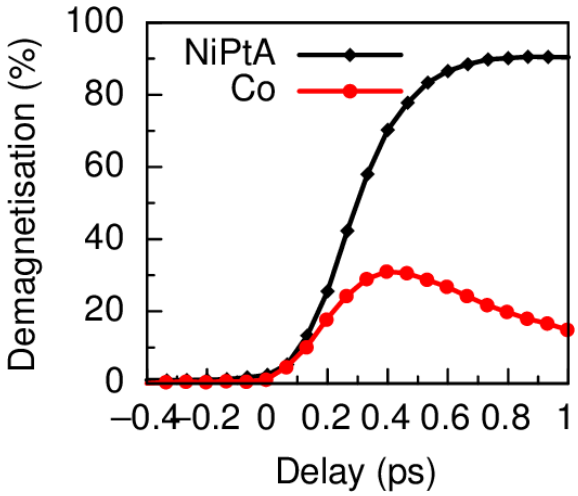

Figure 5.43: A comparison of the demagnetisation rate in the Co reference and Ni/Pt Reference A layers on femtosecond timescales. In each case, the pump fluence is 6mJ/cm^2, and a 300mT out of plane field is applied.

netisation of the layers is prepared in a parallel (P) or antiparallel (AP) state [1]. To determine suitable external fields for use in TR-MOKE measurements of these states, a static MOKE loop is performed using the same experimental setup. This loop is shown in figure 5.44, and displays a strong contrast between all four possible magnetic states. The loop shows that a field of between 50mT and 100mT should be applied in the out of plane direction to prepare an AP state, while greater than 130mT is needed to prepare a P state. It is important to keep in mind that an electromagnet continuously generating a magnetic field will heat up over time, reducing the magnetic field output. Because of this, a field at the higher end of the range is preferable, to avoid the possibilty of losing a field sufficient to reset to the desired state over the course of an experiment.

In figure 5.45 the ultrafast demagnetisation is shown for SFi Sample B in the P state at various fluences. The data shows that the sample can be fully demagnetised by a pump beam with fluence 8.3mJ/cm^2 on a sub-picosecond timescale.

Figure 5.46 shows the ultrafast demagnetisation SFi Sample B in the AP state at various fluences. The demagnetisation remains constant between 2.9mJ/cm^2 and 4.9mJ/cm^2 , indicating that the Ni/Pt layer has fully demagnetised at these fluences, with little difference in the demagnetisatoin of the Co layer. At 6.8mJ/cm^2 the demagnetisation raises further as the cobalt layer also begins to demagnetise to a significant extent. The picosecond scale demagnetisation shown in panel (a) displays an inflexion point in the middle of the approximately 2ps demagnetisation. This inflexion is an observation of the different rate of demagnetisation for the two layers within the exchange coupled stack.

The dependence of ultrafast demagnetisation in SFi Sample B on applied field with pump fluence of 2.3mJ/cm^2 is shown in figure 5.47. While the fluence is too low to have a significant effect on the cobalt layer of the sample, a clear increase in

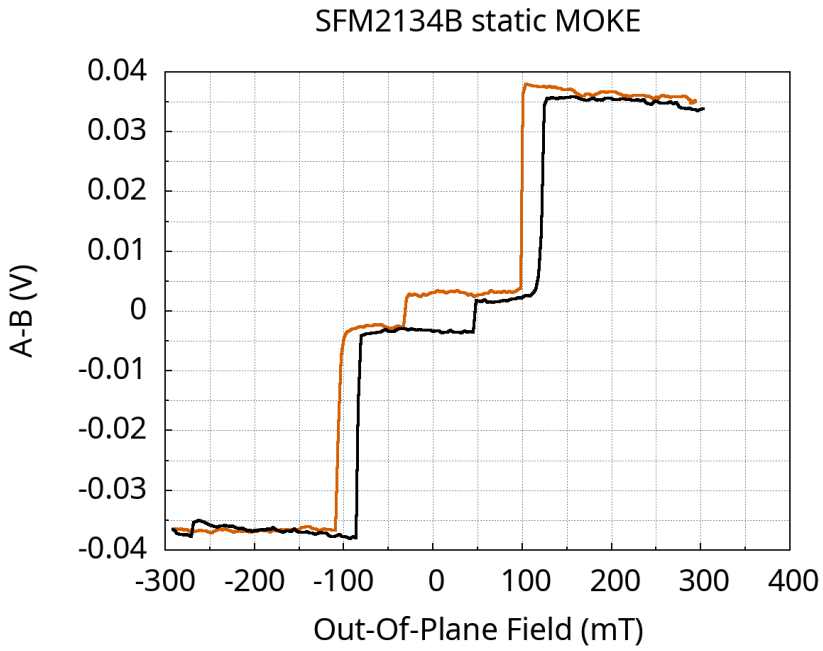

Figure 5.44: MOKE loop of Sample B at room temperature.

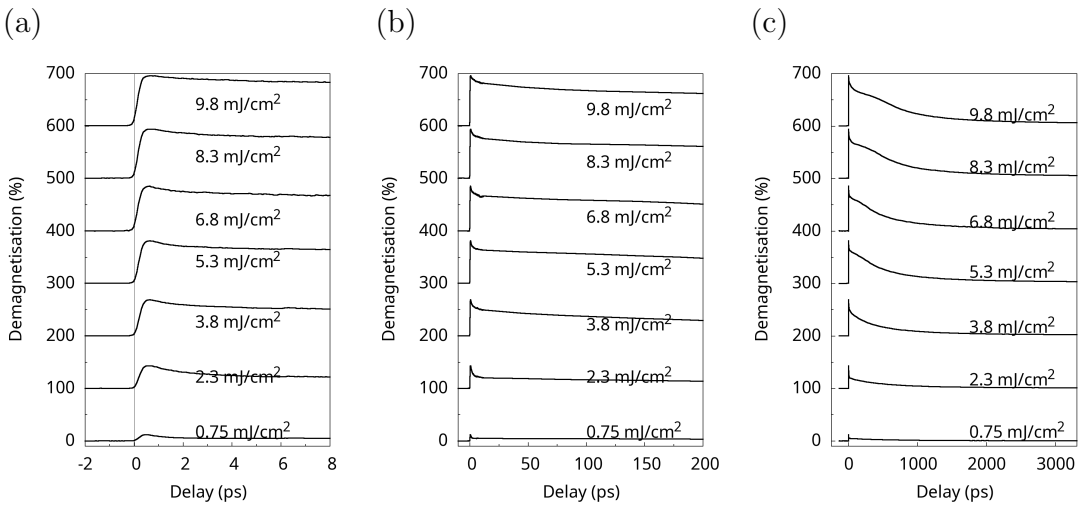

Figure 5.45: TR-MOKE pump-probe measurements of SFi Sample B with a 326mT out of plane applied field and varied fluence. Between the panels shown, the signal is shown on a time scale of (a) 8ps, (b) 200ps, (c) 3ns. The demagnetisaton percentage is based upon comparison of the signal magnitude to the height of the static MOKE hysteresis loop measured in the same setup. The experiment setup is shown in figure 3.6 and uses a pulsed laser source with 100kHz rep rate, 50fs pulse width, 800nm wavelength pump pulse and 400nm probe pulse.

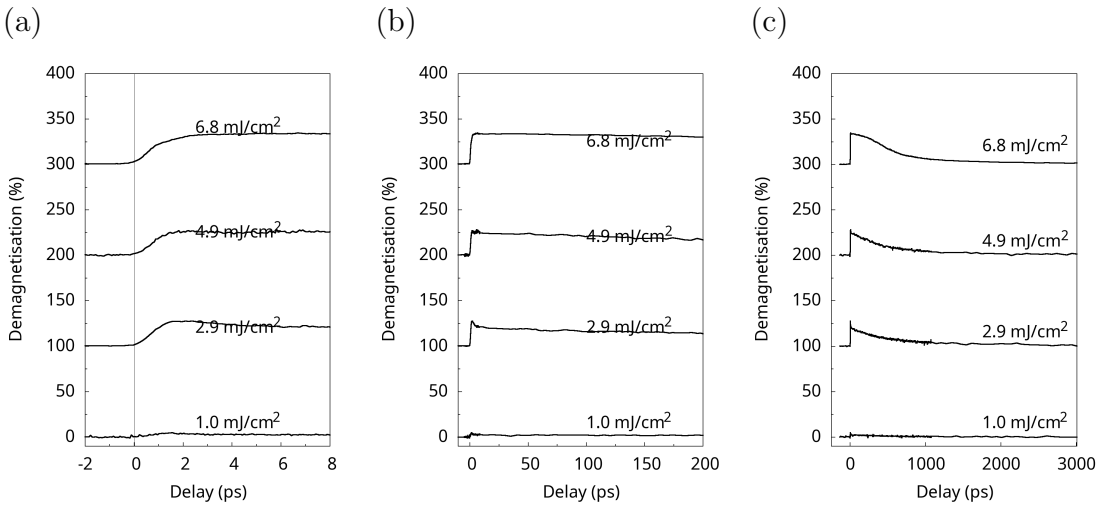

Figure 5.46: TR-MOKE pump-probe measurements of SFi Sample B with a 100mT applied field and varied fluence. Between the panels shown, the signal is shown on a time scale of (a) 8ps, (b) 200ps, (c) 3ns. The demagnetisaton percentage is based upon comparison of the signal magnitude to the full height of the static MOKE hysteresis loop measured in the same setup. The experiment setup is shown in figure 3.6 and uses a pulsed laser source with 100kHz rep rate, 50fs pulse width, 800nm wavelength pump pulse and 400nm probe pulse.

magnitude of the signal can be seen between applied fields of 58mT and 112mT, as the initial state of the sample is switched from AP to P.

5.4.2 Precession

Precessional dynamics in the cobalt reference layer, induced by a 2.7mJ/cm^2 pulse with a field directed in the sample plane are shown in figure 5.48. As the in plane field is increased, the demagnetisation signal at zero delay decreases in magnitude, while the precessional signal amplitude increases. The precession can be seen for approximately two full cycles indicating a strong damping in this system.

The precessional frequency was extracted from a Fourier transform of each signal implemented in Python (using the scipy fftpack library) and is shown in figure 5.49 as a function of field. Due to the weak precessional signal below 200mT, it has only been possible to extract a precession frequency from the data in figure 5.48 for 196mT and above. The data shows a general trend of reduced frequency with increasing field.

The time-resolved precession dynamics of Ni/Pt Reference layer A are shown in figure 5.50. Like in the cobalt layer data, the pulse fluence is 2.7mJ/cm^2, and the resulting precession is strikingly similar in features and trend.

The precession frequency is extracted through the Fourier transform and plotted in 5.51. This shows that for both uncoupled reference layers the precession frequency decreases with applied field.

Precession in SFi Sample B is shown in figure 5.52. For this sample, the precession dynamics show a significant change in behaviour, with generally stronger

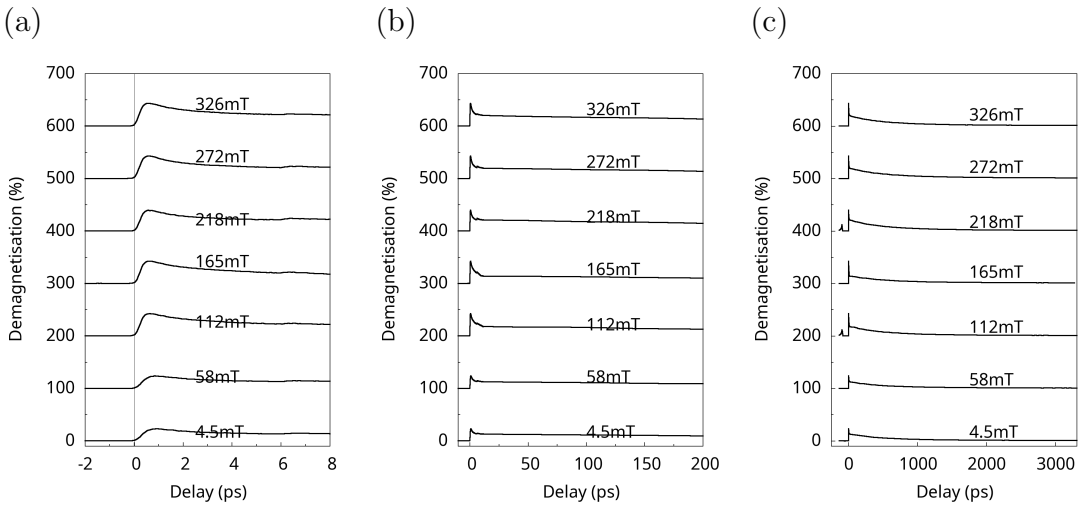

Figure 5.47: TR-MOKE pump-probe measurements of SFi Sample B with a pump fluence 2.3 mJ/cm^2 and varied out of plane field strength. Between the panels shown, the signal is shown on a time scale of (a) 8ps, (b) 200ps, (c) 3ns. The demagnetisaton percentage is based upon comparison of the signal magnitude to the height of the static MOKE hysteresis loop measured in the same setup. The experiment setup is shown in figure 3.6 and uses a pulsed laser source with 100kHz rep rate, 50fs pulse width, 800nm wavelength pump pulse and 400nm probe pulse.

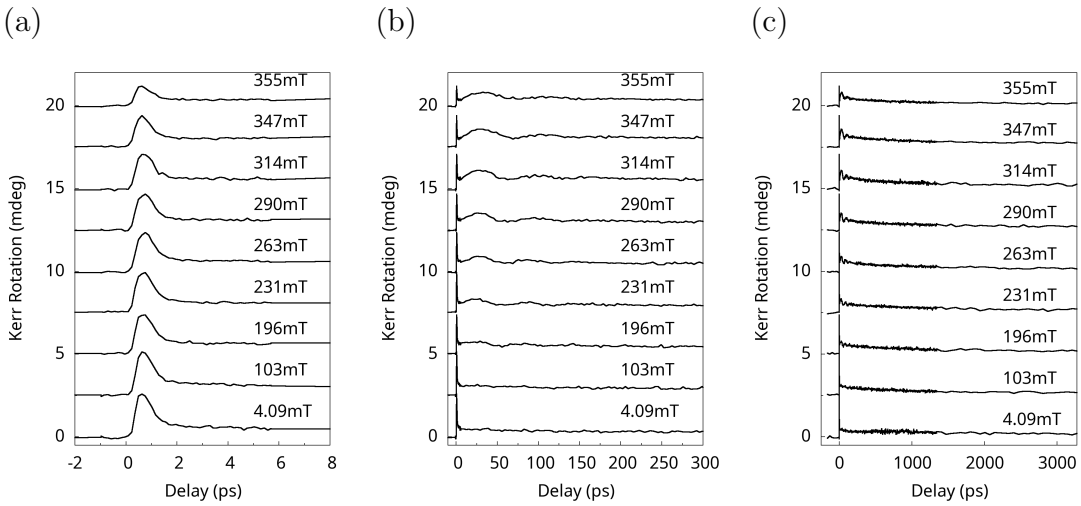

Figure 5.48: TR-MOKE pump-probe measurements of precession in the cobalt reference layer with a pump fluence 2.7 mJ/cm^2 and varied in plane field. Between the panels shown, the signal is shown on a time scale of (a) 8ps, (b) 200ps, (c) 3ns. The experiment setup is shown in figure 3.6 and uses a pulsed laser source with 100kHz rep rate, 50fs pulse width, 800nm wavelength pump pulse and 400nm probe pulse.

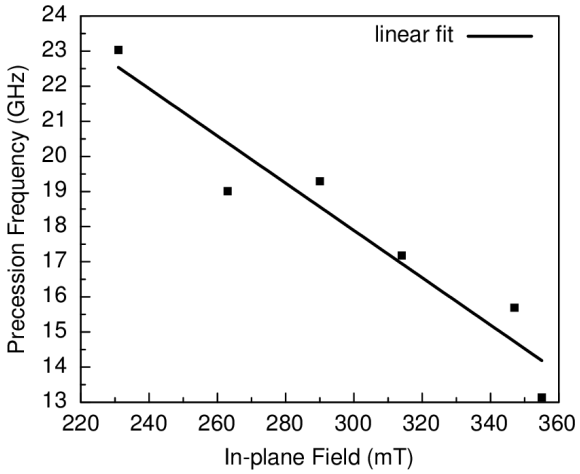

Figure 5.49: Precession frequency vs. field for the cobalt reference layer. The precession frequency (black squares) is extracted from the fast Fourier transform spectra of the TR-MOKE data shown in figure 5.48, where a 2.7 mJ/cm^2 pulse is used to induce precession of the spins in the thin film. The process of parameter extraction is explained in section 3.3.9. A linear fit to the data is shown by the black curve.

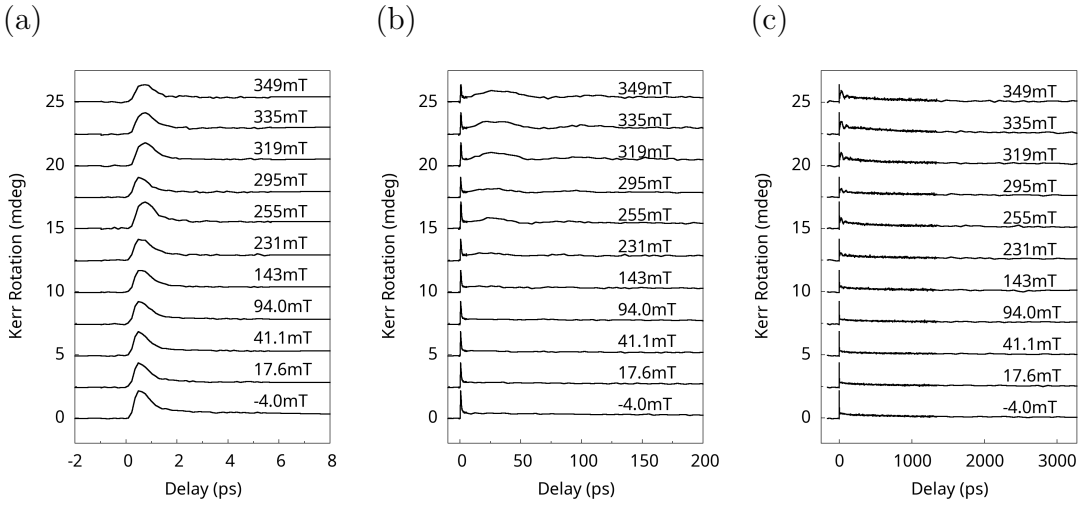

Figure 5.50: TR-MOKE pump-probe measurements of precession in Ni/Pt Reference A with a pump fluence 2.7 mJ/cm^2 and varied in plane field. Between the panels shown, the signal is shown on a time scale of (a) 8ps, (b) 200ps, (c) 3ns. The experiment setup is shown in figure 3.6 and uses a pulsed laser source with 100kHz rep rate, 50fs pulse width, 800nm wavelength pump pulse and 400nm probe pulse.

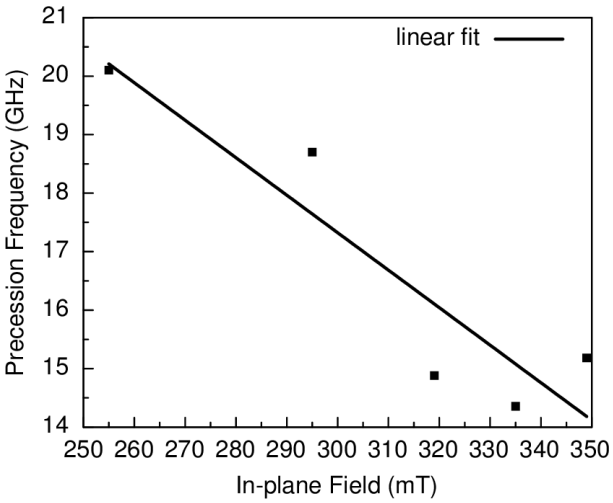

Figure 5.51: Precession frequency vs. field for the Ni/Pt Reference A multilayer. The precession frequency (black squares) is extracted from the fast Fourier transform spectra of the TR-MOKE data shown in figure 5.50, where a 2.7 mJ/cm^2 pulse is used to induce precession of the spins in the thin film. The process of parameter extraction is explained in section 3.3.9. A linear fit to the data is shown by the black curve.

precessional signal, and lower frequency. As can be seen clearly from the extracted frequencies in figure 5.53, compared to the uncoupled reference layers, the full SFi stack shows the opposite dependence of frequency with respect to the in-plane field. In this sample the frequency increases with field. This suggests a significant difference in the dynamics of the net magnetisation, compared to the ferromagnetic constituent layers.

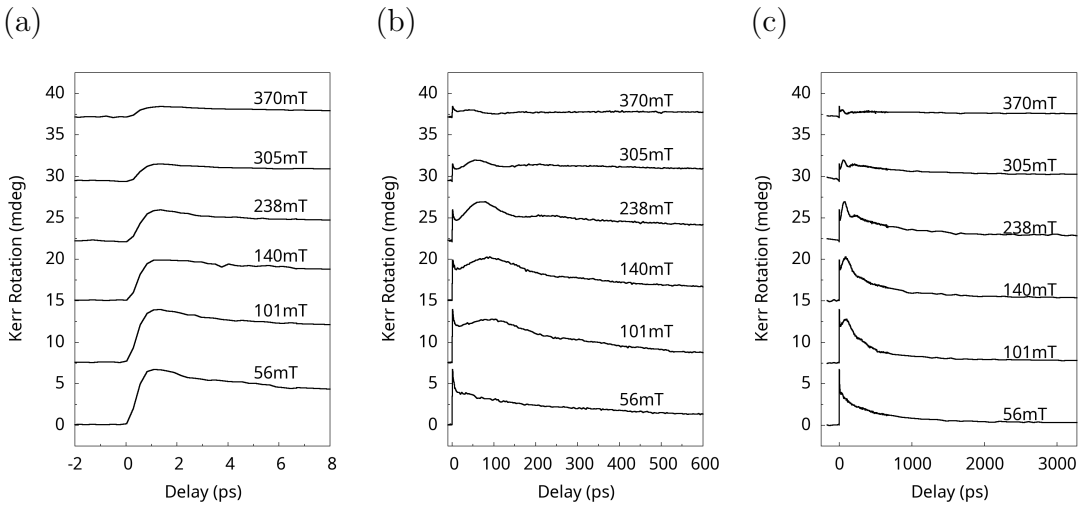

Figure 5.52: TR-MOKE pump-probe measurements of precession in SFi Sample B with a pump fluence 2.9 mJ/cm^2 and varied in plane field. Between the panels shown, the signal is shown on a time scale of (a) 8ps, (b) 200ps, (c) 3ns. The experiment setup is shown in figure 3.6 and uses a pulsed laser source with 100kHz rep rate, 50fs pulse width, 800nm wavelength pump pulse and 400nm probe pulse.

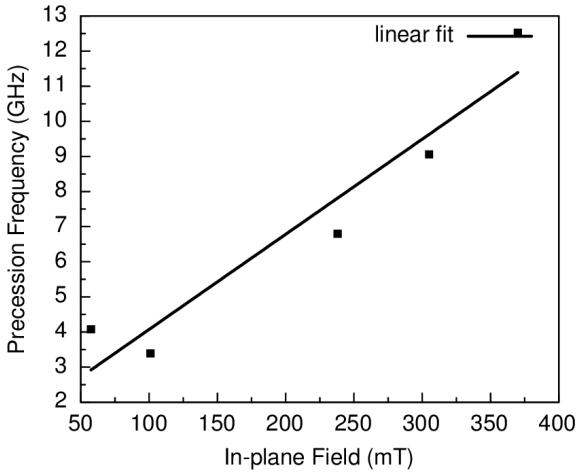

Figure 5.53: Precession frequency vs. field for the SFi Sample B multilayer. The precession frequency (black squares) is extracted from the fast Fourier transform spectra of the TR-MOKE data shown in figure 5.50, where a 2.7 mJ/cm^2 pulse is used to induce precession of the spins in the thin film. The process of parameter extraction is explained in section 3.3.9. A linear fit to the data is shown by the black curve.

5.5 Discussion

Using wide field Kerr microscopy (WFKM), all optical switching (AOS) has been observed in [Ni/Pt] based synthetic ferrimagnets (SFi's). As in the Ni_3Pt based SFi's examined previously [1], AOS was found to be helicity independent allowing reversal between anti-parallel states. Similarly large number of pulses ($> 10^5$) are required, despite the enhanced interlayer exchange coupling. The phenomenon of AOS was again indicated to be driven by a spin current mediated by the iridium interlayer. Unlike in Ni_3Pt based samples, the [Ni/Pt] SFi's display a unidirectional switching, without the ability to toggle switch in a purely optical fashion. The history of field applied to the sample was also shown to play a significant role in the capacity for AOS, which was not observed previously. The increased tunability of samples resulting from the multilayer has allowed for an increase in the temperatures at which AOS is observed. This is related to an increase in the negative remanence temperature, above which AOS cannot be seen, and below which better switching is seen for higher ambient temperatures.

The negative remanence behaviour was studied in greater detail for these samples through observation of the domains that form at the negative remanence temperature. At these temperatures, it was seen that when reducing the field from saturation (parallel state), the all optically switchable positive remanence (antiparallel state) domains form subsequently to (antiparallel state) negative remanence domains. Those positive remanence domains grow most quickly at a specific switching field and growth was found to slow to a halt at remanence, further highlighting the importance of field history. The rate of growth of these domains was found to have an exponential dependance on temperature, with the formation of switchable domains occuring rapidly at low temperatures.

The unidirectional all optical switching is indicative of the formation of an unresolvable domain structure or magnetic defects upon AOS, which result in pinning of the local magnetisation state. This effect means that further optical exposure can no longer effect the state without the subsequent application of an external field to unpin the magnetic structure. Unidirectional switching is closely related to the effect of historical bias fields, in that bias fields allow bidirectional switching via thermal demagnetisation (shown in figure 5.28). The loop shown in figure 5.30 shows a small change in contrast indicating a minor change to the magnetic state that is not visible in the individual WFKM images. This small variance within AP states and significant difference in response to optical exposure gives additional evidence for the formation of an unseen magnetic structure which pins the state.

Time resolved magneto optical Kerr effect (TR-MOKE) measurements show different ultrafast demagnetisation of the two ferromagnetic layers within the SFi. This can be seen by comparison of the demagnetisation rate of uncoupled reference lay-

ers as shown in figure 5.43, and also for the coupled layers within the SFi stack through the inflexion at 6.8mJ/cm^2 fluence in figure 5.46a. This, along with the helicity independent multiple pulse nature of AOS, indicates the transfer of angular momentum between the layers by a transient spin current [1].

In addition to measurements of ultrafast demagnetisation, TR-MOKE was used to observe the precessional dynamics of a Ni/Pt based SFi, and uncoupled ferromagnetic layers. In contrast to the uncoupled layers, the full stack shows a precession frequency proportional to the magnitude of in-plane field. This shows the significant role of interlayer exchange in the magnetisation dynamics when the SFi is taken out of equilibrium.

5.6 Summary

A combination of wide field Kerr microscopy and time resolved Kerr measurements has been used to examine the ultrafast dynamics of Ni/Pt multilayer based synthetic ferrimagnets induced by optical excitation. As in Ni_3Pt based SFi's these samples show a helicity independent all optical switching resulting from a transfer of angular momentum between layers generated during their demagnetisation. The temperatures at which AOS occurs in these systems is increased and the field history of samples has been found to play a large role in the behaviour they display upon optical exposure. The observed AOS was found to be unidirectional, likely as a result of the formation of unresolvable pinned magnetic structures. Despite improvements to the interlayer exchange coupling (IEC) between SFi layers, the number of pulses required for switching has remained comparable to Ni_3Pt based systems. This suggests that even larger IEC may be needed for single pulse switching in transition metal SFi's.

References

[1] Maciej Dąbrowski, Jade N. Scott, William R. Hendren, Colin M. Forbes, Andreas Frisk, David M. Burn, David G. Newman, Connor R. J. Sait, Paul S. Keatley, Alpha T. N'Diaye, Thorsten Hesjedal, Gerrit van der Laan, Robert M. Bowman, and Robert J. Hicken. Transition Metal Synthetic Ferrimagnets: Tunable Media for All-Optical Switching Driven by Nanoscale Spin Current. *Nano Letters*, 21(21):9210–9216, November 2021.

[2] Richard F. L. Evans, Thomas A. Ostler, Roy W. Chantrell, Ilie Radu, and Theo Rasing. Ultrafast thermally induced magnetic switching in synthetic ferrimagnets. *Applied Physics Letters*, 104(8):082410, February 2014.

[3] K. Takanashi, H. Kurokawa, and H. Fujimori. A novel hysteresis loop and indirect exchange coupling in Co/Pt/Gd/Pt multilayer films. *Applied Physics Letters*, 63(11):1585–1587, 1993.

[4] Thomas Williams and Colin Kelley. *Gnuplot 5.4 An Interactive Plotting Program*. http://www.gnuplot.info/docs_5.4/Gnuplot_5_4.pdf, September 2022.

[5] Kenneth Levenberg. A method for the solution of certain non-linear problems in least squares. *Quarterly of Applied Mathematics*, 2(2):164–168, 1944.

[6] Donald W. Marquardt. An Algorithm for Least-Squares Estimation of Nonlinear Parameters. *Journal of the Society for Industrial and Applied Mathematics*, 11(2):431–441, June 1963.

[7] C. D. Stanciu, F. Hansteen, A. V. Kimel, A. Kirilyuk, A. Tsukamoto, A. Itoh, and Th. Rasing. All-Optical Magnetic Recording with Circularly Polarized Light. *Physical Review Letters*, 99(4):047601, July 2007.

[8] A. R. Khorsand, M. Savoini, A. Kirilyuk, A. V. Kimel, A. Tsukamoto, A. Itoh, and Th. Rasing. Role of Magnetic Circular Dichroism in All-Optical Magnetic Recording. *Physical Review Letters*, 108(12):127205, March 2012.

[9] C. H. Lambert, S. Mangin, B. S.D.Ch S. Varaprasad, Y. K. Takahashi, M. Hehn, M. Cinchetti, G. Malinowski, K. Hono, Y. Fainman, M. Aeschlimann, and E. E. Fullerton. All-optical control of ferromagnetic thin films and nanostructures. *Science*, 345(6202):1337–1340, September 2014.

[10] Jung-Wei Liao, Pierre Vallobra, Liam O'Brien, Unai Atxitia, Victor Raposo, Dorothée Petit, Tarun Vemulkar, Gregory Malinowski, Michel Hehn, Eduardo Martínez, Stéphane Mangin, and Russell P. Cowburn. Controlling All-Optical Helicity-Dependent Switching in Engineered Rare-Earth Free Synthetic Ferrimagnets. *Advanced Science*, 6(24):1901876, 2019.

[11] Umut Parlak. *Optically Induced Magnetization Reversal in Co/Pt Multilayers: Role of Domain Wall Dynamics*. Number 232 in Schriften Des Forschungszentrums Jülich. Reihe Schlüsseltechnologien / Key Technologies. Forschungszentrum Jülich GmbH Zentralbibliothek, Verlag, Jülich, 2021.

[12] G. Malinowski, F. Dalla Longa, J. H. H. Rietjens, P. V. Paluskar, R. Huijink, H. J. M. Swagten, and B. Koopmans. Control of speed and efficiency of ultrafast demagnetization by direct transfer of spin angular momentum. *Nature Physics*, 4(11):855–858, November 2008.

Chapter 6

Microcoil Development

A microcoil is a helical or looped strip of conductive material with sub-millimeter dimensions. Owing to their small dimensions, microcoils are able to generate large magnetic fields which could have large practical utility in the study of magnetic materials.

The study of ultrafast magnetisation dynamics (e.g. shown in section 5.4) commonly utilises a pump-probe measurement procedure in which a constant magnetic field is applied to remagnetise and thereby reset the magnetisation state between pump-probe pulse pairs. The magnetisation dynamics induced by the pump pulse can be strongly affected by the continuously applied external field, particularly beyond the tens of picoseconds time scales as shown by [1]. This could result in a divergence from the magnetisation states that might be induced by pulsed excitation. The field assisted nature of ordinary pump-probe measurements of time-resolved magnetisation dynamics prevent the search for all-optical switching behaviour in those studies, acting as a barrier to a better understanding of AOS at ultrafast time scales.

The development of a microcoil system outlined in this section is motivated by a desire to overcome this issues through the eventual implementation of a device capable of producing a reset field into pump-probe measurement systems. A time schematic of the envisioned setup is given in figure 6.1. Such an implementation has a number of requirements. Most notably, the microcoil must produce a magnetic field strong enough to overcome the coercivity of samples. In addition, the dynamics induced by the field pulse must occur fast enough that reset dynamics are completed in the time between pump-probe pairs. Another requirement is the alignment of the optically studied region with the location of the microcoil field.

The first through to the ninth implementations of the microcoil prototype were designed by Dr Thomas H. J. Loughran at the University of Exeter using the SOLIDWORKS 3D computer-aided design software. The tenth and most recent prototype version was designed by modification of the ninth, and best performing, design.

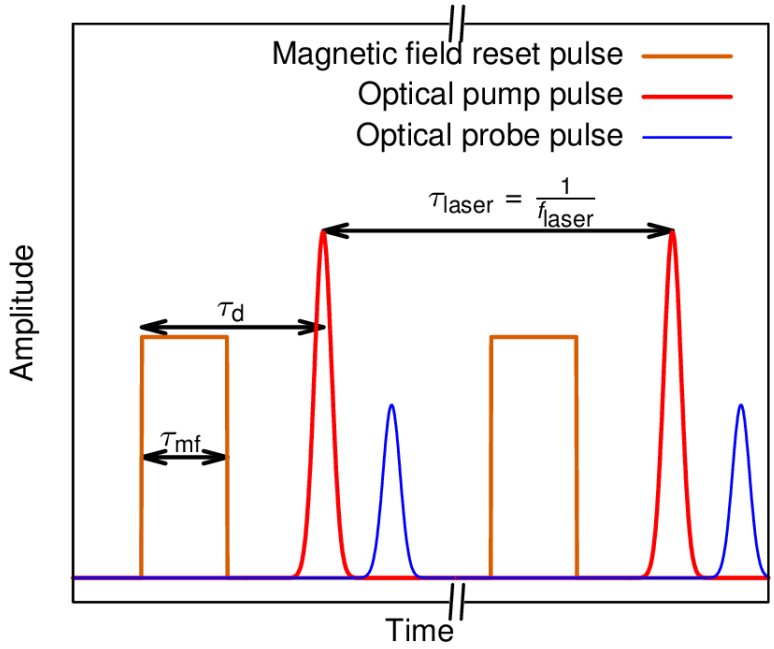

Figure 6.1: A time scheme for the desired pump-probe experiment setup. The magnetic field reset pulse (orange line) with width τ_{mf} precedes the arrival of each pump (red line) probe (blue line) pair to the sample by the delay time τ_d. The delay time must be sufficiently long for the magnetic state to reset before the earliest possible arrival of the probe (and/or pump) pulse.

6.1 Pulse Generation

In order to reset the state of a ferromagnetic or ferrimagnetic sample, a microcoil should be capable of generating enough field H_s to saturate or otherwise switch the magnetisation. Previously, Mackay et. al. demonstrated the generation of pulsed microcoil fields up to 50T [2] using currents up to 3500A, with a pulse repetition rate of 1Hz and pulse width of 30ns. Such large field and small pulse width are not necessary to saturate the thin film samples of general interest for magneto-optical storage, while the pulse repetion rate should be at least 1000 times larger for integration in to the kind of pump-probe measurements performed in section 5.4. In the study by Mackay et. al., the current pulse is generated through the use of a 12nF capacitor bank with repetition frequency determined by the atmospheric composition of a 0.4mm spark gap. In that study, the magnetic field at the centre of a coil (assuming a uniform current distribution) is given by

$$B = \frac{\mu_0 I}{r_i 2(\alpha - 1)} \ln\left(\frac{\alpha^2 + \sqrt{\alpha^2 + \beta^2}}{1 + \sqrt{1 + \beta^2}}\right), \tag{6.1.1}$$

where I is the current in amperes, $\mu_0 = 1.256 \times 10^{-6} \frac{\mathrm{Tm}}{\mathrm{A}}$ is the vacuum permeability, and $\alpha = r_o/r_i$ and $\beta = d/2r_i$, are ratios of the coil dimensions r_o, r_i and d which are the coil outer radius, inner radius and thickness (in meters) respectively. The expression given by Mackay differs slightly from its source (Montgomery [3]), which leads to a reduction in the field given by equation 6.1.1 to about 60% of the determined value. Equation 6.1.1 models the magnetic field due to a microcoil as proportional to the current I passed through the coil, through a factor which generally increases with smaller dimensions r_o, r_i and d of the coil.

The large magnitude and high frequency of currents that can be driven by pulsed laser diode drivers make them a suitable alternative that can be integrated into an experimental system without the need for in-house development of a current driver. The variable frequency AVTech AVOZ-B4-B-P pulsed voltage laser diode driver was identified as a suitable current driver owing to its large maximum current output of 100A, high maximum pulse repetition frequency of 200kHz, and low output impedance specification of $\leq 0.05\Omega$. A special 1Ω impedance 'AV-CLZ1-200' transmission cable, with a male DC-37 connector output is used to provide the current to a device or resistive load. The AVTech driver was supplied with the 'AV-CTL1-ENC' test load shown in figure 6.2a. The test load is a resistor with resistance $R = 1\Omega$, and was used to check the specifications of the unit. The voltage waveform across the load, generated by the driver was observed using a digital oscilloscope with 300MHz bandwidth and 2GSa/s sampling rate. The resulting waveform from a 500ns, 30A current pulse is shown in figure 6.2b. The pulse takes an approximately square shape, with rise and fall time of 100ns.

(a) (b)

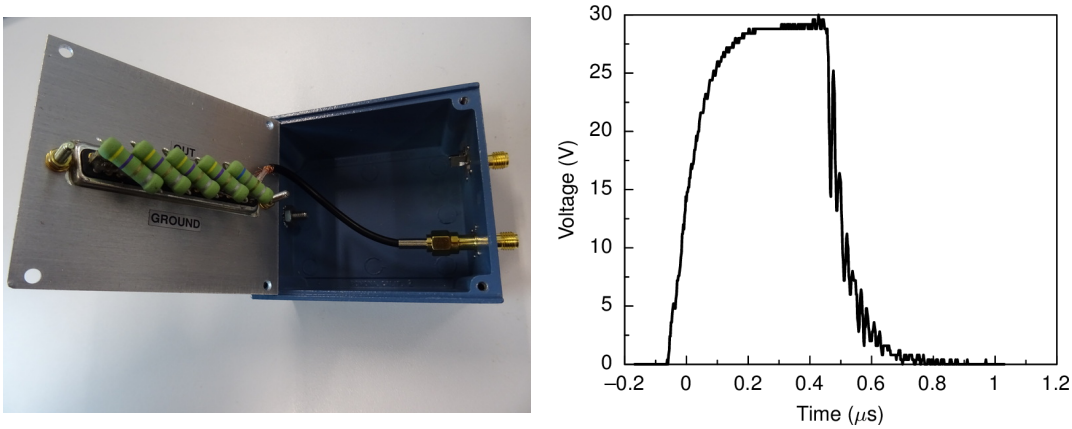

Figure 6.2: Panel (a) shows the 1Ω test load for the AVTech current driver. In panel (b) the voltage waveform measured across the testbox is shown during the application of 30V, 500ns pulses at a 1kHz repetition frequency using a 2m, 1Ω impedance transmission cable.

Because the pulses are approximately square, the power $\bar{P}$ supplied to the load in watts is given by

$$\bar{P} = \frac{f \tau_{\mathrm{mf}} V_p^2}{R}, \tag{6.1.2}$$

where f is the pulse frequency in hertz, τ_{mf} and V_p are width in seconds and voltage level in volts of a square pulse, and R is the resistance of the load in ohms. The maximum pulse width of the driver is 2µs, and the maximum power draw is 400W.

6.1.1 Microcoil Construction

The development of a microcoil suitable for use in pump-probe measurments is an ongoing iterative process. For the initial prototypes, owing to the in-house availablity of university workshop services it was decided that the development should take place through computer-aided design (CAD) of a microcoil circuit and implementation by computer numerical control (CNC) milling of double sided copper clad boards (the board material is glass-reinforced epoxy laminate usually referred to as FR-4, and with the addition of copper layers this is usually referred to as copper clad laminate). This process is better suited for rapid prototyping and testing of individual designs than chemical etching, but is ultimately limited by the size of of drill bits. This is because the milling of smaller features required for larger magnetic fields (through equation 6.1.1) requires smaller drill bits which are expensive, break easily and may not be available.

The microcoil design was implemented on to the copper clad laminate by the University of Exeter physics department workshop using a CNC milling machine and variety of drill bits to remove copper and FR-4 material as specified by a CAD model produced using SOLIDWORKS. The board used is 1.6mm thick, as constrained

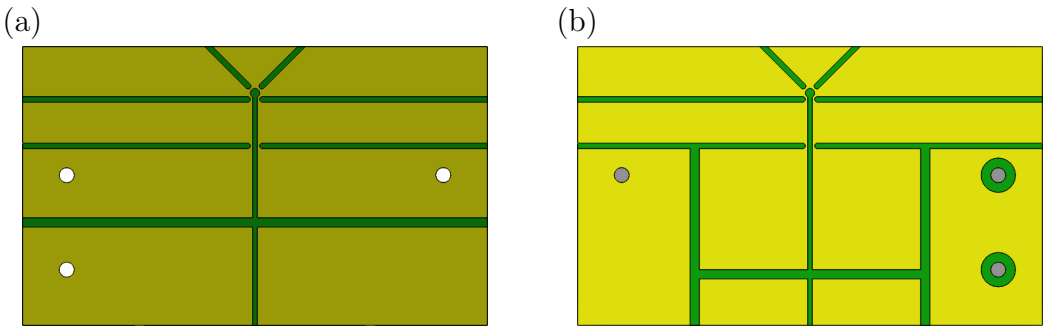

Figure 6.3: An example of the SOLIDWORKS computer aided design microcoil drawings. Panel (a) shows the microcoil side of the board and panel (b) shows the induction coil side. This design contains two vias which are bridged by a single 1 Ω resistor of the type shown in figure 6.6(a). The opposite half of the design contains another via to allow the circuit to be completed by connecting the two sides of the board. Figure 6.5 shows this version of the microcoil in its completed form.

by the gap between pins on the DC-37 connectors, required to join the device to the 1Ω impedance transmission cable. The copper foil which clads each side of the board has a thickness of 35µm. After preparation of the circuit board, the circuit is completed by the introduction of pins to connect the two sides of the board, and by soldering one or more resistors across a break on the side containing the micrcoil, resulting in a device with 1Ω resistance. A female DC-37 connector is then soldered to the edge of the board furthest from the microcoil position, in a way such that the 1-19 row of pins corresponding to the signal line of the AVTech driver connect to the copper on the side containing the microcoil, and pins 20-37 corresponding to the ground line connect to the copper on the other side of the device.

The iteration of microcoil designs corresponded to the realisation of new requirements and the removal of limiting factors. Some of the requirements realised include a ground side loop for inductive testing, space to include resistors in a parallel arrangement and a longer design to allow the microcoil to reach the desired position within the experimental setup. Limitations to be reduced as much as possible include capacitance between the copper on each side of the board, inductance arising from loops in the circuit other than the microcoil and/or the resistor components, and sharp corners in the conductive path which can increase device resistance, inductance and capacitance.

6.1.2 Circuit Waveforms

The first test to be performed on microcoil prototype devices was to check the voltage waveform across the microcoil. To do this, probes connected to a 300MHz bandwidth and 2GSa/s sampling rate oscilloscope were attached to points on the circuit either side of the microcoil, and the current driver was then used to provide pulses to the device. The resultant waveform displayed on the oscilloscope is displayed in figure 6.4b for the first version of microcoil (figure 6.4a). The first, second and third

(a) (b)

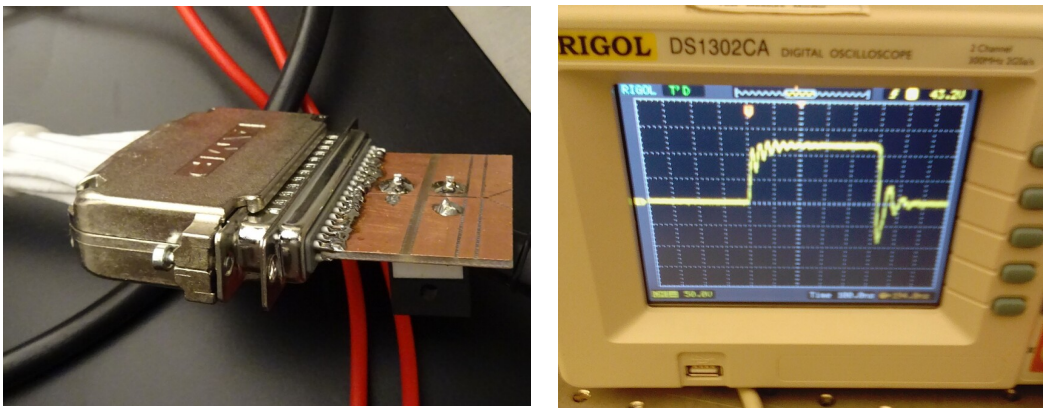

Figure 6.4: The first version of microcoil is shown in panel (a). The side of the board that can be seen in this image is connected to the the signal pins of the DC-37 cable. The circuit is completed by a 1Ω resistor and a pin between the two sides of the board. The side of the board that cannot be seen is connected to the ground pins of the cable. In panel (b) the voltage waveform measured across the microcoil is shown for a 100V, 500ns pulse on the screen of the oscilloscope used to make the measurements shown in this chapter.

microcoil devices used a single 1Ohm, 100W power rated resistor shown in figure 6.6a. The waveform shows a significant ringing signal at the rising and falling edge of the pulse resulting from the microcoil. The magnitude of ringing on the falling edge appears to have a significantly larger magnitude than that seen at the rising edge.

The design of the second microcoil version (shown in panels (a) and (b) of figure 6.5 is similar to the first, but with the resistor and connector pin moved to the outer edge to make space for a second isolated loop on the ground side on the board. This additional loop is used to make measurements of induced voltage shown in section 6.1.3. Measurements to better understand the ringing effect were performed on this microcoil, shown in figure 6.5. Panel (c) of this figure shows the effect of changing the input voltage of pulses passed through the microcoil. The height of the pulse observed in the waveform is proportional to the input voltage, and corresponds reasonably well between input and output. The ringing at the rising edge also increases in magnitude proportionally to the input voltage. At the falling edge however, the magnitude of ringing at the falling edge appears equivalent for 60V and 90V input, indicating a saturation of the falling edge ringing effect. In panel (d), the effect of varied pulse width on the waveform is shown. It is clear that the voltage level, and ringing signals are unaffected by an increase in the pulse width.

It was suspected that the resistors could be a cause of the large ringing signal, and so the single resistor was tested in the absense of the microcoil, along with a parallel arrangement of 3.9Ω resistors shown in figure 6.6 panels (a) and (c) respectively. The results of testing across those arrangements shown in panels (b) and (d) indicate a

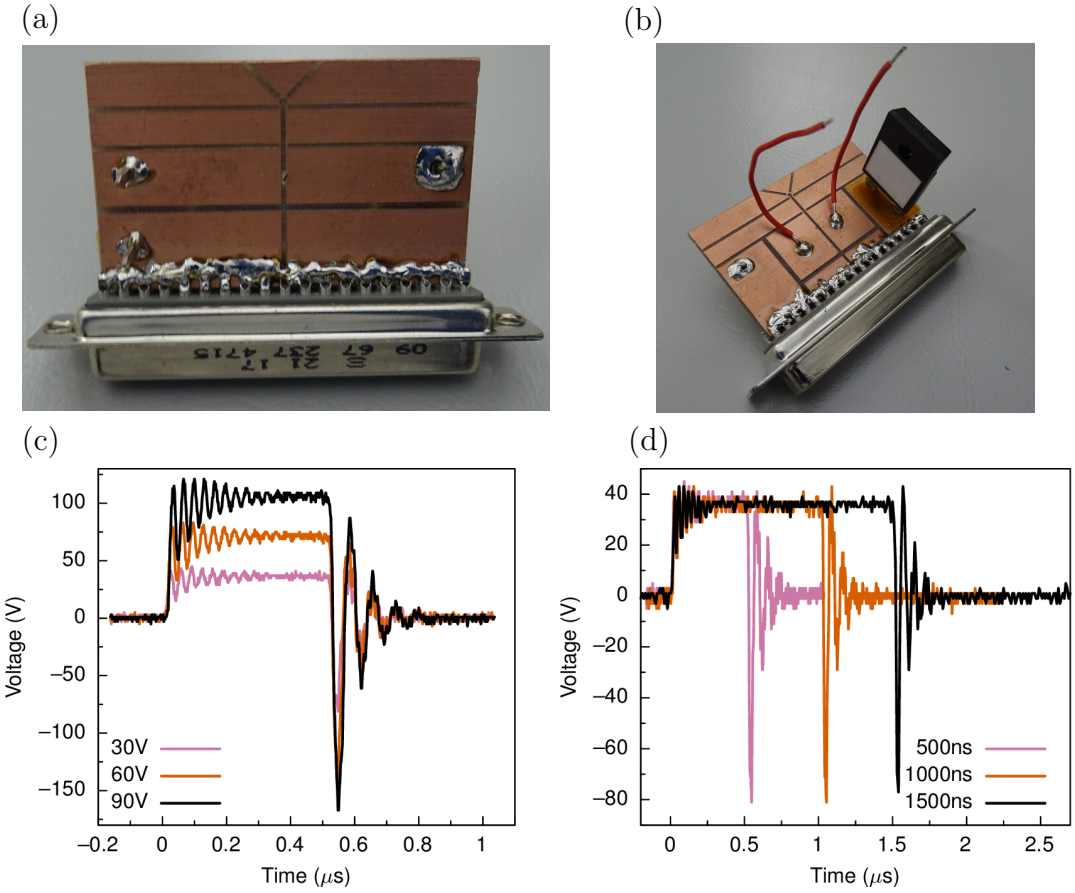

Figure 6.5: The second version of microcoil device is shown in panels (a) and (b). In panel (a), the microcoil can be seen at the top of the device. In panel (b), a test coil for induction measurements (shown for later coil versions in section 6.1.3), with red wires attached for use as probe points can be seen, mirroring the position of the microcoil. The circuit is completed by a 1Ω resistor and a pin between the two sides of the board. In panel (c) the voltage waveform measured across the microcoil is shown for a 500ns pulses at 30V, 60V and 90V for the blue, red and black lines respectively. In panel (d) the waveform of 30V pulses with 500ns, 1000ns and 1500ns widths are shown by the blue, red and black lines respectively.

significant contribution from the single resistor to the unwanted ringing signal.

Between the second and third iteration, a majority of the copper was removed on the ground side of the device to reduce capacitance between the copper on each side of the board. A small coil was left behind to continue the inductive measurements in section 6.1.3, as can be seen in figure 6.7a. The fourth and fifth microcoils were modifications to the second and third versions of microcoil respectively. In both cases, the single resistor was replaced by the parallel arrangement of the resistors seen in 6.6b. The fifth iteration of microcoil can be seen in figure 6.7b. The sixth iteration of microcoil modified the resistors on the same device further by arranging them on a sheet, and did not produce any significant change in the waveform from the fifth. The seventh iteration shown in figure 6.7 was a implemented as a new circuit board with increased length and allowed the resistors to be implemented into the design with minimal extraneous wiring. The ninth iteration of microcoil is shown in figure 6.7d. This version is designed in a way such that the current path can be spread more evenly across the width of the device. The path on each side of this device is closely matched to reduce self-inductance. A comparison of the waveform across the second, third, fifth and seventh iterations can be seen in figure 6.7e. It can be seen that the changes made contributed to a general trend of reducing the ringing observed at the rising and falling edges as desired. The fifth microcoil version is an outlier to this trend, the large ringing due to which is expected to result from the inductance introduced by the long and somewhat looped wires connecting the resistors to the board.

6.1.3 Inductance Tests

The second step taken in the development of a suitable microcoil was to test for a field generated by the coil using a pickup coil.

Through Faraday's law of induction, a change in magnetic flux through a conductive loop induces the flow of current within that loop. This principle of induction can be taken advantage of to understand the behaviour of the magnetic field pulse induced by the microcoil devices.

The initial coil design did not contain an inductive test loop on the ground side of the board, and therefore a crude coil was constructed to determine whether a magnetic field is produced as expected. The coil, and pickup waveform can be seen respectively in panels (a) and (b) or figures 6.8. The device is crude and only offers qualitative information about this initial coil design. In panel (b), the signal shown on the scope is picked up from the pickup-coil placed within 1cm of the microcoil. The signal shows behaviour intiating at the rising and falling edge of the current pulse, and then damping in an oscillating fashion.

Microcoil versions 2-8 were designed with induced voltage measurements in mind. Each of these devices contains a secondary coil with equivalent inner radius to the

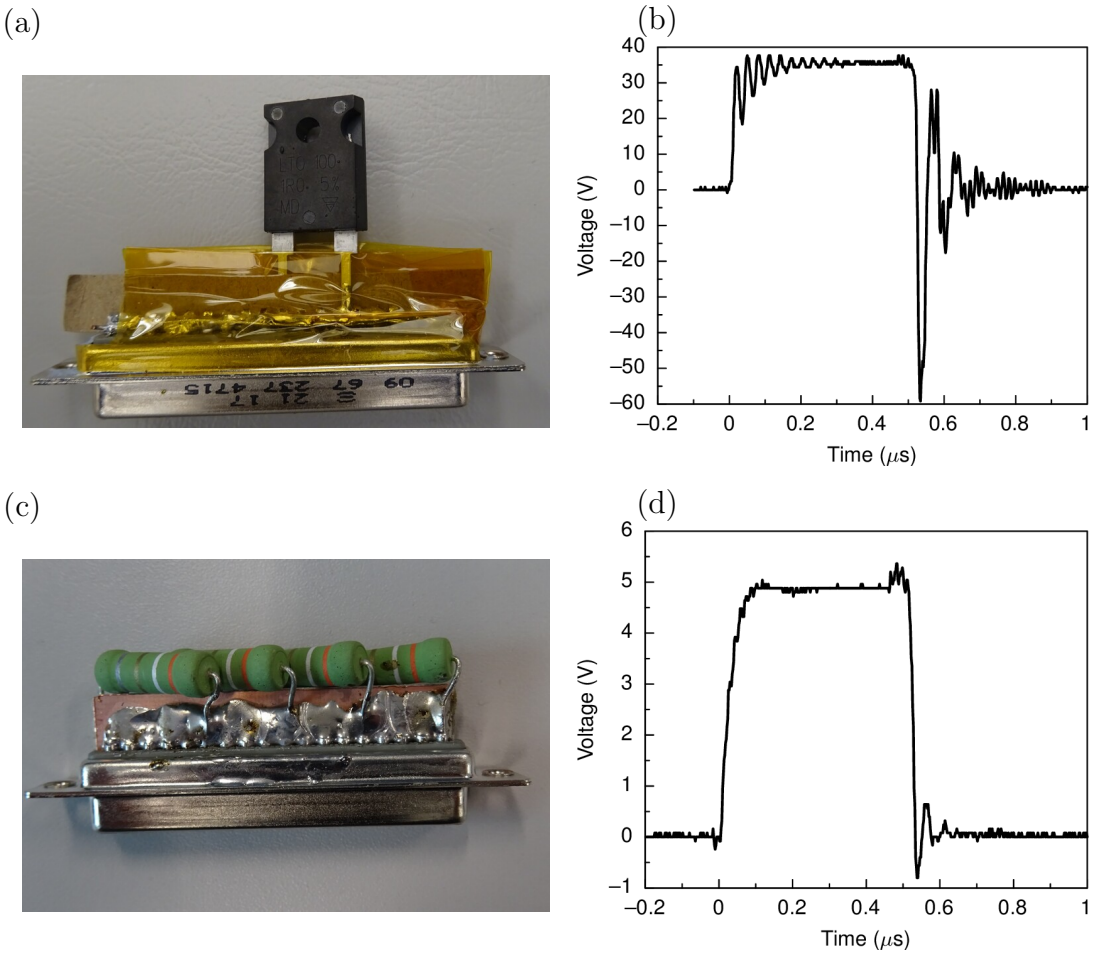

Figure 6.6: Panels (a) and (c) show two of the resistor arrangements used in the microcoil prototypes. The single black resistor shown in (a) is the 'LTO 100' 1Ω, non-inductive, 100W power rated resistor used in microcoil prototypes 1-3. Panel (b) is the waveform across that resistor for a 30V, 500ns pulse. The waveform shows a pulse with significant ringing at the rising and falling edge. Panel (c) shows the parallel arrangement of four 3.9Ω non inductive, 2W power rated 'OY39GKE' resistors used in microcoil prototypes 5-10. The parallel arrangement of resistors results in a resistance value of approximately 1Ω. Panel (d) is the waveform across that arrangement of resostors for a 5V, 500ns pulse. The waveform shows a massive reduction in the ringing at the rising and falling edge compared to the single waveform of the single 1Ω resistor.

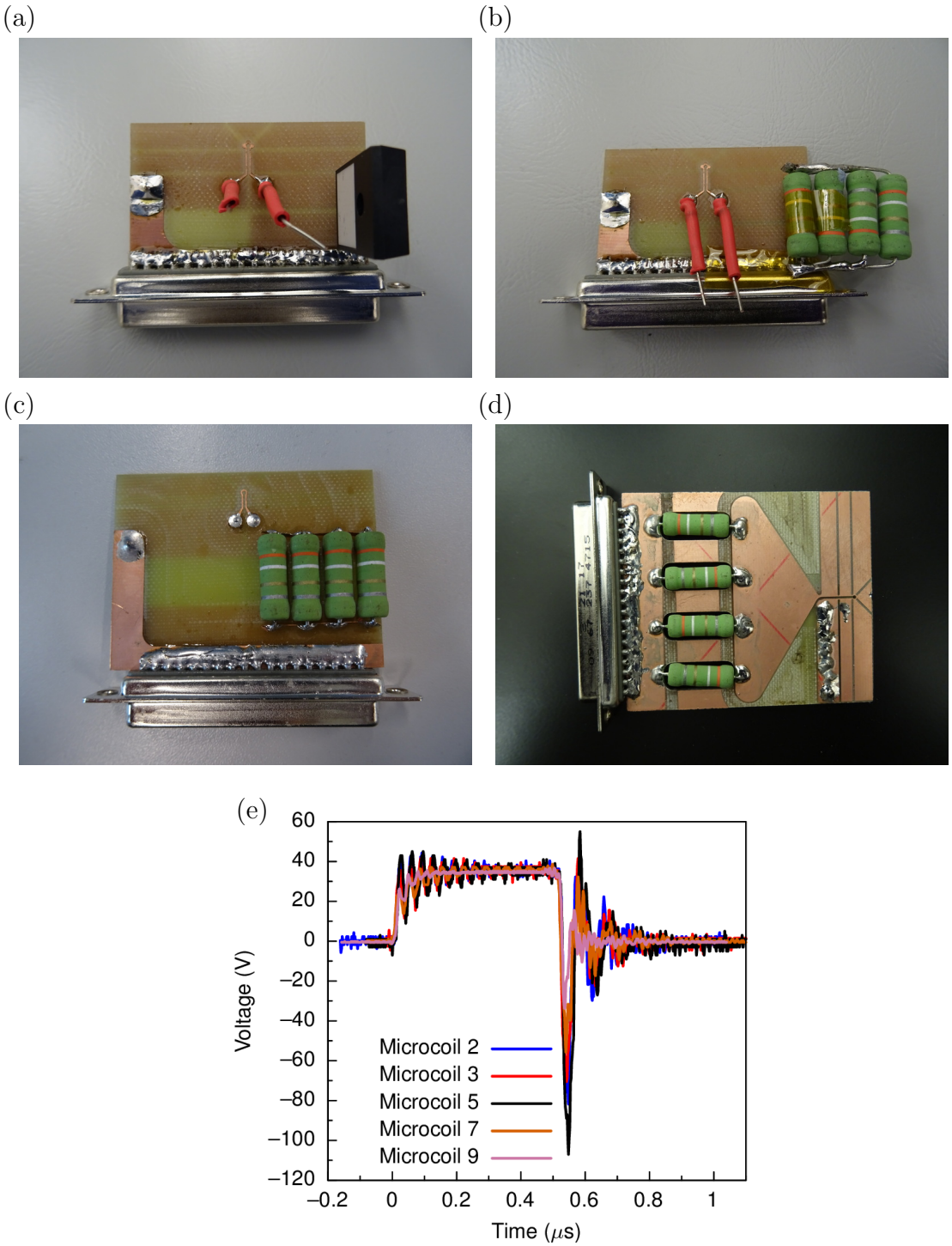

Figure 6.7: A comparison of a number of microcoil prototype devices is shown. Panel (a) shows the third microcoil with minimised excess copper on the side of the board containing the inductive test coil. Panel (b) shows the fifth microcoil which is a modification of the third version to use the arrangement of four Ohmite resistors which had been found to display a smaller ringing signal (see figure 6.6). Panel (c) shows the seventh version of microcoil with reduced length of wiring in the resistor arrangement, reducing the overall inductance of the device. Panel (d) shows the ninth version of microcoil, with conductive path more evenly distributed across the width of the board and better matching path on the front and back sides of the device resulting in reduced inductance. Panel (e) shows a comparison of the waveforms shown by the second version of microcoil, and those shown in panels (a-d).

(a) (b)

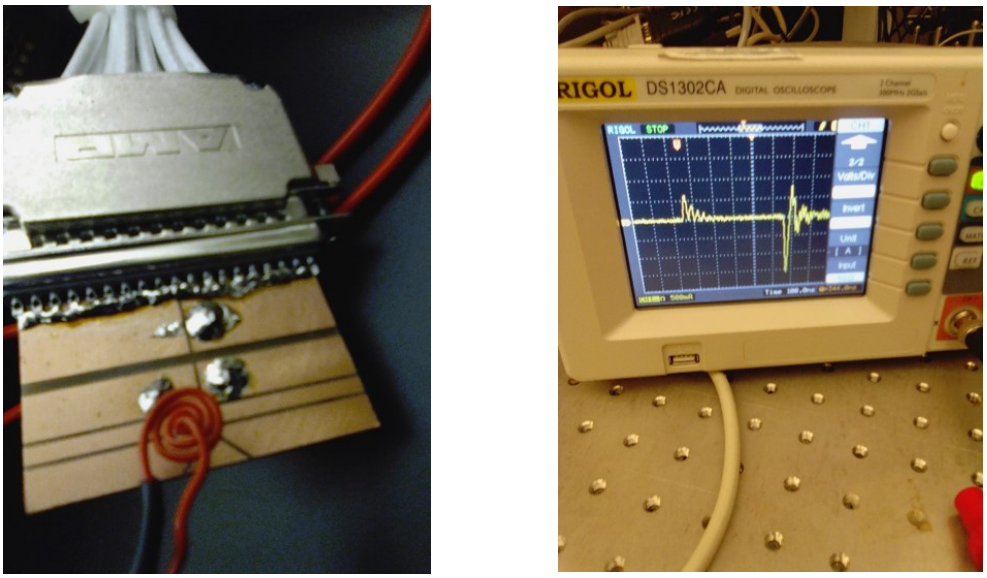

Figure 6.8: Inductive tests performed on the first version of microcoil prototype. Panel (a) shows a makeshift coil used to pick up the signal shown by the oscilloscope in panel (b).

microcoil, but on the opposite side of the board. The results of induced voltage can be better compared using this method as the shape of the test coil and its distance can be kept approximately constant, both of which have a large effect on the shape of the pickup signal. Examples of the waveforms picked up by probing these test loops can be seen in figure 6.9. The fifth and seventh microcoil versions have been shown due to their strongly differing ringing behaviour in the test shown in figure 6.7e. Unlike in that measurment, the induced voltage waveform is similar between the microcoils, with almost equivalent magnitudes of rising and falling edges and their associated ringing.

6.1.4 Identifying the source of ringing

The ringing effects seen in the waveforms obscure the properties of the pulses observed using the oscilloscope. They could also be parasitic effects which reduce the magnitude of the magnetic field produced by microcoil devices. The exact cause of the ringing observed on the rising and falling edge of waveforms has proved difficult to identify. Despite this, the results of the measurements narrow down the number of possible explanations.

The most important observation with regards to the ringing, is that it can be seen whenever both a microcoil is being pulsed and a BNC (or probe) cable is attached to the scope. This occurs regardless of whether the BNC (or probe) is attached to a detector (or probing points on the microcoil), and indicates that the cables used to probe the behaviour of the sample are acting as antennae to pick up the ringing behaviour. Comparison of the waveforms from the testbox (figure 6.2) and

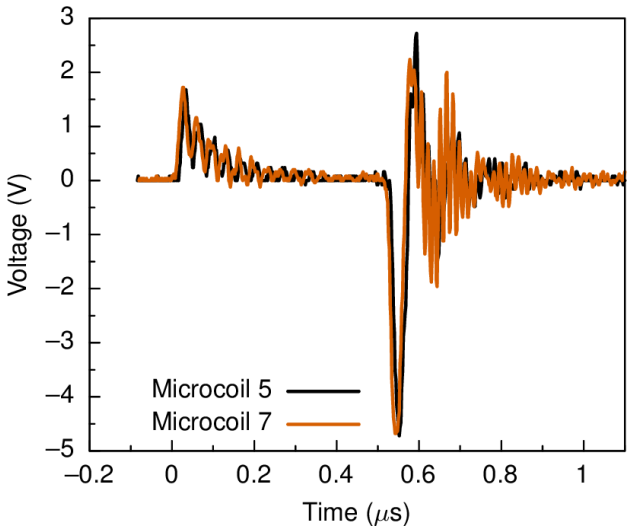

Figure 6.9: The signal picked up by the induction test coil located on the opposite side of the device to the microcoil is shown for microcoil prototype versions 5 and 7. The measurements were performed simulntaneously to the measurements across the microcoil in these devices shown in figure 6.7e using the second channel of the oscilloscope.

Ohmite resistors (figure 6.6b) which have minimal ringing, to those from the various microcoil designs show that the ringing behaviour is inherent to the design of the microcoil device. Changes to the microcoil prototypes intended to reduce capcitance (e.g. version 2 to version 3) and inductance (e.g. version 5 to version 7) have been successful in reducing the ringing effect, but there is a fundamental limit to how far these effects can be reduced. For example, the microcoil itself being a conductive loop results in a contribution to the device inductance. Furthermore the design on a double sided copper clad laminate necessitates the introduction of a second loop in order to connect the signal and ground sides of the device.

6.1.5 Magneto Optical Faraday Effect Measurements

The reductions in ringing obtained by microcoil version 7 were determined to be sufficient to begin using the devices in magneto optical setups, beginning with magneto optical Faraday effect (MOFE) measurements. The ringing is again present in these measurements, but this is thought not to be due to the magnetic behaviour of the samples, but rather due to pickup in the cables between detector and scope in the experimental setup (based on the understanding gained from previous measurements, as explained in section 6.1.4).

The eighth version of microcoil was a modification to the seventh version. A hole was drilled in the FR-4 material within the inner radius of the microcoil loop to allow for initial magneto-optical measurements to be made. The ninth version of microcoil shown in figure 6.7d was the first to be tested extensively in magneto-optical setups.

The measurements shown in this and the following section (6.1.6) were performed

with the tenth microcoil version shown in figure 6.10. This microcoil is characterised by its inner (r_i) and outer (r_o) radius of 0.25mm and 0.30mm respectively. The ninth version of microcoil with $r_i = 0.50$mm and $r_o = 0.75$mm has a similar design and was also used to perform magneto optical measurements. However, those measurements have been excluded from this section due to their similar form, but lower output field.

Figure 6.11 shows the setup used to perform MOFE measurements in order to determine the capabilities of microcoils to produce a suitable reset field. The microcoil is held in place between the poles of the electromagnet using a clamp stand to hold the cable which enters the setup from above. To improve stability a metal rod is firmly attached to the cable using cable ties and velcro straps. A schematic of the experimental setup is shown in figure 3.11. This arrangement was found to be suitably resistant to vibrations and any potential motion of the sample due to the electromagnet field. After difficulty preparing the position of the microcoil in situ, it was found to be much easier to remove the electromagnet from the setup while preparing the optics. When the microcoil is set in place and the electromagnet is moved back in to position, care must be taken to ensure that the field from the electromagnet is perpendicular to the sample plane.

The MOFE measurements are performed in a transmission geometry where the laser is passed through the sample and detected on the other side. This geometry simplifies the setup, as the sample can be mounted directly to the microcoil and the laser can be passed through the hole in the centre of a microcoil, behind which the area of the sample affected by the coil field is directly probed. To perform transmission geometry measurements requires a transparent magnetic material. Magnetic garnet is suitable for this purpose as it is transmissive and has a large Verdet constant. The garnet sample used in this section has a dark orange colour and is suitably transmissive to the 633nm red light of the He-Ne laser used for measurements. Identification of the type of garnet has not been possible, though only a single garnet sample has been used to perform MOFE measurements in the microcoil test setup.

The first tests using this microcoil shown in figure 6.12, were performed with a gain/bandwidth setting of 10^4/50MHz. At this setting, the magneto optical waveforms seen in panel (b) show significant ringing behaviour at the rising and falling edge. In order to determine the switching percentage corresponding to the voltage waveform, the height of a static MOFE loop is measured, shown in panel (a). In that panel, the voltage signal has been calibrated to give a measure of the Faraday rotation. A (microcoil) switching percentage of 0% in panel (b) corresponds to a Faraday rotation associated with the top of the loop. Likewise, a switching percentage of 100% corresponds to a rotation associated with the bottom of the loop. It can be seen that for electromagnet field of 4.6mT, prior to the effect of a pulse the garnet begins in a state close to positive saturation. On application of the 2µs

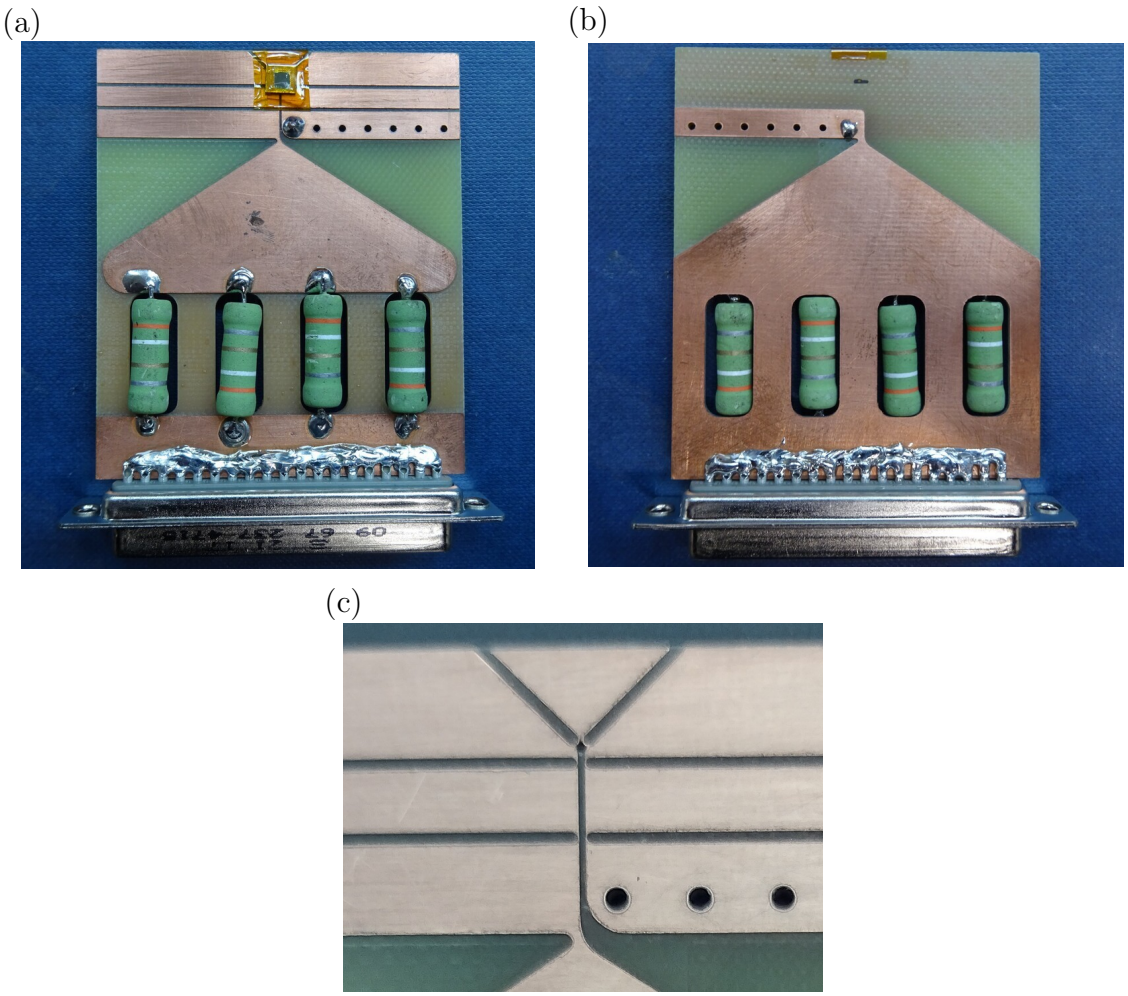

Figure 6.10: Images of the tenth iteration of microcoil. Panel (a) shows the side of the circuit board containing the coil and soldered to the signal row of DC-37 connector pins. A sample is shown fixed in place facing towards the coil using Kapton tape. A square section of tape has been removed from the back of the sample to allow for transmissive (magneto optical Faraday effect) measurements which are possible due to the double side polished sapphire substrate (an early test sample). Panel (b) shows the side of the circuit board soldered to the ground row of connector pins. The position of the hole drilled through the centre of the microcoil has been marked in black to aid alignment of the microcoil in the experimental setup. A single point of connection has been made between the two sides of the circuit board by soldering a wire through the device beneath the microcoil position in the image shown. Panel (c) shows the microcoil shortly after manufacture. The coil was designed using the SOLIDWORKS 3D computer-aided design software, and specified to have inner and outer coil radius of 0.25mm and 0.30mm respectively. The microcoil design was implemented on a double sided copper circuit board by the University of Exeter physics department workshop using a drill press and variety of drill bits. Four 3.9Ω resistors are soldered in a parallel arrangement to complete the circuit, resulting in a device with 1Ω resistance.

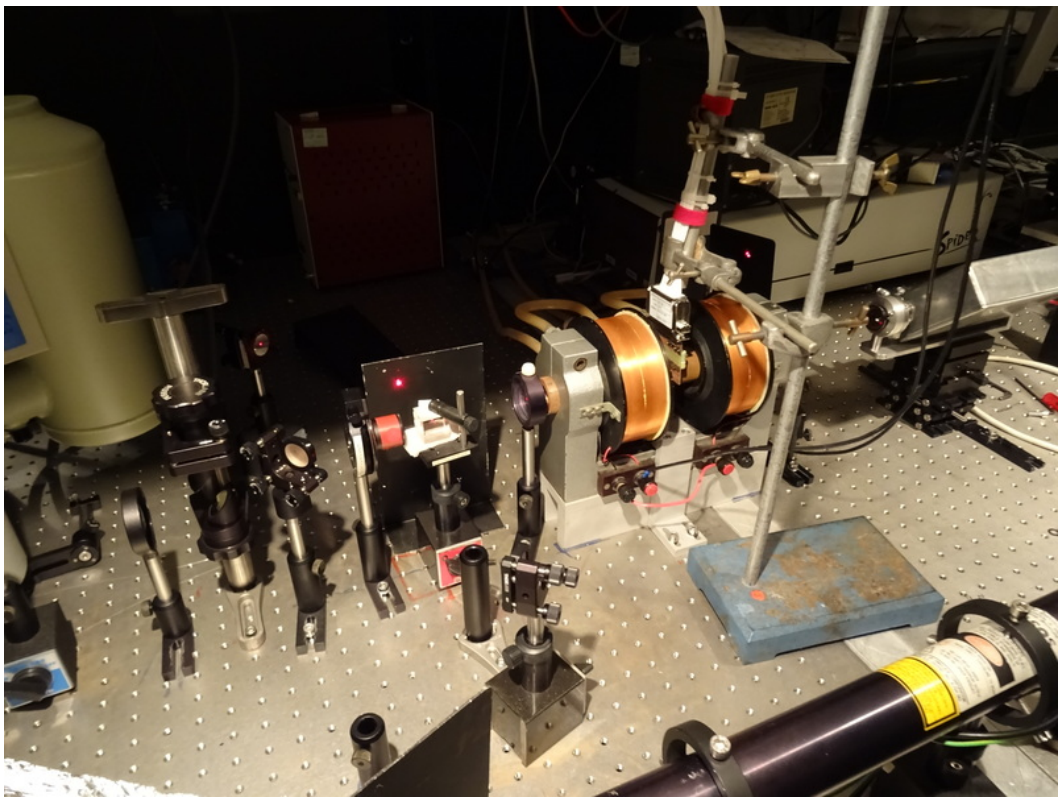

Figure 6.11: A photograph of the setup as used to perform magneto optical Faraday effect measurements in a transmission geometry. A schemetic of the setup can be seen in figure 3.11.

magnetic pulse, the magnetisation is taken to the negative saturation state within approximately 1µs. The garnet remains in the negative saturation state for around 5 µs until the electromagnet field begins a much slower process of return to the initial magnetisation state, which takes place over the course of about 7 µs. When the electromagnet field is set to 8.0mT, a similar amount of switching is seen, but with different behaviour. In that case, the sample begins in a positive saturation state and continues switching for the full 2µs that the microcoil pulse occurs over. The electromagnet field then almost immediately begins returning the sample to the initial state, the completion of which takes place over another 3 µs. These results can be seen much more clearly in figure 6.13b. In figure 6.13, the same measurements were performed using a gain/bandwidth setting of 10^6/0.3MHz. This large reduction in bandwidth removes the high frequency ringing oscillations from the observed waveform, allowing the magnetisation dynamics to be observed independently. Panel (c) shows a measure of the difference between the highest and lowest values for all the electromagnet fields tested for the samples. A range of external fields from -2mT to 8mT show some level of switching between two states. Below -4mT the magnetisation remains in the negative saturation state as a combined effect of the electromagnet field and microcoil pulses. Above 10mT, the microcoil is unable to induce any change in the magnetic state of the garnet against the effect of the magnetic field. In addition to the standard hysteresis loop given by the black

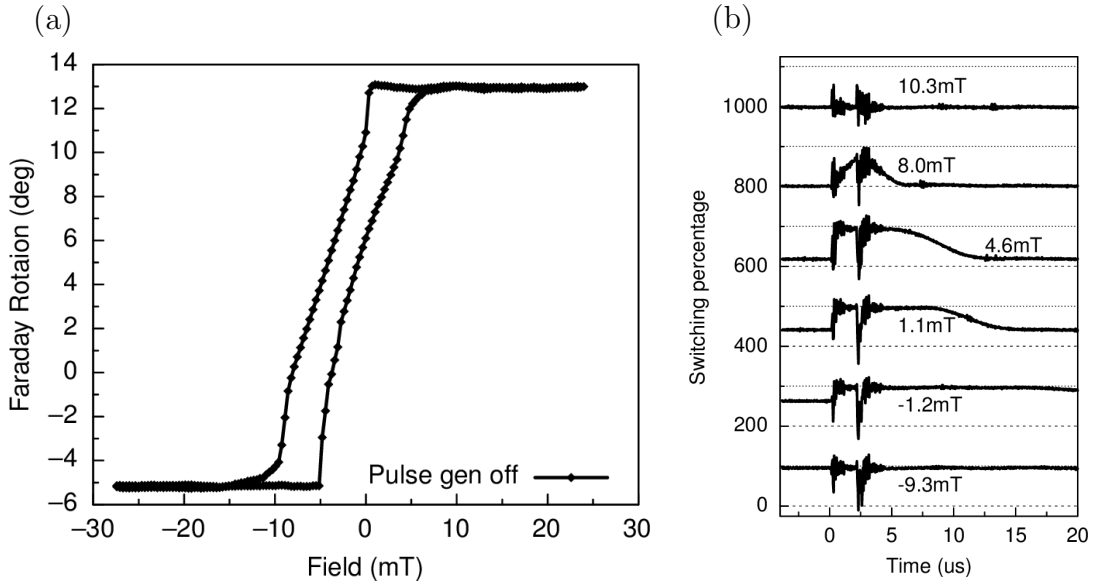

Figure 6.12: Magneto optical Faraday effect measurements of the garnet sample performed using the microcoil setup in a transmission geometry, using the tenth iteration of microcoil, and with detector gain/bandwidth of 10^4/50MHz. Panel (a) show a hysteresis loop measured in the absense of microcoil pulses. Panel (b) shows the Faraday signal waveform measured by the high speed photodetector. The waveform shows a Faraday signal resulting from the application of 100V square pulses with 2µs width and at a repetition rate of 15Hz for different continuous external fields applied to the sample. Switching percentage is a measure of the Faraday rotation occuring towards the negative saturation state as a percentage of the full height of the loop in panel (a). The field pulses from the microcoil are in the negative direction relative to the x-axis in panel (a). A large ringing signal is observed in the waveforms at the rising and falling edge of the pulse.

line in panel (a), a red line shows a loop taken as the microcoil continuously pulses the sample. This loop shows very limited effect on the ability of the electromagnet to set the state of the sample. The loops show wasp-waists indicating the formation of multidomain states around remanence, which may have a strong effect on the dynamics induced by a magnetic pulse.

Estimation of the field produced by a microcoil of this size for a 100A pulse using equation 6.1.1 gives a value of 350mT (or 230mT from the Montgomery expression). Such a large field should easily be able to counter the effect of the +10mT continuous field from the electromagnet, and could be expected to fully switch a sample with saturation fields of the order of 10mT. This does not occur for the garnet sample, which indicates a large response time for the garnet sample. It appears that the process of multidomain state formation in garnet significantly slows the rate at which the garnet can respond, and therefore a short 2µs magnetic field becomes unable to effect the magnetisation against the action of the continuous magnetic field.

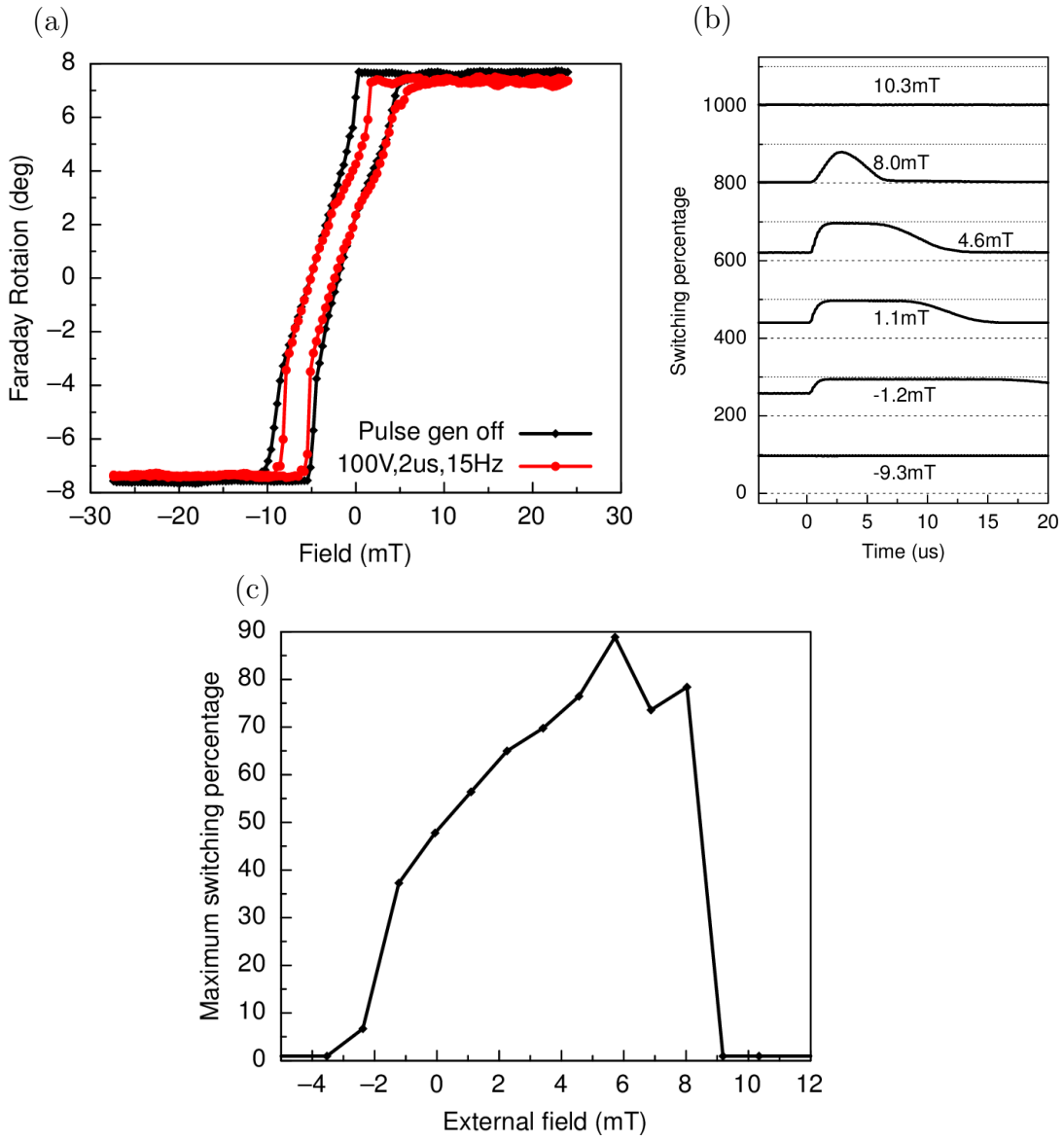

Figure 6.13: Magneto optical Faraday effect measurements of the garnet sample performed using the microcoil setup in a transmission geometry, using the tenth iteration of microcoil, and with detector gain/bandwidth of 10^6/0.3MHz. The black diamonds in panel (a) show a hysteresis loop measured in the absense of microcoil pulses, while the red circles show a loop taken during the application of 100V square pulses with 2µs width and at a repetition rate of 15Hz. These loops were taken with a field settle time of 250ms, allowing for the application of almost 4 pulses during the measurement at each point in the red curve. Panel (b) shows the Faraday signal waveform measured by the high speed photodetector. The waveform shows a measure of the Faraday signal resulting from the application of 100V square pulses with 2µs width and at a repetition rate of 15Hz for different continuous external fields applied to the sample. Switching percentage is a measure of the Faraday rotation occuring towards the negative saturation state as a percentage of the full height of the loops in panel (a). The field pulses from the microcoil are in the negative direction relative to the x-axis in panel (a). In panel (c), the maximum switching percentage due to the microcoil pulses is shown for a range of externally applied fields.

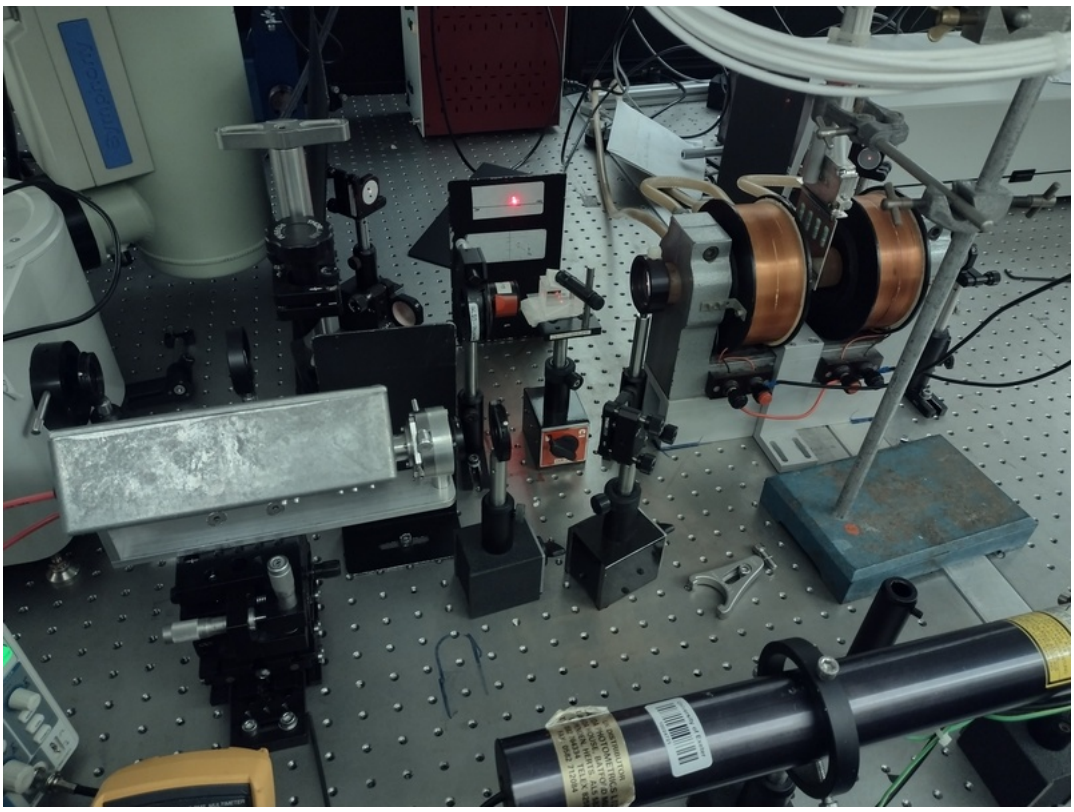

Figure 6.14: A photograph of the setup as used to perform magneto optical Kerr effect measurements in a reflection geometry. A schemetic of the setup can be seen in figure 3.11.

6.1.6 Magneto Optical Kerr Effect Measurements

The tenth iteration microcoil was also tested in a reflection geometry, better suited for measurements on metallic samples where reflection of light is high, and transmission is low or zero. A cobalt-platinum multilayer sample with large perpendicular magnetic anisotropy and coercivity relatively low compared to that predicted for the microcoil (through equation 6.1.1) was used for this purpose.

The magneto optical signal in this Co/Pt sample is far lower than for the magnetic garnet sample meaning that a high gain setting is required to make measurements with sufficient signal to noise ratio. As in the case of the garnet samples, a gain/bandwidth setting of 10^6/0.3MHz was found to be sufficient and also allows for easier comparison to the transmission geometry results.

Panel (a) in figure 6.15 shows the hysteresis loop of Co/Pt measured in this setup with microcoil pulses applied (red circles), and without pulses (black diamonds). Unlike for the garnet sample, the magnetic pulses have a very large effect on the hysteresis of the sample. This is an indication of a faster response time. The pulses move the hysteresis behaviour of the sample to a narrow field range around the positive switching field of the non pulsed loop. In panel (b), samples of the dynamics induced by the microcoil are shown for different electromagnet fields. With a 51mT external field applied, it can be seen that the microcoil can fully switch the

Co/Pt sample from positive to negative saturation when 100V, 2µs current pulses are applied. Panel (c) shows that full switching can occur for a range of fields between about 50mT and 60mT. Given that the sample can be fully switched against the action of a continuous 60mT field, comparison to the hysteresis loop indicates that the microcoil can apply effective fields of up to 120mT to this sample, making it suitable for use as a reset field of up to at least 100mT in pump probe measurements of samples with square loops and PMA.

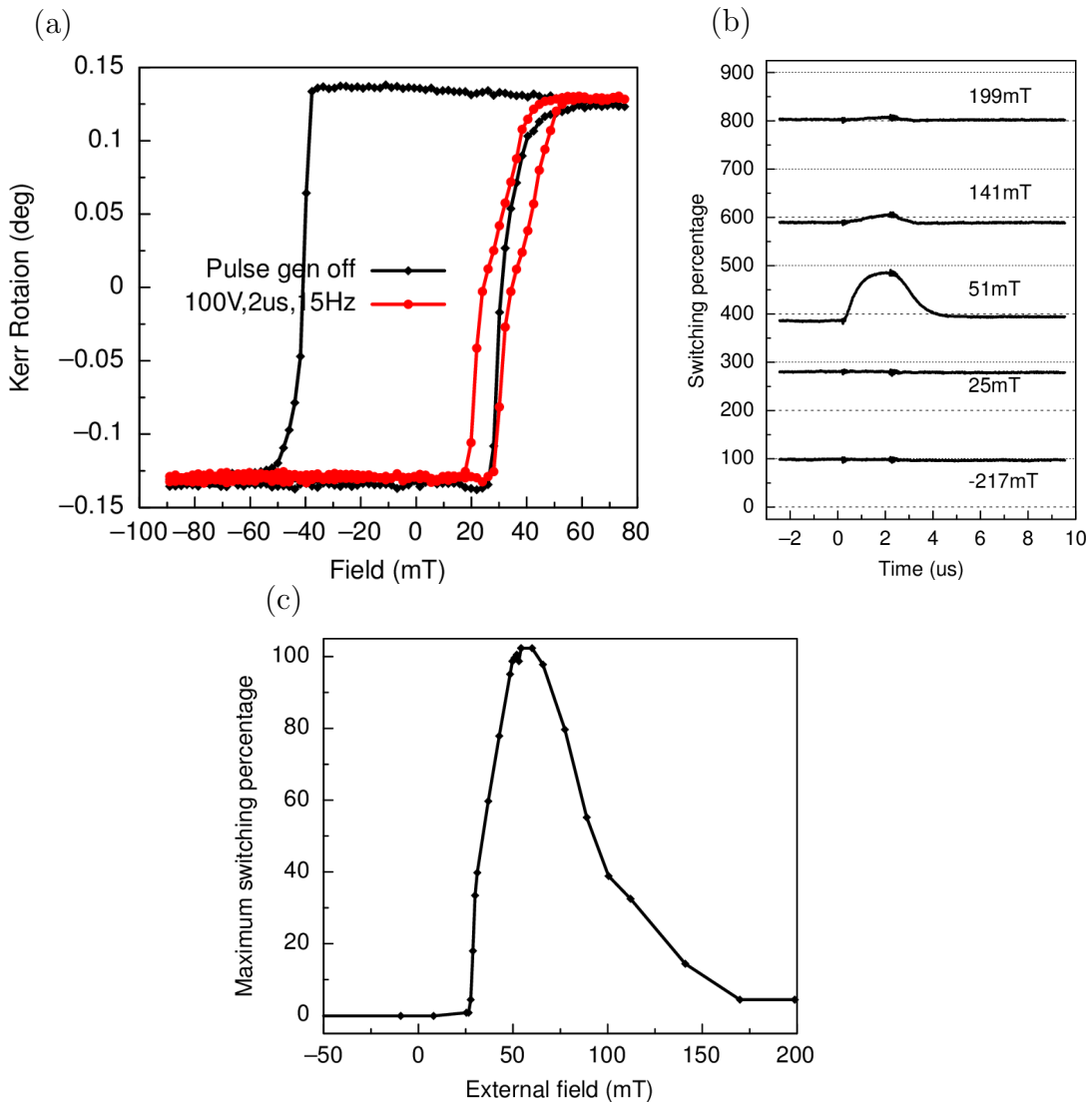

Figure 6.15: Magneto optical Kerr effect measurements of the Co/Pt multilayer sample performed using the microcoil setup in a reflective geometry, using the tenth iteration of microcoil, with detector gain/bandwidth of 10^6/0.3MHz. The black diamonds in panel (a) show a hysteresis loop measured in the absense of microcoil pulses, while the red circles show a loop taken during the application of 100V square pulses with 2µs width and at a repetition rate of 15Hz. These loops were taken with a field settle time of 250ms, allowing for the application of almost 4 pulses during the measurement at each point in the red curve. Panel (b) shows the Kerr signal waveform measured by the high speed photodetector. The waveform shows a measure of the Kerr signal resulting from the application of 100V square pulses with 2µs width and at a repetition rate of 15Hz for different continuous external fields applied to the sample. Switching percentage is a measure of the Kerr rotation occuring towards the negative saturation state as a percentage of theo full height of the loops in panel (a). The field pulses from the microcoil are in the negative direction relative to the x-axis in panel (a). A small ringing signal is observed in the waveforms at the rising and falling edge of the pulse. In panel (c), the maximum switching percentage due to the microcoil pulses is shown for a range of externally applied fields.

6.2 Future Work

The ongoing development of a microcoil for use in pump probe measurements has been an iterative process of improvements in the design of a device which has been manufactured using a CNC mill. The most recent microcoil version shown in figure 6.10 is able to provide effective fields beyond 100mT. Already this device should be capable of providing a reset field for samples with low coercivity in a pump-probe scheme. The field produced by microcoils manufactured in this manner is limited by the size of features that can be milled into the copper clad laminate. To create smaller features will require an alternative method of manufacture such as chemical etching.

Before making a change in the manufacture process, the latest version microcoil needs to be tested in a pump-probe setup to show proof of concept. Implementation will require a better way of fixing the device and sample into position. This could prove tricky in a reflection geometry, where both the pump and probe beams must either pass twice through the hole at the microcoil in the board, or else the sample must sit on the ground side of the board, facing away from the microcoil. In the former case, in order to avoid beam clipping, it will likely be required that the pump and probe are both incident normal to the sample plane, thereby needing to follow the same path to the coil. In the latter case it is likely to prove extremely difficult to overlap the pump, probe and microcoil positions, as the position of the microcoil will be obscured by the sample.

Finding a solution to these issues is likely to be easier while the inner coil radius is 250µm, before scaling to a smaller size.

Further study of the garnet sample in a transmission pump-probe setup, and/or a better understanding of its domains could help to explain the inability to fully switch that sample despite its low coercive field. Understanding its time resolved dynamics in the absence of an external field using such a setup would be a good next step to the development of a generally useful microcoil device.

6.3 Summary

An iterative process of development has been described. In addition to a pulsed magnetic field, the microcoils output a significant ringing signal at the rising and falling edge of the current pulse supplied. Attempts to reduce the capcitance and inductance of successive prototypes has proved successful in reducing the magnitude of this unwanted signal. Furthermore, the microcoils have been shown to be successful in the magnetic control of garnet and Co/Pt samples to the extent that the devices can be considered ready to implement into a pump-probe setup. Assuming successful application of the microcoil devices into such a setup, alternative manufacturing processes should be considered to further reduce the scale of microcoils and thereby increase the magnitude of the pulsed magnetic field output.

References

[1] Fangzhou Wang, Daniel E. Bürgler, Roman Adam, Umut Parlak, Derang Cao, Christian Greb, Sarah Heidtfeld, and Claus M. Schneider. Magnetization relaxation dynamics in multilayers on pico- And nanosecond timescales. *Physical Review Research*, 3(3):033061, September 2021.

[2] K. Mackay, M. Bonfim, D. Givord, and A. Fontaine. 50 T pulsed magnetic fields in microcoils. *Journal of Applied Physics*, 87(4):1996, January 2000.

[3] D. Bruce Montgomery. The generation of high magnetic fields. *Reports on Progress in Physics*, 26(1):69, January 1963.

Chapter 7

Conclusions and Future Work

In this thesis, three studies related to the topic of ultrafast magnetism were presented. The first of these, presented in chapter 4 was a theoretical study of the magnetisation dynamics predicted by the Heisenberg model of ferromagnetism in an open quantum system framework. The second topic, presented in chapter 5, was an experimental study of [Ni/Pt] based synthetic ferrimagnets, their magnetisation dynamics, and capacity for all optical switching. The third, presented in chapter 6, showed the development of microcoil devices for use in time resolved pump probe measurements of magnetic systems with perpendicular magnetic anisotropy.

The extended Heisenberg model outlined in the theoretical study (chapter 4) was shown to result in a generalised dissipative spin dynamics which is guaranteed to obey the quantum fluctuation dissipation theorem. The system is composed of two parts, one composed of spins, and the other composed of harmonic oscillator continua. The coupling between the two systems is a free parameter and through different choices of coupling, different forms of spin dynamics can be explored. The equations of motion were found for two types of coupling relationship, and made semi-classical to show the dynamics predicted on the timescale of precession. Ohmic type coupling, where the coupling is proportional to frequency, results in spin dynamics similar to the Landau Lifshitz Gilbert Brown (LLGB) equation, while a more physically realistic Lorentzian type coupling results in dynamics with non-Markovian behaviour and coloured noise thermal fluctuations. The resonant frequency can be chosen in a Lorentzian framework, and when set much larger than the Larmor precession frequency results in behaviour that converges to the LLGB predictions in the high temperature limit. This is made possible because at high temperatures the zero point quantum noise contributions to fluctuations become neglible.

At low temperatures, the zero point noise results in larger fluctuations than the LLGB prediction, which reduces the ability of spins to align with an external field. This has significant implications for the equilibrium magnetisation of spin systems, and will be important to examine further in future studies.

For resonant frequencies comaprable to the Larmor frequency, the dynamics is

modified at all temperatures, surpressing high frequency fluctuations and allowing a faster rate of spin equilibration.

Progress has already been made in relating the coupling to the experimentally measurable density of states [1]. Further work is needed to develop methods of full quantum mechanical simulation of the dissipative magnetisation dynamics, and/or to simulate many-spin systems. One factor that must be overcome in this regard is the requirement of memory that is introduced into the dynamics. In the LLGB model of spin dyanmics with a fully stochastic white noise, the dynamics are Markovian, and as a result predictions of the dynamics can be determined independently of the previous states. This is not true for more general dissipative dynamics, which (in theory) requires all past states of the system to be recorded and used to determine future states. Without the use of simplifying algorithms and numerical techniques, this requirement will very quickly become hugely demanding of both the data storage and computational capacity of modern hardware in the simulation of many spin systems.

The study of [Ni/Pt]/Ir/Co SFi's (chapter 5) resulted in observations of helicity independent all optical switching (AOS). Through time resolved magneto optical Kerr effect measurements, the switching mechanism was identified as a spin current transfer between ferromagnetic layers during ultrafast demagnetisation. Comparison with Ni_3Pt based SFi's studied previously showed that a similar number of pulses are required for AOS despite the increased interlayer exchange coupling. In the [Ni/Pt] based samples AOS was observed at higher temperatures (taking the limit from room temperature to 330K), and other new behaviours were seen. The samples showed a unidirectional AOS switching, which limits the ability to toggle switch in an all optical fashion. In addition, the capacity for AOS of samples was found to depend strongly on the field history used to prepare the state. When the field is reduced directly from saturation to remanence, it is possible to see AOS. On the other hand, field histories that pass through remanence before remnant optical exposure were found to result only in thermal demagnetisation. Both of these effects are thought to arise from the formation of some magnetic structure pinning the magnetisation, which is unresolvable using wide field Kerr microscopy. It is clear that AOS is far from straightforward in these samples as they show different behaviour and additional criteria for switching than systems previously reported on. These features have been identified, and the static behaviour of these samples has been explored in greater detail at the negative remanence temperature, adding to our understanding of the behaviour at that temperature which is critical to AOS.

In future studies, it would be useful to confirm the existence of such structures and better understand the mechanism behind the effects. To continue in the search for faster AOS further modifications could be made to the SFi structure. For example, it may be possible to further optimise the thickness of the Iridium interlayer to

maximise interlayer exchange coupling and thereby reduce the number of pulses required for AOS. Another approach could be to lithographically pattern the medium [2], as is possible that this could affect the domain structure in a way conducive to improved switching. Other materials may also be considered as ferromagnetic layers in the synthetic ferrimagnet system. FePt is one material that may be considered to replace [Ni/Pt] due to its high anisotropy and general interest in its use for HAMR technology, which has resulted in a focus on research and commericialisation of the material.

The development of a microcoil (chapter 6) has led to a device able to switch samples with perpendicular magnetisation. The field generated is predicted to be sufficient to reset the magnetisation state of samples with square loops and up to 120mT coercivity. This magnitude of field is lower than that predicted theoretically [3, 4], likely resulting from the response time of the sample magnetisation. This response time is driven by the behaviour of domains during a switching event and shoud be studied in full. Further modifcations could be made to the design of the microcoil, including the removal of copper and unused vias. Once the domain properties are better understood, the devices should be tested within pump probe measurements. After a working setup is established, smaller coils manufactured using chemical etching techniques can be considered, in order to raise the magnitude of pulsed fields generated for use with samples of larger coercivity.

References

[1] S. Nemati, C. Henkel, and J. Anders. Coupling function from bath density of states. *Europhysics Letters*, 139(3):36002, July 2022.

[2] B. D. Terris, T. Thomson, and G. Hu. Patterned media for future magnetic data storage. *Microsystem Technologies*, 13(2):189–196, January 2007.

[3] K. Mackay, M. Bonfim, D. Givord, and A. Fontaine. 50 T pulsed magnetic fields in microcoils. *Journal of Applied Physics*, 87(4):1996, January 2000.

[4] D. Bruce Montgomery. The generation of high magnetic fields. *Reports on Progress in Physics*, 26(1):69, January 1963.

Appendix A

Appendix A: Mathematical Tools

A.1 Cross Product

Here the cross product of two vectors $\mathbf{A}$, and $\mathbf{B}$ in a three dimensional space will be identified in form that makes use of summation notation.

Given an arbitrarily chosen set of orthogonal basis vectors $\mathbf{e}_1$, $\mathbf{e}_2$ and $\mathbf{e}_3$, the vectors $\mathbf{A}$ and $\mathbf{B}$ can be written as

$$\mathbf{A} = \begin{bmatrix} a_1 \\ a_2 \\ a_3 \end{bmatrix} = a_1\mathbf{e}_1 + a_2\mathbf{e}_2 + a_3\mathbf{e}_3, \tag{A.1.1}$$

and

$$\mathbf{B} = \begin{bmatrix} b_1 \\ b_2 \\ b_3 \end{bmatrix} = b_1\mathbf{e}_1 + b_2\mathbf{e}_2 + b_3\mathbf{e}_3, \tag{A.1.2}$$

respectively. The cross product of the two vectors is given as

$$\begin{aligned} \mathbf{A} \times \mathbf{B} = \begin{bmatrix} a_1 \\ a_2 \\ a_3 \end{bmatrix} \times \begin{bmatrix} b_1 \\ b_2 \\ b_3 \end{bmatrix} &= \begin{bmatrix} a_2b_3 - a_3b_2 \\ a_3b_1 - a_1b_3 \\ a_1b_2 - a_2b_1 \end{bmatrix} \\ &= (a_2b_3 - a_3b_2)\,\mathbf{e}_1 + (a_3b_1 - a_1b_3)\,\mathbf{e}_2 + (a_1b_2 - a_2b_1)\,\mathbf{e}_3, \end{aligned} \tag{A.1.3}$$

which can be written more compactly by making use of summation notation, and

the Levi-Civata symbol (defined in equation 2.2.7) as

$$\mathbf{A} \times \mathbf{B} = \sum_{\alpha=1}^{3} \sum_{\beta=1}^{3} \sum_{\zeta=1}^{3} a_\beta b_\zeta \epsilon_{\alpha\beta\zeta} \mathbf{e}_\alpha. \tag{A.1.4}$$

A.2 Fourier Transform

The Fourier transform $\mathcal{F}$ is a method for converting between a signal (i.e. function) and its sinusoidal components. For a function $f(t)$ that varies according to time, the application of the Fourier transform results in a function that varies in frequency $\tilde{f}(\omega)$ which describes the set of sinusoidal plane wave oscillations (by amplitude, phase, and frequency) that compose the original function

$$\tilde{f}(\omega) = \mathcal{F}\{f(t)\} = \int_{-\infty}^{\infty} f(t) e^{-i\omega t} dt, \tag{A.2.1}$$

provided the integral converges. Here ω is the angular frequency of the sinusoidal signals that compose $f(t)$.

The inverse fourier transform $\mathcal{F}^{-1}$ is the reverse process, in which the frequency domain representation of a signal can be used to determine it's value in time

$$f(t) = \mathcal{F}^{-1}\{\tilde{f}(\omega)\} = \frac{1}{2\pi} \int_{-\infty}^{\infty} \tilde{f}(\omega) e^{i\omega t} d\omega. \tag{A.2.2}$$

A.3 Generalised Susceptibility

Systems in which the observable quantites respond linearly (i.e. proportionally to the magnitude of perturbation), are referred to as linear response systems. The response r resulting from application of force f in those systems is determined by a quantity known as the susceptibility χ according to [1]

$$r(t) = \int_{-\infty}^{t} \chi(t - t') f(t') dt'. \tag{A.3.1}$$

The susceptibility can be converted to the frequency space by the use of the Fourier transform (equation 2.3.7), where it is referred to as the generalised susceptibility $\chi(\omega)$ and is a complex function

$$\chi(\omega) = \chi_1(\omega) + i\chi_2(\omega), \tag{A.3.2}$$

where the real χ_1 and imaginary χ_2 parts are known as the reactive and dissipative parts respectively.

A.4 Kramers Kronig Relations

The Kramers-Kronig relations are formulae that can be used to convert between real and imaginary parts of a linear response function. This is made possible due to the causality of physical phenomena as can be shown by consideration of the linear response function [2]. In equation A.3.2, the susceptibility $\chi(t-t')$ characterises the response to the force $f(t')$ that acts over a time interval that can be set by selection of the limits of integation. For causality to be enforced, a force at time t' later than the effect $x(t)$ at time t cannot contribute to the response. This is equivalent to ensuring that

$$\chi(\tau) = 0 \text{ when } \tau < 0. \tag{A.4.1}$$

where τ is the time difference $t - t'$. The requirement to ensure that condition can be found by separating the susceptibility into odd ($\chi_{\text{odd}}(-\tau) = -\chi_{\text{odd}}(\tau)$) and even ($\chi_{\text{even}}(-\tau) = \chi_{\text{even}}(\tau)$) parts, which can be given as the odd part

$$\chi_{\text{odd}}(\tau) = \frac{\chi(\tau) - \chi(-\tau)}{2}, \tag{A.4.2}$$

and the even part is given as

$$\chi_{\text{even}}(\tau) = \frac{\chi(\tau) + \chi(-\tau)}{2}. \tag{A.4.3}$$

The superposition of odd and even terms gives

$$\chi(\tau) = \chi_{\text{even}}(\tau) + \chi_{\text{odd}}(\tau), \tag{A.4.4}$$

through which causality (equation A.4.1) is seen to be enforced when

$$\chi_{\text{odd}}(\tau) = \text{sign}(\tau)\chi_{\text{even}}(\tau), \tag{A.4.5}$$

where

$$\text{sign}(\tau) = \begin{cases} -1 & \text{if } \tau < 0 \ , \\ 0 & \text{if } \tau = 0 \ , \\ 1 & \text{if } \tau > 0 \ , \end{cases} \tag{A.4.6}$$

so that contributions to the susceptibility exactly cancel when $\tau < 0$. By consideration of the Fourier transform of the time domain susceptability, it is possible to link its odd and even parts to the real and imaginary parts of the susceptibility in the frequency domain. Applying the Fourier transform (equation A.2.1) to equation

A.4.4, and making use of Eulers formula, $e^{-i\omega\tau} = \cos(\omega\tau) - i\sin(\omega\tau)$, shows that

$$\chi(\omega) = \int_{-\infty}^{\infty} \chi_{\text{even}}(\tau)\cos(\omega\tau)d\tau + \cancel{\int_{-\infty}^{\infty} \chi_{\text{odd}}(\tau)\cos(\omega\tau)d\tau} \\ \cancel{- i\int_{-\infty}^{\infty} \chi_{\text{even}}(\tau)\sin(\omega\tau)d\tau} - i\int_{-\infty}^{\infty} \chi_{\text{odd}}(\tau)\sin(\omega\tau)d\tau, \quad \text{(A.4.7)}$$

where the odd integrals vanish as their positive and negative contributions in τ cancel exactly. Therefore the real and imaginary parts of the generalised susceptibility (equation A.3.2) are given as

$$\chi_1(\omega) = \int_{-\infty}^{\infty} \chi_{\text{even}}(\tau)\cos(\omega\tau)d\tau = \mathcal{F}\{\chi_{\text{even}}(\tau)\}, \quad \text{(A.4.8)}$$

depending on only even parts of the time domain susceptibility, and

$$\chi_2(\omega) = -\int_{-\infty}^{\infty} \chi_{\text{odd}}(\tau)\sin(\omega\tau)d\tau = -i\mathcal{F}\{\chi_{\text{odd}}(\tau)\}, \quad \text{(A.4.9)}$$

depending only on the odd parts. Crucially, these terms are linked to one another in physical systems where causality must hold. This occurs through equation A.4.5, and allows the imaginary part of susceptibility to be fully determined from a complete knowledge of the real part, and vice-versa. Substitution of equation A.4.5 into A.4.9, and the use of the convolution theorem gives

$$\mathcal{F}\{\chi_{\text{odd}}(\tau)\} = \mathcal{F}\{\text{sign}(\tau)\chi_{\text{even}}(\tau)\} = \mathcal{F}\{\text{sign}(\tau)\} * \mathcal{F}\{\chi_{\text{even}}(\tau)\}. \quad \text{(A.4.10)}$$

The Fourier transform of the sign function is given by

$$\mathcal{F}\{\text{sign}(\tau)\} = -\frac{i}{\pi\omega}. \quad \text{(A.4.11)}$$

The convolution of $\frac{1}{\pi\omega}$ with another function is known as the Hilbert transform [2], in this case leading to

$$-i\mathcal{F}\{\chi_{\text{odd}}(\tau)\} = -\frac{1}{\pi\omega} * \mathcal{F}\{\chi_{\text{even}}(\tau)\} = -\frac{1}{\pi}\int_{-\infty}^{\infty} \frac{\mathcal{F}\{\chi_{\text{even}}(\tau)\}}{\omega - \omega'}d\omega', \quad \text{(A.4.12)}$$

which by comparison to equations A.4.8 and A.4.9 leads to the Kramers-Kronig relation

$$\chi_2(\omega) = -\frac{1}{\pi}\text{p.v.}\int_{-\infty}^{\infty} \frac{\chi_1(\omega')}{\omega' - \omega}d\omega', \quad \text{(A.4.13)}$$

which can be used to calculate the imaginary component of the susceptibility from the real part. A second Kramers-Kronig relation can be derived through a similar

method to be

$$\chi_1(\omega) = \frac{1}{\pi}\text{p.v.}\int_{-\infty}^{\infty}\frac{\chi_2(\omega')}{\omega'-\omega}d\omega', \tag{A.4.14}$$

which can be used to calculate the real component of susceptibility from the imaginary part. The integrals in equations A.4.13 and A.4.14 are preceded by 'p.v.' which refers to the Cauchy principle value, which allows the integral to be defined despite the singularity at $\omega' = \omega$.

A.5 Autocorrelation

The autocorrelation R_{XX} of a process describes the statistical relationship between a signal and a copy of itself delayed by a time τ. In other words it describes how dependent the value of that signal is on its previous values. It is calculated by

$$R_{XX}(\tau) = \langle X(t)X(t+\tau)\rangle, \tag{A.5.1}$$

where the angle brackets $\langle\rangle$ indicate the expected value, which is defined by its application to a function $f(X)$ with probability density function p_X, as

$$\langle f(X)\rangle = \int_{-\infty}^{\infty} f(\alpha)p_X(\alpha)d\alpha. \tag{A.5.2}$$

Stochastic processes are those that cannot be predicted deterministically due to the random and therefore unpredictable nature of their evolution. Despite this, they can still be defined probabilistically through statistical measures such as their expected value and autocorrelation.

A stochatic process that is independent of its previous values is said to be Markovian or memoryless, and is a completely random process [3]. However, it is possible that a stochastic process can retain its unpredictable nature, and also evolve to some extent based on its values at previous times. Such a process is non-Markovian. The Wiener-Khinchin theorem states that the Fourier transform (equation A.2.1) of the autocorrelation R_{XX} of a stochastic signal $X(t)$ is the power spectral density [4]

$$S_{XX}(\omega) = \mathcal{F}\{R_{XX}(\tau)\} = \int_{-\infty}^{\infty} R_{XX}(\tau)e^{-i\omega\tau}d\tau. \tag{A.5.3}$$

Through the inverse Fourier transform A.2.2, the autocorrelation function of a signal can be found from the power spectral density by

$$R_{XX}(\tau) = \mathcal{F}^{-1}\{S_{XX}(\omega)\} = \frac{1}{2\pi}\int_{-\infty}^{\infty} S_{XX}(\omega)e^{i\omega\tau}d\omega. \tag{A.5.4}$$

White noise is an example of a Markovian stochastic process as it is defined by its

constant power spectral density, which results in an autocorrelation equal to a delta function centred at zero delay. As an example, assume a temperature dependent, but frequency independent power spectral density $S_{XX} = \mu(T)$. The autocorrelation function is recovered as

$$R_{XX}(\tau) = \frac{1}{2\pi} \int_{-\infty}^{\infty} \mu(T) e^{i\omega\tau} d\omega = \mu(T)\delta(\tau), \tag{A.5.5}$$

which is interpreted as a complete independence in measured values of the (white) noise from any previously measured values, no matter the delay τ between measurements, i.e. a memoryless, Markovian process.

Appendix B

Appendix B: Additional Derivations

B.1 Zeeman Spin Evolution

Here the equation of motion resulting from the Zeeman Hamiltonian will be derived with additional workings shown (in comparison to that given in chapter 2.2.1).

The Zeeman field is given by

$$\hat{\mathcal{H}}_{\text{Zeeman}} = |\gamma_e| \sum_j \hat{\mathbf{S}}_j \cdot \mathbf{B}_{\text{ext}} = |\gamma_e| \sum_j \sum_\beta B^\beta_{\text{ext}} \hat{S}_{j,\beta}, \tag{B.1.1}$$

and the spin at the i'th site can be written in terms of the basis vectors as

$$\hat{\mathbf{S}}_i = \sum_\alpha \hat{S}_{i,\alpha} \mathbf{e}_\alpha. \tag{B.1.2}$$

Using these, the evolution of the spin arising from the Zeeman effect is found by the calculation of

$$\left[\hat{\mathcal{H}}_{\text{Zeeman}}, \hat{\mathbf{S}}_i\right] = |\gamma_e| \sum_j \sum_{\alpha \neq \beta = x,y,z} B^\beta_{\text{ext}} \left[\hat{S}_{j,\beta}, \hat{S}_{i,\alpha}\right] \mathbf{e}_\alpha, \tag{B.1.3}$$

where the well known spin commutation relations are given by

$$\left[\hat{S}_{j,\beta}, \hat{S}_{i,\alpha}\right] = -\left[\hat{S}_{i,\alpha}, \hat{S}_{j,\beta}\right] = -i\hbar\delta_{ij} \sum_\zeta \epsilon_{\alpha\beta\zeta} \hat{S}_{j,\zeta} \tag{B.1.4}$$

Leading to

$$\begin{aligned} \left[\hat{\mathcal{H}}_{\text{Zeeman}}, \hat{\mathbf{S}}_i\right] &= -i\hbar|\gamma_e| \sum_j \delta_{ij} \sum_{\alpha,\beta,\zeta = x,y,z} B^\beta_{\text{ext}} \hat{S}_{j,\zeta} \epsilon_{\alpha\beta\zeta} \mathbf{e}_\alpha, \\ &= -i\hbar|\gamma_e| \sum_{\alpha,\beta,\zeta = x,y,z} B^\beta_{\text{ext}} \hat{S}_{i,\zeta} \epsilon_{\alpha\beta\zeta} \mathbf{e}_\alpha, \end{aligned} \tag{B.1.5}$$

which by use of the cross product identity (equation A.1.4), can be written as

$$\left[\hat{\mathcal{H}}_{\text{Zeeman}}, \hat{\mathbf{S}}_i\right] = i\hbar|\gamma_e|\ \hat{\mathbf{S}}_i \times \mathbf{B}_{\text{ext}}. \tag{B.1.6}$$

The equation of motion for a spin in a magnetic (Zeeman) field is thereby found using the Heisenberg picture of quantum mechanics (equation 2.2.4) as

$$\frac{d\hat{\mathbf{S}}}{dt} = \frac{i}{\hbar}\left[\hat{\mathcal{H}}_{\text{Zeeman}}, \hat{\mathbf{S}}\right] = -|\gamma_e|\ \hat{\mathbf{S}}_i \times \mathbf{B}_{\text{ext}}. \tag{B.1.7}$$

B.2 Conversion between Landau-Lifshitz and Landau-Lifshitz-Gilbert equations

Chronologically, the Landau-Lifshitz (LL) equation was introduced prior to the Landau-Lifshitz-Gilbert (LLG) equation and one or the other is used to model magnetisation dynamics in any given work. Both equations model the same phenomena and as such it is possible to convert between the two, but in many cases such a conversion offers no practical advantage. Therefore, for the sake of simplicity the prefactors to both equations (which determine the rates of precession and damping) are usually treated as independent from one another. The treatment which follows has the LLG equation take a simpler (atomistic) form and then converts it into the LL equation, thereby showing the relationship between the gyromagnetic ratio γ that is found in each model.

Consider the LLG equation (equation 2.2.14)

$$\frac{d\mathbf{S}}{dt} = -|\gamma_e|\left(\mathbf{S} \times \mathbf{B}_{\text{eff}} - \eta\mathbf{S} \times \frac{d\mathbf{S}}{dt}\right). \tag{B.2.1}$$

The cross product of $\mathbf{S}$ with the LLG equation is

$$\mathbf{S} \times \frac{d\mathbf{S}}{dt} = -|\gamma_e|\left(\mathbf{S} \times (\mathbf{S} \times \mathbf{B}_{\text{eff}}) - \eta\mathbf{S} \times \left(\mathbf{S} \times \frac{d\mathbf{S}}{dt}\right)\right). \tag{B.2.2}$$

The triple vector product term

$$\mathbf{S} \times \left(\mathbf{S} \times \frac{d\mathbf{S}}{dt}\right) = \left(\mathbf{S} \cdot \frac{d\mathbf{S}}{dt}\right)\mathbf{S} - (\mathbf{S} \cdot \mathbf{S})\frac{d\mathbf{S}}{dt}, \tag{B.2.3}$$

can be simplified by using the constant magnitude of the spin vector

$$\mathbf{S} \cdot \frac{d\mathbf{S}}{dt} = \frac{1}{2}\frac{d\mathbf{S}^2}{dt} = 0 \tag{B.2.4}$$

to simplify equation B.2.2 as

$$\mathbf{S} \times \frac{d\mathbf{S}}{dt} = -|\gamma_e| \left(\mathbf{S} \times (\mathbf{S} \times \mathbf{B}_{\text{eff}}) - \eta S^2 \frac{d\mathbf{S}}{dt} \right). \tag{B.2.5}$$

which is again expanded by substitution of the LLG equation

$$\mathbf{S} \times \frac{d\mathbf{S}}{dt} = -|\gamma_e| \mathbf{S} \times (\mathbf{S} \times \mathbf{B}_{\text{eff}}) + \eta S^2 |\gamma_e|^2 \mathbf{S} \times \mathbf{B}_{\text{eff}} - \eta^2 S^2 |\gamma_e|^2 \mathbf{S} \times \frac{d\mathbf{S}}{dt}, \tag{B.2.6}$$

which when rearranged shows that

$$\mathbf{S} \times \frac{d\mathbf{S}}{dt} = -\frac{|\gamma_e|}{1 + \eta^2 S^2 |\gamma_e|^2} \mathbf{S} \times (\mathbf{S} \times \mathbf{B}_{\text{eff}}) + \frac{\eta S^2 |\gamma_e|^2}{1 + \eta^2 S^2 |\gamma_e|^2} \mathbf{S} \times \mathbf{B}_{\text{eff}}, \tag{B.2.7}$$

which can be substituted into the LLG equation to give

$$\frac{d\mathbf{S}}{dt} = -|\gamma_e| \mathbf{S} \times \mathbf{B}_{\text{eff}} - \frac{|\gamma_e|^2 \eta}{1 + \eta^2 S^2 |\gamma_e|^2} \mathbf{S} \times (\mathbf{S} \times \mathbf{B}_{\text{eff}}) + \frac{\eta^2 S^2 |\gamma_e|^3}{1 + \eta^2 S^2 |\gamma_e|^2} \mathbf{S} \times \mathbf{B}_{\text{eff}}, \tag{B.2.8}$$

which on rearrangement gives the Landau-Lifshitz equation

$$\begin{aligned}
\frac{d\mathbf{S}}{dt} &= -|\gamma_e| \left(\left(1 - \frac{\eta^2 S^2 |\gamma_e|^2}{1 + \eta^2 S^2 |\gamma_e|^2} \right) \mathbf{S} \times \mathbf{B}_{\text{eff}} + \frac{|\gamma_e| \eta}{1 + \eta^2 S^2 |\gamma_e|^2} \mathbf{S} \times (\mathbf{S} \times \mathbf{B}_{\text{eff}}) \right) \\
&= -|\gamma_e| \left(\frac{1}{1 + \eta^2 S^2 |\gamma_e|^2} \mathbf{S} \times \mathbf{B}_{\text{eff}} + \frac{|\gamma_e| \eta}{1 + \eta^2 S^2 |\gamma_e|^2} \mathbf{S} \times (\mathbf{S} \times \mathbf{B}_{\text{eff}}) \right) \\
&= -\frac{|\gamma_e|}{1 + \eta^2 S^2 |\gamma_e|^2} \left(\mathbf{S} \times \mathbf{B}_{\text{eff}} + |\gamma_e| \eta \mathbf{S} \times (\mathbf{S} \times \mathbf{B}_{\text{eff}}) \right) \\
&= -\gamma' \left(\mathbf{S} \times \mathbf{B}_{\text{eff}} + |\gamma_e| \eta \mathbf{S} \times (\mathbf{S} \times \mathbf{B}_{\text{eff}}) \right)
\end{aligned} \tag{B.2.9}$$

where $\gamma' = \frac{|\gamma_e|}{1 + \eta^2 S^2 |\gamma_e|^2}$.

Appendix C

Appendix C: Python Code

C.1 Pyautogui Kerrlab Automation

This section contains example functions and code written to automate the usage of the KerrLab software provided for use with the Evico wide field Kerr microscope described in section 3.2.

The script was written quickly during the usage of the WFKM setup, and were intended for fast, practical, and essentially one-time usage. As such, many coding best practices (such as appropriate variable scope) were not followed, and the modularity of scripts could be greatly improved with further iteration.

As a result of issues relating to the scope of variables, the examples given here should be considered all together in the order they appear as the Python interpreter is expected to read the script from top to bottom in a monolithic fashion. Failure to do so through the rearrangement of the ordering of functions and declarations without appropriate modification is expected to lead to errors (for example where a function relies on global variables that are yet to be declared).

The first lines of the script import the libraries used, including the 'pyautogui' and 'pywinauto' modules which have similar functionality in the automation of graphical user interface (GUI) based software.

```
import pyautogui
from pywinauto.application import Application
import time
import os
import numpy as np
import warnings
```

An image path is declared. The string gives the location on the filesystem of the WFKM computer where a set of images of the 'KerrLab' software GUI have been placed.

```
kerrlab_image_path = 'C:\\Users\\User\\Documents\\PythonAutoGUI\\KerrlabR66'
```

Variables 'history' and 'stepdelay' are declared with the intention of saving a record of the changes to the (magnetic) field magnitude, and the time interval between those changes during the experiment.

```
history = []
stepdelay = []
filename = 'placeholder'
```

The set_offset function uses 'pyautogui' to enter a field value into the KerrLab software, thereby resulting in the magnetic field provided by the electromagnet being set.

```
def set_offset(fieldmt):
    restoreKerrLab()
    pyautogui.click(offsetcontrollerposition)
    pyautogui.write(10*['delete'])
    pyautogui.write(10*['backspace'])
    pyautogui.write(str(fieldmt))
    pyautogui.click(pyautogui.position(ref[0],ref[1]))
```

The gradset function allows the movement between start and end fields at gradual intervals, with the field step and time delay between steps also being used as inputs.

```
def gradset(start_field, end_field, step, step_delay = 0.2, end_remnant = True):
    rng = np.arange(start_field, end_field + step, step)
    pyautogui.PAUSE = 0
    for field in rng:
        set_offset(str(field))
        history.append(field)
        stepdelay.append(step_delay)
        time.sleep(step_delay)
    if end_remnant is True:
        set_offset(0)
        history.append(field)
        stepdelay.append(step_delay)
        time.sleep(step_delay)
    pyautogui.PAUSE = 0.1
```

Experiment specific parameters are declared, mostly for the purpose of keeping a correct record of the experiment being undertaken (important varibles are made present in save folder and image names). This specific script was intended to be used in the comparison of beam exposures with different pulse repetition rates and therefore 'rep_rates' is a list of values.

```
input_window = pyautogui.getActiveWindow()

temp = 290 #Kelvin
pulse_width = 280 #fs
rep_rates = [10, 100, 1000] #kHz
ip_bias = 0 #mT
power = 300 #mW
state_write_field = None #mT
demag_gate_time = '100us'

sat = 104
step = 104
stepdel = 0.5

reduce_exposure = True
external_gate = False
eg = ''
print('\nConstant parameters of study:')
print('temp = ' + str(temp) + 'K')
print('pulse_width = ' + str(pulse_width) + 'fs')
print('rep_rates = ' + str(rep_rates) + 'kHz\n')

if not reduce_exposure:
    print('reduce_exposure set to False.')

if external_gate:
    print('external_gate set to True')
    eg = 'external_gate' + os.sep

if type(power) == int:
    print('constant power set to ' + str(power) + 'mW\n')
    po = str(power) + 'mW' + os.sep
elif type(power) == list:
    print('Powers ranging through' + str(power) + 'mW\n')
    po = '_'.join([str(p) for p in power]) + 'mW' + os.sep
```

```
else:
    print('power not set, assumed to be the changing variable.\n')
    po = ''

if type(state_write_field) == int:
    if state_write_field >= 0:
        rs = 'p' + os.sep
    elif state_write_field <0:
        rs = 'n' + os.sep
else:
    print('The field at which the background state was written has not been set.
----------Please record (i.e. write down) how the area being imaged was prepared.')
    rs = ''
```

This function is used to put the window for the KerrLab software in focus.

```
def restoreKerrLab():
    warnings.simplefilter("ignore", category=UserWarning)
    app = Application().start(cmd_line=u'"C:\\Program Files (x86)\\Evico Magnetics KerrLab\\KerrLab.exe" ')
    app.KerrLab
    time.sleep(0.3)
```

The 'restorePiezoController' function is used to put the window for the Piezo-electric stage controller in focus.

```
def restorePiezoController():
    warnings.simplefilter("ignore", category=UserWarning)
    app = Application().start(cmd_line=u'"C:\\Program Files (x86)\\Evico Magnetics KerrLab\\KerrLab.exe" ')
    app.LVDChild
    time.sleep(0.3)

def clickPSC(loc, length=0.5, moveAway=True):
    pyautogui.moveTo(loc)
    time.sleep(0.2)
    pyautogui.mouseDown()
    time.sleep(length)
    pyautogui.mouseUp()
    pyautogui.moveTo((loc[0] - 100, loc[1] - 100))
```

The 'fullRangePSC' function is used to control the position of the piezo stage.

```
def fullRangePSC(loc, delay=0.5, reset=False, length = 3.5):
    resetbutton, left, right, up, down, tri, stabblue, stabgrey = findPSCButtons()
    stepsize = pyautogui.locateOnScreen(kerrlab_image_path + os.sep + 'PSCstepsizexy.png')
    stepsizebox = pyautogui.position(stepsize[0] + stepsize[2] + 22, stepsize[1] + 6)
    pyautogui.click(stepsizebox)
    pyautogui.write(20*['backspace'])
    pyautogui.write(20*['delete'])
    pyautogui.write('1E+1')
    if reset:
        clickPSC(resetbutton)
    time.sleep(delay)
    clickPSC(loc, length)

def findPSCButtons():
    restorePiezoController()
    reset = pyautogui.locateCenterOnScreen(kerrlab_image_path + os.sep + 'PSCreset.png')
    left = pyautogui.locateCenterOnScreen(kerrlab_image_path + os.sep + 'PSCleft.png')
    right = pyautogui.locateCenterOnScreen(kerrlab_image_path + os.sep + 'PSCright.png')
    up = pyautogui.locateCenterOnScreen(kerrlab_image_path + os.sep + 'PSCup.png')
    down = pyautogui.locateCenterOnScreen(kerrlab_image_path + os.sep + 'PSCdown.png')
    tri = pyautogui.locateCenterOnScreen(kerrlab_image_path + os.sep + 'PSCTRI.png')
    stabblue = pyautogui.locateCenterOnScreen(kerrlab_image_path + os.sep + 'PSCstabilizeblue.png')
    stabgrey = pyautogui.locateCenterOnScreen(kerrlab_image_path + os.sep + 'PSCstabilizegrey.png')
    return reset, left, right, up, down, tri, stabblue, stabgrey
```

The 'stabilize_on' and 'stabilize_off' functions are used to switch on and off the stabilize switch in the piezo control window.

```
def stabilize_on():
    resetbutton, left, right, up, down, tri, stabblue, stabgrey = findPSCButtons()
    clickPSC(resetbutton)
    while stabgrey != None:
        restorePiezoController()
        clickPSC(stabgrey)
        resetbutton, left, right, up, down, tri, stabblue, stabgrey = findPSCButtons()
    time.sleep(3)

def stabilize_off():
    resetbutton, left, right, up, down, tri, stabblue, stabgrey = findPSCButtons()
```

```
    while stabblue != None:
        clickPSC(stabblue)
        resetbutton, left, right, up, down, tri, stabblue, stabgrey = findPSCButtons()
```

The 'saveimage' function is used to save an image of the measurement with the appropriate location and image name for the experiment.

```
def saveimage(rep_rate, savecount):
        savecount += 1

        input_window.activate()

        set_offset(0)

        if reduce_exposure:
            increase_exposure()

        stabilize_on()

        pyautogui.click(pyautogui.position(ref[0],ref[1]))
        processing = pyautogui.locateOnScreen(kerrlab_image_path + os.sep + 'processing.png')
        if processing == None:
            pyautogui.click(processingtab)
        pyautogui.press('f5')
        time.sleep(2) #May need to be changed if exposure time increases.
        saveimage = pyautogui.locateCenterOnScreen(kerrlab_image_path + os.sep + 'saveimage.png')
        if saveimage == None:
            pyautogui.click(savetab)
            saveimage = pyautogui.locateCenterOnScreen(kerrlab_image_path + os.sep + 'saveimage.png')
        imfolderselectbox = pyautogui.position(saveimage[0], saveimage[1] - 30)
        writepath = os.getcwd() + os.sep + '..' + os.sep + '..' + os.sep + str(temp) + 'K' + os.sep + \
                eg + str(pulse_width) + 'fs' + os.sep + po
        pyautogui.click(imfolderselectbox)
        pyautogui.write(1000*['backspace'])
        pyautogui.write(writepath)
        filenameselectbox = pyautogui.position(saveimage[0] - 298, saveimage[1])
        input_window.activate()
        filename = str(count + 1) + '_' + str(savecount) +'_' + str(rep_rate) + 'kHz'
        #print(filename)
        pyautogui.click(filenameselectbox)
        time.sleep(0.5)
        pyautogui.write(1000*['backspace'])
        pyautogui.write(1000*['delete'])
        time.sleep(0.5)
        pyautogui.write(filename)
        pyautogui.click(pyautogui.locateCenterOnScreen(kerrlab_image_path + os.sep + 'saveimage.png'))
        pyautogui.click(processingtab)
        pyautogui.press('f5')
        input_window.activate()

        resetbutton, left, right, up, down, tri, stabblue, stabgrey = findPSCButtons()
        stabilize_off()
        return 1
```

The exposure of the camera can be controlled using the KerrLab software, and it is worth reducing the value when the surface is exposed to the laser at high repetition rates and/or fluences to avoid damage to the camera. The 'reduce_exposure' function is used to perform this process.

```
def reduce_exposure():
    pyautogui.click(cameratab)
    expboxbl = pyautogui.locateOnScreen(kerrlab_image_path + os.sep + 'exptimeboxbottomleft.png')
    expbox = pyautogui.position(expboxbl[0] + 30, expboxbl[1] - 10)
    pyautogui.click(expbox)
    pyautogui.write(20*['backspace'])
    pyautogui.write(20*['delete'])
    pyautogui.write(laserexposure)
    pyautogui.click(pyautogui.position(ref[0],ref[1]))
```

The 'sub_on' function is used to ensure that the background subtraction switch (used to remove non magnetic features from microscope images) is set on.

```
def sub_on():
    subgrey = pyautogui.locateOnScreen(kerrlab_image_path + os.sep + 'subgrey.png')
    while not subgrey == None:
        pyautogui.click(subgrey)
        subgrey = pyautogui.locateOnScreen(kerrlab_image_path + os.sep + 'subgrey.png')
```

```
def increase_exposure():
    expboxbl = pyautogui.locateOnScreen(kerrlab_image_path + os.sep + 'exptimeboxbottomleft.png')
    if expboxbl == None:
        pyautogui.click(cameratab)
        expboxbl = pyautogui.locateOnScreen(kerrlab_image_path + os.sep + 'exptimeboxbottomleft.png')
    expboxbl = pyautogui.locateOnScreen(kerrlab_image_path + os.sep + 'exptimeboxbottomleft.png')
    expbox = pyautogui.position(expboxbl[0] + 30, expboxbl[1] - 10)
    pyautogui.click(expbox)
    pyautogui.write(20*['backspace'])
    pyautogui.write(20*['delete'])
    pyautogui.write(saveexposure)
```

The numeric values used to set the camera exposure when the laser is switched on and off are declared.

```
laserexposure = '0.002'
saveexposure = '0.02'
input_window.activate()
input('Set the QWP to 315 degrees. Set the power to ' + str(power) + 'mW. The press enter to continue.')
```

The magnetic state of the surface to which the beam will be exposed is prepared by control of the piezoelectric stage, applied field and through use of the laser. Control of the laser shutter is performed manually due to safety considerations. The user is guided through their required actions in the experimental procedure by a sequence of 'input()' functions which print a statement to the screen and require feedback in the form of keyboard entries (into the Python shell) to continue.

```
count = 0
for rep_rate in rep_rates:

    restoreKerrLab()
    ref = pyautogui.locateOnScreen(kerrlab_image_path + os.sep + 'off.png')
    tabref = pyautogui.locateOnScreen(kerrlab_image_path + os.sep + 'KLblack.png')
    if tabref == None:
        tabref = pyautogui.locateOnScreen(kerrlab_image_path + os.sep + 'kerrlablogo.png')
    offsetcontrollerposition = pyautogui.position(ref[0]+ref[2],ref[1]+(2*ref[3]))
    processingtab = pyautogui.position(tabref[0] + 32, tabref[1] + 62)
    cameratab = pyautogui.position(tabref[0] + 135, tabref[1] + 62)
    savetab = pyautogui.position(tabref[0] + 260, tabref[1] + 62)
    piezoref = pyautogui.locateOnScreen(kerrlab_image_path + os.sep + 'PSCgrey.png')

    dcgrey = pyautogui.locateOnScreen(kerrlab_image_path + os.sep + 'DCgrey.png')
    while dcgrey != None:
        pyautogui.click(dcgrey)
        dcgrey = pyautogui.locateOnScreen(kerrlab_image_path + os.sep + 'DCgrey.png')

    if reduce_exposure:
            increase_exposure()

    processing = pyautogui.locateOnScreen(kerrlab_image_path + os.sep + 'processing.png')
    if processing == None:
        pyautogui.click(processingtab)

    print('Beginning procedure to set up state.')

    restorePiezoController()
    searchon = pyautogui.locateOnScreen(kerrlab_image_path + os.sep + 'search_on.png')
    while searchon == None:
        input('Please take a reference image and find a feature to search for before continuing.
----------Take the time to test the stabilize feature.')
        input_window.activate()
        searchon = pyautogui.locateOnScreen(kerrlab_image_path + os.sep + 'search_on.png')


    resetbutton, left, right, up, down, tri, stabblue, stabgrey = findPSCButtons()

    restoreKerrLab()
    testing = False
    if count == 0 and not testing:
        stabilize_off()
        clickPSC(resetbutton)
        input_window.activate()
        A = input('Use the xy stage to find a non exposed position on the sample, focus the microscope,
------------------and stabilise using the piezo. Or type [skip] to skip the setup.')
        #A = 'skip'
```

```
        if not A == 'skip':
            stabilize_on()
            set_offset(10)
            sub_on()
            input_window.activate()
            input('\nClose the shutter, then set the rep rate to 10kHz. Prepare the visible region as
------------------fully written with +10mT and then press enter to continue.')
            set_offset(10)
            input_window.activate()
            input('\nClose the shutter and take a background image, then press enter to continue.')
            set_offset(-10)
            input_window.activate()
            input('\nWrite the left half of the screen with -10mT and position the beam back into the
------------------original spot. Then close the shutter and press enter to continue.')
            stabilize_off()
            fullRangePSC(left, reset=False)
            fullRangePSC(right, reset=False, length=1)
            set_offset(-10)
            input_window.activate()
            input('\nSet the QWP to 45 degrees. Then open the shutter and draw a vertical line with
------------------the beam. Then return the beam to its original position, close the shutter, and
--------press enter to continue.')

        set_offset(0)
        restoreKerrLab()
        resetbutton, left, right, up, down, tri, stabblue, stabgrey = findPSCButtons()
        restorePiezoController()
        clickPSC(resetbutton)

    resetbutton, left, right, up, down, tri, stabblue, stabgrey = findPSCButtons()
    stabilize_off()
    clickPSC(resetbutton)

    def bias_vert_reset(up=up, down=down, shutterOpen=True, skipso=False, biasfield='+10mT'):
        set_offset(int(biasfield[:-2]))
        if not skipso:
            if shutterOpen:
                input_window.activate()
                input('\nClose the shutter, set laser to 10kHz, open the shutter and then press enter
--------------to continue.')
            else:
                input_window.activate()
                input('\nOpen the laser shutter and then press enter to continue.')
        restorePiezoController()
        fullRangePSC(down)
        fullRangePSC(up)

    def bias_left_reset(left=left, up=up, down=down, shutterOpen=True):
        fullRangePSC(left, reset=False)
        bias_vert_reset(biasfield='+10mT', shutterOpen=shutterOpen)

    def bias_right_reset(right=right, up=up, down=down, shutterOpen=True, length=2.5):
        fullRangePSC(right, reset=False, length=length)
        bias_vert_reset(biasfield='-10mT', shutterOpen=shutterOpen)

    def full_bias_reset():
        resetbutton, left, right, up, down, tri, stabblue, stabgrey = findPSCButtons()
        clickPSC(resetbutton)
        input_window.activate()
        input('Set the QWP to 315 degrees. Then press enter to continue.')
        bias_left_reset()
        input_window.activate()
        input('\nClose the laser shutter. Then press enter to continue')
        input('\nSet the QWP to 45 degrees. Then press enter to continue')
        #clickPSC(resetbutton)
        bias_right_reset(shutterOpen=False, length=1)
        fullRangePSC(right, reset=False)
        bias_vert_reset(biasfield='-10mT', skipso=True)
        input_window.activate()
        input('Close the shutter. Then press enter to continue.')
        set_offset(0)

    stabilize_off()

    if count == 0:
        restoreskip = input('Does the domain wall need to be restored? [y/n]')
    else:
        restoreskip = 'y'

    if not restoreskip == 'n':
        clickPSC(resetbutton)
        fullRangePSC(down, reset=False)
        set_offset(10)
```

```
        input('Set the rep rate to 10kHz. Then open the shutter and clear the right hand side of
----------the field of view. Then press enter to continue.')
        input('Position the beam into the setup position. Then press enter to continue.')
        set_offset(-10)
        input('Open the shutter and clear the left hand side of
----------the field of view, without crossing the domain wall. Then press enter to continue.')
        input('Position the beam into the setup position and close the shutter. Then press enter to continue.')
        fullRangePSC(up, reset=False)
        set_offset(10)
        input('Set the QWP to 45 degrees. Then open the shutter and clear the right hand side of
----------the field of view Then press enter to continue.')
        input('Position the beam into the setup position. Then press enter to continue.')
        set_offset(-10)
        input('Open the shutter and clear the left hand side of the field of view, without crossing
----------the domain wall. Then press enter to continue.')
        input('Position the beam into the setup position and close the shutter. Then press enter to continue.')

    set_offset(-10)
    print('\nDO NOT SKIP THIS STEP!!')
    input('Set the rep rate to 10kHz. Then open the shutter and position the beam into the setup
----------position. Then press enter to continue.')
    input('\nClose the laser shutter, press enter to continue.')
    set_offset(0)
    full_bias_reset()
    set_offset(0)
    set_offset(-10)
    print('\nDO NOT SKIP THIS STEP!!')
    input('Set the rep rate to 10kHz. Then open the shutter and position the beam into the measurement
----------position. Then press enter to continue.')
    input('\nClose the laser shutter, press enter to continue.')
    set_offset(0)
    input('\nSet the rep rate to ' + str(rep_rate) + 'kHz, then press enter to continue.')
    clickPSC(resetbutton)
    stabilize_on()
    init_check = input('Visually confirm the initial state. Then press enter to continue.')
```

Finally the measurements are performed. In this case the 'fullRangePSC' function is used to scan the beam across a domain wall. The experimentalist is required to manually set the beam polarity. Images are saved before and after the process to allow for the precise determination of the effects of beam exposure.

```
    #Measurements
    savecount = 0
    clickPSC(resetbutton)
    stabilize_on()
    savecount += saveimage(rep_rate, savecount)
    stabilize_off()
    set_offset(0)
    #315QWP
    resetbutton, left, right, up, down, tri, stabblue, stabgrey = findPSCButtons()
    fullRangePSC(down, reset=False)
    input_window.activate()
    print('\nMeasurements begin now.')
    input('Set the QWP to 315 degrees. Afterwards, press enter to continue.')
    if reduce_exposure and count > 3:
        reduce_exposure()
    input('\nOpen the shutter, then move the beam horizontally across the domain wall into the
----------RHS position. Afterwards, press enter to continue.')
    input('\nClose the shutter and press enter to continue.')
    #45QWP
    fullRangePSC(up, reset=False)
    input_window.activate()
    input('\nSet the QWP to 45 degrees. Afterwards, press enter to continue.')
    input('\nOpen the shutter, then move the beam horizontally across the domain wall into the
----------original position. Afterwards, press enter to continue.')
    input('\nClose the shutter and press enter to continue.')
    input_window.activate()

    set_offset(0)
    resetbutton, left, right, up, down, tri, stabblue, stabgrey = findPSCButtons()
    while stabgrey != None:
        restorePiezoController()
        clickPSC(stabgrey)
        resetbutton, left, right, up, down, tri, stabblue, stabgrey = findPSCButtons()
    clickPSC(resetbutton)

    savecount += saveimage(rep_rate, savecount)

    input_window.activate()
    count += 1
```

```
input('Set the QWP to 315 degrees. Then press enter to continue.')
```

C.2 Spin Dynamics Python Code

This section contains the functions written in Python that were used to simulate single-spin dynamics and thermal noise in chapter 4. The scripts depend on the numerical Python library 'numpy', scientific Python library 'scipy', and the library 'tqdm' which is used to implement a progress bar into the command line output during the execution of for-loops. Python version 3.10.10 was used to execute the scripts in the preparation of this work, along with numpy version 1.24.2, scipy version 1.10.1 and tqdm version 4.64.1.

The libraries are imported as

```
import numpy as np
import numpy.random as rn
import scipy.fftpack as ft
import scipy.integrate as od
import scipy.interpolate as intpl
from tqdm import tqdm
```

Physical constants used throughout the functions are set using

```
hbar=1.05E-34
kB=1.38E-23
gam=-1.76E11
```

It is important to note that a dimensionless temperature referred to as 'barT' is commonly used as input to the following functions, rather than the temperature in Kelvin. To determine the 'barT' from the temperature 'T' in Kelvin, the following values are declared within scripts

```
omegaL = np.abs(gam)*Bext_norm
barT = kB*T/(hbar*omegaL)
```

where 'Bext_norm' is the user defined magnitude of the externally applied field in units of Tesla.

The Lorentzian kernel given in equation 4.2.85 is implemented as

```
def K_Lor(N,range_end,prm):
    dwb = 2.0*np.pi/(2.0*range_end)
    mv = np.arange(-N,N-1)
    w = mv*dwb+0.00000000001
    w0,Gamma,A=prm
    return A/(w0**2 - w**2 - 1j*w*Gamma)
```

Coloured noise given in equation 4.2.103 (with PSD given by equation 4.2.62) is implemented as

```
def b(barT,S0,prm,Nsam,N,range_end,ns=[]):
    # Fails if both not len(ns) == 0, and Nsam > 1.
    # This is because setting the input means having only a single sample.
    dt = range_end/N
    dwb = 2.0*np.pi/(2.0*range_end)
    mv = np.arange(-N,N-1)
    tvb = mv*dt
    w = mv*dwb+0.00000000001
    w0,Gamma,A=prm
    barh=hbar/S0
    if len(ns)==0:
        noise=rn.normal(scale=1.0/np.sqrt(dt),size=(N,Nsam))
    else:
        noise=ns
    psdd=barh*np.imag(K_Lor(N,range_end,prm))/np.tanh(w/(2.0*barT))
```

```
    gwv=np.sqrt(psdd)
    gwt=np.real((dwb/(2.0*np.pi))*ft.fftshift(ft.fft(gwv))*np.exp(1j*N*dwb*tvb))
    res=np.zeros((N,Nsam))
    for i in np.arange(Nsam):
        res[:,i]=np.convolve(noise[:,i],gwt,mode='valid')*dt
    return tvb, res
```

Where the high temperature limit is assumed (with PSD given by equation 4.2.80), the noise is implemented as

```
def b_classical(barT,S0,prm,Nsam,N,range_end,ns=[]):
    dt = range_end/N
    dwb = 2.0*np.pi/(2.0*range_end)
    mv = np.arange(-N,N-1)
    tvb = mv*dt
    w = mv*dwb+0.00000000001
    w0,Gamma,A=prm
    barh=hbar/S0
    if len(ns)==0:
        noise=rn.normal(scale=1.0/np.sqrt(dt),size=(N,Nsam))
    else:
        noise=ns
    eta = A*Gamma/w0**4
    psdd=(barh*2.0*barT*eta)*(1.0+0.0*w)
    gwv=np.sqrt(psdd)
    gwt=np.real((dwb/(2.0*np.pi))*ft.fftshift(ft.fft(gwv))*np.exp(1j*N*dwb*tvb))
    res=np.zeros((N,Nsam))
    for i in np.arange(Nsam):
        res[:,i]=np.convolve(noise[:,i],gwt,mode='valid')*dt
    return tvb, res
```

The autocorrelation of noise is determined using

```
def corr(barT,S0,prm,Nsam,N,range_end,seed=None,ns=[]):
    dt = range_end/N
    res = np.zeros(N)
    if len(ns) == 0:
        np.random.seed(seed)
        _, bv = b(barT,S0,prm,Nsam,N,range_end)
    else:
        _, bv = b(barT,S0,prm,Nsam,N,range_end,ns=ns)
    for i in np.arange(-N/2,N/2):
        res[int(N/2+i)] += np.sum(bv[int(N/2+i),:]*bv[int(N/2),:])/Nsam
    return res
```

The power spectral density of noise (e.g. shown by the black diamonds in figures 4.4 and 4.5) is determined using

```
def psd(barT,S0,prm,Nsam,N,range_end,seed=None,ns=[]):
    dt = range_end/N
    wv = 2.0*np.pi*ft.fftfreq(N,dt)
    cr = corr(barT,S0,prm,Nsam,N,range_end,seed=seed,ns=ns)
    psd = ft.ifft(cr)*(len(cr))*dt
    return wv, psd
```

Lorentzian single spin simulations (equations 4.2.93, 4.2.94 and 4.2.102, shown in figure 4.6) are implemented using

```
def M_sim(T,S0,prm,N,range_end,Bn,seed=None,ns=[]):
    np.random.seed(seed)
    dt=range_end/N
    nv=np.arange(-int(N/2),int(N/2))
    tva = nv*dt
    Bext_norm = np.linalg.norm(Bn)
    w0,Gamma,A=prm
    if len(ns) == 0:
        nssx=rn.normal(scale=1.0/np.sqrt(dt),size=(N,1))
        nssy=rn.normal(scale=1.0/np.sqrt(dt),size=(N,1))
        nssz=rn.normal(scale=1.0/np.sqrt(dt),size=(N,1))
    else:
        nssx=ns[0]
        nssy=ns[1]
        nssz=ns[2]
    if all([seed == None, len(ns) == 0]):
        _,bx = b(T,S0,prm,1,N,range_end)
        _,by = b(T,S0,prm,1,N,range_end)
        _,bz = b(T,S0,prm,1,N,range_end)
        bx_int=intpl.interp1d(tva,bx[:,0])
```

```
        by_int=intpl.interp1d(tva,by[:,0])
        bz_int=intpl.interp1d(tva,bz[:,0])
    else:
        _,bx = b(T,S0,prm,1,N,range_end,nssx)
        _,by = b(T,S0,prm,1,N,range_end,nssy)
        _,bz = b(T,S0,prm,1,N,range_end,nssz)
        bx_int=intpl.interp1d(tva,bx[:,0])
        by_int=intpl.interp1d(tva,by[:,0])
        bz_int=intpl.interp1d(tva,bz[:,0])
    bn=lambda t: np.array([bx_int(t),by_int(t),bz_int(t)])
    def system(V,t):
        res=np.zeros(9)
        s=V[0:3]
        p=V[3:6]
        x=V[6:9]
        Bext_dimless = Bn/Bext_norm
        Beff=Bext_dimless-x+bn(t)
        res[0:3]=np.cross(s,Beff)
        res[3:6]=-(w0**2)*x-Gamma*p+np.sign(gam)*A*s
        res[6:9]=p
        return res
    resa=od.odeint(system,[np.sign(gam),0,0,0,0,0,0,0,0],tva[1:N-2])
    Nn=len(tva[1:N-2])
    M=resa[:,0:3]
    return M
```

Where only the z-component of Lorentzian single spin dynamics is required as output, it is implemented as

```
def Mz_sim(T,S0,prm,N,range_end,Bn,seed=None):
    M = M_sim(T,S0,prm,N,range_end,Bn,seed=seed)
    return M[:,2]
```

Spin dynamics of an ensemble with Lorentzian dynamics (figure 4.7) is implemented as

```
def Mz_ave(T,S0,prm,N,range_end,Bn,num_avg=500):
    lst = []
    for i in tqdm(range(num_avg)):
        output = Mz_sim(T,S0,prm,N,range_end,Bn)
        lst.append(output)
    return [float(sum(col))/len(col) for col in zip(*lst)]
```

Ohmic single spin simulations (equation 4.2.107, shown in figure 4.6) are implemented using

```
def M_sim_classical(T,S0,prm,N,range_end,Bn,seed=None,ns=[]):
    np.random.seed(seed)
    dt=range_end/N
    nv = np.arange(-int(N/2),int(N/2))
    tva = nv*dt
    Bext_norm = np.linalg.norm(Bn)
    w0,Gamma,A = prm
    eta = A*Gamma/w0**4
    if len(ns) == 0:
        nssx = rn.normal(scale=1.0/np.sqrt(dt),size=(N,1))
        nssy = rn.normal(scale=1.0/np.sqrt(dt),size=(N,1))
        nssz = rn.normal(scale=1.0/np.sqrt(dt),size=(N,1))
    else:
        nssx=ns[0]
        nssy=ns[1]
        nssz=ns[2]
    if all([seed == None, len(ns) == 0]):
        _, bxc = b_classical(T,S0,prm,1,N,range_end)
        _, byc = b_classical(T,S0,prm,1,N,range_end)
        _, bzc = b_classical(T,S0,prm,1,N,range_end)
        bx_intc = intpl.interp1d(tva,bxc[:,0])
        by_intc = intpl.interp1d(tva,byc[:,0])
        bz_intc = intpl.interp1d(tva,bzc[:,0])
    else:
        _, bxc = b_classical(T,S0,prm,1,N,range_end,nssx)
        _, byc = b_classical(T,S0,prm,1,N,range_end,nssy)
        _, bzc = b_classical(T,S0,prm,1,N,range_end,nssz)
        bx_intc = intpl.interp1d(tva,bxc[:,0])
        by_intc = intpl.interp1d(tva,byc[:,0])
        bz_intc = intpl.interp1d(tva,bzc[:,0])
    bn=lambda t: np.array([bx_intc(t),by_intc(t),bz_intc(t)])
    def system(V,t):
        res = np.zeros(3)
```

```
        f = 1.0/(1.0+eta**2) #Required to convert to the Landau-Lifshitz form.
        s = V
        Bext_dimless = Bn/Bext_norm
        Beff = f*(Bext_dimless+bn(t)) - (eta*f)*np.cross(s,Bext_dimless+bn(t))
        res = np.cross(s,Beff)
        return res
    resa=od.odeint(system,[np.sign(gam),0,0],tva[1:N-2])
    M=resa
    return M
```

Where only the z-component of Ohmic single spin dynamics is required as output, it is implemented as

```
def Mz_sim_classical(T,S0,prm,N,range_end,Bn,seed=None):
    M = M_sim_classical(T,S0,prm,N,range_end,Bn,seed=seed)
    return M[:,2]
```

Spin dynamics of an ensemble with Ohmic dynamics (figure 4.7) is implemented as

```
def Mz_ave_classical(T,S0,prm,N,range_end,Bn,num_avg=500):
    lst = []
    for i in tqdm(range(num_avg)):
        output = Mz_sim_classical(T,S0,prm,N,range_end,Bn)
        lst.append(output)
    return [float(sum(col))/len(col) for col in zip(*lst)]
```

References

[1] L. D. Landau and E. M. Lifshitz. *Course of Theoretical Physics Volume 5, Statistical Physics Part 1.* 1980.

[2] Stephen H. Hall and Howard L. Heck. *Advanced Signal Integrity for High-Speed Digital Designs.* Wiley : IEEE, Hoboken, N.J, 2009.

[3] James Kirkwood. *Markov Processes.* CRC Press, 1 edition, April 2015.

[4] Shlomo Engelberg. *Random Signals and Noise: A Mathematical Introduction.* CRC Press, Florida, 1 edition, October 2006.